Proc. Symp. Ultrason. Electron., Vol. 25, (2004) pp. 219-220
27-29 October, 2004

Conversion of 45º rotated X-cut $KNbO_3$ Plates to Y-cut Plates by Compression

Kiyoshi Nakamura, Norihiro Chiba and ○Shigeo Ito (Tohoku univ.)

1. Introduction

Ferroelectric potassium niobate ($KNbO_3$) [1] single crystals are expected as lead-free and high-coupling piezoelectric materials. Yamanouchi et al. [2] have reported that the coupling factor K of the Rayleigh-mode surface acoustic wave (SAW) is very high, 73%, for Y-X $KNbO_3$ plates. Nakamura et al. have reported that the coupling factors for the thickness-extensional mode, k_t, are as high as about 70% at 45º-52º rotated X-cuts [3]. This value of k_t is the highest among all known piezoelectrics.

$KNbO_3$ single crystals belong to the point group mm2 of an orthorhombic system at room temperature and have a pseudo-cubic structure. Therefore, four kinds of domain states, 180°, 120°, 90°, and 60° can exist in the crystals and the domain states tend to be sensitive to a shock or an abrupt temperature change. Especially, 60º domains often occur by a stress. To the best of our knowledge, however, there has been no report on the basic behavior of domains with a stress in $KNbO_3$. It is important for practical application of $KNbO_3$ to understand the effects of a stress on domains.

If the high-k_t 45º X-plate could be converted to the high-k_{SAW} Y-plate by a mechanical stress, it would be of great interest. From such a viewpoint, we attempted to convert the 45º rotated X-cut plate (45º X-plate) to the Y-cut plate (Y-plate) by compression. To obtain a better understanding of domain-behavior, we observed domain evolution during linearly increasing the applied stress using a developed system consisting of a polarizing microscope combined with a stress application mechanism and a video camera.

This paper reports on the results of these experiments, and discussion is given to the domain-behavior, based on the video-recorded pictures.

2. Experimental procedure

$KNbO_3$ single crystal has a pseudocubic perovskite structure. The pseudo-cube is being slightly elongated along the Z-axis parallel to the spontaneous polarization. Figure 1(a) schematically shows the unit cell of the pseudocubic structure whose upper surface corresponds to the major surface of the 45º X-plate (45º X-face), while Fig. 1(b) and Fig. 1(c) show the unit cells obtained by rotation of it by 90º and -90° around the $[100]_{pc}$ axis, respectively. The upper surfaces of Fig. 1(b) and Fig. 1(c) correspond to the

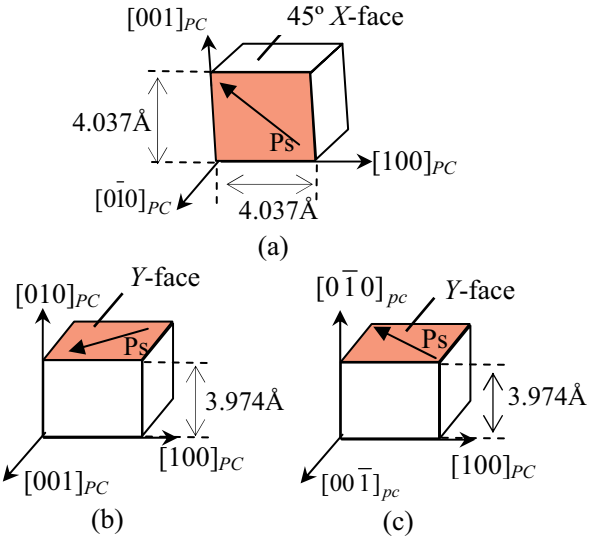

Fig. 1. Relationship between 45º X-plate and Y-plate.

major surface of the Y-plate (Y-face). The 45° X-plate and the Y-plate are in the relation of 60° domains. The lattice spacing of the 45º X-face in Fig. 1(a) is 4.037 Å, while that of the Y-face in Fig. 1(b) or Fig. 1(c) is 3.974 Å that is the minimum one. From these facts, we have supposed that if a large compressive stress is applied to the unit cell along the $[001]_{pc}$ direction in Fig 1(a), it could be converted to the unit cell in Fig 1(b) or Fig. 1(c), that is, the high-k_t 45º X-plate would be converted to the high-k_{SAW} Y-plate. The lattice spacing of $(001)_{pc}$ will be shortened due to the compression and then may suddenly become the minimum one, 3.974 Å, when the stress exceeds a threshold. In consequence, the original minimum lattice spacing of $(010)_{pc}$ elongates to 4.037 Å since it can be no longer minimum. Therefore, the 45º X-face may be converted to the Y-face. However, since the probability of the conversion to the structure of Fig. 1(b) is equal to that of Fig. 1(c), this may result in coexistence of two-types of Y-domains. To completely convert the structure of Fig. 1(a) to that of Fig. 1(c), a tensile stress along the $[\bar{1}10]_{pc}$ direction or a compressive stress along $[110]_{pc}$ direction must be applied to the 45° X-plate. However, it is difficult to apply these forces simultaneously together with the compression along $[001]_{pc}$ direction. Alternatively, we applied a compressive force tilted toward the $[\bar{1}10]_{pc}$ axis to the 45° X-face so that the component of the force along $[\bar{1}10]_{pc}$ direction might arise.

Figure 2 schematically shows a stress applica-

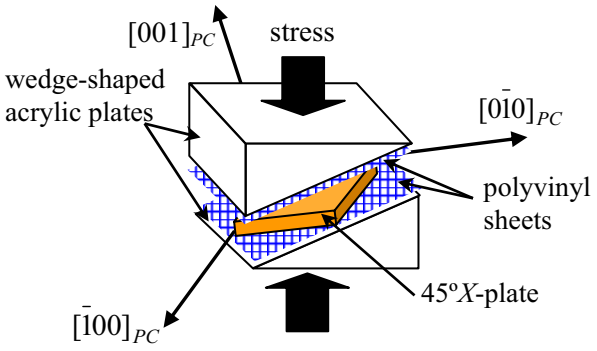

Fig. 2. Schematic of a stress application setup.

tion setup. The 45º *X*-plate is placed between two wedge-shaped acrylic plates. An oblique compressive force can be applied to the sample through the acrylic plates. Polyvinyl-chloride sheets are inserted between the sample and the acrylic plates so that the applied stress may be uniform.

3. Experiments and Results

With the tool shown in Fig. 2 we applied an oblique stress to a mirror-polished 45º *X*-plate of 7x7x1.2 mm^3, while observing the domain states using a polarizing microscope equipped with a video camera. Figure 3 shows a number of micrographs of the domain evolution during application of the stress in time sequence. Figure 3(a) shows the original plate before applying the stress. When the stress linearly increased to 6.6 MPa, a narrow domain appeared in the central region of the plate (Fig. 3(b)). The domain-wall angle of 73° with respect to the $[010]_{pc}$ axis indicates that this is a *Y*-domain. The dark belt-like region shows the domain wall extending from the top surface to the bottom obliquely with an angle of 45º. The solid and broken lines in Fig. 3 indicate the domain walls on the top and bottom surfaces, respectively. Although the applied stress was kept at 6.6 MPa, this narrow domain rapidly extended to the both lateral directions (Fig. 3(c), (d), (e)) and the *Y*-domain reached to the edges (Fig. 3(f)) in about 10 sec. In consequence, the 45º *X*-plate was completely converted to the *Y*-plate in the central region as expected. However, 45º *X*-domains still remained in the top-right and bottom-left corners of the plate. This cannot be explained satisfactorily, but the applied stress might not be uniform at the edge regions.

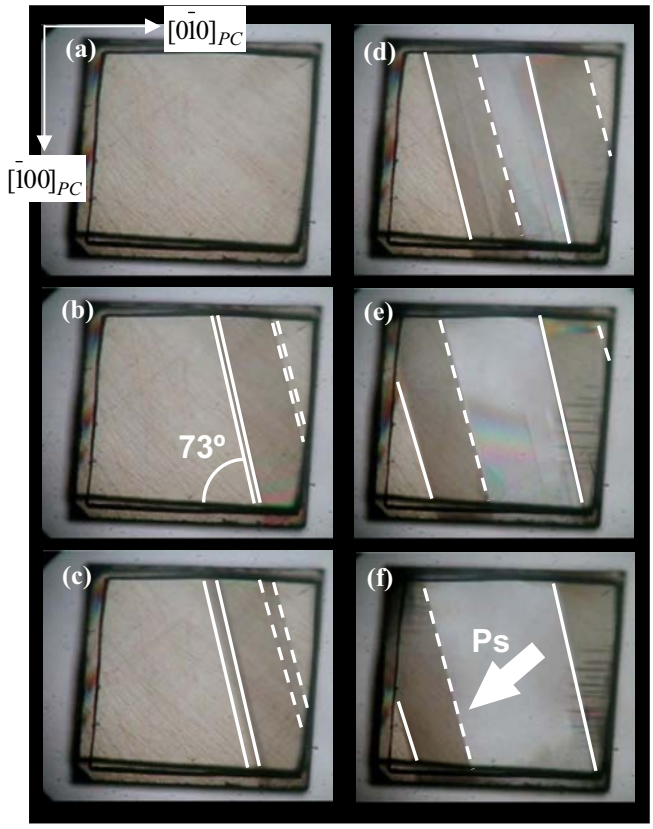

Fig. 3. Polarizing micrographs of domain evolution.

To ascertain whether the 45º *X*-plate has really converted to the *Y*-plate, XRD rocking curves of (110) and (001) reflections, which are correspond to the 45º *X*-face and the *Y*-face, respectively, were measured before and after applying the stress. The results are shown in Fig. 4. After applying the stress, a large (001) peak appeared, while a small (110) peak still remained. The area ratio of the 45º *X*-domain to the *Y*-domain was evaluated to be approximately 1:9.

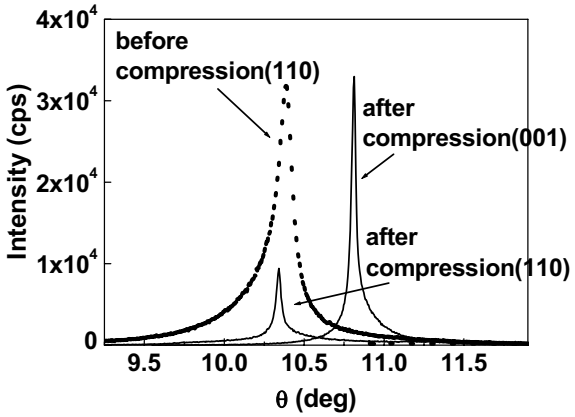

Fig. 4. XRD rocking curves before and after applying the stress.

5. Conclusion

In conclusion, we successfully converted the high-k_t 45° rotated *X*-cut $KNbO_3$ plate to the high-k_{SAW} *Y*-cut plate by applying a compressive force tilted toward the $[\bar{1}10]_{pc}$ axis to the 45° *X*-face. The domain evolution during application of a stress was observed and video-recorded using the system consisting of a polarizing microscope combined with a stress application mechanism. This observation revealed that the conversion occurs by a stress of 6.6 MPa. The X-ray diffraction analysis indicated that 90% of the 45º rotated *X*-cut plate was converted.

Reference
[1]B. T. Matthias, Phys. Rev. **75**, p.1771 (1949)
[2]K. Yamanouchi et al. Electron. Lett., **33**, p.193 (1997)
[3]K. Nakamura et al. IEEE Trans. Ultrason., Ferroelect. Freq. Contr., **47**, p.750 (2000)

Proc. Symp. Ultrason. Electron., Vol. 25, (2004) pp. 221-222
27-29 October, 2004

Exploration of piezoresponse and applicability based on Nb-doped lead zirconate titanate ceramic

Bing Huei Chen* (Nan Jeon Institute of Technology), Cheng Liang Huang and Long Wu

Abstract

In this presentation, modified lead zirconate titanate (PZT) piezoceramics with a composition Zr/Ti=53/47 containing 1 mole% Nb were prepared by conventional ceramic technology sintering powder compacts. Replacement of Ti^{+4} by Nb^{+5} in such perovskite type solid solutions was accomplished by the creation of cation vacancies. Modified ceramics were explored as a function of firing temperature to acquire exceedingly good piezoelectric characterizations. Under the processing conditions, calcined at 850^0C for 2 h, and then sintered at 1250^0C for 2 h, PZT piezoceramic showed the minimum mechanical quality factor Q_m 50 and maximum electromechanical coupling factor k_p 0.62. Measured P-E hysteresis loop illustrated that the remanent polarization (P_r) and coercive field (E_c) were 8.63 μC/cm^2 and 17.2 kV/cm, respectively. A fundamental planar mode appeared and the resonance frequency was around 200 KHz, which was suitable for piezoelectric resonator and filter applications. Besides, we also fabricated a disk-shaped sample simulated by pulse generator and surveyed the applicability of piezoresponse.

Keywords: Electromechanical coupling factor; Mechanical quality factor; Resonance frequency; Pulse generator; Piezoresponse

* Address all correspondence to this author E-mail: chenbh@ms28.hinet.net

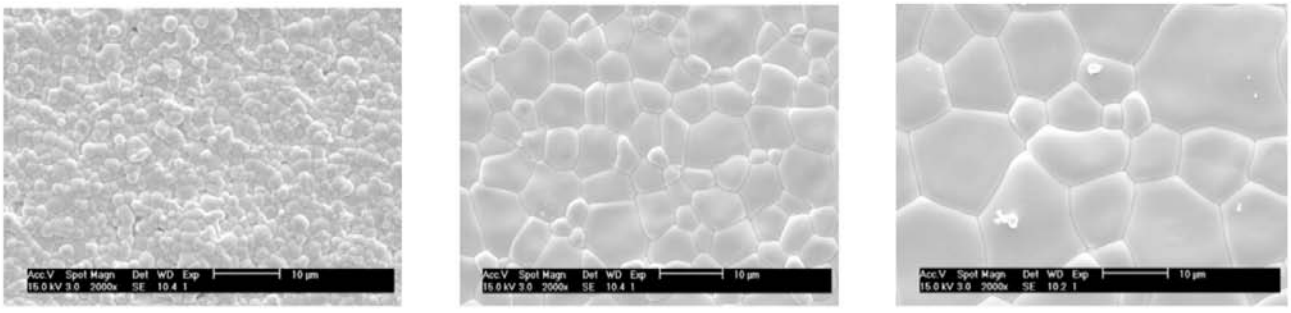

(a) (b) (c)

Fig. 1 SEM of surface morphology of PZT ceramics doped with 1 mole% Nb_2O_5 calcined at 850°C for 2 h, and sintered at (a) 1100°C (b) 1200°C (c) 1250°C for 2 h.

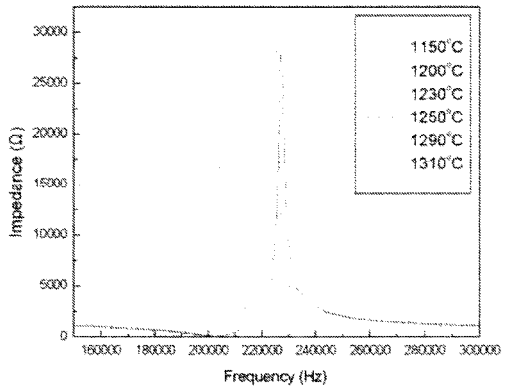

Fig. 2 Variation of impedance with frequency for the poled doped with Nb_2O_5 PZT ceramic calcined at 850°C for 2 h, sintered at various temperatures for 2 h.

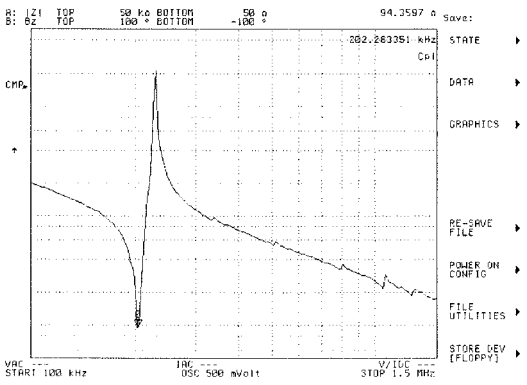

Fig. 3 Variation of impedance with frequency for the doped with Nb_2O_5 PZT ceramic calcined at 850°C for 2 h, sintered at 1250°C for 2 h.

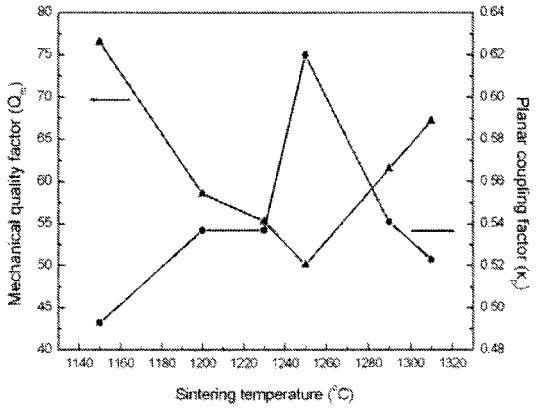

Fig. 4 Variation of piezoelectric properties for doped with Nb_2O_5 PZT ceramic calcined at 850°C for 2 h, sintered at various temperatures for 2 h.

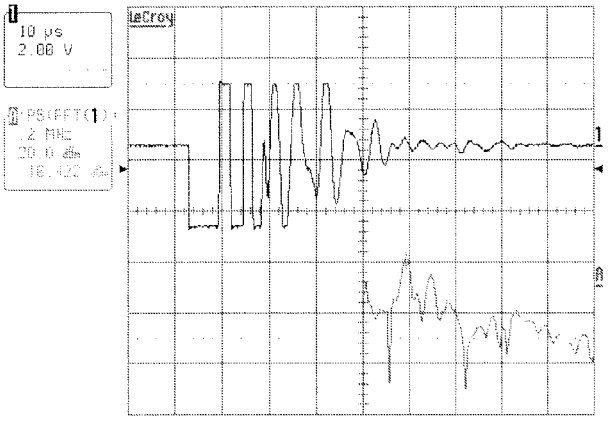

Fig. 5 Pulse-echo response of a PZT ceramic doped with Nb_2O_5 calcined at 850°C for 2 h, sintered at 1250°C for 2 h.

References

1. H.Haertling, Ferroelectrics, 75 (1987) 25.
2. F.Scott, C.A.Paz de Araujo, Science, 246 (1989) 1400.
3. V.A.Isupov, Ferroelectrics, 46 (1983) 217.
4. N.Venevtsev,G..S.Zhdanov, Acad.Sci.USSR, 20 (1956) 161.
5. S.B.Majumder, B.Roy, R.S.Katiyar, S.B.Krupanidhi, J.Appl.Phys. 90 (2001) 2970
6. R.Gerson, J.Appl.Phys. 31 (1960) 188.
7. R.Bechmann, Proc. IRE, 49 (1961) 509.
8. P.Gr.Lucuta, Fl.Constantinescu, D.Barb, J.Am.Ceram.Soc. 68 (1985) 533.
9. R.B.Atkin, R.M.Fulrath, J.Am.Ceram.Soc. 54 (1971) 265.
10. R.Bechmann, Proc. IRE, 49 (1961) 509.
11. Y.S.Ng, S.M.Alexander, Ferroelectrics, 51 (1983) 81.
12. K.Okazaki, K.Nagata, J.Am.Ceram.Soc. 56 (1973) 82.

Acknowledgement

The work was supported by NJTC.

Proc. Symp. Ultrason. Electron., Vol. 25, (2004) pp. 223-224
27-29 October, 2004

Evaluation of Piezoelectric and SAW characteristics of GdCOB crystal

○Takashi Nishida, Tadashi Shiosaki (Nara Inst. of Sci. and Tech., Mat. Sci.)

1. Introduction

The various materials for surface acoustic wave (SAW) device applications have been researched. We have studied piezoelectricity of $ReCa_4O(BO_3)_3$ (ReCOB, Re=Y, Gd, La and so on) crystals that have fairly optical properties. A few studies of their piezoelectric properties were reported.[1,2] In particular, good piezoelectric properties may be expected for GdCOB (Re=Gd) crystal because of large nonlinear optical coefficients. We have measured SAW characteristics of the GdCOB, and maximum coupling coefficient k^2 of ~1% was reported [1], however only X, Y and Z cuts were evaluated. In this study, material constants of GdCOB crystal were measured, and SAW theoretical calculations used the constants were performed.

2. Experiments

Material constants were measured by resonance-antiresonance methods. LF impedance analyzer (HP4192A, HP) and GdCOB resonators prepared at size of 13.5mm x 4.5mm x 1.5mm were used for the measurements. Scheme of the measurement of ReCOB crystals has not been established completely, due to point group *m* (monoclinic) of ReCOB. Then, we used a measurement scheme[2] that was similar Mason's method[3] for point group *2*. The material constants of GdCOB measured by Wang [4] seem to contain measurement error.

The SAW calculations were performed with Campbell's method.[5] However, the calculation method was improved, in order to analyze various SAW propagation modes such as leaky SAW.[6] The both material constants measured by Wang and us were utilized for calculation, and results obtained were compared with measured results.[1]

tnishida@ms.aist-nara.ac.jp

3. Results and Discussions

The resonance measurement of GdCOB (ZXt) θ and (XZt)θ cuts (θ=0, 22.5, 45, 67.5°) were performed, and elastic constants s_{11}, s_{12}, s_{22}, s_{66} and s_{22}, s_{23}, s_{33}, s_{44} were measured. In order to identify vibration modes, resonance frequencies of various cuts were compared, and their vibration was also observed by laser doppler vibrometor. From the (YXw)45, (ZYw)45 and (YZtw)45/45 cuts, s_{13}, s_{55}, and s_{46} were also measured. The values obtained are summarized in Table I.

Table I The elastic constants measured by resonance-antiresonance methods.

Elastic constants s (10^{-12} m^2/N)				
s_{11}	s_{12}	s_{13}	s_{22}	s_{23}
7.60	-1.17	-1.33	7.15	-4.62
s_{33}	s_{44}	s_{46}	s_{55}	s_{66}
8.93	27.9	-3.49	25.6	17.8

SAW simulations were performed using the material constants by Wang. The results obtained of Z-cut are shown in Fig.1, and results measured[1] are also shown in Fig.2. From their comparison, 0th and 1st modes measured identified as Rayleigh and leaky modes, respectively.

The SAW calculations at whole cutting and propagation directions were also performed. Fairly good result was obtained at euler angle of ϕ =0°, as shown in Fig.3. In particular, maximum velocity (4000m/s) and coupling (k^2~1.1%) were obtained at near of θ =90° (Y-cut).

The angular dependences between properties measured and calculated shown in Fig.1, 2 were agreed, however, velocities calculated were quite higher than measured velocities because of errors of material constants by Wang. In their constants, some problems such as s_{12}>0 were shown, and improvements of mode identification and selection of cutting directions may be required. Therefore, our constants newly measured (Table I) were also

used for calculations. Their results are shown in Fig.4. It was revealed that new calculation results were noticeably improved by the material constants.

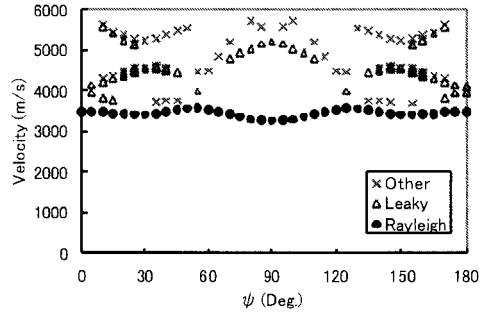

(a) Velocity

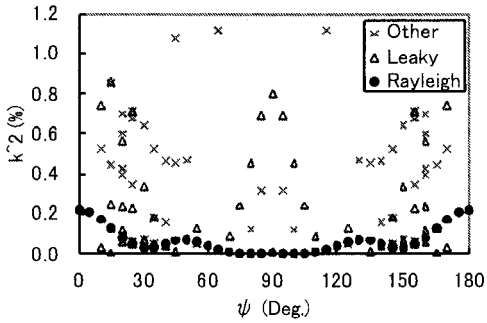

(b) couplig k^2

Fig. 1 The relationships SAW properties calculated on GdCOB Z cut and propagation direction (ψ).

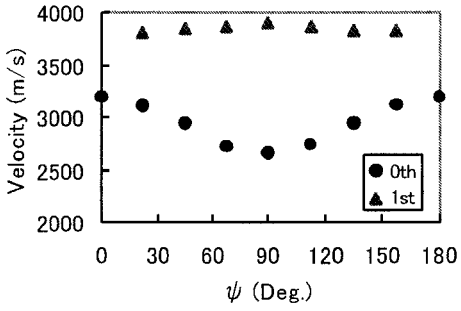

(a) velocity

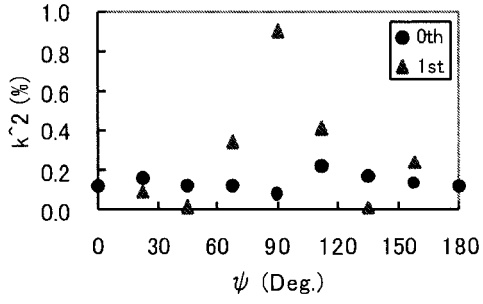

(b) coupling k^2

Fig. 2 The relationships SAW properties measured on GdCOB Z cut and propagation direction (ψ).[1]

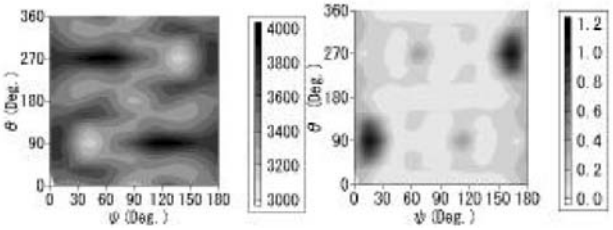

(a) Velocity (b) coupling k^2

Fig. 3 The SAW properties calculated (ϕ =0°)

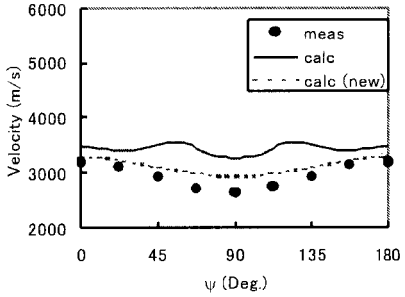

Fig. 4 The dependence of SAW velocity on ψ and material constants. (Z cut)

3. Concusions

From the results of SAW simulation by calculation, it was revealed that the higher and lower velocity modes measured identified as Rayleigh and leaky waves, respectively. Maximum velocity and coupling may be obtained in the calculation for GdCOB Y cut. Material constants were also measured accurately, revealing that precision of SAW calculation were improved succesfully.

Acknowledgement

We would like to thank H. Nakao and M. Nishida (Sakai Chem. Co.) for preparation GdCOB crystals.

References

1. T. Nishida, T. Amano, T. Shiosaki, H. Nakao, M. Nishida and H. Mizutani, Proc. 2001 IEEE Ultrasonics Symp. (2002), 179.
2. H. Takeda, H. Sako, H. Simizu, K. Kodama, M. Nishida, H. Nakao, T. Nishida, S. Okamura, T. Shikida and T. Shiosaki, Jpn. J. Appl. Phys. **42** (2003) 6081.
3. W. Mason, Phys. Rev. **70** (1946) 705.
4. J. Wang, X. Hu, X. Yin, R. Song, J. Wei, Z. Shao, Y. Liu, M. Jiang, J. Mater. Res. 16 (2001) 790
5. J. Campbell and W. Jones, IEEE Su-15 (1698) 209.
6. Y. Shimizu, Y. Endo and T. Watanabe, Jpn J. Appl. Phys 26 (1987) 162.

Proc. Symp. Ultrason. Electron., Vol. 25, (2004) pp. 225-226
27-29 October, 2004

Photoacoustic and Photoluminescence Characterization of Mn-doped ZnS Nanoparticle: Study of UV Irradiation Effect

○Almira B. Cruz, Qing Shen and Taro Toyoda
(The University of Electro-Communications, Department of Applied Physics and Chemistry, Course of Coherent Optical Science)

1. Introduction

The study of compound semiconductor in the nanometer is generating interest among a lot of researchers belonging to various fields. Among the different kinds of semiconductors available for research, ZnS has generated their interests owing to its various opto-electronic application.[1] One of the avenues that research has been focusing on is the effect of doping ZnS with Mn^{2+} ion. Prior researches[2-4] have indicated that due to the high quantum efficiency exhibited by ZnS:Mn, they may form a new class of luminescent material with applications to displays, lighting and laser.

In this study, we investigate the effect prolonged UV exposure on ZnS:Mn samples containing varying the amount of Mn^{2+} dopant. The change in the photoacoustic (PA) and photoluminescence (PL) intensities before and after UV irradiation is looked into.

2. Experimental Procedure

Nanocrystalline ZnS:Mn with varying Mn^{2+} concentrations was synthesized using an inorganic synthesis method.[5] Zn acetate was combined with Mn acetate (in varying concentration) in methanolic solution and reacted with sodium sulfide to obtain ZnS:Mn. The resulting colloid was centrifuged and dried for 24 at 50°C. The resulting sample had a calculated particle diameter of 2 nm (from XRD pattern using Scherrer equation).

Using a photoacoustic spectrometer, the optical absorption spectra of the samples were obtained. PA spectroscopy is a photothermal technique that enables us to obtain information on the nonradiative processes occurring in the sample as well as a spectrum that is similar to the optical absorption of the sample. Since the technique detects differences in acoustic waves as a direct consequence of the change in temperature caused by periodic heating of the material, one can easily obtain absorption spectrum even with opaque and powdered samples. The PA set-up uses a xenon lamp as the light source, a monochromator to produce the desired wavelength, a mechanical chopper to produce the desired modulation frequency and PA cell to hold the sample in an airtight chamber. This chamber has a small channel at the periphery in which a microphone was inserted.

E-mail address: mira@jupiter.pc.uec.ac.jp

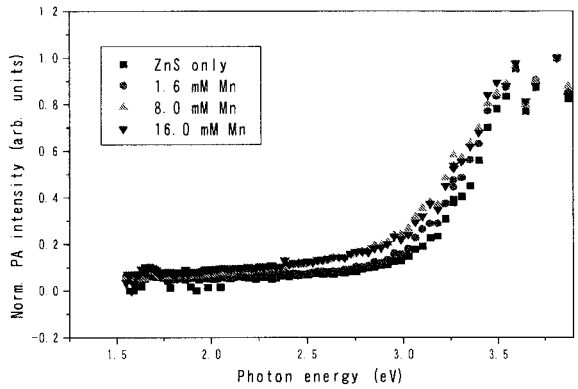

Figure 1: PA spectra for the different ZnS:Mn samples with varying Mn^{2+} concentration (from 0-16 mM).

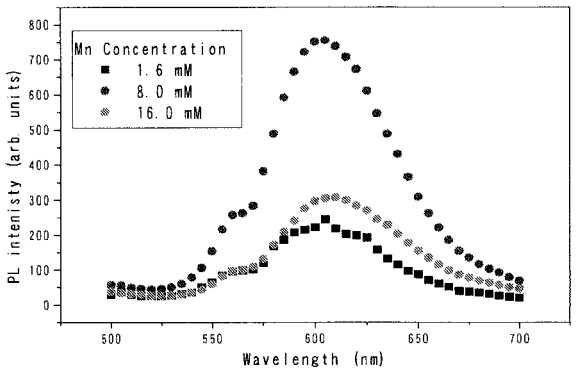

Figure 2: PL spectra for the different ZnS:Mn samples with varying Mn^{2+} concentration (from 1.6 -16 mM).

The PL set-up is similar to the PA set-up except that in place of a PA cell, a combination monochromator and photomultiplier detected the photoluminescence. PL spectra ware observed in the wavelength range of 500-700 nm with an excitation wavelength of 340 nm.

The UV irradiation time dependence measurements for both PA and PL intensities were conducted at an excitation wavelength of 340 nm at ambient conditions. The PL was detected at 595 nm, the measured PL peak for the samples. The conditions for the PA and PL measurements were fixed as far as possible in order to compare the PA and PL signal intensities for each sample directly.

2. Results and Discussion

The obtained PA spectra are seen in Fig. 1. All samples showed peaks at around 3.8 eV, attributed

to the lowest transition energy due to quantum confinement effects.[6] It can be observed that there is a slight difference in the PA intensity as the photon energy decreases. This could be accounted for by the Mn dopant in the system. Taking the spectral difference between ZnS:Mn samples and the ZnS sample, we find a peak at approximately 3.2 eV. This could correspond to the topmost energy level (^{4}E) in the excitation spectrum of the bulk ZnS:Mn^{2+} at room temperature. A recent study by Tanaka et al. has stated that there is a similar localized structure for Mn^{2+} in both the bulk and nanosized particles. [7]

In Fig. 2, we find the PL spectra exhibit a peak at 595 nm. It was found that varying the Mn concentrations affected the PL intensity. Increase in the dopant concentration yielded a PL intensity increase. But, if too much Mn^{2+} is present, a decrease in the PL intensity is observed. In this set, optimum concentration was determined to be 8.0 mM. This may be explained by concentration quenching (QC). During QC, the increased availability of the dopant ion increases the number of energy transfer between the initially absorbing ion to another identical ion instead of radiation (luminescence). After a number of such processes, a transfer to a quenching site (e.g. defect) may become involved, thus further decreasing the radiative process. [8]

After prolonged exposure to UV, it was found that the there were changes in both the PA and PL intensities of the samples. Fig. 3 and Fig. 4 shows the PA and PL intensity dependencies with respect to UV irradiation time respectively. In the PA intensity measured after UV irradiation, no apparent correlation to the Mn concentration was found. On the other, the PL intensity after UV exposure was found to increase with increasing Mn concentration.

It can also be seen that upon irradiation, a decrease in the PA intensity can be obtained for all samples indicating a possible decrease in the nonradiative processes during irradiation time. A reflected increase in the radiative process was also observed through the increase in the PL intensity (exhibited by all samples). This could indicate that a corresponding increase in the radiative processes. This increase maybe explained by photochemical reactions that may occur with oxygen during irradiation. (It can be noted that the experiment was done in air, thus is exposed to a supply of oxygen.) These photochemical reactions have been previously observed for the ZnS matrix (as evidenced by the blackening of the sample upon exposure to sunlight). The products of these reactions (e.g., $ZnSO_4$ or $Zn(OH)_2$) may serve as a passivating layer around the nanoparticles, increasing the quantum efficiency.

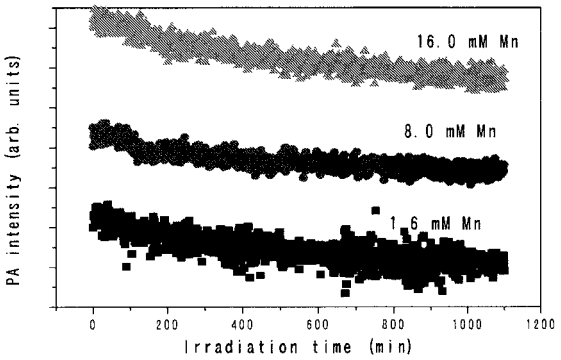

Figure 3: Photoacoustic intensity time dependence (exposure at 340 nm exposure).

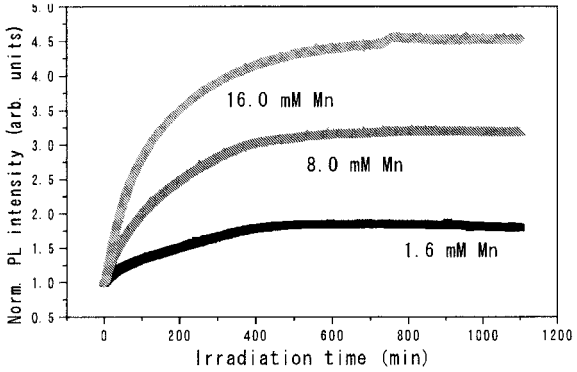

Figure 4: Photoluminescence intensity time dependence (exposure at 340 nm exposure).

Acknowledgment

This work was in part supported by a Grant-in-Aid for Scientific Research (No. 14750645 and 15510098) from the Ministry of Education, Culture, Science and Technology (MEXT) of the Japanese Government.

References

1. N. Karar, F. Singh, and B.R. Mehta: J. Appl. Phys. **95** (2004) 656.
2. 2. W.G. Becker, and A.J. Bard: J. Phys. Chem. **87** (1983) 4888.
3. R.N. Bhargava, D. Gallager, X. Hong, and A. Numiko: Phys. Rev. Lett. **72** (1994) 416.
4. A.A. Bol, and A. Meijernik: J. Lumin. **87-89** (2002) 472.
5. M. Konishi, T. Isobe, and M. Senna: J. Lumin. **93** (2001) 1.
6. T. Toyoda, J. Matsuzawa and Q. Shen: Jpn. J. Appl. Phys. **41** (2002) 3383.
7. M. Tanaka, J. Qi, and Y. Masumoto: J. of Lum. **87-89** (2000) 472.
8. M. D. Lumb: *Luminescence Spectroscopy* (Academic Press Inc., Ltd. London, 1978) p.70.

Proc. Symp. Ultrason. Electron., Vol. 25, (2004) pp. 227-228
27-29 October, 2004

Effect of Adhesion Force between Crack Planes in Analytical Solution of Nonlinear Contact Vibration

◎ Yoshikazu Ohara, Tsuyoshi Mihara and Kazushi Yamanaka (Tohoku Univ.)

1. Introduction

Detection of closed crack is not easy because the ultrasound is partially transmitted. To solve this problem, superharmonics ($2f$) has been expected where f is the frequency of input waves. [1] However, S/N ratio of superharmonics is not very high, because it is generated also in piezoelectric transducers and liquid media. On the other hand, subharmonics ($f/2$) has mush higher S/N ratio since it is generated only at closed cracks (Fig.1).[2] Subharmonic generation depends on the crack parameters, such as crack opening displacement, closure stress and crack length. Especially, closure stress is one of the most important parameters governing both the crack extension and the detectability in UT.

In this study, adhesion force has been introduced into the reported model[2]. Then, we analytically examined the effect of adhesion force on the threshold behavior of subharmonic ultrasound, which has been recently reported in some papers[3-5]. This may be one possible way to estimate crack closure stress.

2. Analytical Theory

In this report, it is assumed that subharmonic generation is caused by the variation of time-averaged displacement, which occurs because the input side crack plane vibrating with high frequency displaces the opposite side by the contact vibration[6]. We introduced adhesion force f_d into the reported model[2], as shown in Fig.1. The analytical solution of time-averaged displacement variation x_a is

$$x_a = \frac{k}{s}x_c + a\left(1+2\frac{k}{s}\right) - 2\sqrt{\frac{k}{s}a\left(\frac{k}{s}+1\right)(a+x_c)+\frac{f_d^2}{4ks}}, \quad (1)$$

where x_c is initial crack closure displacement, k is the stiffness of output side crack plane, s is the contact stiffness of crack and a is input wave amplitude.

First, it is assumed that subharmonic generation is caused by time-averaged displacement variation. The analytical results of eq.(1) with different adhesive forces are plotted against input wave amplitude a in Fig.2. In general, x_a is lowered as x_c increased. This is because the effective force acted on output from input crack plane is suppressed due to crack closure displacement in advance. When input wave amplitude overcomes the effect of closure stress, subharmonic ultrasound is produced at a threshold amplitude. Thus, the observation of threshold behavior may be one of possible way to estimate the crack closure stress.

However, in the case without adhesion force

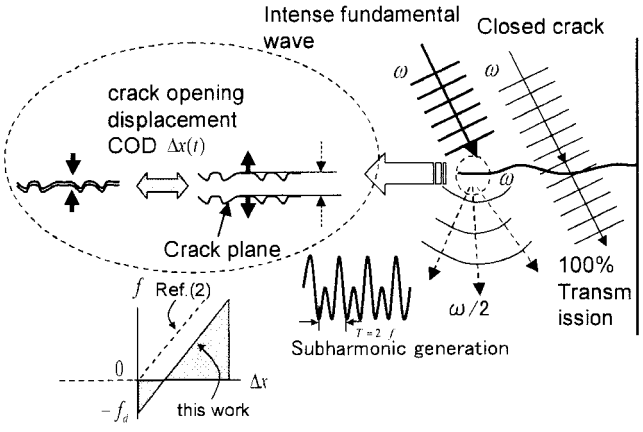

Fig. 1. Model of subharmonic generation at crack.

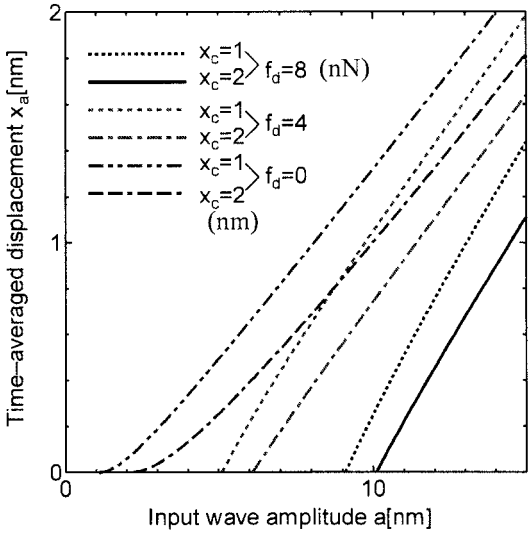

Fig. 2. Observed subharmonic amplitude ratio vs input wave amplitude.

($f_d = 0$), time-averaged displacement variation x_a smoothly rises with an input wave amplitude. Therefore, it is not easy to determine a clear threshold. On the contrary, in the case of $f_d = 4$, 8 nN, threshold behavior obviously appeared and the threshold value increased with the adhesion force f_d. Therefore, the adhesion force may help easy detection of the threshold.

3. Comparison of Analytical Solution with Experimental Result

Experiment has been conducted by using a fatigue crack in an aluminum alloy (A7075), as shown in Fig.3 .[7] The crack was extended from a notch in a three-point bending fatigue test with the maximum stress intensity factor K_{max}=14 kgf/mm$^{3/2}$ and the minimum stress intensity factor K_{min}=2 kgf/mm$^{3/2}$. The nonlinear ultrasound measurement was performed using an 45° oblique incidence longitudinal wave. The crack was partially closed with closure stress after bending load test. The crack opening displacement was controlled by applying and removing a static bending load of up to 100 kgf. The subharmonic amplitude ratio, which is subharmonic amplitude (3.2 MHz) divided by fundamental amplitude (6.4 MHz) of transmitted wave through closed crack, is plotted against input wave amplitude at each bending load in Fig.4 (vertical axis of left side).

A static bending loading at the experiment is equivalent to the variation of initial crack closure displacement x_c at analysis. In order to reproduce the experimental result by the analytical theory, analysis of eq.(1) was performed by selecting appropriate x_c, f_d under $s = k = 1$ (N/m). Time -averaged displacement variation x_a was also plotted against input wave amplitude, where $f_d = 6$ nN and $x_c = -3.6 \sim -0.4$ nm, where vertical scale of right side is adjusted to fit with experimental result. The analytical solution of $x_c = -3.6$ and -2.8 nm was almost fitted with experimental results of the bending load of 100 and 80 kgf. In particular, for the first time, the experimentally observed clear threshold was reproduced by an analytical solution. This may show the validity of the model. However, the experimental results with the bending load below 60 kgf was not fitted with analytical solution. This is because the parameters or the model are still different from the actual interaction between large amplitude ultrasound and closed cracks.

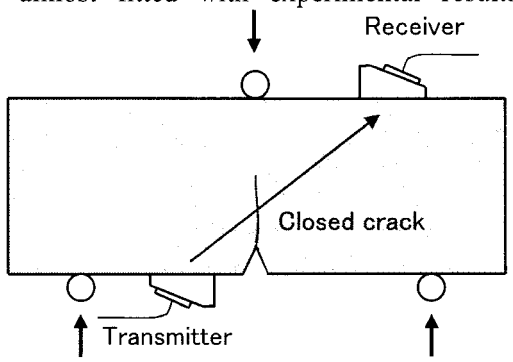

Fig. 3 Experimental setup.

In future works, we need to make the analytical model approach to actual cracks and perform the comparison with many experimental results at various conditions. The clarification of relationship between the threshold behavior and closure stress may be one of possible way to estimate the crack closure stress.

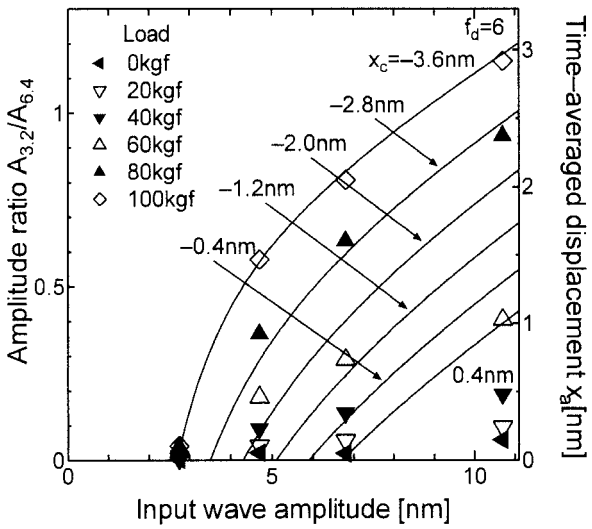

Fig. 4. Comparison of analytical solution with experimental results.

References

1. Y. Zheng, R. G. Maev and I. Y. Solodov : Can. J. Phys. **77** (1999) 927.
2. K. Yamanaka, T. Mihara and T. Tsuji : Jpn. J. Appl. Phys. **43-5B** (2004) 3082.
3. I. Y. Solodov and B. A. Korshak : Phys. Rev. Lett. **88-1** (2002) 014303-1.
4. I. Y. Solodov, N. Krohn and G. Busse : Ultrasonics **40** (2002) 621.
5. A. Moussatov, V. Gusev and B. Castagnede : Phys. Rev. Lett. **90-12** (2003) 124301-1.
6. K. Yamanaka, H. Ogiso and O. Kolosov : Appl. Phys. Lett. **64** (1994) 178.
7. M. Akino, T. Mihara and K. Yamanaka : Rev. Prog. QNDE **23B** (2004) 1256.

Proc. Symp. Ultrason. Electron., Vol. 25, (2004) pp. 229-230
27-29 October, 2004

CRACK DETECTION IN MATERIALS USING THE RANDOMIZED HOUGH TRANSFORM IN ULTRASONIC IMAGERY

T.Merazi Meksen* **M. Boudraa*** **R.Drai****

* LCPTS Faculté d'Electronique et d'Informatique
Université des Sciences et Technologies H.B – BP32 EL ALIA- Alger- ALGERIE
** LTSI Centre de recherche en Soudage et Contrôle –Chéraga-Algerie
merazi_t@msn.com

Abstract

The work we present here is an application of an image processing algorithm on ultrasonic imagery in order to detect crack defects in thick engineering structures.This algorithm is based on the Randomized Hough Transform (RHT), an approach of the Hough Transform, widely used for detecting parametrized templates in black and white images .The RHT permits to reduce considerably the calculations and consequently the storage requirement and the computing time needed .

In our article, we will first , briefly describe the ultrasonic image formation and the preprocessing work wich transform the image into a curve describing the defect on which we apply then the RHT.

Keywords : non destructive testing , ultrasonic imagery , Randomized Hough Transform.

1.Introduction

In non destructive testing of materials , the recognition of the defect is a very useful information for a fast decision-making. The capacity of memories and the rapidity of the computers permit today to apply algorithms of image processing to the ultrasonic imagery [2]. The Hough Transform is a traditional tool for detecting simple curves in an image , but its first version which consists in considering all the pixels of the image, requires much memory and computing time. We use therefore an approach suggested by Lei Xu [1] which selects randomly a sufficient number of pixels on the curve to recognize . A preprocessing is first necessary to reduce the image to a curve on which the treatement will be done . In the case of crack the result is a parabola .

2. Image formation

For detecting cracks , the ultrasonic acquisition technique we use is the Time Of Flight Diffraction (TOFD) . It is based on the measure of the time of flight of the diffraction echos of ultrasonics produced by the extremities of the crack [6]. We use in this case a symetrical and separate transmetter- receiver pair (Figure 1).The longitudinal probes are applied with an angle of incidence of 45° .

The interaction between the ultrasonic signal and the extremities of the crack gives rise to diffraction arcs of parabola in the B-SCAN display which is a representation of the amplitude of the coming back ultrasonic signals according to a section perpendicular to the inspection surface.The image resultant is shown in figure 2.

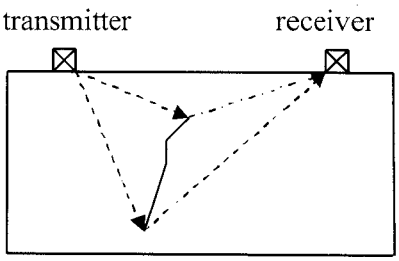

Figure 1:crack detection

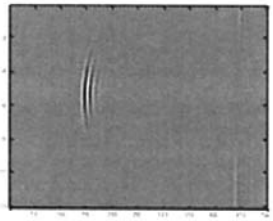

Figure 2. TOFD image

Thus, if we know how to detect parabola in an image and obtain the position of the summit point , we can detect and locate the corresponding crack in the structure.

3. Image preprocessing

The aim of the preprocessing , is to transform the initial image to a binary one containing only a curve caracteristic of the defect detected.

We limit first our work to the region containig the crack (figure 2).

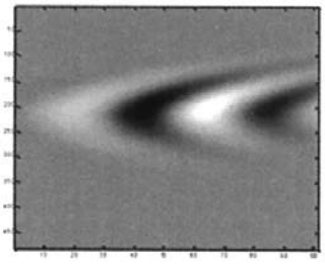

Figure 3 :Region considered of the image

The next step is cancelling all the pixels whose amplitude is lower than half of the maximum value, and assign the value one to the others. the binary image obtained is shown on figure 4.

For applying the randomized Hough transform , we consider the curve constituted by the points where the level passes from the black to the white (Figure 5).

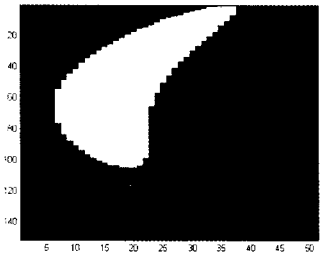

Figure 4. binary image

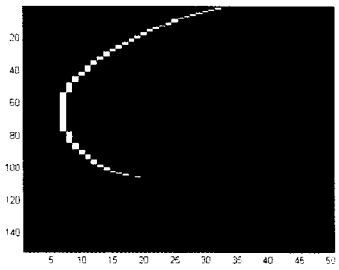

Figure 5.Points resultant from the preprocessing

4. The Randomized Hough Transform

4.1 *Principle of the Hough transform*

The Hough transform is a standard technique for detecting parametrized templates , such as lines,circles etc... [4],[5]. It consists of three steps :

1) A pixel in the image is transformed into a parametrized curve.
2) Valid curve's parameters are binned into an accumulator where the number of curves in a bin equals its score
3) A curve with a maximum score is selected from the accumulator to represent a curve in the image.

This basic Hough transform suffers many difficulties stemming from binning the curves (large accumulators and much processing time).

4.2 *The Randomised Hough Transform*

To reduce these problems of the HT, Lei Xu [1] proposed an approch wich selectes randomly n pixels from the image and fits them to a parametrised curve. If the pixels fit within a tolerance they are added to an accumulator with a score .Once a specified number of pixel sets are selected ,the curve with the best score is selected from the accumulator and its parameters are used to represent the curve in the image .

4.3 *parabola Hough Transform..*

The equation of parabola can be written:

$$y = ax^2 + bx + c \quad (1)$$

The dimension of the accumulator array corresponds to the number of unknown parameters in the equation. if we will consider the top like origin , parameters to be found will be then a and b and the Hough space (the accumulator) will be defined by these two parameters .

4.4 *Applying the Randomised Hough Transform*

1) The accumulator array A(a,b) is set to zero .

2) For several triplets of points $P1(x_1 , y_1)$, $P2(x_2 , y_2)$ and $P3(x_3 , y_3)$ selected randomly on the curve Figure 5 , the parameters a and b are calculated from equation (1) and a vote of 1 is added to the corresponding cell of accumulator array :

$$A(a, b) = A(a , b) + 1$$

3) The maximum of A indicates the parabola detected.

The accumulator resulting in our case is shown in figure 6. After a number sufficient of selections we can recognize the parabola present in our image by considering the peak of the accumulator .

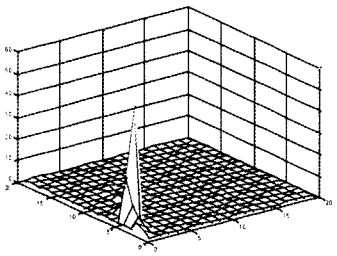

Figure 6 .Hough space 3D

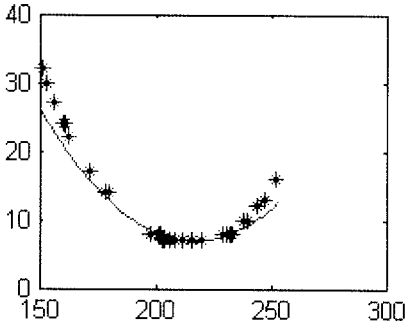

Figure 7. Parabola calculated and points randomly selected from the initial image.

5. Conclusion

We presented an application of the Randomized Hough Transform in pattern recognition of defects in ultrasonic imagery.The results obtained are very satisfactory being given the considerable reduction of time processing .The computing will be tested in a forthcoming for detecting in a structure several cracks and the algorithm improved in order to indicate the position of the top of the parabola and thus the extremity of the crack .

References

[1]Lei Xu ,"A new curve detection methode : Randomized Hough Transform" Pattern Recognition letters, 331-338,1990.

[2]J.Moysan , "Imagerie Numérique ultrasonore pour la Detection Automatique de Défauts en contrôle non destructif " ,thèse de l'institut national des sciences appliquées de Lyon ,1992.

[3] A.Rosenfeld ,Digital picture processing ,vol 2, academic pressing ,seconde edition ,New York.,1982.

[4]H.Maitre , "Un panorama de la transformation de Hough ", Traitement du signal , vol.2 , n°4,pp.305-317,1985.

[5]D.Ioannou , "Circle recognition through a 2D Hough transform and radius histogramming, Image Vision Comput. " 17,15-26 1999.

[6]L.F.C.Lew Yan Voon , " Gradient-based Hough Transform for the Detection and Characterization of Defects during Non-destructive Inspection " Proceeding of Symposium on Electronic Imaging Science and technology ,California , vol 3029 pp 140-146, 1997.

Proc. Symp. Ultrason. Electron., Vol. 25, (2004) pp. 231-232
27-29 October, 2004

Surface wave EMAT with mutual correlation method

Katsuhiro Kawashima (Tokyo Univ. of Tech., School of Bionics.)

1. Introduction

Electromagnetic acoustic transducer for surface waves (SW-EMAT) can detect surface flaws in metallic materials. It does not need water which has bad influence on the surface flaw detection ability of conventional ultrasonic transducers. But the sensitivity of SW-EMAT decreases rapidly with the increase of the air gap between it and the sample surface. Here, it is shown that sensitivity is improved by a mutual correlation method.

2. Experiment and results

The measurement system used is shown in Fig. 1. An artificial surface flaw (length: 10mm, depth: 0.4 mm) was made on the surface of an aluminum thick plate (thickness: 15mm). Burst pulses (frequency: 2.1MHz, repetition frequency 100Hz, 20 waves in a burst) are generated, power-amplified and fed to the transmitting SW-EMAT(T). Surface waves are generated, propagate on the surface, are reflected by the surface flaw and the sample edge, and detected by the receiving SW-EMAT(R). The distance between the two SW-EMATs is 10 cm. The principle of SW-EMAT is now well known[1)-3)]. The two SW-EMATs have the same structure (Fig. 2). It consists of a meandering coil (width: 30mm, length: 40mm,wire pitch: 1.2mm) and a permanent magnet (magnetic field is perpendicular to the sample surface and the strength is 3kG), similar to the B'-d type shown in Table 1 of Ref. 2.

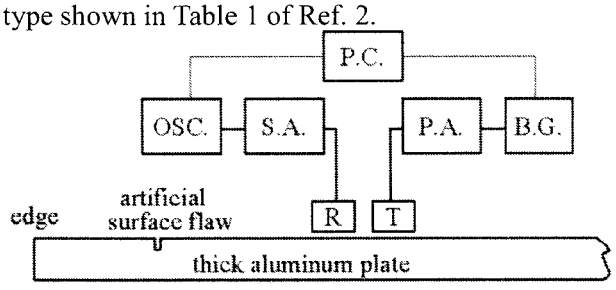

Fig.1 Measurement system for surface wave EMAT

B.G.: burst pulse generator, P.A.: power amplifier, S.A.: signal amplifier, OSC.: digital oscilloscope, P.C.: personal computer, T: transmitting SW-EMAT, R: receiving SW-EMAT

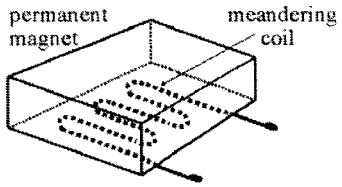

Fig.2 Structure of surface wave EMAT

In obtaining one of the measured results shown in Fig. 3, the middle point of the two SW-EMATs was 500mm and 750mm away from the flaw and the sample edge respectively, and LO (lift-off: air gap between the bottom surface of the EMAT and the sample surface) was 0.3mm. T is the transmitting burst pulse, C is the direct surface wave from the transmitting SW-EMAT to the receiving SW-EMAT. F is the flaw echo(the surface wave reflected by the flaw) and E is the edge echo(the surface wave reflected by the sample edge).

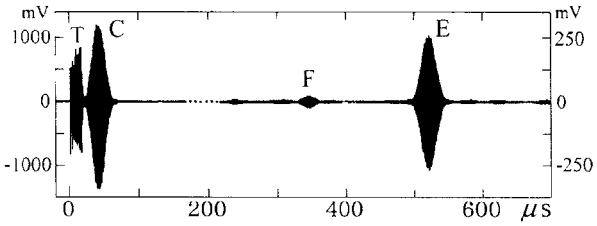

Fig.3 Flaw echo(F), edge echo(E) and direct wave(C) detected by the receiving SW-EMAT

C is referred to the vertical axis on the left. F and E are referred to the vertical axis on the right.(D_F:500 mm, LO:0.3mm, average of 256 measurements.)

Measurements were done for various distances (250,500,750 and 1000mm) and LOs(0.1, 0.3 and 0.6mm) and the measured results are shown in Fig. 4. The flaw echo F is clearly detected in Fig. 4(a), for which the distance(D_F) between the flaw and the middle point of the two SW-EMATs was 250mm and LO was 0.1mm. F becomes smaller for larger D_F and LO. The flaw echo F in Fig. 4(h) is barely recognizable(D_F:1000mm,LO:0.3mm) but for larger LO the flaw echo F is completely hidden under the noise level in Fig. 4(l) (D_F:1000mm,LO:0.6mm).

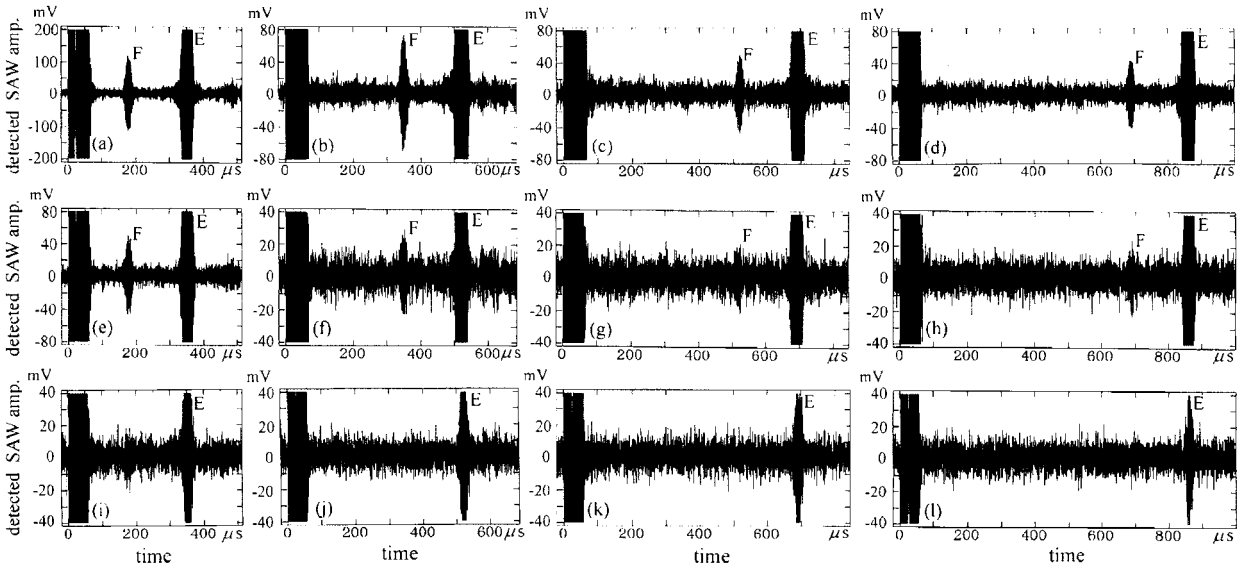

Fig. 4 Flaw(F) and edge(E) echoes detected by the receiving SW-EMAT (obtained by a single burst pulse) The distance(D_F) between the flaw and the SW-EMAT is 250mm for (a), (e) and (i), 500mm for (b), (f) and (j), 750mm for (c), (g) and (k), 1000mm for (d), (h) and (l). The air gap(LO) between the bottom of the SW-EMAT and the sample surface is 0.1mm for (a), (b), (c) and (d), 0.3mm for (e),(f),(g) and (h), 0.6mm for (i),(j),(k) and (l).

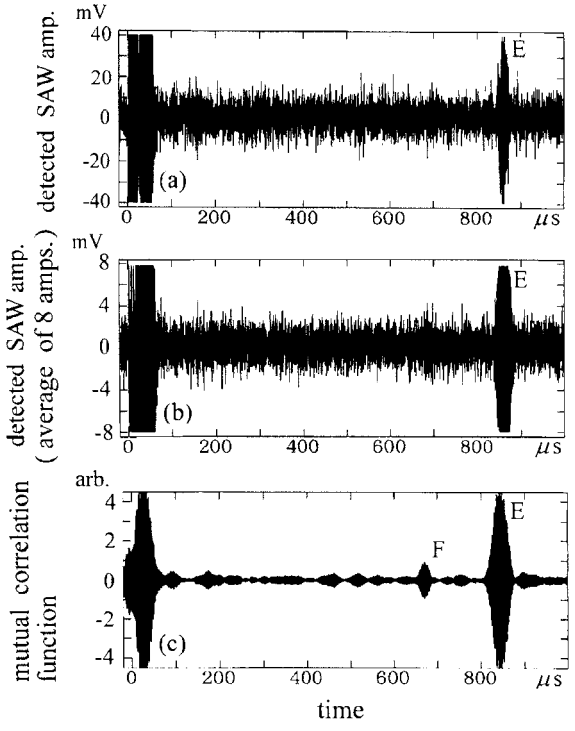

Fig. 5 Improvement of S/N

(a): obtained by a single burst pulse (the same figure as Fig. 3(l)). (b): average of 8 measurements. (c): mutual correlation between the direct wave C and the whole detected signal of (b) . D_F is 1000mm and LO is 0.6mm.

To improve S/N(signal to noise ratio) the simple averaging of 8 measurements were done for the severest condition(Fig. 4(l):D_F is 1000mm and LO is 0.6mm) and the result is shown in Fig. 5(b), but still the flaw echo is not recognized. In Fig. 5(a), the same figure as Fig. 4(l) is shown for the comparison purpose. Then a mutual correlation function between the direct wave C and the whole detected signal of Fig.5(b) was calculated and the result is shown in Fig. 5(c), in which the flaw echo F is clearly recognized.

3. Summary

A small artificial surface flaw on the surface of an aluminum thick plate was measured by SW-EMAT. The flaw echo was detected by a single burst pulse for the short distances and small LOs but it was impossible to detect it for a large distance(1000mm) and LO(0.6mm). It became clearly recognized after a combined digital signal processing of an averaging(8) and a mutual correlation.

References

1. K.Kawashima: Ouyoubutsuri 52 (1983) 1032
2. K.Kawashima: Hihakaikensa 34 (1985) 796
3. B.W.Maxfield: Materials Evaluation 45 (1987) 1166

Proc. Symp. Ultrason. Electron., Vol. 25, (2004) pp. 233-234
27-29 October, 2004

A Nanometer Order Resolution Displacement Measurement System Using an Air-Coupled Ultrasonic Wave

◎ Katsuhiro Sasaki, Morimasa Nishihira and Kazuhiko Imano (Akita Univ.)

1. Introduction

The resolution of displacement measurements using air-coupled ultrasonic waves is limited by the ultrasonic wavelength λ in the time-of-flight method. A higher-frequency measurement for improving the resolution cannot be achieved because of the huge attenuation of ultrasonic waves in air. High acoustic-impedance mismatching between air and ultrasonic transducers is another source of difficulty. By using the phase detection technique, a resolution smaller than λ is obtained, however, few studies of the method of measuring nanometer order displacements have been reported.[1] We have only recently developed an air-coupled ultrasonic system for displacement measurements by introducing the phases of the multi-reference-wave.[2] One of the limiting factors for a resolution in this system is the voltage resolution. In this paper, an improved displacement measurement system for overcoming this limitation is described.

2. System and Method

Figure 1 shows the schematic / block diagram of the displacement measurement system. An ultrasonic wave of 40 kHz (λ=8.5 mm at 20℃ in air) is transmitted and received in the transmission mode in air. Then, the ultrasonic wave propagates a distance z. This system is the basis of our previous system,[2] in which the shifted phases δ_i (i=0, 1, ···, N-1) of the multi-reference-wave are introduced to accurately detect the phase information of $\phi(z)$.[2, 3] The received signal is mixed with the reference waves and then fed to a low-pass filter to detect the phase detection outputs P_i, as expressed in eq. (1)

$$P_i = P(\delta_i, z) = A\cos(\delta_i - \phi(z)) = a_1 \cos\delta_i + a_2 \sin\delta_i \,, \quad (1)$$

where A is the amplitude of the phase detection outputs. The phase $\phi(z)$ can be expressed using a_1 and a_2 as,

$$\phi(z)=\tan^{-1}(a_2/a_1)+n\pi \quad (n=0, 1, 2, \cdots). \quad (2)$$

Using the least squares method, a_1 and a_2 are determined

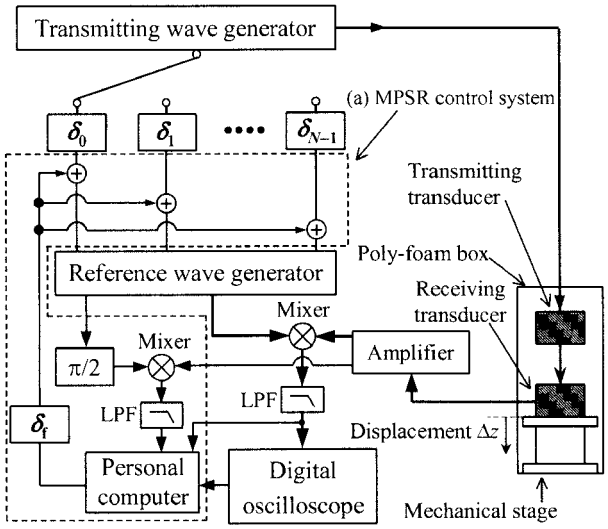

Fig. 1 Schematic / block diagram of the displacement measurement system controlling the maximum phase-sensitive region (MPSR).

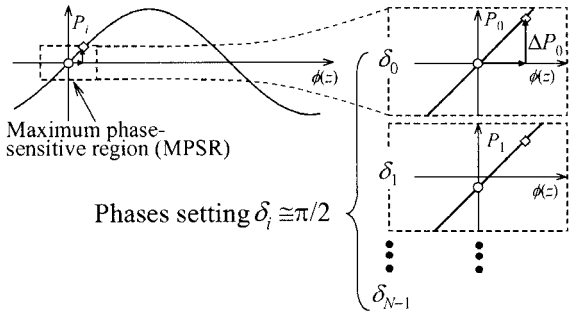

Fig. 2 Phases δ_i of the multi-reference-wave set around the MPSR.

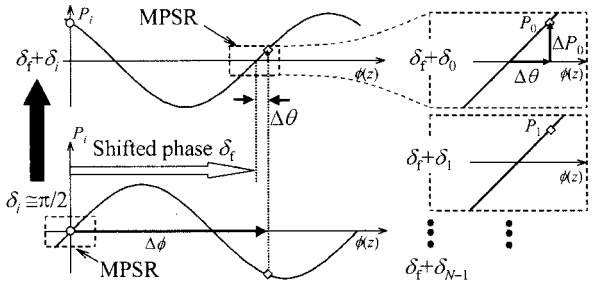

Fig. 3 Phases δ_i of the multi-reference-wave shifted to $\delta_f+\delta_i$ for controlling the MPSR.

so as to minimize the sum of the squared differences between P_i and the measured values of P_i. In our previous method,[3] the phases δ_i are shifted by four-step of $\pi/2$ and P_i are measured at each step of δ_i. This method is the well-known four-step type of phase-shifting (FPS) method. In the FPS method, the resolution for detecting P_i is determined by the voltage measurement resolution ΔV in the system. Thus, the variation ΔP_i of P_i, which is smaller than ΔV, cannot be detected. The high-phase-sensitivity is required for enlarging ΔP_i, however, the phase-sensitivities are approximately zero for $\delta_0=0$ and $\delta_2=\pi$. To overcome above problems, the phases δ_i are suitably set around the maximum phase-sensitive region (MPSR), which exists at the point $\delta_i \cong \pi/2$, as shown in **Fig. 2**. The maximum phase-sensitivity is obtained for the multi-phase detection point. The variation ΔP_i of the maximum sensitive phase detection outputs P_i can be magnified larger than ΔV, so that the resolution for detecting P_i can be improved. To always detect P_i around the MPSR, the MPSR control system is newly introduced as shown in Fig.1(a). When the distance z is varied to $z+\Delta z$ using a mechanical stage, the phase difference $\Delta\phi$ is estimated as the phase δ_f using the quadrature detection as follow,

$$\delta_f = \tan^{-1}(P'(\delta_0+\pi/2, z+\Delta z) / P'(\delta_0, z+\Delta z)) + n\pi, \qquad (3)$$

where $P'(\delta_i, z+\Delta z)$ are the measured values of $P(\delta_i, z+\Delta z)$. The detectable range of δ_f is limited to between $-\pi/2$ and $\pi/2$, however, this range can be extended from 0 to 2π using the phase compensation.[4] When the phases δ_i are exactly shifted to $\delta_f+\delta_i$ in the feedback loop enclosed with the broken line in Fig.1(a), the phase detection region is controlled to the MPSR as shown in **Fig. 3**. Then, P_i can be detected with the high-resolution using our method and the small phase difference $\Delta\theta=\Delta\phi-\delta_f$ is calculated. The displacement Δz is finally expressed as,

$$\Delta z = (\lambda/2\pi)\cdot\Delta\phi = (\lambda/2\pi)\cdot(\delta_f+\Delta\theta). \qquad (4)$$

3. Experimental Results

Figure 4 shows the experimental results for evaluating our method (N=4). The standard deviations (SD) for the FPS method are about 0.4 μm, which is equivalent to the 12 bit voltage resolution ΔV in the system. The SDs for our method are significantly decreased, namely, the resolution of the phase detection for our method can be improved to better than ten times the FPS method. A resolution of 60 nm (λ/130,000) can be achieved. **Figure 5** shows the experimental results for evaluating the MPSR control system (N=4). The displacement of up to 8 mm (≅λ) is successfully measured. The SDs in Fig.5 are below to 2 μm, which is due to translation errors of the mechanical stage.

4. Conclusion

A resolution of 60 nm (λ/130,000) has been achieved with a measurable displacement range of 8 mm (≅λ) using the MPSR control system based on our method. In the future, we plan to modify this system to make it applicable to a dynamic displacement measurement.

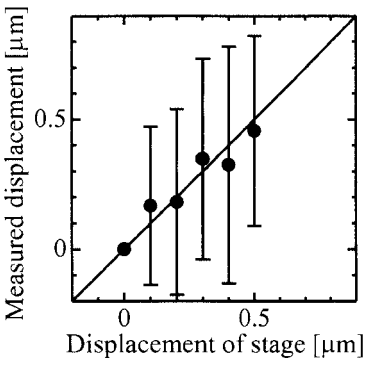

(a) FPS method

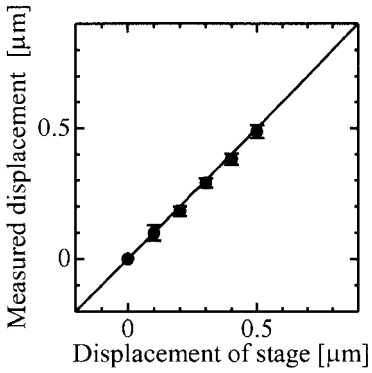

(b) Our method

Fig. 4 Experimental results for evaluating our method.

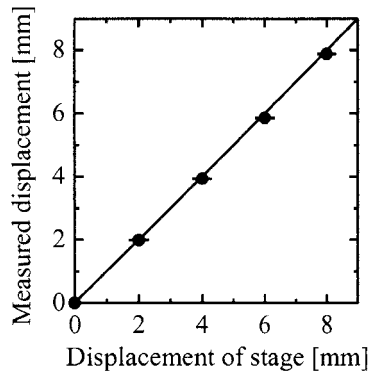

Fig. 5 Experimental results of the displacement measurement of up to 8 mm, which is approximately equal to the ultrasonic wavelength λ.

References

1) Z. Kojiro, *et al.*: *Ultrason.* **35** (1998) 563.
2) K. Sasaki, *et al.*: *Jpn. J. Appl. Phys.* **43** (2004) 3071.
3) K. Imano, *et al.*: *Jpn. J. Appl. Phys.* **35** (1996) 3177.
4) M. Nishihira, *et al.*: *IEICE. Tech. Rep.* **EMD2001-61** (2001) 35.

Proc. Symp. Ultrason. Electron., Vol. 25, (2004) pp. 235-236
27-29 October, 2004

Quantitative Evaluation of Surface Roughness by Air Coupled Ultrasound

◎ Deden Dian Sukmana and Ikuo Ihara (Nagaoka Univ. of Technology)

1. Introduction

The quantitative measurement of surface roughness of materials is very important to control the quality of the material surface. The stylus profiling and optical reflection methods have been recognized as conventional techniques to evaluate the roughness [1]. In the former work, we presented the feasibility of an air-coupled ultrasound using broadband capacitance transducers to evaluate the surface roughness [2]. It had been found in the previous work that the amplitude of coherent components of reflected waves from rough surfaces decreases with the surface roughness. In the present work, the behavior of incoherent components of scattered waves from rough surfaces has been examined. The relationship between the amplitude of the incoherent components and the roughness parameters are investigated theoretically and experimentally. The Kirchhoff based scattering model is used.

2. Experimental

The measurement system is shown in **Fig. 1**. A pair of broadband air coupled capacitance transducers (Micro Acoustic Co., BAT) having center frequency of 0.5 MHz is used in a pitch-catch configuration. The working distance between the transducer and specimen surface is 35 mm. A square wave pulser (Ritec, SP-801A) and a broadband receiver (Ritec, BR-640A) are employed to transmit and receive wide-band ultrasonic pulse waves. Nine sandpapers having different roughness were used for the specimens and were bonded on a steel plate to make flatness. A polished stainless plate was used as a reference specimen having smooth surface. **Fig. 2** shows the surface profiles of each specimen obtained using a stylus profilometer. The height and lateral parameters used for evaluating suface profile in this work are the root mean square roughness *Rq* and the mean spacing of the profile irregularities *RSm* (JIS B0601:2001). The

E-mail: ihara@mech.nagaokaut.ac.jp

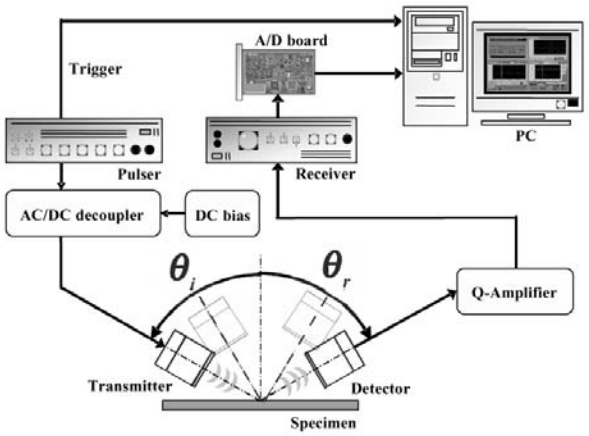

Fig.1 Schematic diagram of the experimental set-up.

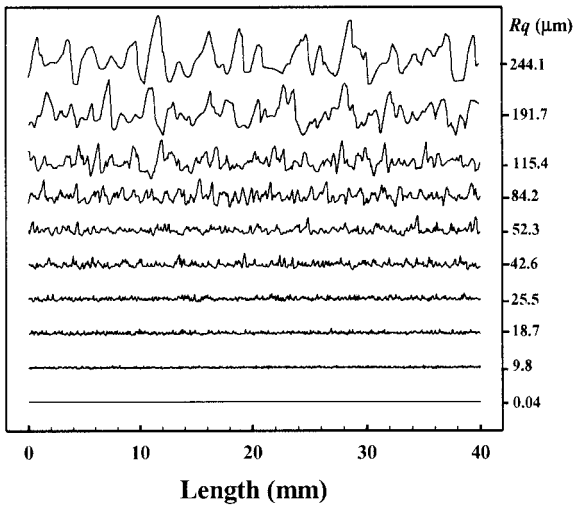

Fig.2 Surface profiles of each specimen measured by a stylus-method.

Rq and *RSm* of the specimens are deviated from 0.04 to 244.1 μm and from 83 to 2025 μm, respectively. The transmitter is driven by the pulser with the repetition rate of 0.5 kHz. The coherent component was measured in the specular configuration ($\theta_i=\theta_r$). The incoherent component was measured at incident angle of $\theta_i=60°$, with different reflection angles of $\theta_r=0°\sim75°$.

3. Results and discussion

The ultrasonic wave is incident onto the specimen surfaces at $\theta_i=60°$ and the scattered wave is measured at $\theta_r=0°\sim75°$. **Fig. 3** shows the changes of the

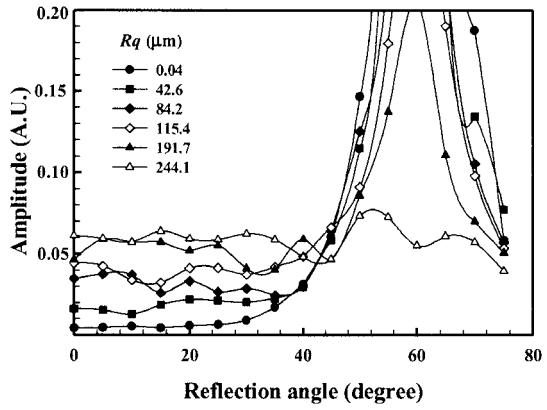

Fig.3 The effect of reflection angles on the amplitude of scattered waves.

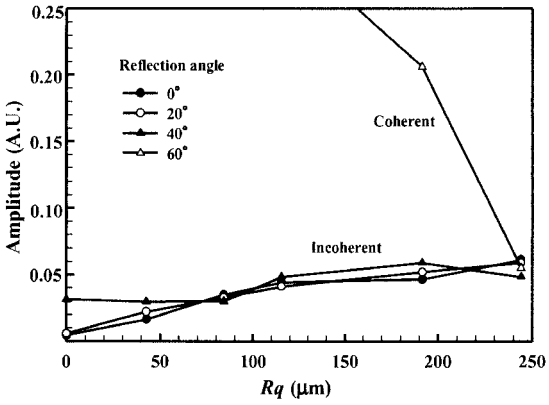

Fig.4 Relationship between the amplitude of scattered waves and the roughness.

amplitude of the scattered waves as function of incident angle. The amplitude increases at θ_r=0°~50° as *Rq* increases, while it decreases at around specular angles θ_r=50°~70°. A rougher surface scatters the incident waves into various directions and reduce the coherent component in the specular direction. At *Rq*=244.1 μm, the coherent component disappeared and the incoherent component dominated the scattered waves. **Fig. 4** shows the relationship between *Rq* and the amplitude of the scattered wave. The amplitude of the incoherent components increases slightly as *Rq* increases.

Fig. 5 shows the effect of the surface correlation length λ_o [3] and *Rq* on the amplitude of incoherent component, which is calculated from Kirchhoff based scattering model written as [4],

$$I_{incoherent} = \frac{k^2 F^2 \lambda_0^2 e^{-g}}{4\pi r^2} A_M \sum_{n=1}^{\infty} \frac{g^n}{n!n} exp\left(-\frac{k^2(A^2+B^2)\lambda_0^2}{4n} \right) \quad (1)$$

where $g = k^2 Rq^2 (\cos\theta_i + \cos\theta_r)^2$, k is the wave number. It is noted that the incoherent component depends on not only height distribution such as the surface

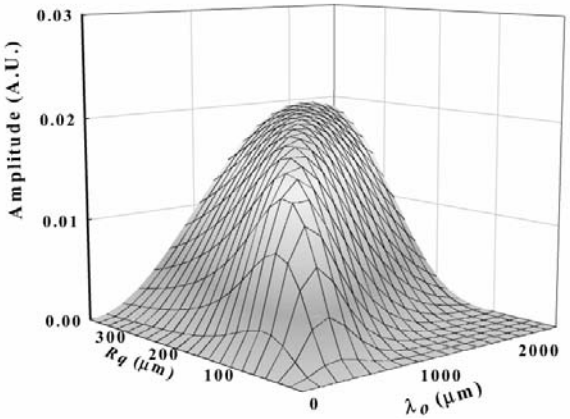

Fig.5 The amplitude distribution of incoherent component as function of surface roughness *Rq* and surface correlation length λ_o (θ_i=60°, θ_r=20°).

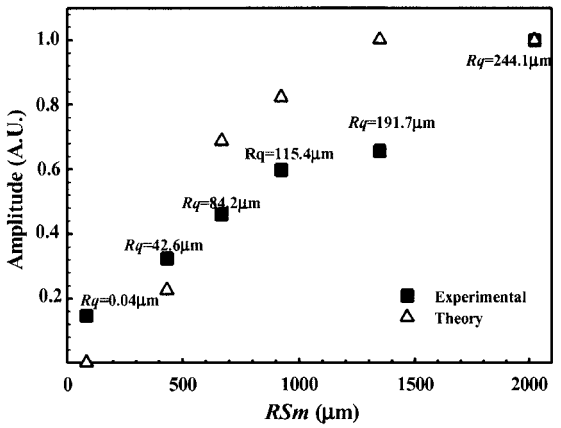

Fig.6 Relationship between the amplitude of incoherent component and *RSm* (θ_i=60°, θ_r=20°).

roughness *Rq* but also lateral distribution such as the surface correlation length of surface profile, while the coherent component is sensitive to only *Rq* [2].

Fig. 6 shows the relationship between the amplitude of the incoherent component and *RSm*, obtained experimentally and theoretically. It is considered that the incoherent component could be useful to estimate the lateral parameter of surface profile such as *RSm*.

Acknowledgement

The financial support from Grant-In-Aid for Scientific Researches (B14350397) by JSPS is appreciated.

References

1. DJ. White House : Meas. Sci. Technol. **8** (1997) pp.955-972.
2. Deden DS, et al. : Proc. Symp. Ultrason. Electron. **24** (2003) pp.101-102.
3. Y.P Zhao : *A Simple Introduction to Rough Surface Characterization*, 2000.
4. J.A. Ogilvy : *Theory of Scattering from Random Rough Surfaces* (Bristol, IOP, 1991).

Proc. Symp. Ultrason. Electron., Vol. 25, (2004) pp. 237-238
27-29 October, 2004

Effect of a Waveguide in the Ultrasonic Phase Conjugate Imaging System

○Masahiro Ohno, Takahiro Kato (Chiba Institute of Technology),
Akira Kokubo (Univ. of Tokyo), Ken Yamamoto (Kobayasi Institute of Physical Research)

1. Introduction

Acoustic microscopes and acoustic flaw detectors are widely used both in material sciences and in industrial non-destructive testing. Such C-mode systems provide images of surface and sub-surface elastic properties with high quality for well-prepared samples. However, the images easily deteriorate if the sample has surface roughness, through which ultrasound suffers deflection and wavefront deformation. We have been trying to overcome this disadvantage by using ultrasonic phase conjugate waves. Introducing a real-time phase conjugator into an ultrasonic imager enables automatic correction of wavefront deformation, which leads to diminishing the surface effect. Our past study showed that this method effectively worked on relatively soft samples, such as agarose gels[1-3]. In this paper, we present the results of our trial to extend this method to solid samples such as metals. The degree of beam deflection and wavefront deformation becomes larger if the acoustic velocity of the sample is much greater than that of water. We show that a combination of a waveguide and a phase conjugator functions well in such situations.

2. Experimental setup

Figure 1 shows the placement of the sample and imaging components. An ultrasonic transducer emits tone-burst incident waves towards the lower surface of the sample suspended in water. The reflected wave changes its direction and wavefront in accordance with the shape of the sample surface. A waveguide, placed underneath the focus, collects reflected waves propagating in various directions and leads them to the phase conjugator. The ultrasonic phase conjugator is a block of PZT ($PbZr_xTi_{1-x}O_3$) ceramics fixed at the bottom of a waterbath with its upper surface contacting water. This ceramic block has a pair of electrodes on its sidefaces, on which electric fields, at a frequency twice the ultrasonic frequency, are applied. Then, in the volume between electrodes, the phase conjugate wave of the incident ultrasonic wave is generated automatically as a result of the parametric interaction via nonlinear piezoelectricity. The phase conjugate wave, according to its "time-reversed" property, retraces the incoming path and reaches the transducer. In our system, the sample is two-dimensionally scanned and the above process is reiterated synchronously. The resultant image will show the square of the modulus of the ultrasonic reflectivity of the sample, since the ultrasound is reflected at the sample surface twice. The effect of the phase of the reflectivity, which mainly carries the information of the shape of the surface, is diminished.

The waveguide in this system works as follows: 1)It collects waves reflected (or scattered) in a wide solid angle from the sample. That is, it increases the effective aperture of the phase conjugator. 2)It enlarges the range of the incident angle distribution at the water/phase conjugator interface. This will average and smooth the effect of incident-angle-dependent phase conjugate reflectivity[4] that usually acts to deteriorate the fidelity of phase conjugate waves. 3) It realizes a configuration in which the phase conjugator is placed apart from the sample surface. This will decrease the multiple reflection between the sample surface and the top surface of the phase conjugator, causing a high signal-to-noise ratio in ultrasonic images.

3. Experimental results

Experiments were done with the following conditions: ultrasonic frequency 10MHz, duration 10-25 μ s, focal length 30mm, transducer diameter 6mm, PZT size 10(X)×5(Y)×40(Z)mm, electrode length 30mm, pump electric frequency 20MHz, its

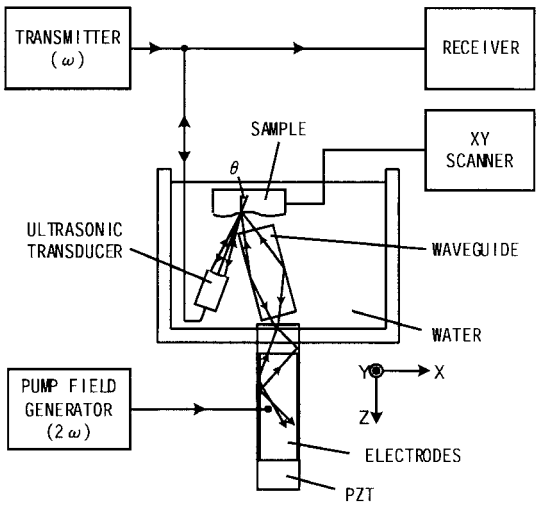

Fig. 1 Setup of the main part of the imaging system

peak power 2.0kW, waveguide (made of aluminum) size 9×5.5×34mm. **Figures 2** show the images of a copper plate with a relief pattern. Its surface has a grain-like undulation with two different materials, a stainless steel film and resin as large as the grain diameter, attached. In the conventional ultrasonic image (b), the influence of the surface undulation is dominant and two spots of impurities are hardly recognizable. On the other hand, the image with a phase conjugator becomes as (c), in which the stainless film emerges as a bright spot, the resin dark. **Figures 3** are the result of sub-surface imaging. The sample is an aluminum block having a shallow trench and a linear hollow space 1mm underneath and perpendicular to the trench. For this sample, the sub-surface hollow was imaged as bright lines both in conventional and in phase conjugate images. However, the hollow just underneath the trench is not observable in the conventional image because of the beam deformation. In contrast, the phase conjugate image shows the hollow almost independent of the existence of the trench, as if X-rays were used. In **Figs. 4** are shown the results for an aluminum block with a sandpaper-like surface and a sub-surface hollow.

4. Conclusions

An ultrasonic C-mode imaging system with an ultrasonic phase conjugator and a waveguide has been built and images have been obtained for metal samples with surface undulations. Surface or sub-surface elastic properties were visualized with less influence of surface roughness. The waveguide worked to enlarge the effective aperture of the conjugator as well as to smooth and improve the images.

Acknowledgement

This work was supported by Grant-in-Aid for Scientific Research (13450037).

References

1) M. Ohno: Proc. 10th Conf. Ultrason. Electron., Tokyo, 1989, Jpn. J. Appl. Phys. **29** Suppl. Pt. 1, (1990) 299.

2) M. Ohno, K. Yamamoto, A. Kokubo, K Sakai and K. Takagi: J. Acoust. Soc. Am. **106**, 1330 (1999) 1330.

3) K. Yamamoto, M. Ohno, A. Kokubo, K Sakai and K. Takagi: J. Acoust. Soc. Am **106**, (1999) 1339.

4) M. Ohno, B. R. Tittmann, A. Kokubo and K. Takagi: Ultrasonics **39**, (2001) 425.

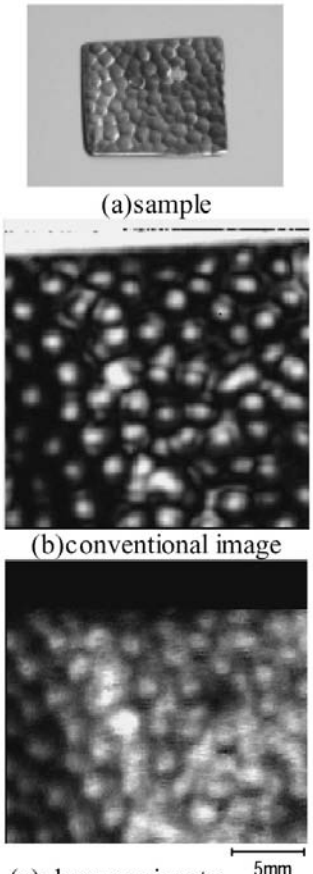

Fig. 2 Iamges of a relief-patterned copper plate with a spot of stainless and a spot of resin

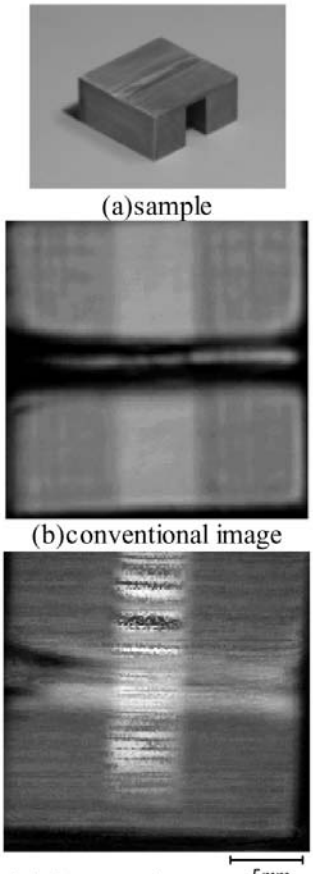

Fig. 3 Images of an aluminum block with a trench and a sub-surface hollow

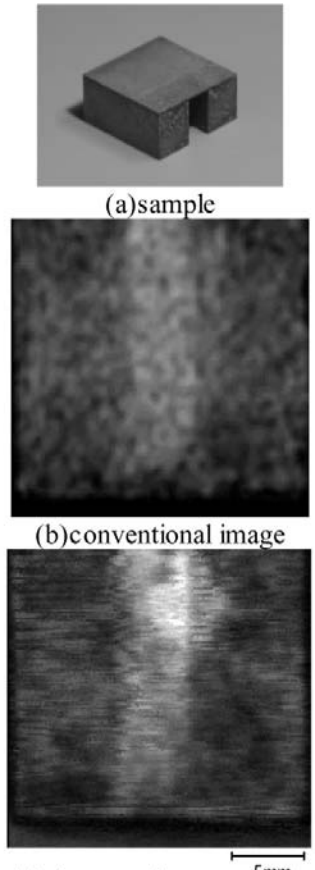

Fig. 4 Images of an aluminum block with rough surface and a sub-surface hollow

Proc. Symp. Ultrason. Electron., Vol. 25, (2004) pp. 239-240
27-29 October, 2004

Study on the handlings of FDTD method to analyze sound fields

○Yoshiki NAGATANI, Masahide MURAKAMI, Yasuto HARA, Yoshiaki WATANABE
(Doshisha Univ.)

1. Introduction and Background

Along the remarkable evolution of the PC in recent years, precise 3D simulation of sound fields in large-scale model using FDTD method becomes general and practical. However, the reliability of FDTD method intended for elastic tissues is not examined enough.

In this study, handling techniques of acoustic and elastic FDTD method are discussed focusing on shear waves propagating in elastic materials.

2. Fundamentals of FDTD method

FDTD (Finite Difference Time Domain) method has been used for analyzing electromagnetic fields. FDTD method involves difference formulas in both time-domain and spatial-domain, and has advantages on calculating time response of wave function. Electric and magnetic intensity in electromagnetic field are related to sound pressure (or stress) and particle velocity in sound field.

3. Acoustic and Elastic FDTD method

Acoustic FDTD is applicable to analyzing sound fields in fluids. Elastic FDTD can also handle phenomena in elastic tissues. The followings are governing equations of acoustic FDTD;

$$-\frac{1}{\kappa}\frac{\partial p}{\partial t}=\frac{\partial v_x}{\partial x}+\frac{\partial v_y}{\partial y}+\frac{\partial v_z}{\partial z} \quad (1)$$

$$-\rho\frac{\partial v_x}{\partial t}=\frac{\partial p}{\partial x} \quad (2)$$

$$-\rho\frac{\partial v_y}{\partial t}=\frac{\partial p}{\partial y} \quad (3)$$

$$-\rho\frac{\partial v_z}{\partial t}=\frac{\partial p}{\partial z} \quad (4)$$

where p is sound pressure, v_i is particle velocity, κ is volume elasticity module, and ρ is density of medium.

These equations should be transformed into difference equations per head, then (1) and (2) (3) (4) would be alternately calculated in each step to update sound fields in the simulation model.

In addition, elastic FDTD method requires parameters of both normal and shear stresses instead of sound pressure, so that it can deal with vertical and shear waves in elastic tissues.

To implement these, therefore, acoustic FDTD requires 16bytes for each lattice and elastic requires 36bytes (when assigning 4bytes for each variable).

4. Simulation model

First, we considered a simple model shown in **Figure 1**. The width of simulation field is 200[mm] × 160[mm] × 160[mm] and the size of each lattice

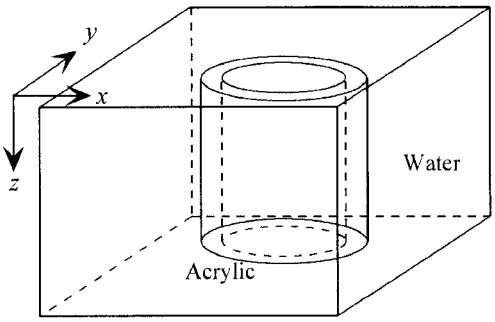

Figure 1 Simulation model.

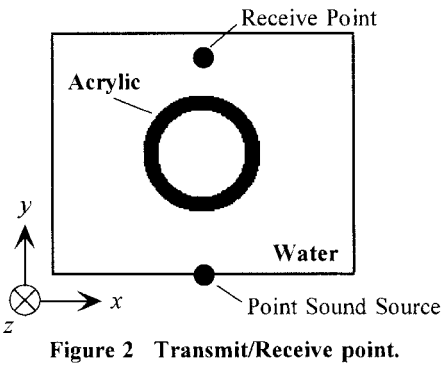

Figure 2 Transmit/Receive point.

E-mail: nagatani@usl.doshisha.ac.jp

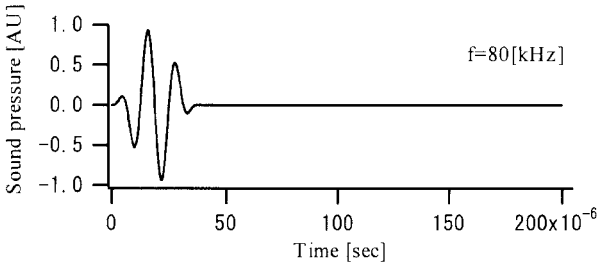

Figure 3 Transmitted waveforms.

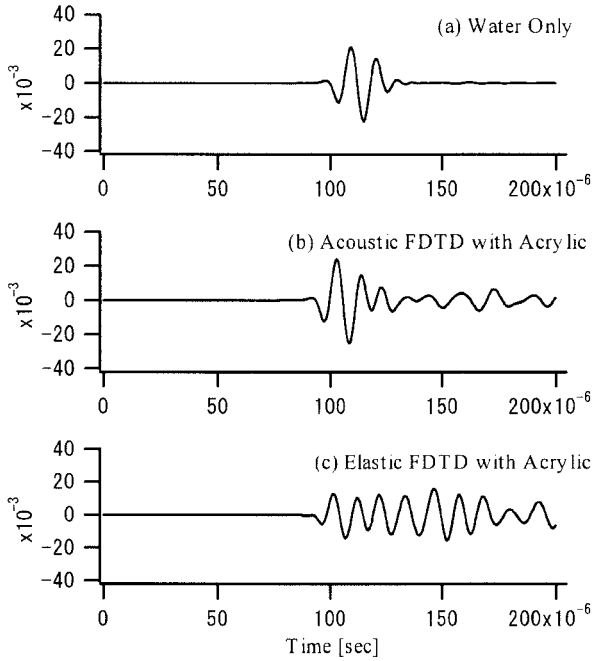

Figure 4 Received waveforms.

is 1[mm^3]. An acrylic tube is settled in water, which outside radius is 40[mm] and inside is 30 [mm]. The time step is 0.2[μs]. From the source point shown in **Figure 2**, signal wave shown in **Figure 3** was transmitted.

5. Simulation Outputs

5.1. Calculated Waveforms

Figure 4 (a) is the received waveforms without any acrylics in the simulation field. Proportional shape as transmitted waveforms comes out. Acoustic and elastic FDTD with an acrylic tube results in Figure 4 **(b)** and **(c)** which are completely dissimilar.

5.2. Entity of Shear waves

To confirm this reason, the sound pressure/stress distributions at 80[μs] are shown in **Figure 5**; **(b)** is sound pressure by acoustic FDTD, **(c-1)** **(c-2)** is normal and shear stress by elastic FDTD. The difference between 4(b) and 4(c) is affected by shear stresses inside acrylic shown in 5(c-2).

The details of shear stress can be read out in diagrams such as **Figure 6**, that are vectorial elements of three dimensions of X-Y, Y-Z, Z-X. They indicate that, on this surface, Y-Z nor Z-X shear stress is not propagating, but X-Y.

6. Conclusion

In this study, usability and importance of indicating shear stresses of each coordinate system are suggested. Elastic FDTD simulation says some challenging parameters of not only sound pressure but behaviors of elastic materials.

References

1. Y. Tanikaga : Analysis of Intracranial Acoustic Wave Propagation by FDTD method (2003)
2. T. Sakaguchi : Research on perception mechanism of bone-conducted ultrasound (2002)
3. M. Sato : Dansei Shindou · Hadou no Kaiseki Nyuumon (Morikita Publishing, 2003)

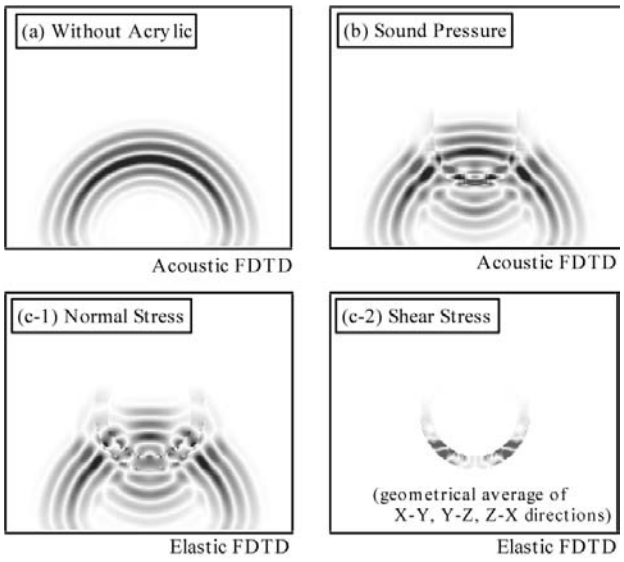

Figure 5 Comparison of sound pressure/stress distribution at 80[μs] between Acoustic and Elastic FDTD.

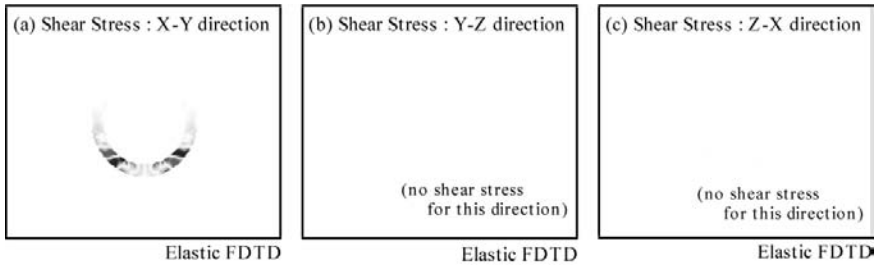

Figure 6 Vectorical elements of shear stresses.

Proc. Symp. Ultrason. Electron., Vol. 25, (2004) pp. 241-242
27-29 October, 2004

Imaging of picosecond longitudinal acoustic pulses in a transparent medium

○Motonobu Tomoda, *Roberto Li Voti, Osamu Matsuda and Oliver B. Wright
(Graduate School of Engineering, Hokkaido University, *Università di Roma "La Sapienza", Italy)

1. Introduction

Picosecond ultrasonics has proved very successful for the nondestructive characterization of thin films and nanostructures. In the conventional setup [1] light pulses from an ultrashort pulsed laser (known as the pump pulses) generate longitudinal ultrasonic pulses in opaque thin films in the frequency range 10-1000 GHz. Delayed light pulses (the probe pulses) detect any ultrasonic pulses that return to the surface after reflection from subsurface features through variations in reflectivity. The ultrasonic strain pulse shape depends on the acoustic generation mechanisms and the acoustic propagation processes, and is influenced by the optical absorption depth, ultrafast carrier diffusion, and ultrasonic attenuation in particular. Measurement of the strain pulse shape by analysis of the probe light variations allows these generation and propagation processes to be investigated. However, with the conventional surface detection method as described above, this can only be done when the strain pulse returns to the surface. Here we present a new technique in picosecond ultrasonics that allows the strain pulse shape to be measured continuously in a transparent medium.

2. Principle

To explain the principle, we select the simple geometry of a thin opaque film deposited on a transparent substrate, as an example. The ultrasonic pulses are generated in the film by illumination from the transparent substrate side. The picosecond ultrasonic pulses transmitted to the transparent medium induce a weak modification of the refractive index distribution therein through the photoelastic effect. As a consequence the optical reflectivity of the sample as measured by the optical probe pulses is perturbed. A Fredholm integral relationship is known to relate the change in the optical reflectivity to the perturbed refractive index distribution inside the sample [1-3]. To visualize the spatial ultrasonic strain distribution in the transparent substrate at a given time after excitation, we solve the inverse problem of computing the strain field from the observed perturbation in the reflectivity as a function of the probe beam angle of incidence using *s*-polarized probe light. The solution is obtained by the singular value decomposition method involving the decomposition of the kernel of the Fredholm integral into an appropriate complete set of singular functions [4]. These functions are used to reconstruct the strain pulse profile. The propagation of the acoustic strain pulse can be animated by repeating the inversion process for a sequence of delay times between the optical pump and probe pulses.

e-mail address: mtomoda@eng.hokudai.ac.jp

3. Experimental technique and simulation

A possible experimental setup is shown in **Fig. 1**. We confine the treatment in this paper to a description of a viable experimental technique and a trial simulation of realistic results. As a sample, we take a 10 mm radius hemisphere of BK7 glass whose flat surface is coated with a thin Al film of thickness ~500 nm. This is mounted on a rotation stage. Infrared light pulses of duration ~100 fs and repetition rate 80 MHz making up a pump beam of centre wavelength 830 nm from a Ti:sapphire laser are converted to blue light pulses of wavelength 415 nm in a BBO crystal (β-BaB_2O_4). The pump beam is chopped at 2 MHz by an acousto-optic modulator (AOM) and generates longitudinal ultrasonic pulses at a frequency of ~50 GHz (~100 nm in wavelength) in the sample. The probe beam

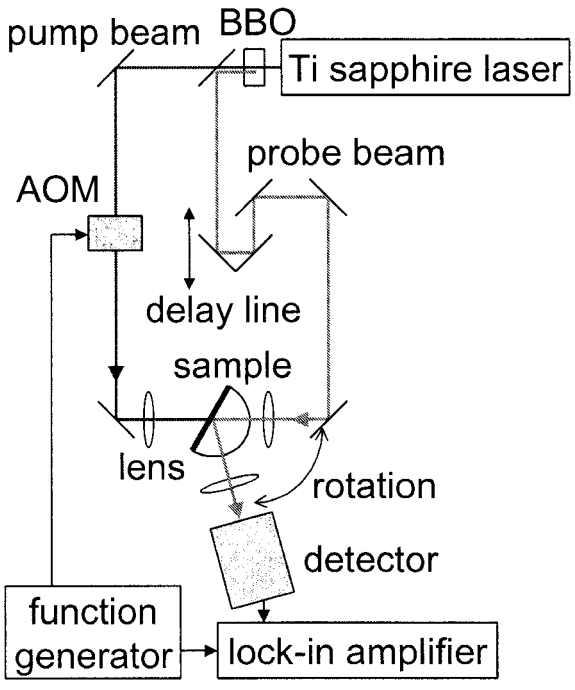

Fig. 1. Experimental setup.

is delayed in an optical delay line and monitors the changes in reflectivity of the sample at *s*-polarized incidence as a function of the angle of incidence (in the range 10 ° - 70 °) and the delay time between corresponding pump and probe optical pulses. A lock-in amplifier set to operate at the chopping frequency is used to detect the small changes in reflectivity ($\sim 10^{-5}$) induced by the ultrasonic pulses. The propagating ultrasonic strain distribution for each delay time can be calculated from this angle scan data.

As a numerical example we reconstruct a strain pulse travelling in BK7 glass corresponding to this experimental setup at a fixed delay time (**Fig. 2**). Initially we simulate the ultrasonic strain pulse distribution $\eta_3(z)$ [solid line in Fig. 2. (a)] based on ultrasonic generation using a simplified model of the generation mechanism (including the effect of carrier diffusion processes by assuming an effective optical absorption depth of 100 nm) and neglecting ultrasonic attenuation. Then we calculate a model data set for the reflectivity change $\Delta R/R$ (induced by the strain distribution) as a function of the probe incidence angle at 1° intervals [Fig. 2. (b)]. To provide a realistic example we have added 5 % Gaussian noise to each data point. The reconstructed strain distribution $\eta_3(z)$ is shown by the dashed line in Fig. 2. (a). The reconstructed strain profile reproduces the actual profile to ~50 nm spatial resolution, indicating that this method should be viable in practice to this accuracy. Experiments are now in progress to verify this method directly.

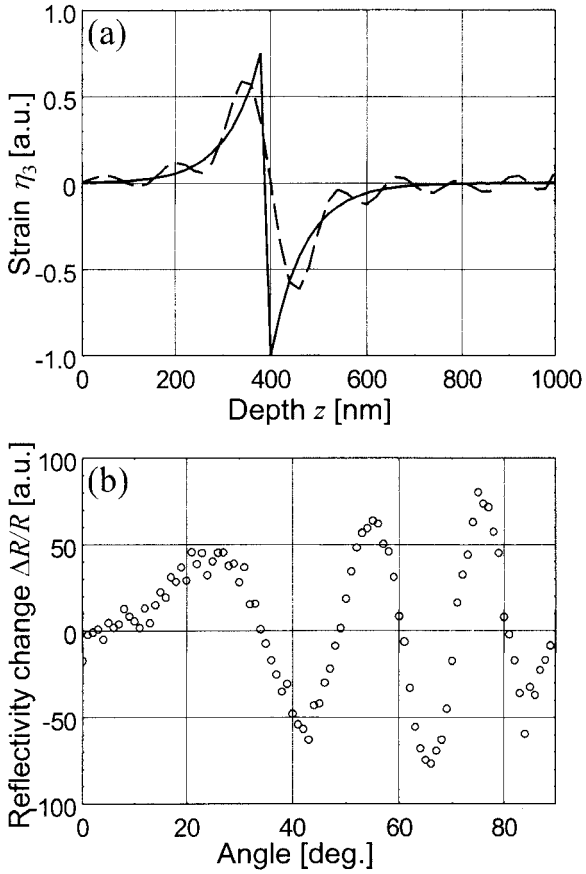

Fig. 2. These graphs illustrate the reconstruction process for an ultrasonic strain pulse travelling in BK7 glass at a fixed time after optical excitation. (a) Simulated strain distribution (solid line), and reconstructed strain distribution (dashed line). (b) Simulated relative reflectivity change, with 5 % Gaussian noise added, as a function of the probe angle of incidence.

Acknowledgment
This work was partially supported by a Grant-in-Aid for Scientific Research from the Japan Society for the Promotion of Science.

References

1. C. Thomsen, H. T. Grahn, H. J. Maris, and J. Tauc: Phys. Rev. B **34**, 4129 (1986).
2. O. Matsuda and O. B. Wright: J. Opt. Soc. Am. B, **19**, 3028 (2002).
3. O. Matsuda and O. B. Wright: Rev. Sci. Inst. **74**, 895 (2003).
4. J. F. Power: Rev. Sci. Inst. **73**, 4057 (2002).

Proc. Symp. Ultrason. Electron., Vol. 25, (2004) pp. 243-244
27-29 October, 2004

Elastic and magnetic anisotropy in Co/Pt superlattices: Measurement by RUS/Laser method

○Nobutomo Nakamura[a)], Hirotsugu Ogi, Masahiko Hirao (Osaka Univ., Grad. Sch. Eng. Sci.)
Teruo Ono (Kyoto Univ., Inst. Chem. Res.)

1. Introduction

In ferromagnetic thin films, an easy magnetization axis usually lies parallel to the film surface because of the shape magnetic anisotropy. However, in superlattice thin film, which consists of noble metal and ferromagnetic material, the easy magnetization axis can be perpendicular to the film surface when the ferromagnetic layers are ultrathin. This magnetic property is called perpendicular magnetic anisotropy (PMA). In the case of Co/Pt superlattice thin films, PMA appears when Co layer thickness is less than about 14 Å.[1)] Therefore, Co/Pt superlattice thin film is attracting many attentions because it can be a candidate for high-density perpendicular magnetic recording media and magneto-optical recording media. Combination of many factors such as crystal magnetic anisotropy, shape magnetic anisotropy, interfacial magnetic anisotropy, and magnetoelastic anisotropy determines the degree of PMA and physical background for PMA is not completely understood. Many experimental facts indicate that elastic strain caused by lattice misfit between Co and Pt is considered to be indispensable for PMA.

When Co/Pt superlattice thin film shows PMA, Pt (111) is parallel to the film surface and makes complete bonds with Co in a (0001) plane at the interfaces. Lattice misfit between Pt (111) and Co (0001) is as large as 10%. Then, the absolute values of in-plane elastic strains of Co and Pt layers are larger than 0.01. Such a large elastic strains never occur in bulk materials because of dislocation movements. The elastic strain must affect not only magnetic property but also elastic constants through lattice anharmonicity. Then, Co/Pt superlattice thin films must show a correlation between PMA and elastic constants, and the correlation gives an important knowledge of physical mechanism of PMA. However, no studies measured the elastic constants of Co/Pt superlattice thin films because of the difficulty for determining thin-film-elastic constants. In this study, we determine the anisotropic elastic constants of Co/Pt superlattice thin films using resonant ultrasound spectroscopy (RUS) coupled with laser-Doppler interferometry[2)]. We found a correlation between the elastic constants and PMA for the first time.

a) nobutomo@me.es.osaka-u.ac.jp

2. Specimens

Co/Pt superlattice thin films are deposited on monocrystal Si substrates, measuring 6.0×4.5×0.2 mm^3, by an ultra-high-vacuum evaporation method. We prepared three kinds of Co/ Pt superlattice thin films whose bilayer thicknesses D ($=d_{Co}+d_{Pt}$) were 17.7, 94, and 184 Å. We kept the thickness ration α ($=d_{Pt}/d_{Co}$) 4. Their bilayer number n was 500, 100, and 50, and the total thickness ($=(d_{Co}+d_{Pt})\times n$) was 0.89, 0.94, and 0.92 μm, respectively. The bilayer thicknesses were determined from X-ray diffraction spectra. X-ray diffraction spectra from multilayer thin films show many peaks. The peak angles and X-ray wavelength determines D accurately.

Because thin films are usually elastically anisotropic between the in-plane and out-of-plane directions, we assume that our specimens show transverse isotropy with the five independent elastic constants C_{11}, C_{33}, C_{12}, C_{13}, and C_{44}.

3. RUS/Laser Method

Mechanical free-vibration resonance frequencies of film/substrate specimen depend on mass densities, dimensions, and all independent elastic constants of the film and substrate. Therefore, thin film elastic constants are inversely determined by measuring the resonance frequencies using other measurable parameters. This method is called RUS. In the conventional RUS method, however, ambiguity of vibration modes of observed

resonance frequencies occurred. We overcame this long-running problem by combining RUS with laser-Doppler interferometry.

Resonance frequencies were measured by a piezoelectric tripod in vacuum, which allowed very accurate measurements; scatterings of the measured resonance frequencies were 0.01% or less.

The determination takes three steps. (i) We determine the elastic constants of the Si substrate alone by the RUS/laser method before depositing the film. (ii) After that, we deposit the thin film on the substrate. Resonance frequencies change depending on the density and elastic constants of the deposited thin film. (iii) We inversely determine the elastic constants of the film from the resonance-frequency shifts.

In order to demonstrate large contributions of thin-film elastic constants to the resonance frequencies, we calculated the resonance-frequency shifts by deposition of films: We assumed an oriented monocrystal Si substrate (6.0×4.5×0.2 mm^3) and an isotropic film with 1-μm thickness. We fixed the film density to be 8.932 g/cm^3 and changed the elastic constants in three cases; (i) C_{11}=99.0 and C_{44}=23.5 GPa, (ii) C_{11}=198 and C_{44}=47 GPa (corresponding to copper), and (iii) C_{11}=297 and C_{44}=70.5 GPa. **Figure 1** shows the results. The frequency shifts vary between -0.75 and 0.2% (about 1% difference), depending on the elastic constants. Thus, the frequency shift is sensitive to the film elastic constants. The frequency shifts are of the order of 1 %, which is larger in magnitude than the measurement accuracy by one or two orders.

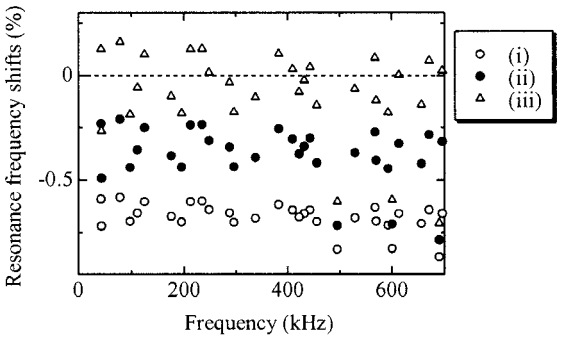

Fig.1 Elastic-constant dependencies of resonance frequency shifts. (i), (ii), and (iii) indicate thin film elastic constants (C_{11} (GPa), C_{44} (GPa)) are (99.0, 23.5), (198.0, 47.0), and (297.0, 70.5), respectively.

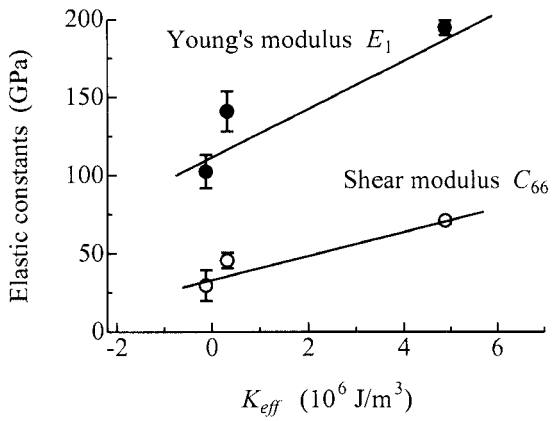

Fig.2 Relationship between elastic constants and effective magnetic anisotropy energy of Co/Pt superlattice thin films.

4. Results and Discussion

We measured magnetic hysteresis loops along the in-plane and out-of-plane directions using superconducting quantum interference device (SQUID). We calculate an effective magnetic anisotropy energy K_{eff} from the hysteresis loops[3], which indicates the degree of PMA. (Positive value of K_{eff} means that the Co/Pt superlattice shows PMA.) The effective magnetic anisotropy energy decreases as the bilayer thickness increases. Considering the fact that the elastic strain is indispensable for PMA, this result indicates that the elastic strain is reduced as the bilayer thickness increases.

Figure 2 shows a relationship between determined elastic constants and effective magnetic anisotropy energy. Simple rule of mixture predicts the same elastic constants for the three supelattices because of the same volume fraction. However, determined in-plane Young's modulus E_1 and shear modulus C_{66} obviously increase as the effective magnetic anisotropy energy increases. Thus, there is a correlation between the elastic constants and PMA. We attribute this to the reduction of elastic strain near the interfaces.

References

1. P. F. Carcia: J. Appl. Phys. **63** (1988) 5066.
2. N. Nakamura, H. Ogi, and M. Hirao: Acta Mater. **52** (2004) 765.
3. Y. Kamada, Y. Hitomi, T. Kingetsu, and M. Yamamoto: J. Appl. Phys. **90** (2001) 5104.

Proc. Symp. Ultrason. Electron., Vol. 25, (2004) pp. 245-246
27-29 October, 2004

B/A Measurement for Liquid Samples Using an LN Transducer with Inverted-Domain Layer

○Shigemi Saito, Akira Yamamoto (Tokai Univ.) and Kiyoshi Nakamura (Tohoku Univ.)

1. Introduction

A $LiNbO_3$ plate with a ferroelectric inversion layer performed through heat treatment[1] is sensitive even at the second-order resonance. When a sinusoidal acoustic wave is emanated from this plate, the second harmonic component nonlinearly generated within a medium can be detected by receiving the sound reflected at the propagating path[2]. Applying this principle to a focused beam formed by an acoustic lens, a new finite-amplitude method to measure the acoustic nonlinearity parameter *B/A* of liquid sample is presented.

2. Experimental System

As shown in **Fig.1**, a focusing system consists of an acoustic lens with a curvature radius d of 8 mm and an aperture radius of 5 mm furnished at the center of a synthetic silica [sound speed c_0=5953 m/s, density ρ_0=2203 kg/m^3] disk with a 100-mm diameter and a 7.76-mm thickness. At a room temperature, a liquid sample is filled in a cylindrical glass cell of 23-mm inner diameter attached on the lens surface. A reflector rod with a flat top of 10-mm diameter is supported by a z stage. A tungsten rod to realize total reflection and a Duracon rod whose specific acoustic impedance Z_D is 3.32 MRayl are employed. The two-way transducer is a 0.19-mm thick LN plate with a ferroelectric inversion layer, apodized with a Gaussian weighting electrode[3]. The radiated 19-MHz burst wave returns from the reflector set at the focal plane. **Figure 2** shows the square root of the received signal amplitude at various frequencies measured as a two-way sensitivity of the transducer. Since the similar sensitivity is obtained at 38 MHz, the second harmonic sound can be detected. In the present system, a second harmonic component of about 2% is contained in the FG output. This decreases to 1% after a round-trip transmission in water. Since the amplitude of the second harmonic sound generated within the lens is estimated to be 1/50 times that generated by the propagation in water, the nonlinearity of the lens is neglected.

ssaito@scc.u-tokai.ac.jp

3. Measurement of Linear Property

Since the second harmonic generation in proportion to $(1+B/2A)/\rho c^3$ is reduced at lower pressure levels, the attenuation coefficient α is also influential. The linear property ρ, c and α must be measured for estimating the *B/A*.

(1) Measurement of sound speed c: The focal distance depends on the sound speed in the medium. Assume that the top of the tungsten rod is set Δz closer so that the received amplitude attains the maximum. Then the sound speed c in a sample is obtained by $c=[c_W d-(c_0-c_W)\Delta z]c_0/[c_0 d-(c_0-c_W)\Delta z]$, where c_W=1483 m/s and ρ_W=1000 kg/m^3 are the sound speed and density in water at 20°C.

(2) Measurement of density ρ: When the Duracon rod decreases the reflected amplitude R(<1) times. The density is derived by $\rho = (1 \pm R)Z_D/[(1 \mp R)c]$, where the double sign works in the same order as $\rho c \gtrless Z_D$. Usually $\rho c < Z_D$ for liquids.

(3) Measurement of attenuation α: Emanating the burst of 19 MHz or 38 MHz, the sound amplitude

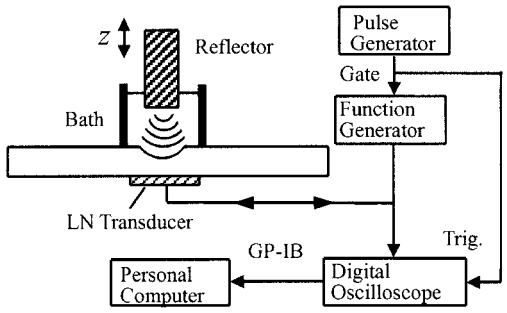

Fig.1. Experimental arrangement.

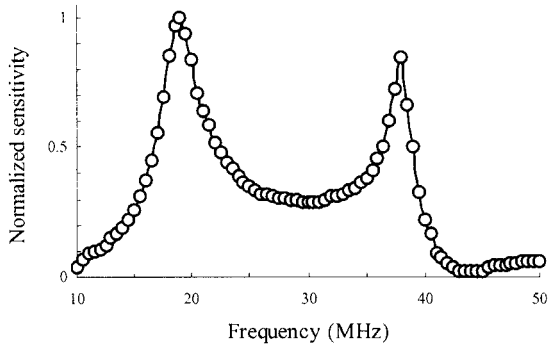

Fig.2. Frequency dependence of sensitivity.

reflected from the tungsten rod is observed. Assume that the amplitudes turn to be R_1 and R_2 times the case of water at each frequency. This change is caused by the mismatch with the lens, in addition to inherent attenuation. Integrating these effects, the attenuation is derived as

$$\alpha_n = \frac{c_0 - c}{c_0 - c_W} n^2 \alpha_W - \frac{1 - c/c_0}{2d} \ln(R_n \frac{\rho_W c_W}{\rho c}) - \frac{1 - c/c_0}{d} \ln(\frac{\rho_0 c_0 + \rho c}{\rho_0 c_0 + \rho_W c_W}) \quad (n=1,2),$$

where α_W=9.03 Np/m is the attenuation coefficient in water at the fundamental frequency .

The result for four alcohol samples is listed on **Table I**. They are in reasonable agreement with the literature values at 20°C in parentheses. [4,5]

Table I. Measured linear property.

Sample	Methanol	Ethanol	Butanol	Benzyl
ρ(kg/m^3)	794(791)	784(789)	782(810)	1049(1045)
c(m/s)	1125(1121)	1173(1182)	1268(1258)	1496(1540)
α_1(Np/m)	14(12)	21(19)	30(30)	31(34)
α_2(Np/m)	49(47)	73(76)	117(119)	128(137)

4. Measurement of Nonlinearity Parameter

The ratio R_{P2} of the received second harmonic amplitudes for the case where the cell is filled with sample and for the case with water is measured. Using the successive approximation solution for the KZK equation [6], the nonlinearity coefficient β=1+$B/2A$ is given by the following relation.

$$\beta = \frac{\rho c^2}{\rho_W c_W^2} (\frac{\rho c + \rho_0 c_0}{\rho_W c_W + \rho_0 c_0})^3 \times \exp(\alpha_2 D - 4\alpha_W D_W) F \beta_W R_{P2} = G \beta_W R_{P2},$$

where β_W is the value of β in water(3.5), D=d/(1-c/c_0) and D_W=d/(1-c_W/c_0). F is a factor to take the focusing gain and sound attenuation into account the generation and propagation of second harmonic sound, which is given as follows:

$$F = \exp(\alpha_2 D - 4\alpha_W D_W) \left| \frac{\int_0^{2D_W} \frac{\exp(2\alpha_W z')}{h_W(z')} dz'}{\int_0^{2D} \frac{\exp(2\alpha_1 z')}{h(z')} dz'} \right|,$$

where $h(z)$=$2\xi z$-jk(1-z/D), $h_W(z)$=$2\xi z$-jk_W(1-z/D_W), and ξ=170000 m^{-2} is the Gaussian coefficient on the source. Since the second harmonic amplitude decreases in highly dissipative samples, the value of F significantly increases with attenuation while $F \approx 1$ for the sample with sound speed and attenuation similar to water. For a highly dissipative sample, the measurement error of α_1 and α_2 may cause a considerable error in B/A.

The measured amplitudes of the second harmonic through water and alcohol samples are shown in **Fig.3**. Together with R_{P2} obtained from the figure and G calculated from the linear property, the obtained B/A is listed on **Table II**. A reasonable agreement is found with the literature values.

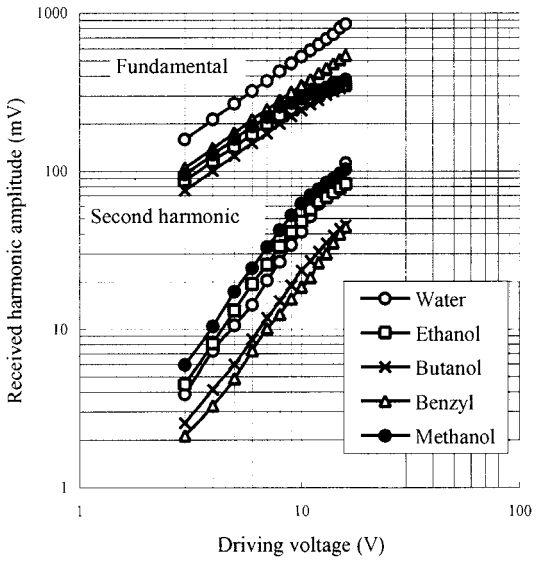

Fig.3. Harmonic amplitude of the reflected sound through alcohol samples.

Table II. Measured B/A values.

Sample	Methanol	Ethanol	Butanol	Benzyl
R_{P2}	1.59	1.16	0.58	0.44
G	1.00	1.46	3.17	4.03
B/A	9.1(9.6)	9.9(10.5)	10.7(10.7)	10.3(10.2)

5. Conclusion

Utilizing an LN transducer with inverted-domain layer, a 19-MHz focused beam was formed in a few-ml liquid sample. The acoustic nonlinearity parameter B/A was successfully measured through the 38-MHz sound detection.

References

1. K. Nakamura: Jpn. J. Appl. Phys. **31** (1992) Suppl.31-1, 9.
2. S. Saito, Y. Kameyama and K. Nakamura: Jpn. J. Appl. Phys. **40** (2001) 3664.
3. S. Saito, Y. Kameyama and K. Nakamura: Acoust. Sci & Tech. **24** (2003) 406.
4. R. T. Beyer: *Nonlinear Acoustics* (Department of the Navy, 1974) p.101.
5. P.-K. Choi : *Cho-Onpa Binran* (Maruzen, Tokyo, 1999) p.709.
6. S. Saito : J. Acoust. Soc. Jpn.(E) **16**(1995) 29.

Proc. Symp. Ultrason. Electron., Vol. 25, (2004) pp. 247-248
27-29 October, 2004

Terahertz ultrasonic generation and detection in GaAs/AlGaAs quantum wells

◎T. Tachizaki, O. Matsuda, *T. Fukui, **J. J. Baumberg, and O. B. Wright

(Graduate School of Engineering, Hokkaido University, *Reserch Centre of Integrated Quantum Electronics, Hokkaido University, **School of Physics and Astronomy, University of Southampton)

1 Introduction

The advance of semiconductor fabrication and processing technology has lead to the routine construction of devices with characteristic dimensions of the order of 100 nm or less, often in the form of many layers of different materials. However, conventional noncontact inspection techniques such as local probe microscopy or electron microscopy only allow access to the surface region. Laser picosecond acoustics has been shown to be a viable method for investigating buried nanostructures such as quantum wells [1]. This method relies on the excitation and detection of terahertz ultrasonic pulses using ultrashort light pulses.

Here we develop this method using a sample containing several quantum wells with a higher time resolution than previously used for this type of sample [2]. The ultrasonic strain pulse shape depends strongly on the confined electron and hole wavefunctions, and so this sample is interesting from a fundamental point of view. Moreover, the localized nature of the optical absorption in the quantum wells allows much higher ultrasonic frequencies to be obtained compared to bulk samples.

2 Experiment

A GaAs/$Al_{0.3}Ga_{0.7}As$ quantum well structure was prepared on a GaAs (100) substrate by MOVPE (metalorganic vapour phase epitaxy). GaAs/AlGaAs quantum wells of three different thicknesses (4.5, 7.6 and 3.1 nm) were incorporated at depths ~300, 350 and 450 nm, respectively (as shown in **Fig. 1**), spaced sufficiently to avoid any carrier tunnelling between them. GaAs and AlGaAs are suited for such ultrasonic experiments because they have nearly identical acoustic impedances, thus preventing multiple acoustic reflection and simplifying the data analysis. Moreover, they are ideal for the growth of lattice-matched crystalline structures with a low defect density.

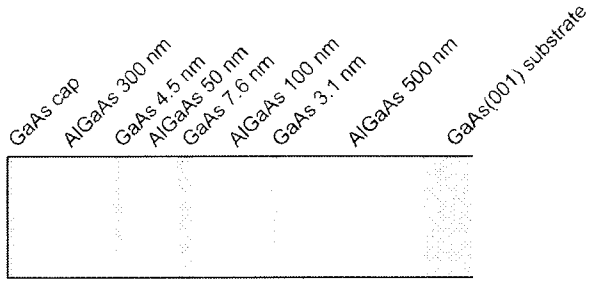

Figure 1: A GaAs/$Al_{0.3}Ga_{0.7}As$ quantum well structure: three different thickness quantum wells are buried.

After illumination of the sample with ultrashort optical pulses in the infrared, the light is transmitted straight to the quantum wells through the transparent AlGaAs layers, and excites longitudinal ultrasonic pulses therein. The generation is predominantly due to an electronic mechanism rather than due to thermal expansion [1,2]. These strain pulses are detected upon arrival at the sample surface by ultrashort optical probe pulses in the visible. This technique is known as the optical pump and probe technique.

The pump light pulses have a wavelength of 810 nm, a duration of ~ 500 fs (at full width at half maximum), and a repetition rate of 82 MHz. The probe light pulses of wavelength 405 nm (derived from the same laser in a second harmonic crystal) and of duration ~ 100 fs are used to monitor optical reflectivity changes δR and phase changes $\delta\phi$ caused by the strain pulses arriving at the surface. (In contrast to the pump light pulses, the probe light pulses only penetrate into the thin top GaAs cap layer and partly

into the first AlGaAs layer.) The optical reflectivity and phase changes of the sample are monitored with the probe beam in a common-path optical interferometer [3]. The experimental results are shown in **Fig. 2**.

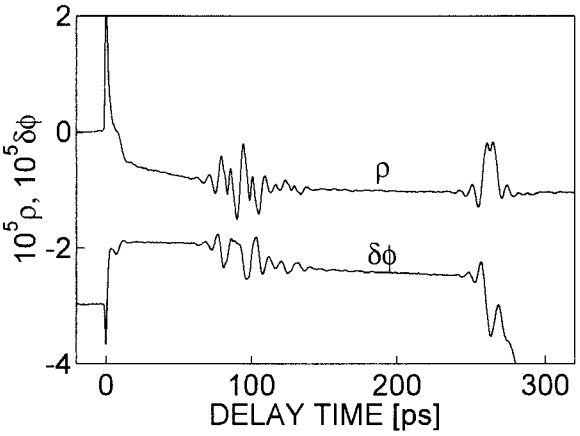

Figure 2: The real and the imaginary parts of the complex reflectance change: $\rho = \delta R/2R$ and phase change $\delta\phi$ respectively. The upper curve corresponds to ρ and the lower to $\delta\phi$.

3 Discussion of results and numerical simulations

In Fig. 2 the features at around 100 ps and after 250 ps are caused by the ultrasonic pulses arriving at the sample surface from the quantum wells and from the GaAs substrate, respectively. The downward step in the phase change $\delta\phi$ between 50 ps and 150 ps is a result of the sample bulging out after the reflection of the (compressive) ultrasonic pulses from the sample surface. (The sharp signal at 0 ps and the decay immediately following this are the effect of photoexcited nonequilibrium electrons.)

We carried out numerical simulations that take account of the ultrasonic pulse generation, propagation and detection processes in the sample [4]. One example of such a simulation is shown in **Fig. 3** together with the experimental results. The improvement of the time resolution compared with previous experiments on a similar sample [2] allows a better fit to be obtained. The important fitting parameters here are the ultrasonic attenuation coefficient of AlGaAs and the photoelastic constants of GaAs and AlGaAs at the probe light wavelength.

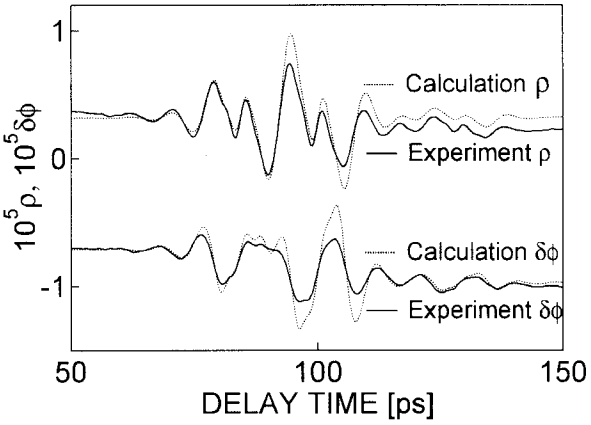

Figure 3: Comparison between the experimental results and the numerical simulations. The dashed lines correspond to the simulations. The upper two curves represent ρ and the lower two represent $\delta\phi$.

In future we hope to be able to solve the inverse problem of deriving the ultrasonic strain pulse shape from the data, and hence provide a measure of the carrier wavefunctions.

References

1. J. J. Baumberg, D. A. Williams, and K. Köhler, Phys. Rev. Lett. **78**, 3358(1997).

2. O Matsuda, I. Ishii, T. Fukui, J. J. Baumberg, and O. B. Wright, Physica B **316-317**, 205(2002).

3. D. H. Hurley and O. B. Wright, Opt. Lett. **24**, 1305(1999).

4. O Matsuda and O. B. Wright, J. Opt. Soc. Am. B **19**, 3028(2002).

Proc. Symp. Ultrason. Electron., Vol. 25, (2004) pp. 249-250
27-29 October, 2004

Real time imaging of surface acoustic waves on a sphere

◎ Hiroto Yamazaki, Osamu Matsuda and Oliver B. Wright (Graduate School of Engineering, Hokkaido University)

1. Introduction

The propagation of surface acoustic waves on a sphere is different from that on a planar surface [1]. The curvature of the surface of a sphere gives rise to dispersion effects and complex focusing behaviour in the case of a single crystal. Because of possible applications to ball devices based on surface acoustic waves, there is much interest in characterizing how surface acoustic waves propagate on the surface of elastically isotropic or anisotropic spheres [2].

Laser generated surface acoustic waves on spheres were studied by Royer [3]. Using a similar laser ultrasonics technique we present here a new method for imaging surface acoustic waves on spheres in real time at frequencies up to 1 GHz. This allows the propagation to be studied in much greater detail than possible with point-by-point measurements.

2. Experiment

The experimental setup is shown in **Fig. 1**. This is based on the optical pump-probe method and on a variation of an ultrafast surface wave imaging technique [4]. As a sample we use glass (BK7) balls of diameter 1 mm and 2 mm coated with aluminium films. The Al of thickness ~60 nm is sputtered either on one half of the sphere or alternatively on the whole sphere. Pump optical pulses of duration ~1 ps, energy ~0.5 nJ and central wavelength 830 nm from a mode-locked Ti:sapphire laser of repetition rate 80 MHz (period 12.5 ns) are focused onto the surface of the sample at normal incidence using a Selfoc micro-lens after passage through a flexible monomode optical fiber. The optical fiber and micro-lens are fixed to a biaxial rotation stage so that the pump optical pulses always illuminate the same point on the ball while the stage rotates for purposes of scanning the detection point. Bulk and surface acoustic waves are launched from the optically irradiated area of a few microns in diameter through the thermoelastic effect.

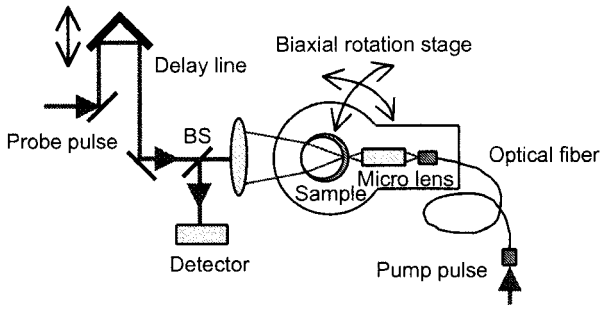

Fig. 1 Experimental setup for surface acoustic wave imaging on spheres.

Normally-incident delayed optical probe pulses of central wavelength 415 nm produced by a second-harmonic generation crystal are used to detect the intensity changes of a point on the sample through the photoelastic effect. This couples the strain associated with the surface waves to the permittivity tensor through the photoelastic constants. The change of the permittivity leads to a reflectivity change. In the first type of experiment performed the probe pulses are incident from the transparent side of the ball that is half-coated with Al in order to detect the surface acoustic waves in the region near the excitation point. In this case the glass ball serves as a lens to focus the probe beam. In the second type of experiment the probe pulses are incident from the opposite side of the ball that is completely coated with Al in order to detect the surface acoustic waves in the region diametrically opposite the excitation point. Angular scanning of the sample stage (with attached micro-lens and fiber) with respect to the probe spot allows surface wave imaging at any chosen delay time between the pump and probe optical pulses. The process is repeated at a series of pump-probe delay times to form an animation of the surface wave propagation in real time. Chopping the pump beam at 1 MHz and lock-in detection are used to improve the signal-to-noise ratio. The typical relative reflectivity change is 10^{-6}.

e-mail : hirotoy@eng.hokudai.ac.jp

3. Results and discussions

Fig. 2 (a) shows an image of the surface acoustic waves for a 2 mm diameter glass ball half-covered with Al, obtained with the first experimental configuration in which the imaging is carried out near the source of the surface acoustic waves. The Rayleigh-like surface waves are clearly visible as circles, owing to the elastic isotropy. The velocity of surface waves for BK7 is ~3 km s^{-1}. The imaged region corresponds to 10°×10° (~175 ㎛×175 ㎛). The dark region at the center of the images is caused by refractive index changes associated with the temperature rise induced by the pump pulses. Because of the broad wave number spectrum of the surface acoustic wave pulses, velocity dispersion should be evident at sufficiently long propagation distances. In the present experiments, however, the dispersion due to surface curvature is negligible because of the relatively short ultrasonic wavelengths excited (~10 ㎛). Moreover, the Al film is thin enough for the effect of thin film dispersion not to be noticeable. The frequency range involved is 100 MHz - 1 GHz.

Fig. 2 (b) shows surface wave images for a 1 mm diameter glass ball completely covered with Al. The imaged region corresponds to 20°×20° (~175 ㎛ × 175 ㎛). The surface acoustic waves departing from the excitation point converge to the pole (at the point diametrically opposite to the source), following the curvature of the ball. The surface waves then diverge from this pole. The superposition of these counterpropagating wave fronts produces an interference effect consistent with the periodic behavior (at a period 12.5 ns) that is in fact observed. In this second experiment, in which the Al covers the whole sphere, the glass ball does not act as a lens, and so the lateral resolution is lower compared with the first experiment.

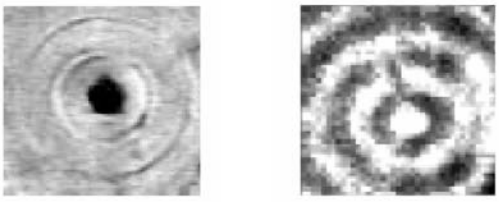

(a) 10×10 degrees (b) 20×20 degrees

Fig. 2 Surface acoustic wave images for BK7 glass spheres coated with a thin film of Al (a) on half of the sphere and (b) on the whole sphere.

4. Summary

In summary, we have demonstrated the real-time imaging of surface acoustic waves on isotropic spheres using an ultrafast optical technique. This method can be applied in future to anisotropic balls to investigate the effect of surface curvature and anisotropic propagation effects.

Acknowledgment

This work is partly supported by a Grant-in-Aid for the 21th Century Center of Excellence (COE) Programme entitled 'Topological Science and Technology'.

References

1. I. A. Viktorov: *Rayleigh and Lamb Waves* (Plenum, New York, 1967).
2. S. Akao, N. Nakaso, T. Ohgi and K. Yamanaka: Jpn. J. Appl. Phys. **43** (2004) 3067.
3. D. Royer, E. Dieulesaint, X. Jia and Y. Shui: Appl. Phys. Lett. **52** (1988) 706.
4. Y. Sugawara, O. B. Wright, O. Matsuda, M. Takigahira, Y. Tanaka, S. Tamura and V. E. Gusev: Phys. Rev. Lett. **88** (2002) 185504.

Proc. Symp. Ultrason. Electron., Vol. 25, (2004) pp. 251-252
27-29 October, 2004

Basic study on the Evaluation of the Quality of Rice Grains by the use of Photoacoustic Imaging

◎Manabu Suzuki[1], Katsuhiko Miyamoto[2] and Tsutomu Hoshimiya[1]
([1]Graduate School of. Applied Physics, Tohoku Gakuin Univ.
[2]Research Institute of Electrical Communication, Tohoku Univ.)

§ Introduction

Recently quality evaluation and control have been more important in various fields. In biology and agriculture, quality evaluation of the food plant has been performed by many inspection methods. Until now, evaluation of the grain of the crops has been performed for the corn alone by photoacoustic spectroscopy in the infrared region.[1)]. We have been developed the application of photoacoustic microscope (Photoacoustic Microscope: PAM) to the pollen analysis.[2-3)] In this study, the quality evaluation of the grains of the rice --perfect grain, blackened grain, or grain of rice blast ("Imochi-byo") -- by the use of PAM was performed.

§ Apparatus

In a PAM, the modulated light energy absorbed by the sample is converted into acoustic or elastic energy via the conversion of the light into thermal energy.

The basic experimental setup used for the measurement is the same as that used in the previous publications.[2-3)] and shown in **Fig. 1**. The Ar laser beam was focused and scanned over the specimen surface by pulse stages driven by linear-motors. The PA signal detected by a highly sensitive condenser microphone (Brewer & Kaejer 4166) was processed with a lock-in amplifier, reconstructed as amplitude and phase images, and displayed and recorded by a personal computer. Amplitude and phase PA images were stored as spread-sheet data, and those are available to be processed such as integration or noise reduction easily.

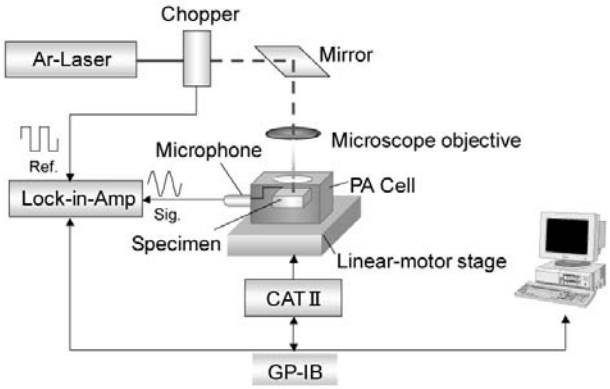

Fig.1 Basic experimental set up

§ Specimens

The specimens collected for this study is good rice grains and bad(partly blackened) rice grains. Bad rice grains have black color inside or over the surface. The photographs of good and bad rice grains are shown in **Fig.2** and **Fig.3**, respectively.

---

tpth@tjcc.tohoku-gakuin.ac.jp

§ Experimental Results and Discussion

Photoacoustic images for good and bad rice grains were shown in **Figs.4** and **5**,

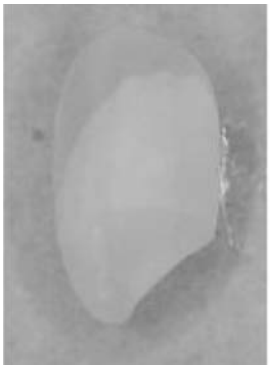

Fig. 2 The photograph of a good rice grain.

Fig. 3 The photograph of a bad rice grain

respectively.

The measured area was 6mm×6mm, with resolution of 50 × 50 pixels. Modulation frequency was fixed to be 90Hz. For a good rice grain, the obtained PA image shows a uniform image, because the homogeneous absorption occurred due to the homogenous color of the grain. On the contrary, the PA image of a bad grain shows a strong signal region due to an inhomogeneous a strong absorption caused by a colored region. The results show that a PA signal makes it possible to evaluate the quality of rice grains.

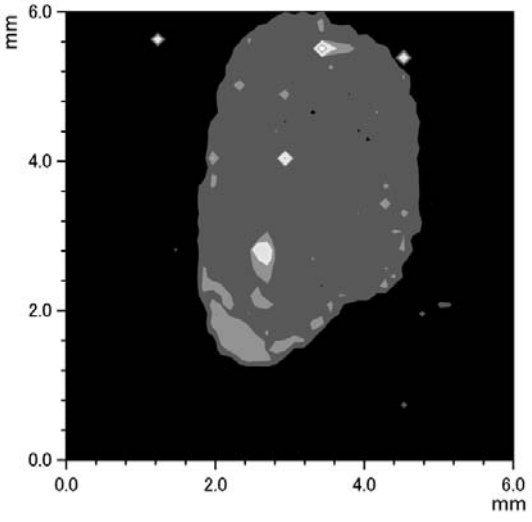

Fig. 4 The PA image of a good rice grain.

§ Conclusion

In this study, PAM was applied to evaluate the quality of rice grains for the first time. Due to the difference in the absorption of the laser beam, the homogeneity of rice grains was measured as thermal images. The resolution was good enough to evaluate a single grain of rice particle. This method has an advantage
In addition to the conventional video image evaluation or macroscopic optical absorption method, PA imaging has an ability to evaluate the quality and healthiness, such as Imochi disease, of rice grains

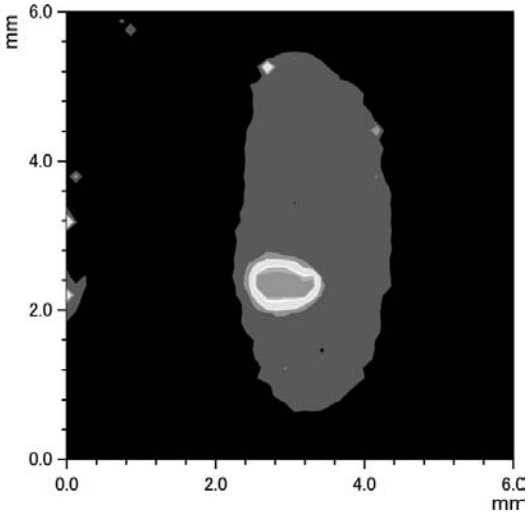

Fig. 5 The PA image of a blackened rice grain.

Reference

[1]B.Hardins: Agricultural Research, 12 (1999. April).

[2] K.Miyamoto and T. Hoshimiya: Jpn. J. Appl. Phys., vol.42, Part1, No,5B, 3084 (2003.5).

[3]K.Miyamoto and T. Hoshimiya: Proceedings of the 2003 IEEE Ultrasonics Sympisium、P3M-8 (Honolulu, 2003.10).

Proc. Symp. Ultrason. Electron., Vol. 25, (2004) pp. 253-254
27-29 October, 2004

Mathematical Representation of Interaction between Elastic and Dielectric Energy in Piezoelectric Transducer Using Exponential Function of Matrix

Michio Ohki (Natl. Def. Acad., Japan)

1. Introduction

The exponential function of matrix can be used for representing the mode coupling between plural modes on a distributed-parameter basis. **Figure 1** shows the mode coupling between two modes x_a and x_b on the infinitesimal interval ds, expressed with a (2,2) matrix A. The mathematical expression for this phenomenon is given by

$$\frac{\mathrm{d}}{\mathrm{d}s}\begin{pmatrix} x_a \\ x_b \end{pmatrix} = A\begin{pmatrix} x_a \\ x_b \end{pmatrix}, \qquad (1)$$

and its solution is

$$\begin{pmatrix} x_a(s) \\ x_b(s) \end{pmatrix} = \exp(sA)\begin{pmatrix} x_a(0) \\ x_b(0) \end{pmatrix}. \qquad (2)$$

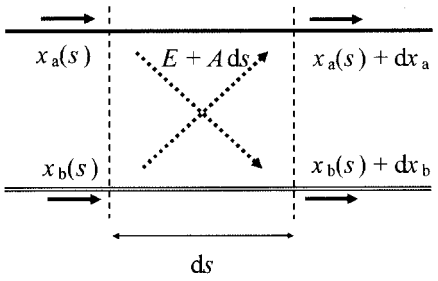

Fig. 1 Mode coupling between x_a and x_b. (E: unit matrix)

In this paper, the interaction between elastic and dielectric energy in the piezoelectric transducer is discussed, based on the formulation using exp(sA) and the calculation of infinite geometric series of matrix, Neumann series. In Mason's circuit the dielectric energy component is represented by lumped parameters C_0 and $-C_0$, the function of which is replaced with a matrix operation in this study.

2. Formulation of Complex Series Dynamics Using exp(sA)

In the previous paper[1], the resonance effect in the piezoelectric transducer with the boundary condition of 'whole drive' and 'free mechanical boundaries' was represented by the flow and superposition of a complex dynamical variable η_a in the circuit structure shown in **Fig. 2(a)**, where the

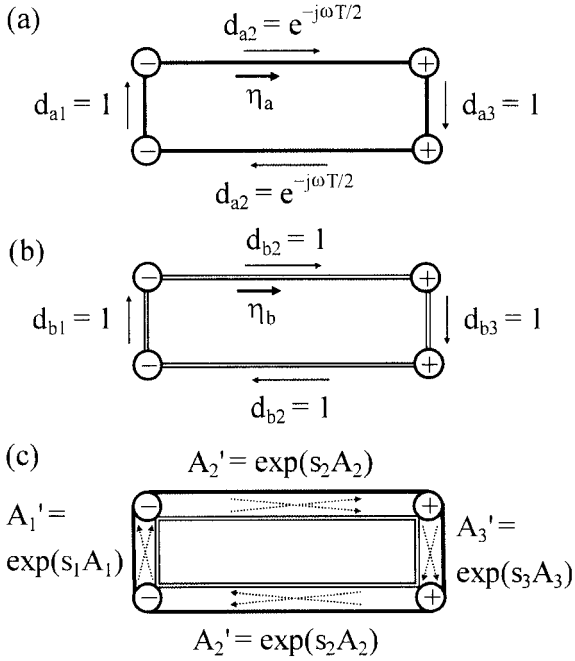

Fig. 2 Circuit structures used in the 'complex series dynamics'. (a) In the case of elastic energy; (b) In the case of dielectric energy; (c) In the case of 'mode coupling' between cases (a) and (b).

circuit had four terminals for inputting and outputting η_a, and the propagation phase factors of η_a between the neighboring terminals were given by

$$d_{ai} = \exp(\phi_{ai}), \quad (i = 1, 2, 3)$$
$$\phi_{a1} = \phi_{a3} = 0, \quad \phi_{a2} = -j\omega T/2. \qquad (3)$$

In eq. (3), T is a propagation time of η_a around the circuit that is determined by the acoustic velocity.

The superposition of η_a's on the output terminals, which was represented by infinite geometric series, was considered for all the combination of input-output terminals. This procedure provided the frequency characteristics of the transducer as a function of ω, by which the resonance effect in the transducer was expressed. This result was identical to what we observed in the 'mechanical part' of Mason's circuit.

Here the 'electrical part' of Mason's circuit is assumed to be also represented by the similar circuit structure, as shown in **Fig. 2(b)**, with the following propagation phase factors:

$$d_{bi} = \exp(\phi_{bi}), \quad \phi_{b1} = \phi_{b2} = \phi_{b3} = 0. \qquad (4)$$

The superposition of η_b's in Fig. 2(b) gives constant (non-resonant) frequency characteristics, since the phase factors in eq. (4) do not depend on ω.

The above two 'modes,' 'elastic' and 'dielectric' one, respectively, are assumed to be 'coupled' between the neighboring terminals on the circuit structure shown in **Fig. 2(c)**, based on the mechanism depicted in Fig. 1, where the matrix A in Fig. 1 is considered in each section of Fig. 2(c) (labeled 1, 2 and 3, as shown in this figure), and each A_i is the sum of a matrix D_i for propagation phase and a matrix U_i for mode coupling:

$$A_i = D_i + U_i \quad (i = 1,2,3), \qquad (5)$$

where

$$D_i = \frac{1}{s_i}\begin{pmatrix} \phi_{ai} & 0 \\ 0 & \phi_{bi} \end{pmatrix}, \qquad (6)$$

$$U_i = \log\begin{pmatrix} \sqrt{1-u_i^2} & u_i \exp(j\theta_i) \\ -u_i \exp(-j\theta_i) & \sqrt{1-u_i^2} \end{pmatrix}, \qquad (7)$$

where ϕ_{ai} and ϕ_{bi} are given by eqs. (3) and (4), respectively, and u_i and θ_i are regarded as coupling parameters. U_i is derived from the logarithmic function of a unitary matrix and becomes a Hermitian alternating matrix. Matrix $\exp(s_iA_i)$ is regarded as a 'propagation factor with mode coupling' in each section of the circuit in Fig. 2(c), and s_i is also regarded as a coupling parameter.

Neumann series in terms of $\exp(s_iA_i)$ are considered for all the combination of input-output terminals, the superposition of which becomes a function of ω. An appropriate propagation loss is introduced for the convergence of the series, and the polarity of terminal, positive or negative, is multiplied in the input and output processes. (See ref. 2 as well with regard to the formation of Neumann series.)

3. Results and Discussion

Interaction between elastic and dielectric energy causes the shift of resonance frequency of the system: $\Delta\omega > 0$ for the piezoelectric transverse (T-) effect and $\Delta\omega < 0$ for the piezoelectric longitudinal (L-) effect, which can be obtained by the calculation described in sec. 2, as shown below.

The calculation result of $|\eta_a|$ with mode coupling is shown in the lines labeled 'C' in **Fig. 3(a)**, where the calculation parameters are as follows:

$(s_1, s_2, s_3) = (2, 1, 2)$, $(u_1, u_2, u_3) = (0.5, 0.25, 0.5)$,
$(\theta_1, \theta_2, \theta_3) = (\pi/2, \pi/2, \pi/2)$,

and the result when the mode coupling does not occur; that is, when $(u_1, u_2, u_3) = (0, 0, 0)$, is shown in the lines labeled 'UC' in Fig. 3(a), which indicates that $\Delta\omega < 0$ and that $|\Delta\omega|$ becomes smaller as the degree of resonance mode becomes higher. For reference, the frequency characteristics of the admittance $|Y|$ of Mason's circuit for the L-effect with appropriate circuit parameters are shown in **Fig. 3(b)**, which precisely agrees with the result of Fig. 3(a) when $\Delta\omega$ is considered to be the difference between electrical resonance and antiresonance angular frequencies, $\omega_r - \omega_a$, in which ω_a reflects the 'intrinsic' resonance state in L-effect. This correspondence suggests the reasonableness of the present method. (Influence of 'residual' elastic components on $\Delta\omega$ is also included successfully.)

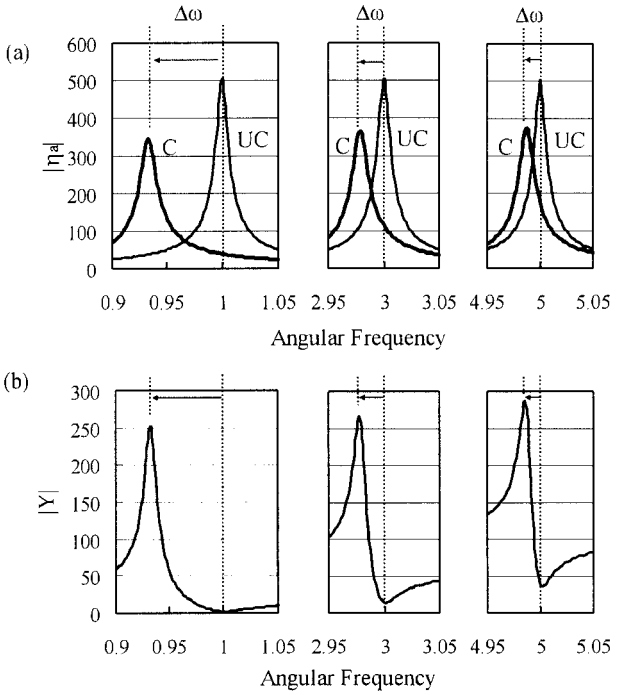

Fig. 3 (a) Calculation results of 'elastic mode' $|\eta_a|$. 'C': with mode coupling; 'UC': without mode coupling. (b) Dependence of admittance $|Y|$ on ω calculated with Mason's circuit for the L-effect.

'Switching' from L-effect to T-effect can be performed by changing the sign of some s_i's: for example, when (s_1, s_2, s_3) is changed from (2, 1, 2) to (–2, 1, –2), the result of $\Delta\omega > 0$ is obtained.

In Mason's circuit, although the elastic resonance effect is treated distributed-parameter-wise, the lumped parameter is still used for the dielectric component and its coupling effect with the elastic one, and the unrealistic negative capacitance $-C_0$ appears inevitably. In this study, on the other hand, the phenomenon can be dealt with in a unified manner on a distributed-parameter basis.

References

1. M. Ohki and K. Toda : Jpn. J. Appl. Phys. **41** (2002) 3413.
2. M. Ohki and K. Toda : Jpn. J. Appl. Phys. **40** (2001) 3505.

Proc. Symp. Ultrason. Electron., Vol. 25, (2004) pp. 255-256
27-29 October, 2004

Resonance Patterns of Piezoelectric Partial-Drive Systems without Mechanical Impedance Matching

Michio Ohki (Natl. Def. Acad., Japan)

1. Introduction

Resonance frequencies and intensities of a piezoelectric transducer are dependent on the electrical and mechanical boundary condition of the transducer. For example, in the systems of **Figs. 1(a)** and **1(b)** that are one-dimensinal piezoelectric transducers driven on a spatially partial domain of $\xi' < \xi < \xi''$ with mechanical boundaries B' and B" at the edge, each of resonance frequencies and intensities varies according to those conditions. However, when these resonances are considered in the frequency domain (ω-domain) as a whole, the 'pattern' of resonance has some mathematical regularity. In this paper, the effect of mechanical impedance mismatch inside the transducer shown in Fig. 1 on the 'resonance pattern' is discussed.

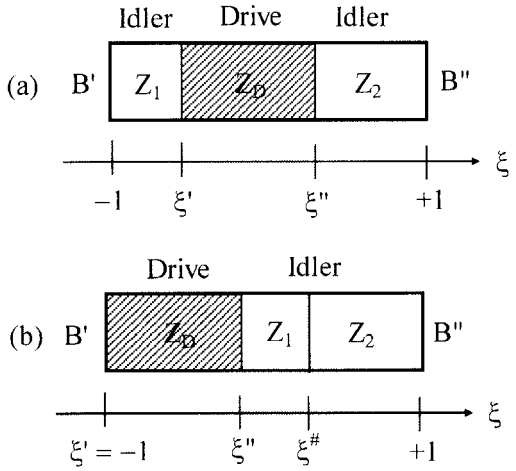

Fig.1 Partial-drive piezoelectric transducer with mechanical impedance Z_D in the 'drive' domain and Z_1 and Z_2 in the 'idler' domains.

2. Classification of Resonance Pattern

Typical resonance patterns in the ω-domain are shown in **Figs. 2(a)** and **2(b)**, in which Fig. 2(a) shows a pattern in the case of mechanical impedance matching; that is, $Z_1 = Z_D = Z_2$ in Fig. 1, and Fig. 2(b) in the case of mismatch.

The resonance pattern can be divided into some sub-patterns (detailed patterns in a pattern), each of which is a set with the same resonance intensity; for example, patterns labeled A, B and C in Fig. 2,

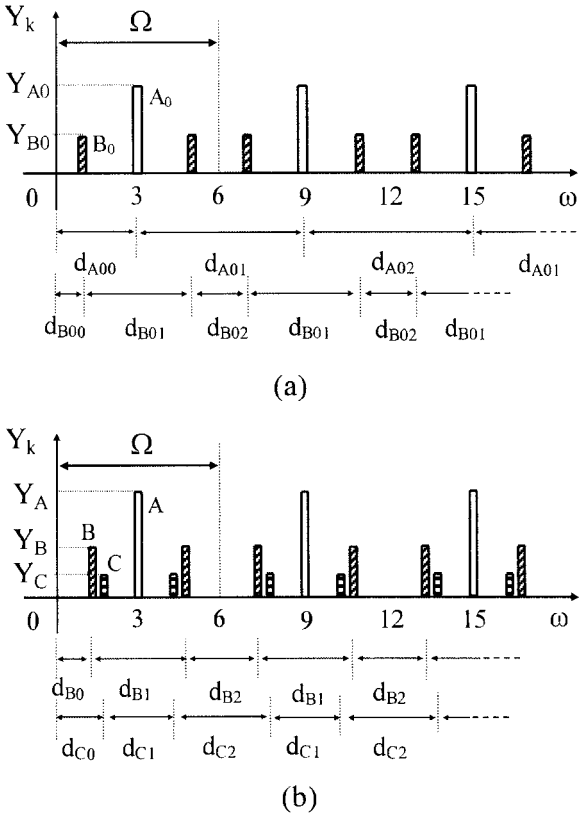

Fig.2 Examples of 'resonance patterns'. (a) In the case of mechanical impedance matching. (b) In the case of impedance mismatch. Y_k: resonance intensity of the pattern k. ω: normalized frequency.

where subscript 0 is added in the case of impedance matching.

The period Ω can be observed for the pattern as a whole. Each of patterns A, B,... has some regularity for its location on the ω-axis, which can be expressed with a set of three numbers, d_{k0}, d_{k1} and d_{k2}, where k is a label for the pattern. For example, in the cases of patterns $k = A_0$ and $k = B_0$ in Fig. 2(a), $(d_{k0}, d_{k1}, d_{k2}) = (3,6,6)$ and $(1,4,2)$, respectively. The period Ω, the location rules (d_{k0}, d_{k1}, d_{k2}) and the intensities Y_k characterize the resonance pattern for a given boundary condition.

When the impedance matching is broken, resonance frequencies of some patterns are shifted by $+\Delta\omega_k$ and $-\Delta\omega_k$, which are located alternately on the ω-axis; for example, the resonance frequencies

of pattern B in Fig. 2(b) are $\omega = 1 + \Delta\omega_B$, $5 - \Delta\omega_B$, $7 + \Delta\omega_B$, $11 - \Delta\omega_B$, $13 + \Delta\omega_B$, ... ($\Delta\omega_B > 0$ in this figure), and (d_{B0}, d_{B1}, d_{B2}) equals ($1 + \Delta\omega_B$, $4 - 2\Delta\omega_B$, $2 + 2\Delta\omega_B$) as a result of 'modulation' by $\Delta\omega_B$. Resonance intensity is also changed due to the impedance mismatch.

Here we introduce the following infinite series p_k for pattern k:

$$p_k = p(d_{k0}, d_{k1}, d_{k2}; \Delta\omega_k)$$
$$= \frac{8}{\pi^2}\left[(d_{k0} + \Delta\omega_k)^{-2} + (d_{k0} + d_{k1} - \Delta\omega_k)^{-2}\right.$$
$$+ (d_{k0} + d_{k1} + d_{k2} + \Delta\omega_k)^{-2} + (d_{k0} + 2d_{k1} + d_{k2} - \Delta\omega_k)^{-2}$$
$$+ (d_{k0} + 2d_{k1} + 2d_{k2} + \Delta\omega_k)^{-2} + (d_{k0} + 3d_{k1} + 2d_{k2} - \Delta\omega_k)^{-2}$$
$$\left. + \cdots\right] \quad (1)$$

and the 'density of mode' that is given by

$$\hat{Y} = p_A Y_A + p_B Y_B + p_C Y_C + \cdots . \quad (2)$$

3. Features of $\hat{Y}$ and Ω

In this section, $\hat{Y}$ and Ω are obtained for various boundary conditions, and their features are discussed.

When $(\xi', \xi'') = (-1/3, 1/3)$, $(B', B'') = (f, f)$ ('f' is the abbreviation of 'free') and $Z_1 = Z_2$ ($= Z$) in the system shown in Fig. 2(a), only two resonance patterns A and B appear regardless of whether $Z = Z_D$ or not. When $Z = Z_D$, patterns A_0 and B_0 have the resonance frequencies with (d_{A00}, d_{A01}, d_{A02}) = (3, 6, 6) and (d_{B00}, d_{B01}, d_{B02}) = (1, 4, 2), respectively. The calculated results of Y_A, $\Delta\omega_A$, Y_B, $\Delta\omega_B$ are shown in **Fig. 3**. ($\Delta\omega_A = 0$ in any case.) The calculation is performed using Mason's circuit with transmission lines,[1] and Y_k is obtained from the appropriately normalized maximum value of admittance $|Y|$ for the pattern k in the mechanical part of the circuit. The value of $\hat{Y}$ is calculated with eq. (2), using the data of Fig. 3 and the values of

$$p_A = p(3,6,6; \Delta\omega_A = 0) = 0.111111$$

and $p_B = p(1,4,2; \Delta\omega = \Delta\omega_B)$ shown in **Fig. 4**, which always results in $\hat{Y} = 1/3$ in the range of $0 < Z < \infty$. For example, when $Z/Z_D = 0.7$ ($r = 0.176$ and $\Delta\omega_B = 0.09474$ in Fig. 3), $p_A Y_A + p_B Y_B = 0.1111 \times 1.250 + 0.7556 \times 0.2573 = 0.3333$. The 'conservation of density of mode'[2] is satisfied even for $0 < Z < \infty$.

Moreover, $\hat{Y} = a$ ($0 < a < 1$) is always obtained for the systems shown in Fig. 2(a) and 2(b), as long as the conditions of $(\xi''-\xi')/2 = a$ and $(B', B'') = (f, f)$ are satisfied.

In the above example, $\Omega = 6$ is obtained. The value of Ω is determined by the values of ξ' and ξ'' with the following procedure:

(1) Calculate the ratio of the propagation times of acoustic wave in three domains in Fig. 1, in the form of $a_n/a_d : b_n/b_d : c_n/c_d$, where $a_n/a_d + b_n/b_d + c_n/c_d = 1$, and the greatest common divisor (GCD) of each numerator and denominator is 1;

(2) Calculate the least common multiple (LCM) of a_d, b_d and c_d, and double it, which gives the value of Ω, as long as the resonance intensities belonging to different patterns does not 'degenerate' (that is, does not have the same value). If the degeneration occurs, Ω is reduced appropriately to its divisor.

In the above example, $(\xi'+1) : (\xi''-\xi') : (1-\xi'') = 1/3 : 1/3 : 1/3$, and LCM of $a_d = 3$, $b_d = 3$ and $c_d = 3$ is 3, and $\Omega = 3 \times 2 = 6$ is obtained. The value of Ω is conserved for $0 < Z < \infty$, since the degeneration of resonance intensity does not occur in this example. Information on Ω is useful when the electrical equivalent circuit with lumped parameters is constructed.

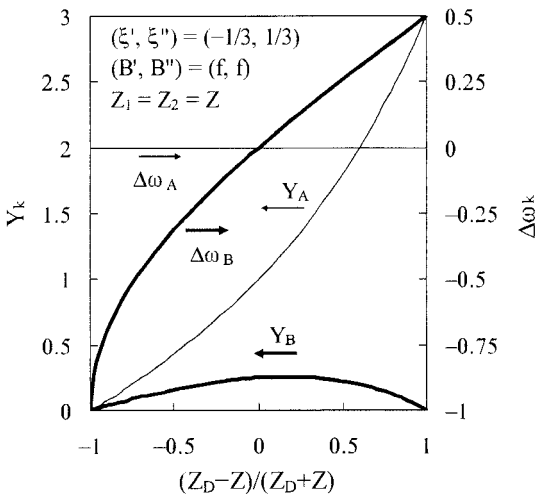

Fig. 3 Calculation example of Y_k and $\Delta\omega_k$ as a function of $r = (Z_D-Z)/(Z_D+Z)$.

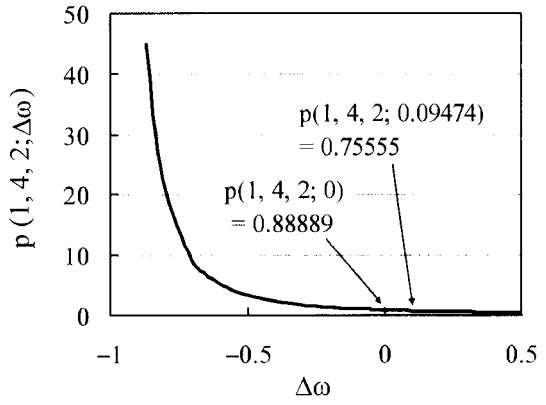

Fig. 4 Values of infinite series $p(1, 4, 2; \Delta\omega)$.

References

1. M. Ohki and K. Toda : Jpn. J. Appl. Phys. **41** (2002) 3413.
2. M. Ohki: *Proc. ICA 2004*, p.I-653.

Proc. Symp. Ultrason. Electron., Vol. 25, (2004) pp. 257-258
27-29 October, 2004

Time transient analysis of a high speed optical microscanner

Harumichi Sato, Maxim Lebedev and Jun Akedo
National Institute of Advanced Industrial Science and Technology (AIST)

1. Introduction

Optical scanners have been actively researched in the field of micro electro mechanical systems (MEMS), and show potential applications in optical communications and display. Because optical scanners are made of silicon, however, they are brittle and thus are easily broken at the base of the beam of the mirror due to concentrated stress. Piezoelectric ceramics are one of several materials used to drive microscanners. However, the process for fabricating these ceramics on the scanners is complex and difficult, because it involves a conventional MEMS process. The processing cost therefore limits the application of such microscanners. In designing a microscanner, analysis of the vibration is required. Frequency resonance analysis typically involves a finite element method (FEM)[1]. However, because such analysis cannot clarify how to generate and propagate acoustic waves from piezoelectric ceramics, time transient analysis is necessary to improve the microscanner design.

Two major methods are used for time transient analysis: implicit method and explicit method. The implicit method calculates piezoelectricity naturally, but requires large CPU time and memory because a large inverse matrix needs to be calculated. In contrast, the explicit method does not require an inverse matrix to be calculated, but it can not calculate piezoelectricity naturally. Wojcik developed a hybrid method in which the mechanical equation is solved dynamically (explicit method) and the electrical equation is solved quasi-statically (implicit method)[2]. This hybrid method, however, has yet to be validated to simulate piezoelectric MEMS devices.

To overcome these problems, in this study first we developed and fabricated an optical microscanner made of stainless steel (SUS304) and driven indirectly by acoustic waves generated by lead zirconate titanate (PZT) thick film (deposited using the aerosol deposition, or AD, method[3])[4]. Then, we did a time transient analysis of this microscanner by using a hybrid method involving an FEM program we developed.

2. Fabrication of a Stainless Steel Optical Microscanner

Figure 1 shows a schematic of the microscanner that we developed. First, a PZT thick film (1mm×1mm×10μm) was deposited on SUS304 (30μm thick) by using an AD method. The AD method is a gas deposition method without vaporization of the material, can deposit thick films from several micrometers to several millimeters, and is much easier than the conventional MEMS process. In the microscanner, an asymmetric mirror (Fig. 2) was used to convert vertical vibration into a rotational force[1]. When the potential was defined as 80V at f=15.8kHz, the mirror scaned about 17 degrees (i.e., scanning angle $\alpha \approx 17$).

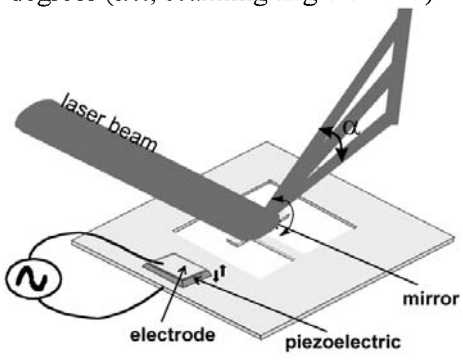

Fig. 1 Schematic of microscanner configuration

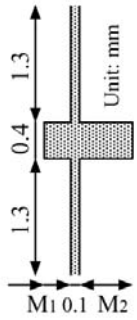

Fig. 2 Mirror and beams

3. FEM analysis of the Microscanner

In our FEM model, the y=0 surface was defined as a plain-symmetric surface, and was divided into rectangular parallelepiped elements whose dimensions were 25-200μm×100-216.7μm×5-7.5μm. The piezoelectric constant (d_{33}) was 150pm/V, and the ground electrode was set at the z=0 surface of the PZT and the $V = \sin(2\pi ft)$ electrode was set at the z=10μm surface. The time step of the calculation was 0.5ns, because the z-thicknesses of elements were thin. By using a hybrid method, we calculated an inverse matrix for only the electrical equation of the PZT part. Thus, much less computer memory is needed for this analysis compared with that needed if the implicit method was used alone. Therefore, we could use a direct method to calculate inverse matrixes even though a 3D-model

of the microscanner was calculated.

Figure 3 shows intensity modulation images for the z-displacement when the frequency (f) was 17kHz. Because the z-thickness of the model was much smaller than the x-length and y-width, the z-axis in this figure was scaled up by a factor of about 40 to clearly show the results. Fixed points, which were required to simulate our experiment and also not to move the model, were set at (x,y,z)=(6,0,–0.03) and (–6,3.1,–0.03). The small rectangular parallelepiped at the z=0 surface was the PZT film. Based on these simulation results, both the film and the SUS304 beneath the film deform, while secondary vibrations are simultaneously generated. After these deformations were generated, A_0-mode Lamb waves and edge waves are then propagated in the –x-direction.

Because our microscanner uses an asymmetric mirror, we analyzed the effect of this asymmetry by using our FEM program to compare two types of model mirror (Table 1). Type 2, which had larger asymmetry, had a rapid rise up time(Fig.4). Type 1 had a high rotation-amplitude(Fig.4). Figure 5 shows the frequency dependence of maximum scanning angle ($\alpha = 2\theta$) for Types 1 and 2, clearly showing that the resonance frequency for both types was about 17kHz. Therefore, the scanning angle α for Type 2, which has dimensions similar to those for our stainless steel optical microscanner, was about 8 degrees when the potential was 80V. Although this simulated scanning angle α is about half that of the actual angle, this is good agreement as a first simulation. The difference is due to the difference in shape between the actual microscanner and the FEM model, because the resonance frequencies are also different.

Finally, we simulated the piezoelectricity as a z-force ($f_z = f_0 m d_{33} \omega^2 \sin(\omega t)/2$) by using the typical explicit method. Although this method is computationally faster than the hybrid method, its results were difficult to compare with the scanning angle of the actual microscanner, and did not show any secondary vibrations.

4. Conclusion

A time transient analysis by hybrid method was applied to simulate a piezoelectric MEMS device to confirm the effectiveness of the method. Simulation results confirmed that the mirror in the device is driven by the acoustic waves generated by the PZT film, and when the asymmetry was increased, the scanning angle decreased. To design a more efficient microscanner, this relationship between asymmetry and scanning angle must be considered.

Acknowledgment

Thanks are due to Prof. K. Yamanaka and Dr. H. Ogiso for helpful discussions about this work. This research was partially supported by the NEDO Project "Nano Structure Forming for Advanced Ceramic Integration Technology in Japan Nano-technology Program" of Japan.

References

1. K.Yamada and T.Kuriyama : Proc. MEMS98 p.110.
2. G.L.Wojcik *et al.* : Proc. IEEE Ultrason. Sym. 1993 p.1107.
3. J.Akedo and M.Lebedev : Appl. Phys. Lett. **77** (2000) 1710.
4. M.Lebedev *et al.* :Proc. IEEE Ultrason. Sym. 2004 (to be published).

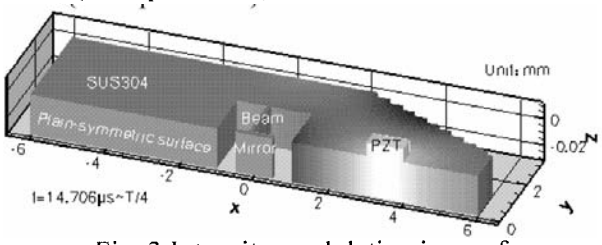

Fig. 3 Intensity modulation image for z-displacement

Table 1 Dimensions of model mirrors (Fig. 2)

	Type 1	Type 2
M1	0.44	0.3
M2	0.46	0.6

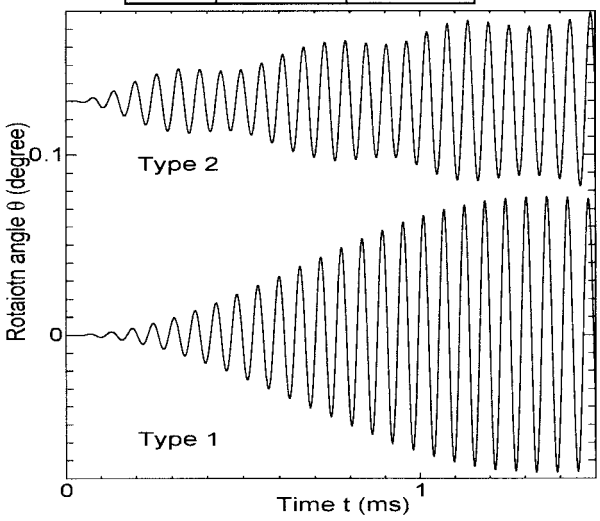

Fig. 4 Rotation angle of model mirrors

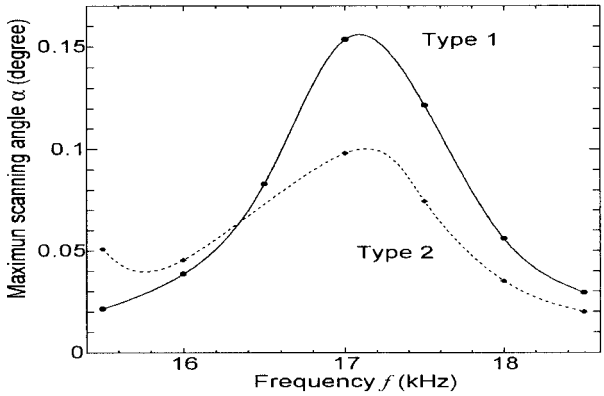

Fig. 5 Frequency dependency of maximum scanning angle for different model mirror dimensions (Table 1)

Proc. Symp. Ultrason. Electron., Vol. 25, (2004) pp. 259-260
27-29 October, 2004

A micro-mass sensing method by QCM vibrator using Thickness Twist Mode

Naotake Okada, Takayuki Kikuchi, Yukihisa Osugi
Research and Development Division, NGK INSULATORS, LTD

1 Introduction

The QCM (quartz crystal microbalance) sensor is used for micro-weighing applications such as for thin film thickness monitoring, and also is being developed for biotechnology applications, such as recognition of specific proteins, DNA, RNA, and viral particles [1]. It is necessary to sense at less than the 10^{-12} gram level. We proposed a new sensing method and a newly designed vibrator for the QCM sensor using a thickness-twist-mode vibrator made from an AT-cut quartz crystal. The sensing method of conventional QCM sensors detects the frequency shift at thickness-shear-mode resonance frequency by adding mass on its electrode surface. [2] Correspondingly, this new sensing method detects the change of the vibration balance caused by the mass difference of two driving electrodes at thickness-twist-mode. Our sensor has the advantage of sensing the small difference of the mass balance, which is caused by the reaction of chemical adsorption.

2 Principle of new QCM sensor

The new QCM sensor is sandwiched between three pairs of electrodes as shown in **Fig. 1**.

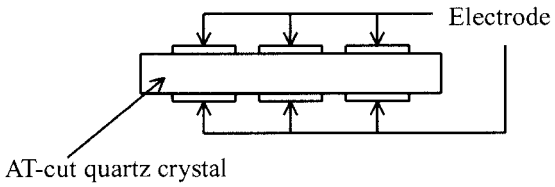

Fig.1 Cross-section view of new QCM sensor

The driving electrodes (the four black parts) are connected in reversed-parallel as shown in **Fig. 2**. By applying an alternating electric field across this thin AT-cut quartz crystal, their driving electrodes are charged in reversed phase, and the quartz crystal is oscillated by vibration motion with the central node at the thickness-twist-mode resonance frequency. The white, central detecting electrode is the central node of reserved vibration motion under balanced conditions. The output signal from the detecting electrode is zero, but the output signal is generated with its unbalanced degree because of the piezoelectric effect. If the absorption film is coated on one side of the driving electrodes and a specific substance is absorbed on the film, an amount of mass of the specific substance is weighed by measuring the output signal change of the central detecting electrode.

The new operational sensor has two advantages compared with conventional QCM sensors as follows.

a) The method has high sensitivity.
b) The sensitivity does not depend on the thickness of quartz.

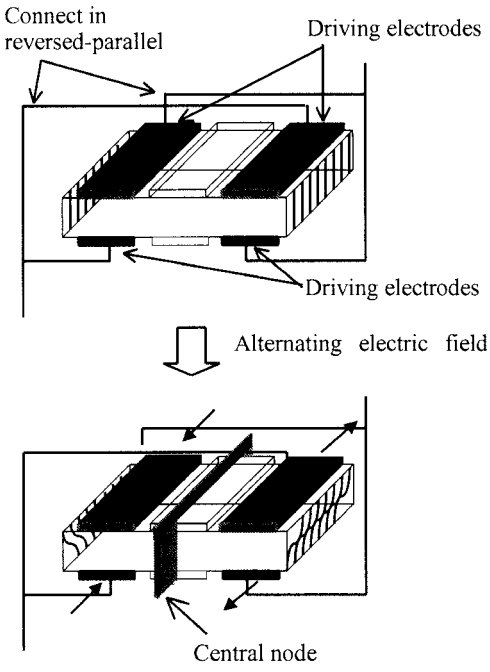

Fig.2 Schematic representation of the thickness-twist-mode vibrational motion

3 Process of quartz resonators

A prototype quartz resonator of our proposed QCM sensor is shown in **Fig. 3**. A quartz crystal with a thickness of 160 μm is cut by dicing (8mm × 16mm). The electrodes are coated on both sides by vacuum evaporation method. The composition is Cr (200 Å (base)) and Au (1000 Å). The diameter of the electrode is ϕ 5mm. The absorption film is not coated.

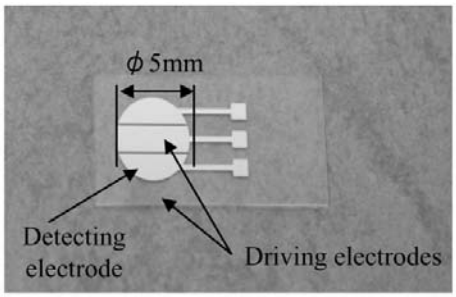

Fig. 3 Prototype quartz resonator

4 Experiment method

The driving electrodes are swept by impedance mode of impedance analyzer (HP 4194A) and the thickness-twist-mode resonance frequency is obtained. The driving electrodes are swept by gain-phase mode of impedance analyzer, and the output signal of the detecting electrode is measured. The output signal is represented as the ratio of output current signal to driving current. The output signal is measured by changing the mass on the electrode. The mass change is simulated by laser processing of the driving electrode because of quantifying the mass change. The mass change is calculated from film thickness of the electrode and the processing area. Both sides of the quartz resonator are exposed to water in these water experiments.

5 Results

5-1 Impedance property

Impedance measurement results in air and in water are shown in **Table 1**. In water the resonance frequency shifts down 10 kHz, CI (Crystal Impedance) increases. Q value decreases to 1,000 compared with in air because resonance of quartz is much attenuated by the viscosity resistance of water.

Table 1 Impedance properties

	In air	in water
Resonance frequency fr(MHz)	10.075	10.061
Equivalent circuit constant R(Ω)	19	1041
Equivalent circuit constant √(Ca/L)(pS)	865	1130
Q value	61,700	851

5-2 Sensitivity in air

The signal change in the detecting electrode versus mass change in air is shown in **Fig.4**. The signal change is proportional to mass change. The detecting sensitivity is 4.1×10^{-8}(1/pg).

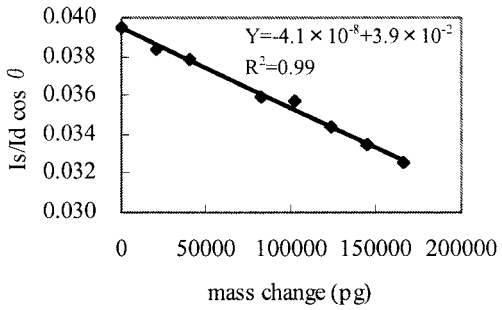

Fig. 4 Sensitivity in air

5-3 Sensitivity in water

As with the above experiment in air conditions, the sensitivity in water is measured. The result is shown in **Fig. 5**. The signal change is proportional to mass change. The detecting sensitivity is 4.81×10^{-8}(1/pg).

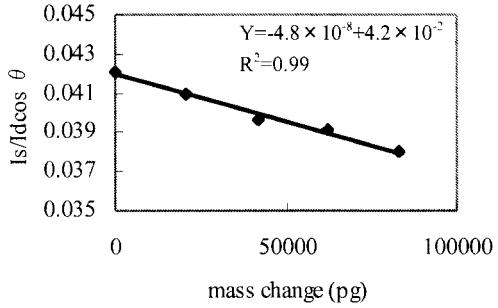

Fig. 5 Sensitivity in water

6 Analysis

The sensitivity in air is equivalent to the sensitivity in water. The theoretical sensitivity is not influenced by driving oscillation damping if the driving current which is equivalent to the current in air can be passed.

The limit of sensitivity in air is 0.02×10^{-15} gram, and 0.88×10^{-15} gram in water.

7 Conclusions

The new method and the resonator for QCM sensor using thickness-twist-mode vibration show promising performance in terms of mass sensitivity. The theoretical mass sensitivity of this sensing method is 10^{-15} gram. This sensor also would take advantage of the innate temperature stability of quartz AT-cut crystal vibration because that is the only detected change of mass balance on the resonator as compared with the ordinary QCM sensor that detects the change of resonant frequency. We will continue to study the temperature stability of this sensor's performance and develop a highly stable sensor element by passivation coating, stable mounting, and by using a circuit for high frequency driving and detecting.

8 Acknowledgements

We would like to express our deepest thanks to Professor Yoshiro Tomikawa of Yamagata University for his useful suggestions. We would like to thank S. Ishikawa for initial work on this new sensor, and M. Tani for evaluation method. Special thanks are due to S. Gouji for process of quartz resonator. Thank you also to Jim V. Castle for English proofreading.

9 References

[1] Y. Okahata and H. Furusawa, IEEJ Trans. SM, Vol. 123, No.11, 2003, pp. 459-464

[2] D. A. Buttry and M. D. Ward, Chem. Rev. 1992, 92, pp. 1355-1379

Proc. Symp. Ultrason. Electron., Vol. 25, (2004) pp. 261-262
27-29 October, 2004

Propagation Characteristics of SH-Type Surface Acoustic Wave on Langasite with Thin Films

Shoji Kakio, ○ Masaya Nozawa and Yasuhiko Nakagawa (Univ. Yamanashi)

1. Introduction

In a previous work, we reported the coupling factor K^2 and the temperature characteristic of a pure shear-horizontal (SH)-type surface acoustic wave (SAW) on (0°, 20°, 90°)-cut langasite (LGS) with a high-density thin film, such as a Au film or a tantalum pentoxide (Ta_2O_5) dielectric film[1]. The measured values of K^2 were 0.80% and 0.61% for the sample with a Au film and that with a Ta_2O_5 film, respectively. For both films, the measured frequency shifts in the temperature change showed that a temperature characteristic with a zero temperature coefficient of delay (TCD) can be obtained by choosing the film thickness.

In this paper, the propagation characteristics, mainly the propagation loss and the bulk wave radiation loss of the SH-type SAW on the (0°, θ, 90°)-cut LGS with these films, are investigated experimentally. The cut angles θ of 0°, 10° and 20° were chosen because K^2 of 1.0% and a zero TCD can both be expected around these cut angles[1].

2. Sample fabrication

The fabrication conditions of the sample were the same as those given in our previous paper[1]. Two types of simple delay line samples were fabricated using a (0°, θ, 90°)-cut LGS substrate and a double-electrode interdigital transducer (IDT) pair with the wavelength (λ) of 20 μm, an overlap length of 100 λ and a 30-finger pair. One sample is the Au/LGS structure with an IDT pair and a metallized propagation path formed by a dc-sputtered Au film with a thickness of 0.015 λ. The other is the Ta_2O_5/Al/LGS structure in which an rf-sputtered Ta_2O_5 film was deposited on a conventional Al-IDT pair with a thickness of 0.02 λ and a free propagation path. For each conditions, samples with the propagation path lengths L of 50 λ and 300 λ were fabricated to estimate the propagation loss.

E-mail: kakio@yamanashi.ac.jp

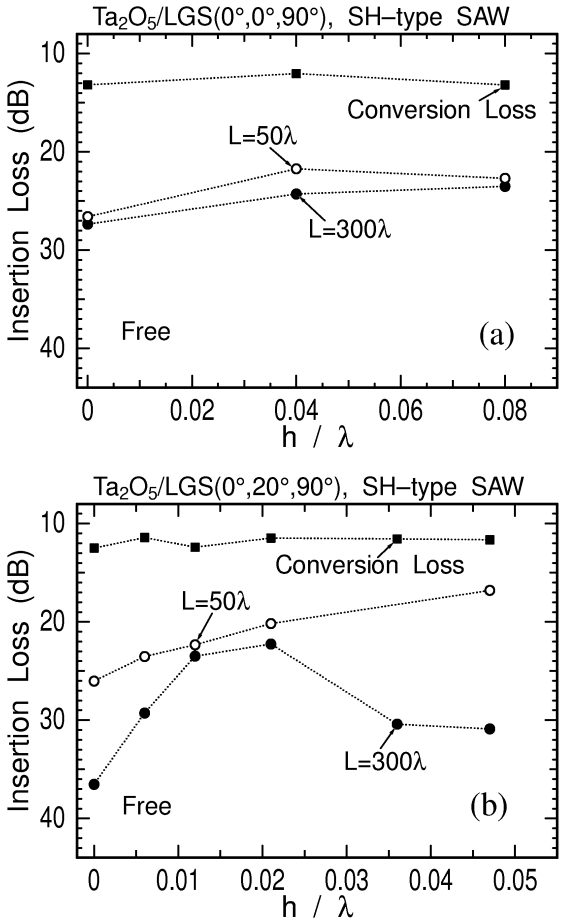

Fig. 1: Insertion loss on (0°, θ, 90°)-cut LGS with Ta_2O_5 film for (a) θ=0° and (b) θ=20°.

3. Insertion loss

The insertion losses at the center frequency for the Ta_2O_5 film as a function of the normalized film thickness h/λ are shown in **Fig. 1** for (a) θ=0° and (b) θ=20°, respectively.

In the case of θ=20°, the insertion loss of L=50 λ decreased monotonically with the film thickness and that of L=300 λ showed the minimum value at around 0.02 λ. The insertion loss for θ=0° was decreased by 4∼5 dB by loading with a Ta_2O_5 film. In the case of θ=10°, the values and the film thickness dependence of the insertion loss were the almost same as those in the case of θ=0°.

The measured losses for the Au film with a thickness of 0.015 λ are shown in **Table I**. These losses showed a relatively small value at θ=10°, among the range of cut angles.

Table I : Measured losses for Au film. (Metallized, 0.015λ)

θ	Insertion Loss(50λ)[dB]	Insertion Loss(300λ)[dB]	Conversion Loss[dB]	Propagation Loss[dB/λ]	Bulk Wave Radiation Loss[dB]
0°	17.3	19.3	11.9	0.008	4.8
10°	14.7	17.1	10.4	0.010	3.5
20°	15.8	19.7	10.6	0.016	3.9

4. Propgation loss

The estimated propagation losses with the Ta_2O_5 film are shown as a function of h/λ in **Fig. 2**. The propagation loss for θ=20° showed the minimum value at the film thickness of 0.012 λ. It is considered that, similarly to the case of ST-90°X quartz with the Ta_2O_5 film[2], once the propagation loss is reduced by the trapping effect due to loading with the Ta_2O_5 film, it is then increased by the acoustical loss of the Ta_2O_5 film. On the other hand, for θ =0° and 10°, the values of the propagation loss were less than 0.01dB/λ even with the existence of the Ta_2O_5 film.

5. Bulk wave radiation loss

The bulk wave radiation loss from the IDT can be estimated by subtracting the propagation loss and the conversion loss from the insertion loss[2]. **Figure 3** shows the bulk wave radiation loss for the Ta_2O_5 film. In the case of θ=20°, the bulk waves radiation loss decreased to less than 1 dB at the Ta_2O_5 film thickness of 0.05 λ, from 11 dB in the sample with no film. On the other hand, for θ =0° and 10°, the bulk wave radiation loss of 7∼9 dB remained after loading with the Ta_2O_5 film.

From the above results, it is clear that the energy trapping effects due to loading with the Ta_2O_5 film depend on the cut angle.

6. Conclusions

The propagation characteristics, mainly the propagation loss and the bulk wave radiation loss of the SH-type SAW on (0°, θ, 90°)-cut LGS with Au or Ta_2O_5 film, are investigated experimentally.

In the case of θ=20°, the propagation loss showed the minimum value at the Ta_2O_5 film thickness of 0.012 λ, and the bulk wave radiation loss also decreased to less than 1 dB at 0.05 λ. On the other hand, for θ =0° and 10°,

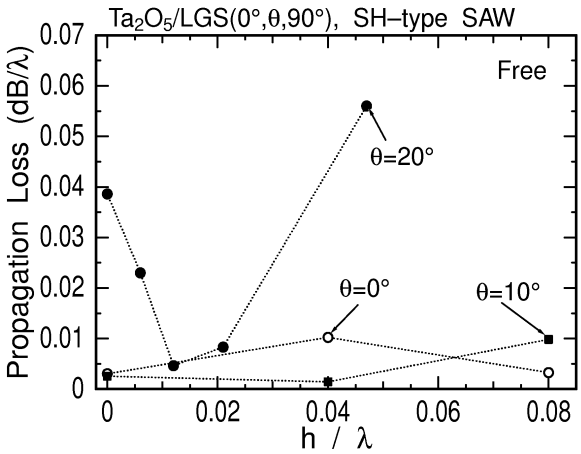

Fig. 2: Propagation loss on (0°, θ, 90°)-cut LGS with Ta_2O_5 film.

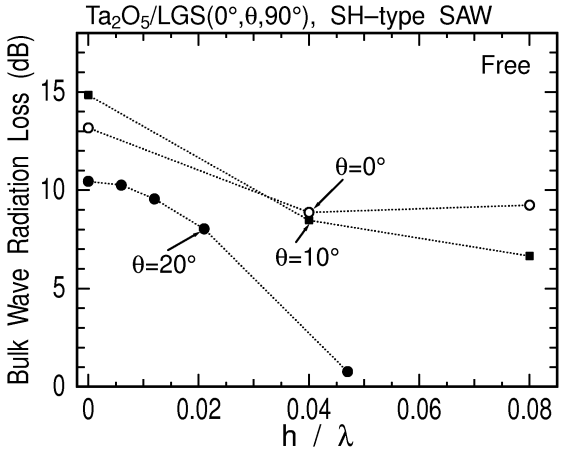

Fig. 3: Bulk wave radiation loss on (0°, θ, 90°)-cut LGS with Ta_2O_5 film.

the values of the propagation loss were less than 0.01dB/λ even with the existence of the Ta_2O_5 film, and the bulk wave radiation loss of 7∼9 dB remained after loading with the Ta_2O_5 film. The energy trapping effects of loading with the Ta_2O_5 film depend on the cut angle.

References

[1] S. Kakio, M. Nozawa, and Y. Nakagawa: Jpn. J. Appl. Phys. **43**(2004)2992.

[2] S. Kakio, Y. Shimatai, and Y. Nakagawa: Jpn. J. Appl. Phys. **42**(2003)3161.

Proc. Symp. Ultrason. Electron., Vol. 25, (2004) pp. 263-264
27-29 October, 2004

Study of second harmonic in a nonlinear surface acoustic wave

Yoshiaki Tokunaga, Toshio Nakaya, Atsushi Yasuno (ODES R&D Center of Kanazawa Institute of Technology), and Toshiharu Minamikawa (Industrial Research Institute of Ishikawa)

1. Introduction

Nonlinear surface acoustic wave (NLSAW) has not been studied almost until now because of phenomenon being too complicated. We pay attention especially to second harmonic in the NLSAW from a point of view of the *new science* which handled regions, jumping over a reductionism, such as chaos, soliton, fractal, and complex system. Up to now, the second harmonic (2^{nd} harmonic) has never been paid special attention because it has been considered to be of little value for engineering use. We take a great interest of character of the 2^{nd} harmonic from a point of view of the *new science* which is bonanza of seeds for engineering application in near future. In this report we descried experimental facts on the 2^{nd} harmonic in the NLSAW of $LiNbO_3$.

2. Sample and Experimental Setup

We used a $LiNbO_3$ crystal of SAW grade type with 128° Y cut X propagation.

Figure 1 shows schematic figure of our sample. A regular type IDT with 20 pair electrodes having center frequency near 50MHz was used as a NLSAW generator.

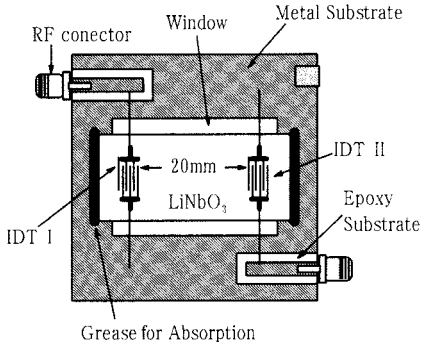

Fig.1. Schematic picture of experimental sample.

Analysis of temporal and spatial propagation characteristic of the NLSAW between IDT I and IDT II were carried out by optical probing technique[1] using He-Ne laser. Experimental setup was similar to the setup used in ref.2.

3. Experimental result and Discussions

We have great and attractive interest in character of the 2^{nd} harmonic. First of all, full width at half-maximum (FWHM) of envelope profile in the 2^{nd} harmonic is shorter than that of the fundamental one as shown in Fig.2.

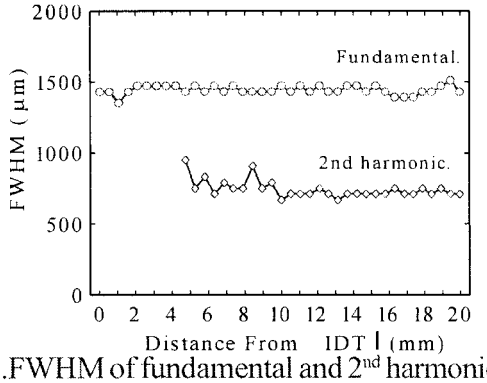

Fig.2.FWHM of fundamental and 2^{nd} harmonic.

In addition, envelope profile of the 2^{nd} harmonic is close to a soliton profile simulated numerically by KdV equation as shown in Fig.3.

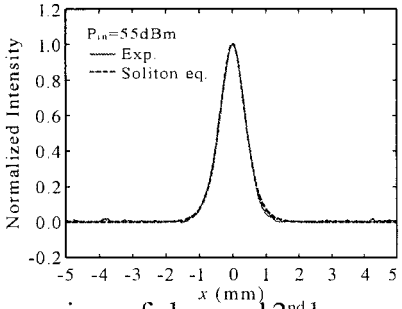

Fig.3. Comparison of observed 2^{nd} harmonic profile and simulation one by KdV eq.

From these results we predict that the 2nd harmonic may be a kind of a soliton. In order to confirm weather or not our prediction is reasonable, we attempted to be clashed two 2nd harmonics in middle space between two IDTs. As we know, the soliton has the property passed without changing the form by the collision, even if it was made to collied from the opposite direction.

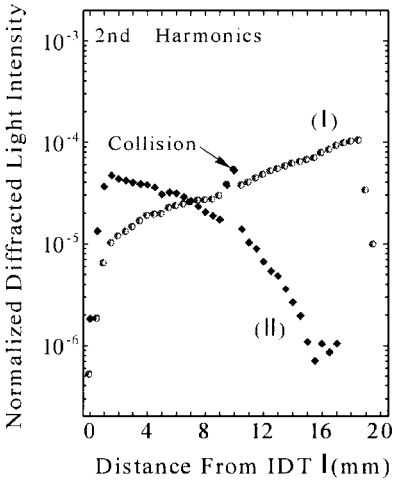

Fig.4. Collision of the two 2nd harmonics.

Figure 4 shows the experimental result. It was proven that total intensity of the 2nd harmonic in clash position equalized with the sum of individual intensity of the two 2nd harmonics. This is just one of representative characters of the soliton.

Figure 5 shows a comparison between FWHMs in a fundamental and the 2nd harmonic when they passed through the gold thin film (dispersive material) evaporated on the substrate. The 2nd harmonic is conserved the FWHM even if it passed through the metal thin film. The FWHM in the fundamental, however, is widened by experiencing metal thin film. From these facts, we consider that the 2nd harmonic is a kind of a soliton. We define it as *a surface acoustic soliton like wave* (SASLW).

Conclusion

In an experiment of $LiNbO_3$ dielectric single crystal with 128° Y cut X propagation axis using IDT with regular type 20 pairs, character of the 2nd harmonic in NLSAW was investigated by optical probing technique.

It was shown that the 2nd harmonic in the NLSAW had a great possibility of the SASLW.

References

(1) E.G.H.Lean and C.G.Powell : Proc.IEEE.Vol.58,No.12b (1970) 1939

(2) Y.Tokunaga, S.Kanno, and S.Minamikawa : The 23rd Symposium on UES (2002) 357

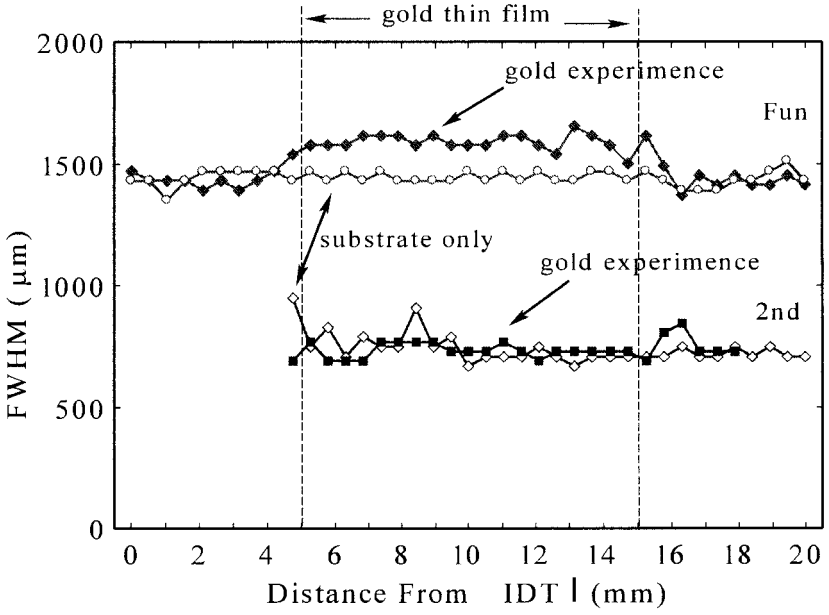

Fig.5. FWHM in fundamental and 2nd harmonic passed gold thin film.

Proc. Symp. Ultrason. Electron., Vol. 25, (2004) pp. 265-266
27-29 October, 2004

A Balanced SAW Oscillator for Short Range Transmitters

Yao-Huang Kao, and Yi-Ran Wang

Institute of Communication Engineering, National Chiao-Tung University
Hsin-Chu, Taiwan, R.O.C. 30050

Abstract

A balanced oscillator suitable for transmitters with high-Q SAW resonators in short range applications are proposed. With the balanced structure, the most undesired spurious of the second harmonic can be easily suppressed. The low cost transmitter with minimum external components can be obtained.

1. Introduction

There are two types of transmitter in short-range keyless applications. One is the SAW based transmitter, and the other is the phase locked based transmitter [1-3]. The former one has the features of simplicity, high current efficiency, and low cost. According to the regulation, the spurious must be lower than a certain level, say as 40dB [4]. A normal method is to add a band pass filter after the oscillator [1]. Here, focus is on the former one. To satisfy the regulation and achieve low cost, a novel integrated circuit with balanced SAW oscillator is presented. The outputs of the balanced oscillator possess inherently in phase in even harmonics and 180° out of phase in odd harmonics. The functional block of the transmitter is illustrated in Fig. 1. The balanced outputs are fed to the differential stage. The strategy is using the differential amplifier to cancel the undesired even harmonics. All even harmonics are in phase in the balanced output and can in principle be completely cancelled.

As for the odd contents, they are treated in two steps. One part is determined by controlling the extent of negative resistance, and the other part is suppressed by the output network consisted of matching capacitors and antenna. The attenuation factor for the specific third harmonic is about 19dB with the simple loop antenna and two tuning capacitors in parallel [2]. With such an arrangement the transmitter can be shrunk into a simple package with minimal external components.

The transmitter is featured with the functions of FSK and ASK. The FSK is generated by pulling the SAW resonator with the internal capacitors, and ASK is obtained by controlling the current of the output stage. The output power is maximized with the output impedance matching.

2. Balanced Oscillator

An alternative is illustrated in Fig. 2a, which is deduced from one-pin SAW oscillator as shown in Fig. 2b, where one of the pins (Node B) of the resonator is ac-grounded [5]. As a matter of fact, the oscillator consisted of transistor M_1, two capacitors C_{out} and C_{in}, and the SAW resonator is a Colpitts oscillator. The SAW resonator acts as an inductor. Transistor M_2 acts as a current source. To form a balanced one, the pin B is connected to the corresponding node of another copied one as shown in Fig. 2a. Conceptually, the one-port resonator can be decomposed into two series-connected ones. The circuit in Fig. 2a can be viewed as two identical oscillators and are mutually coupled through the SAW resonator. Under fundamental vibration mode, the polarity of the opposite plates of the resonator is out of phase, which leads to the corresponding outputs of two oscillators 180° out of phase. The penalty is the twice of current consumption. The CMOS process is employed to save the current dissipation. Four extra transistors S_{FSK} play the role of switches for FSK function. The modulation speed can achieve 50kbps.

During design phase, the negative resistance seen from node A and B is tuned to overcome the corresponding positive one from the resonator. The negative resistance is set to -37.5ohm, which is roughly two times of the equivalent series resistance R_m of SAW resonator as listed in table I. The calculated waveforms of balanced oscillator are shown in Fig. 3. Noted that the waveform is indeed 180° out of phase.

Table I Equivalent circuit parameters of a 433.92MHz SAW resonator

$R_m = 18.1489\ \Omega$
$L_m = 76.28057\ \mu H$
$C_m = 1.764233\ fF$
$C_0 = 1.822466\ pF$

3. Suppression of Even Harmonics

The even harmonics are then suppressed by feeding output signals to the differential output stage. Because even harmonics are in phase, they can in principle be totally cancelled. To avoid the degradation from nonlinear distortion, the dynamical range of the differential stage is enhanced by adding two degenerated resistors R_S in the source as shown in Fig. 4. Table II reveals the ratios of harmonics before and after the differential output stage. The reduction factor 23dB in the second harmonic is remarkable. In the meantime, the degradation in third harmonic is negligible. It is noted that the cancellation of second harmonic is limited by the nonlinear distortion. The ASK function is performed by turning the switch S_{ASK} on/off. The switching speed reaches 400kbps.

Table II Harmonic ratios before and after the differential output stage

	2/1 ratio	3/1 ratio
Oscillator Output	24.95dB	35.70dB
Differential Output	48.11dB	42.35dB

4. Loop antenna

For differential applications, a small loop antenna is employed as shown in Fig. 5. The loop size is about $5\times2cm^2$. The evaluated radiation resistance is much less than the output impedance of transmitter. To achieve conjugate matching, a transformer and two small tuning capacitors C_{tune} and C_m are inserted. Capacitor C_{tune} is for resonant frequency tuning and can be built on pc board. The effect of filtering with respect to third harmonic is about 10 dB, which leads to total 40dB reduction for the third harmonic. The levels in the higher harmonics can be neglected. The simulated results are listed in the following table III. The chip is now under the fabrication by the TSMC 0.25um CMOS process.

Table III The simulated results of the transmitter

Specifications	Simulated Results
Battery	2.5V
Frequency	434.08MHz
DC Current	15mA
Power Consumption	37.5mW
Instant Power	46mW
Sleep Current	9nA
Transition Time from Sleep	85us
Transition Time to Sleep	50us
FSK data rate	50kbps
ASK data rate	400kbps
Output RF Power	0dBm

5. Conclusions

The work is to study a low cost SAW-based transmitter. The core is the construction of the balanced oscillator with one port SAW resonator, which gives to high rejection ratio for the harmonic near the carrier. The need for the external shaping filter can be relaxed and the cost is saved.

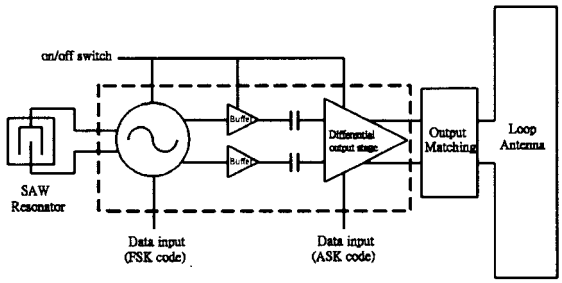

Fig. 1 The block diagram of transmitter

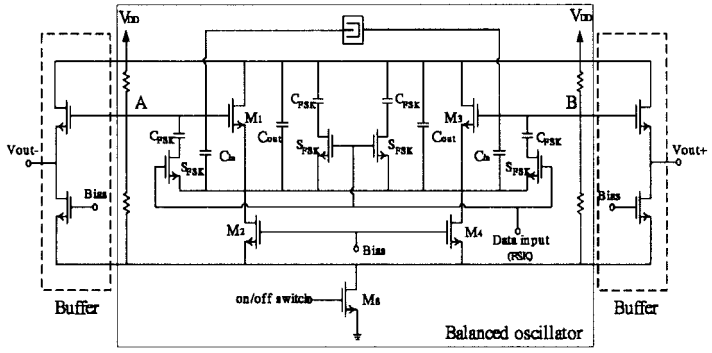

(a)

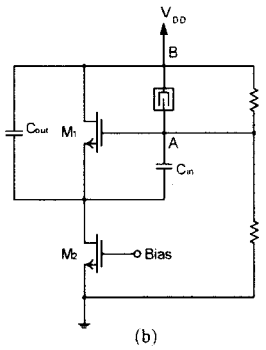

(b)

Fig. 2 (a) Balanced oscillator with FSK and on/off switch and (b) One-pin SAW oscillator

References:

[1] D. L. Ash, SAW-Based Hybrid Transceivers in Slam Package with Frequency Range from 200 to 1000MHz, IEEE Ultrasonic Sym., pp. 389-398, 1998.

[2] B. Schirdewahn, etc., A Low-Cost SAW- Resonator Transmitter for Radio Control Applications in the 70cm Band, IEEE Asia-Pacific Microwave Conference, Adelaide, pp. 531-534, 1992.

[3] A. Laute and J. Peter, A Fully Silicon Monolithic Integrated 868/915MHz FSK/FM/ASK Transmitter Chip, Silicon Monolithic Integrated Circuits in RF Systems, Topical Meeting, pp. 38-42, 2000.

[4] EN 300 220-1, European Standard (ETSI) Telecommunication Series, V1.2.1 (1997).

[5] J. T. Santos and R. G. Meyer, A One-Pin Crystal Oscillator for VLSI circuits, IEEE J. Solid- State Circuits, vol. Sc-19, pp. 228-236, 1984.

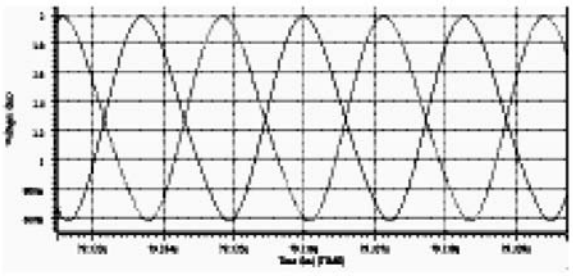

Fig. 3 Output waveforms of the balanced oscillator

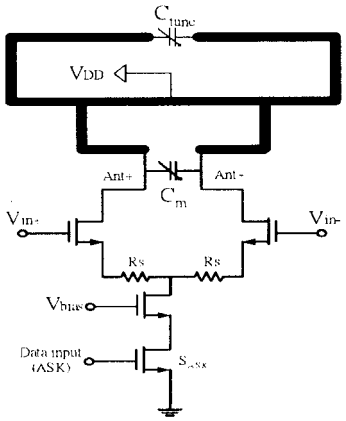

Fig. 4 Differential output stage with ASK switch

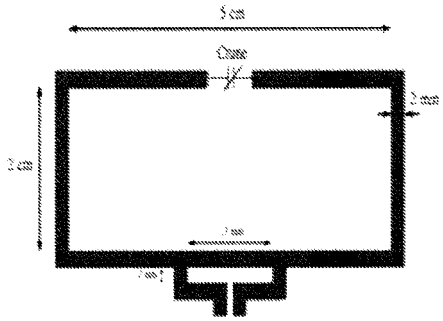

Fig. 5 Loop antenna

Proc. Symp. Ultrason. Electron., Vol. 25, (2004) pp. 267-268
27-29 October, 2004

Effect of Ultrasonic Wave on Degradation of Organic Chemical Substance

○Yasumasa Yoshida, Mamoru Kuwabara and Jian Yang (Dept of Material Processing Eng Nagoya Univ.)

Abstract

The effect of ultrasonic wave on degradation of an organic substance in aqueous solution was investigated using the methylene blue as a modeled substance. The ultrasonic wave employed in this experiment was of output power of 50 W and of frequency of 42.0 kHz. The rate of decomposition of methylene blue was determined by measuring light absorbance of the methylene blue. For the methylene blue decomposition by the ultrasonic irradiation under various solvent conditions, it was found that the Fenton action of ferrous ion with a catalytic role represented the most significant effect on decomposition of methylene blue.

1. Introduction

It is well known that with the ultrasonic wave irradiated into a liquid, very high temperature and pressure fields are liable to form in it because the generated cavitation bubbles almost adiabatically expand and compress at a high frequency due to the corresponding sound pressure variation. This results in production of the hydroxyl radical by the heat disassembly of the water vapor in the cavitation bubbles. In the present study, in order to establish an effective ultrasonic technique for promoting the composition of an organic substance, the effects of various operating conditions on the yield of decomposition of the organic substance was investigated, by use of the methylene blue as a modeled substance.

2. Experimental setup

The setup of the experiment is shown in Fig.1. The methylene blue solution was charged into the reactor in the center of the cylindrical acrylic resin vessel, in the bottom of which the bolted Langevine-type transducer of ultrasonic wave was attached. The height of the methylene blue solution in the reactor was adjusted to be the same as the height of the distilled water in the outer cylindrical vessel. Moreover, the upper part above the liquid surface in a reactor was maintained inert atmosphere by blowing argon gas into it. Under atmospheric pressure, the water temperature in the vessel was held to predetermined temperature, by means of distilled water was circulated with a pump, and the ultrasonic wave of frequency 42.0 kHz that fulfills resonance conditions within a distilled water tub was irradiated. Absorbance of the methylene blue solution was measured using the spectrophotometer. Moreover, the change in pH of the methylene blue solution was also simultaneously measured with a pH meter.

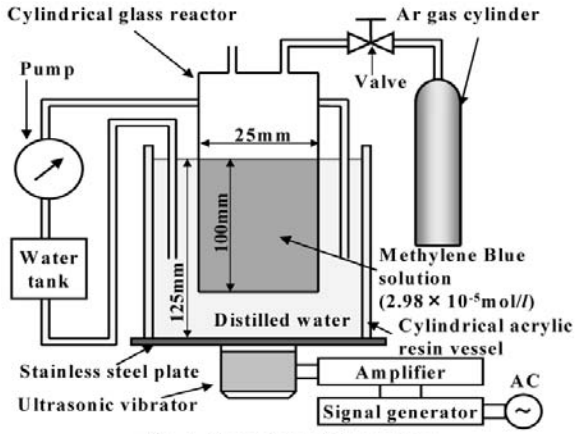

Fig. 1. Experimental apparatus

3. Results and discussion

3.1 Degradation of methylene blue aqueous solution under irradiation of ultrasound

Figure 2 shows the relation between absorbance of the methylene blue aqueous solution and its wavelength with irradiation of ultrasound of output of 50 W. Irradiation time was 0, 60 and 120 min. Without ultrasonic wave irradiation, a peak of absorbancy was confirmed at 665 nm of wave length. Absorbancy wave length of 665 nm is of the color of blue-green. Based on these results, degradation rate of methylene blue was determined by absorbancy at the wave length of 665 nm. From the change in absorbancy at 0, 60 and 120 min, it is

confirmed that methylene blue aqueous solution was degraded by irradiation of ultrasound. The reason of the degradation was considered to be that the hydroxyl radical, which has powerful oxidization power, was formed in the heat decomposition of the water molecule by the acoustic cavitation decomposed methylene blue.

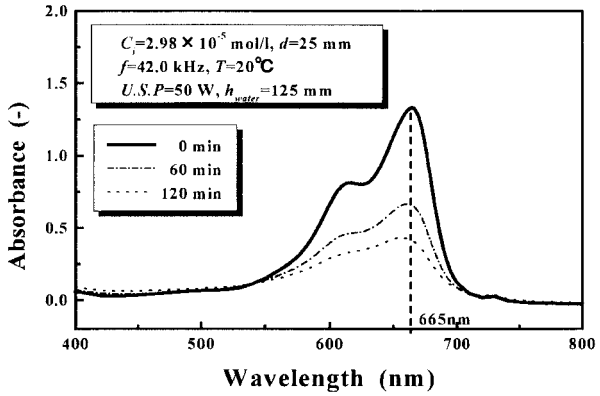

Fig. 2. Relation between absorbance of methylene blue aqueous solution and wavelength under irradiation of ultrasound.

3.2 The effect of various kinds of solvent

Figure 3 shows the relation between the rate of decomposition of the methylene blue and the irradiation time of ultrasound under various solvent conditions.

With a methanol solvent, since it hardly decomposed, the methylene blue is also not decomposed. So it is deduced that the existence of water is essential to its decomposition

As for the methylene blue solution, in which hydrogen peroxide was added, the rate of decomposition decreased a little. The hydrogen peroxide seems not to disassemble into hydroxyl radical by the irradiation of ultrasound under the present conditions.

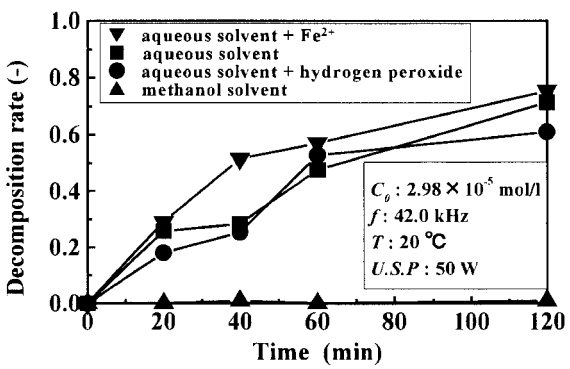

Fig.3 Effect of solvent kinds on decomposition rate of methylene blue.

On the other hand, the rate of decomposition of methylene blue solution increased when Fe^{2+} ion was added. Generally, the mixed solution containing Fe^{2+} ion and hydrogen peroxide is called Fenton solution. It has a strong oxidization action. Although, as for hydroxyl radical produced in heat disassembly of water, one part is used to decompose methylene blue directly, and the other part is used to form hydrogen peroxide. However, since Fe^{2+} ion exists, hydrogen peroxide will turn back to hydroxyl radical immediately. This is considered that the promotion of decomposition of the methylene blue is due to the synergistic effect of the catalyst action of the Fe^{2+} ion [1], and the irradiation of the ultrasound.

4.Conclusion

By the investigation of the acoustic cavitation induced degradation of methylene blue solution as an organic substance, it was confirmed the hydroxyl radical formed during thermal decomposition of the water molecule has a powerful oxidization power to decompose methylene blue. Although hydrogen peroxide is generated in the solution under the irradiation of ultrasound [2], the addition of Fe^{2+} ion can re-disassembles hydrogen peroxide into hydroxyl radical. Consequently, the decomposition of methylene blue was promoted. The present study on the ultrasonic decomposition of methylene blue clearly suggested desirable operating indices to promote sonochemical decomposition of other general organic substances involved in aqueous solution.

References

[1] P.K.Malik and S.K.Sahad, *Separation Purification Technology*, 31(2003), p.241.

[2] Kondou, Kuwabara, Okumura: CAMP-ISIJ, 16(2003), p.111.

Proc. Symp. Ultrason. Electron., Vol. 25, (2004) pp. 269-270
27-29 October, 2004

Simultaneous Regional Actuation at Two Points in Object by Controlling Phase Between Acoustic Radiation Forces

○ Yoshifumi Nishio, Hideyuki Hasegawa and Hiroshi Kanai
(Tohoku University)

1. Introduction

In recent years, some remote actuation methods based on acoustic radiation force have been reported. Fatemi and coworkers proposed an imaging method called ultrasound-stimulated ac oustic emission (USAE)[1]. Acoustic radiation pressure, $P_{\mathrm{R}}(t)$, exerted on the interface between two different media is a function of the energy density, $e(t)$, and the specific acoustic impedances, Z_1 and Z_2, of the media. The energy density, $e(t)$, is proportional to the square of the sum of the sound pressures, $p_1(t)$ and $p_2(t)$, generated by the two transducers. In the intersectional area of the two beams, therefore, an oscillatory radiation pressure $P_{\mathrm{R}}(t)$ with the frequency difference, Δf, is applied to the interface. The radiation force produces acoustic emission which is closely related to the mechanical frequency response of the medium.

In this paper, as illustrated in Fig. 1(a), when the elastic modulus of the media is far smaller than that of the object, an acoustic radiation force may generate only the change in position of the object. In such cases, the mechanical properties of the object cannot be estimated. In order to generate the strain of the object even in such cases, two acoustic radiation forces with phases of θ and $\theta + \pi$ were applied at two different positions in the object as shown in Fig. 1(b). Furthermore, the displacements of two points, where the two radiation forces were applied, were measured by the ultrasonic *phased tracking method.*

2. Principle

When two ultrasonic beams with sound pressures of $p_0(t)$ at slightly different frequencies, f and $f + \Delta f$, are crossed each other, at the interface of the object the cyclically oscillating radiation pressure, $P_{\mathrm{R}}(t)$, at the frequency difference Δf is given by [1, 4]

$$P_{\mathrm{R}}(t) = (1 + R^2)\frac{p_0^2}{\rho_1 c_1^2}\cos\Delta\omega t, \qquad (1)$$

where p_0, ω, and $\Delta\omega$, are the amplitude of the sound pressure of each ultrasound beam, angular frequency of the incident wave ($\omega = 2\pi f$), and difference in angular frequency ($\Delta\omega = 2\pi\Delta f$), respectively.

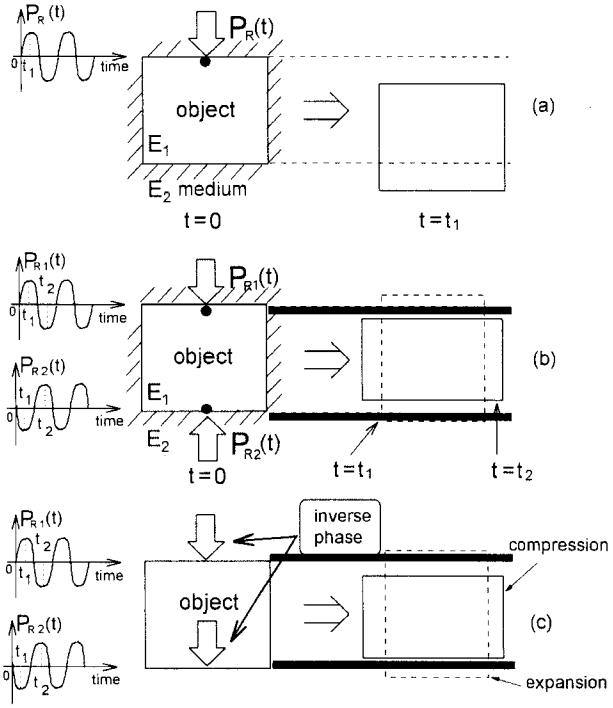

Figure 1: (a) A model of a parallel motion of an object using one acoustic radiation force. (b) A model of a strain of an object using two acoustic radiation forces. (c) A model of strain of object using inverse-phase acoustic radiation forces.

In this paper, in order to generate the regional strain inside the object, we use two phase controlled acoustic radiation pressures, $P_{\mathrm{R1}}(t)$ and $P_{\mathrm{R2}}(t)$, given by

$$P_{\mathrm{R1}}(t) = (1 + R^2)\frac{p_{01}^2}{\rho_1 c_1^2}\cos\Delta\omega t, \qquad (2)$$

$$P_{\mathrm{R2}}(t) = (1 + R^2)\frac{p_{02}^2}{\rho_1 c_1^2}\cos(\Delta\omega + \pi)t. \qquad (3)$$

As shown in Fig. 1(c), by applying these phase-controlled acoustic radiation pressures at two points of the object, the regional strain is generated inside the object.

3. Experiments

Figs. 2(a) and 3(a) show the M-mode images of the object. In each figure, the difference frequency $\Delta f = 10$ Hz was employed. Acoustic radiation pressures, $P_{\mathrm{R1}}(t)$ and $P_{\mathrm{R2}}(t)$, shown in Figs. 2(b) and 3(b) were calculated based

on eq. (1) as follows: The density, ρ_2, and the sound speed, c_2, of the object were measured as 1.1×10^3 kg/m^3 and 1.47×10^3 m/s, respectively, in a separate experiment. By assuming the density, ρ_1, and the sound speed, c_1, of water to be 1.0×10^3 kg/m^3 and 1.5×10^3 m/s, respectively, the pressure reflection coefficient, R, and the energy reflection coefficient, R^2, were respectively calculated as 0.038 and 0.0014.

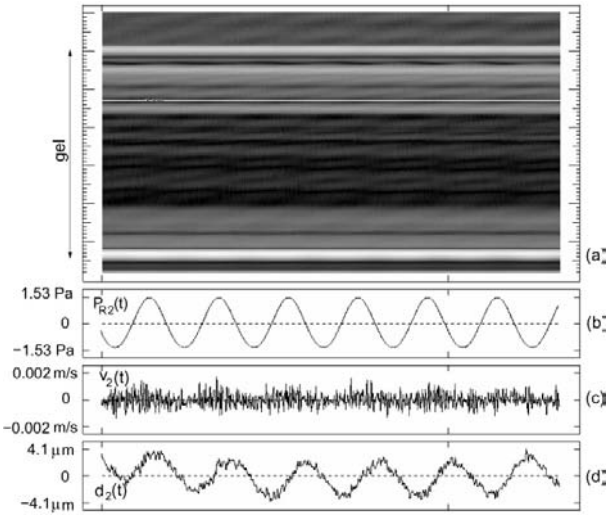

Figure 2: Results for the position radiated by 3-MHz ultrasound. (a) M-mode image of gel. (b) Estimated acoustic radiation pressure, $P_{\mathrm{R}2}(t)$. (c) Vibration velocity of the object, $v_2(t)$, obtained by the ultrasonic *phased tracking method.* (d) Displacement of the object, $d(t)$.

In this study, the amplitudes of the applied voltages, V_0, were set to be 90 V for 1 MHz transducer and 23 V for 3 MHz transducer, to make the amplitudes of the acoustic radiation forces almost similar. By neglecting the attenuation of the media surrounding the object, the amplitudes of the sound pressures, p_{01} and p_{02}, were calculated to be 130 kPa, respectively. In this paper, by assuming the object to be a totally absorbing material ($R = 0$) and considering the angles, θ_1 and θ_2, of the transducer for the actuation from the vertical axis, the vertical components of the acoustic radiation pressures, $P_{\mathrm{R}1}(t)$ and $P_{\mathrm{R}2}(t)$, exerted on the two points in the object were calculated as 1.84 Pa for 1 MHz transducer and 1.53 Pa for 3 MHz transducer. The difference in the phase of the acoustic radiation forces is 180 degrees. However, the difference in the phase of the measured displacements at two points is 120 degrees. The amplitudes of the measured displacements of these two points were 3.5 μm actuated by 1 MHz transducer and 4.8 μm actuated by 3 MHz transducer. From these results, using the proposed method, the regional strain inside object was successfully generated and measured with ultrasound.

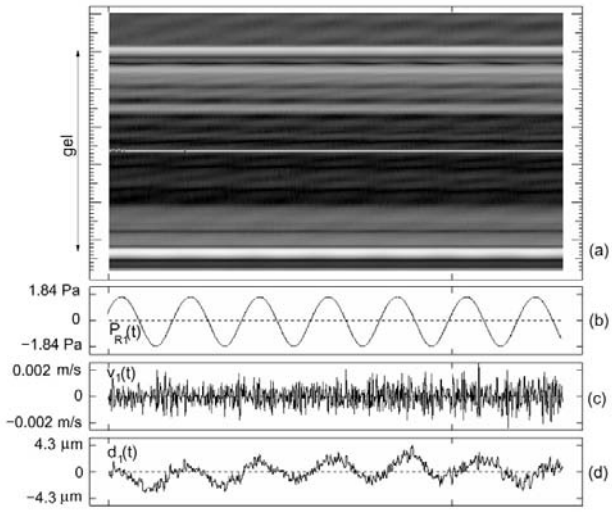

Figure 3: Results for the position radiated by 1-MHz ultrasound. (a) M-mode image of gel. (b) Estimated acoustic radiation pressure, $P_{\mathrm{R}2}(t)$. (c) Vibration velocity of the object, $v_2(t)$, obtained by the ultrasonic *phased tracking method.* (d) The displacement of the object, $d(t)$.

4. Conclusions

In this study, in order to generate the regional strain inside the object, we constructed an experimental setup for application of cyclic remote actuation in the object using two focused ultrasonic transducers. The phase difference between two acoustic radiation forces, which were respectively applied at two different positions in the object, was controlled to be 180 degrees. The phase difference of the measured displacements by the ultrasonic *phased tracking method* was 180 degrees indeed. These results show potential of the proposed method for generation of the regional strain inside the object for tissue characterization.

Reference

1. M. Fatemi and J. F. Greenleaf: IEEE Trans. on Med. Imag. **21** (2002) 1.

2. K. Nightingale, et. al.: Ultrasound in Med. Biol. **28** (2002) 227.

3. H. Kanai, M. Sato, Y Koiwa, and N. Chubachi, IEEE Trans. on UFFC **43** (1996) 791.

4. K. Michishita, H. Hasegawa and H. Kanai: Jpn. J. Appl. Phys. **42** (2003) 4608.

Proc. Symp. Ultrason. Electron., Vol. 25, (2004) pp. 271-272
27-29 October, 2004

Imaging of Cross-Sectional Elasticity of Arterial Wall by Comparing Measured Change in Thickness with Model Waveform

○ Jiang Tang, Hideyuki Hasegawa and Hiroshi Kanai
(Tohoku University)

1. Introduction

Recently, increase in the number of patients suffering from myocardial infraction or cerebral infraction has become a serious social problem. Therefore, it is important to diagnose atherosclerosis in an early stage because such circulatory diseases are mainly caused by atherosclerosis. Since the elasticity of the arterial wall changes as atherosclerosis develops, the evaluation of the regional elasticity of the arterial wall using ultrasound is useful for the diagnosis of atherosclerosis. For assessment of elasticity of the arterial wall, the change of several tenth of microns in wall thickness due to heartbeat is measured by the phased tracking method[1] with transcutaneous ultrasound. For various reasons, for example, extremely small deformation of the wall, low S/N of echo, and non-smooth luminal surface, etc., the minute change in thickness during one heartbeat cannot be successfully measured in some cases. In this paper, a method is proposed for evaluation of the reliability in measurement of the minute change in wall thickness by calculating the difference between the measured and model waveform.

2. Principle

An ultrasonic beam was sequentially scanned at 60 positions in the carotid artery with a linear-type probe of 7.5 MHz. Along each beam, multiple points are set in the arterial wall and layers with thickness of 375 μm are defined between each adjacent two points. The change in thickness of each layer is obtained by measuring displacements at these two points using the *phased tracking method*. The lowest value of the change in thickness was validated as being 0.5 μm[2].

In our matching process, a template waveform was prepared as the model waveform $H_0(t)$ of the change in wall thickness. First of all, as shown in Fig. 1, the model waveform $H_0(t)$ was expanded or compressed to the same length as the measured waveform $y(t)$ in the time axis using a linear interpolation. The model waveform after interpolation, $h_0(t)$, is expressed by the model before interpolation, $H_0(t)$. Then, as shown in Fig. 2, the amplitude of the resultant model waveform $h_0(t)$ is normalized by A by minimizing the error α between the model waveform $h_0(t)$ and the measured waveform $y(t)$ as follows:

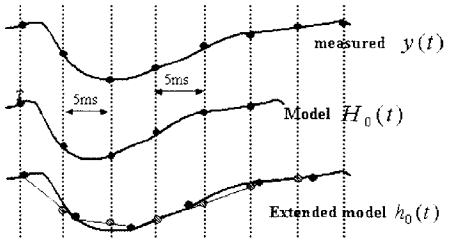

Figure 1: Linear interpolation.

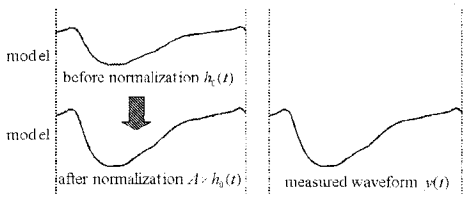

Figure 2: Amplitude normalization.

$$\alpha = \sqrt{\frac{\sum_{t=0}^{N-1} |Ah_0(t) - y(t)|^2}{\sum_{t=0}^{N-1} |Ah_0(t)|^2}}, \tag{1}$$

where A is a constant which expresses the difference in amplitude between the measured and model waveforms, and N is the number of the discrete sampled points of the data during one heartbeat. In order to minimize α, the partial derivative of α with respect to A is set to zero, that is,

$$\frac{\partial \alpha}{\partial A} = 0. \tag{2}$$

Then, the constant A which minimizes α can be determined as follows:

$$\hat{A} = \frac{\sum_{t=0}^{N-1} |y(t)|^2}{\sum_{t=0}^{N-1} |y(t) \cdot h_0(t)|}. \tag{3}$$

The constant $\hat{A}$ determined by eq. (4) is substituted for eq. (2) to calculate the minimum error α_{min}, which is used to estimate the difference between the measured and model waveform.

3. Experiments

Fig. 3 shows the image of cross-sectional elasticity of the arterial wall by comparing measured change $y(t)$ in thickness with a model waveform. In this image, the elasticity was displayed only when the constant $\widehat{A}$ is larger than 0, which means that the layer should become thin during one heartbeat.

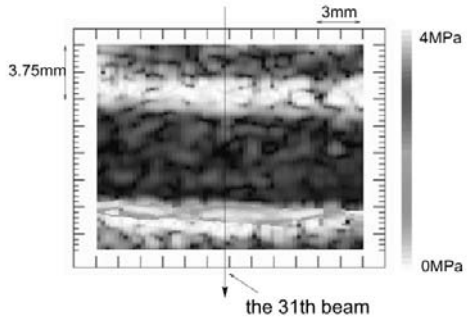

Figure 3: Cross-sectional image of elasticity of the common carotid artery of a healthy subject.

To get a more exact evaluation, we divided the error α_{min} into bias error b_{min} and random error r. In this experiment, the waveforms of the change in thickness, $\{y_k(t)\}$, were measured in successive M heartbeats, where k=0,1,$\cdots$,M. From the averaging of these waveforms $\{y_k(t)\}$, the mean waveform $y_0(t)$ is obtained. Using eq. (2), the minimum bias error b_{min} between the model waveform $h_0(t)$ and the mean waveform $y_0(t)$ is calculated by

$$b_{min} = \sqrt{1 - \frac{\left(\sum_{t=0}^{N-1} h_0(t)y_0(t)\right)^2}{\sum_{t=0}^{N-1}\left(h_0(t)\right)^2 \cdot \sum_{t=0}^{N-1}\left(y_0(t)\right)^2}}. \quad (4)$$

The normalized random error r between average waveform $y_0(t)$ and the measured waveforms $\{y_k(t)\}$ of M heartbeats is defined as follows:

$$r = \sqrt{\frac{\frac{1}{M}\cdot\sum_{k=1}^{M}\left(\sum_{t=0}^{N-1}|y_k(t)-y_0(t)|^2\right)}{\sum_{t=0}^{N-1}|\widehat{A}h_0(t)|^2}}. \quad (5)$$

Figure 4 shows the relationship between the estimated value of $\widehat{A}$ and the bias error b_{min} in the 31st beam. r is the average value of random errors of the several heartbeats. In Fig. 4, there is a tendency that when $\widehat{A}$ became larger, b_{min} became smaller. The magnitude of the change in thickness in media is larger that of intima and adventitia. Figure 4 also shows that the random error r in media is smaller than that of intima and adventitia. Figure 5 shows the difference of change in thickness between media and adventitia.

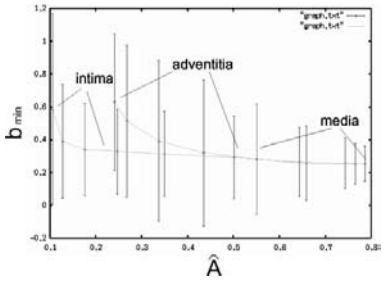

Figure 4: Error distribution in the 31th beam.

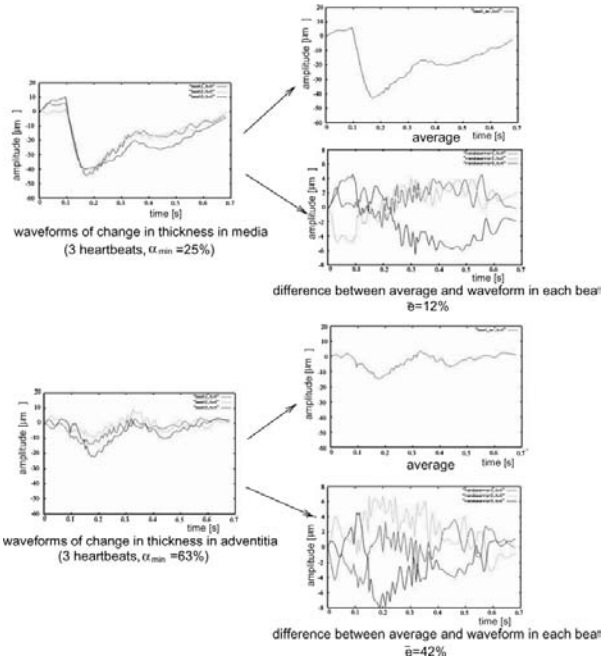

Figure 5: Waveforms of change in thickness.

4. Conclusions

In this paper, a method was proposed to evaluate the reliability by calculating the error between the measured and template waveforms. It is possible that the reliability of the elasticity image will be improved by excluding waveforms with large bias error and the measured elasticity will be evaluated by using the random error.

Reference

1. H. Kanai, M. Sato, Y. Koiwa, and N. Chubachi: IEEE Trans. UFFC. **43** (1996) 791.
2. H. Kanai, M. Sato, Y. Koiwa, et al.: Electron. Lett. **35** (1999) 949.

Proc. Symp. Ultrason. Electron., Vol. 25, (2004) pp. 273-274
27-29 October, 2004

Change in Elasticity in Intima-Media Region of Brachial Artery Caused by Flow-Mediated Dilation

○ Masataka Sugimoto, Hideyuki Hasegawa, and Hiroshi Kanai.
(Tohoku Univ.)

1. Introduction

Endothelial dysfunction is considered to be an initial step of arteriosclerosis [1]. For assessment of the endothelium function, brachial artery flow-mediated dilatation (FMD) caused by increased blood flow has been evaluated with ultrasonic diagnostic equipment. In conventional methods, the change in artery diameter caused by FMD is measured [2]. Although the arterial wall has the layered structure (intima, media, and adventitia), such a structure is not taken into account in conventional methods because the change in diameter depends on the characteristic of the entire wall. In this study, to make use of such a layered structure, we divide the wall of the brachial artery into multiple layers with the same thickness, and the elasticity of each layer is obtained by *the phased tracking method* [3]. Based on the difference in vasoreactivity among intima, media, and adventitia regions, our proposed method provides a great possibility for improving sensitibity in evaluation of endothelium function by measuring the transient in elasticity only for the intima-media region including smooth muscle.

2. Methods

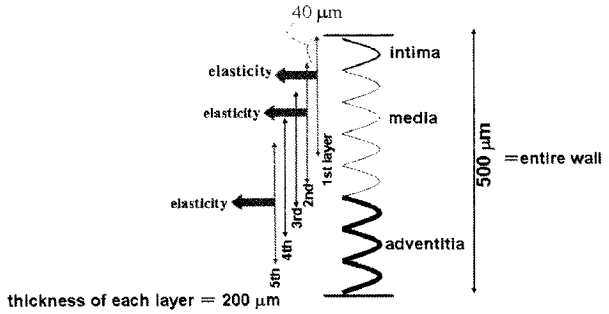

Figure 1: Posterior wall of the brachial artery were divided into 5 layers with the same thickness.

Blood flow of brachial artery is shut by surrounding the forearm with a cuff at a pressure of 250 mmHg for 5 minutes [2]. After release of the cuff, nitric oxide, which is generated by the endothelium in response to the shear stress due to increased blood flow, makes the smooth muscle in the media relax [4]. We measured the change in elasticity of the intima-media region of the artery due to FMD for 2 minutes with a 10 MHz linear-type probe [5]. Multiple points were preset from the intima to the adventitia along the ultrasonic beam. Figure 1 shows how to divide the posterior wall of the brachial artery into 5 layers with the same thickness. The arterial wall was divided into 5 layers with a thickness of 200 μm, which corresponds to 10 sampled points. Adjacent layers were overlapped by 160 μm. In this study, transients in elasticity were measured the first, second, and fifth layers. The first, second, and fifth layers were supposed to correspond to the intima-media, media, and adventitia regions, respectively. For the elasticity estimation, the change in thickness of each layer was measured by the *phased tracking method* [3]. The elasticity of each layer was obtained from the maximum value of the change in thickness of each layer during one heartbeat and sphygmo pressure [5].

3. Experimental results

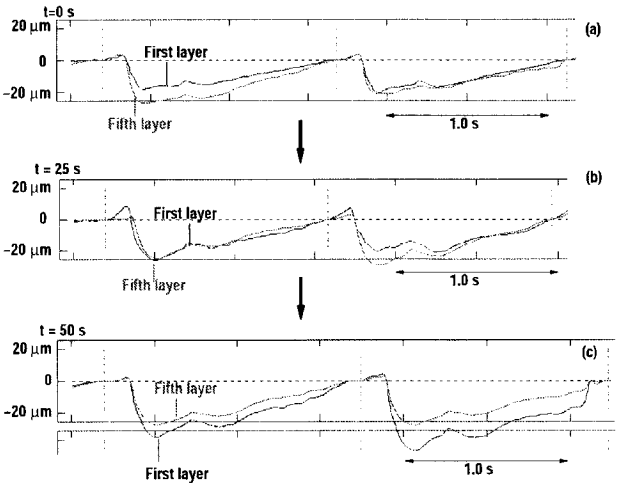

Figure 2: Transients of the change in thickness of the intima-media layer (the first layer) and the adventitia layer (the fifth layer). (a)At t=0 s. (b)At t=25 s. (c)At t=50 s.

Figure 2 shows the transient of the change in thicknesses of the intima-media layer (the first layer) and the adventitia layer (the fifth layer) just after recirculation for 23-year-old male. The cuff was released at t=0. The clear increase was found in the maximum change in thickness during one heartbeat for the intima-media layer (the first layer)(t=0 s: 18.5 μm $\rightarrow$ t=25 s: 26.6

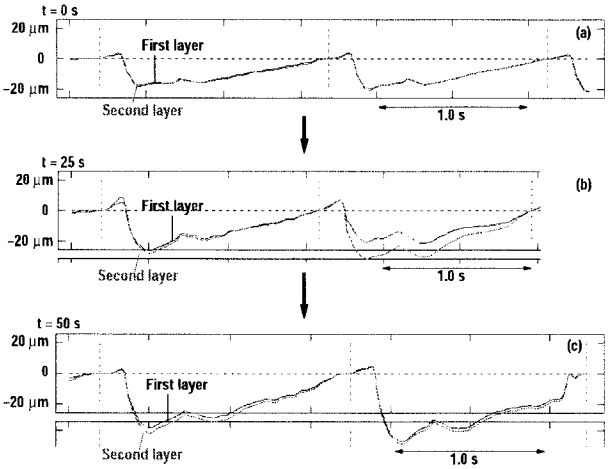

Figure 3: Transients of the change in thickness of the intima-media layer (the first layer) and the media layer (the second layer). (a)At t=0 s.(b)At t=25 s.(c)At t=50 s.

μm $\rightarrow$ t=50 s: 35.9 μm). On the other hand, no increase was found for the adventitia layer (the fifth layer)(t=0 s: 27.2 μm $\rightarrow$ t=25 s: 25.6 μm $\rightarrow$ t=50 s: 28.0 μm). As well as the intima-media layer, Figure 3 shows that the clear increase was found in the maximum value of the change in thickness (t=0 s: 19.8 μm $\rightarrow$ t=25 s: 31.6 μm $\rightarrow$ t=46.1 μm) for the media layer (the second layer). The maximum values of the change in thickness of the intima-media layer (the first layer) and those of the media layer (the second layer) increased by almost 100%.

Figure 4 shows the transients in elasticity of the intima-media layer (the first layer), the media layer (the second layer), and the adventitia layer (the fifth layer). The clear decrease was found in the elasticity of the layer in the intima-media region (t=0 s: 497 kPa $\rightarrow$ t=25 s: 434 kPa $\rightarrow$ t=50 s: 249 kPa $\rightarrow$ t=111 s: 379 kPa). Maximun decrease was almost 50% compared to that at t=0 s. As well as the intima-media layer (the first layer), similar result was obtained for the media layer (the second layer)(t=0 s: 530 kPa $\rightarrow$ t=25 s: 344 kPa $\rightarrow$ t=50 s: 237 kPa $\rightarrow$ t=111 s: 321 kPa). Maximum decrease was almost 50% compared to that at t=0 s. On the other hand, the elasticity of the layer in the adventitial region did not change so much throughout the measurement (t=0 s: 440 kPa $\rightarrow$ t=50 s: 384 kPa $\rightarrow$ t=111s : 475 kPa). These results can be well explained by the fact that nitric oxide generated by the endothelium specifically makes smooth muscle in the media relax. Moreover, the FMD of 50% measured by the proposed method was much greater than that of 10% measured by the conventional method. From these results, for evaluation of endothelium function, the measurement of the decrease in elasticity of the intima-media region is found to be more effective than the measurement of the increase in diameter in conventional methods.

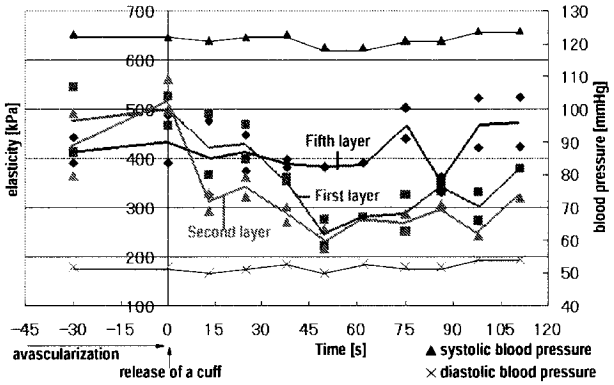

Figure 4: Transients in elasticity of the intima-media layer (the first layer), the media layer (the second layer), and the adventitia layer (the fifth layer)

4. Conclusion

From the measured transients in elasticity, it is supposed that only the layers in the intima-media region became soft in response to nitric oxide. In conventional methods, the mechanical property of the adventitial side, which was not changed by FMD, is inseparable in the measurement of the change in diameter. In this paper, we proposed a method with a possibility for improving sensitivity in evaluation of the endothelium function by measuring the transient in elasticity due to FMD only for the region including smooth muscle.

References

1. R. Ross: N. Engl. J. Med. **340** (2004) 115.
2. M. Hashimoto, M. Akishita, M. Sato, et al: Circulation **92** (1995) 3431.
3. H. Kanai, M. Sato, Y. Koiwa, et al: IEEE Trans. Ultrason. Ferroelect. Freq. Contr. **43** (2001) 791.
4. G. M. Rubanyi, J. C. Romero, P. M. Vanhoutte: Amer. J. Physiol. **250** (1986) 1145.
5. H. Hasegawa, H. Kanai, N. Hoshimiya, et al: J. Med. Ultrason. **31** (2004) 81.

Proc. Symp. Ultrason. Electron., Vol. 25, (2004) pp. 275-276
27-29 October, 2004

Construction of Reference Data for Classification of Elasticity Images of Arterial Wall

○Jun Inagaki, Hideyuki Hasegawa, and Hiroshi Kanai (Tohoku Univ.)
Masataka Ichiki (Sendai Hospital of East Railway Company)
Fumiaki Tezuka (Sendai Medical Center)

1. Introduction

Cerebral infarction and myocardial infarction are mainly caused as terminal symptoms of atherosclerosis. Therefore, it is important to diagnose atherosclerosis in an early stage. Rupture of atherosclerotic plaque is probably the most important factor underlying the sudden outbreak of the acute coronary syndrome [1]. Direct characterization of the composition and vulnerability of atherosclerotic plaque may offer insight into the mechanism of plaque regression and progression [2),3)]. The change in elasticity is caused greatly by the change in composition of the arterial wall due to development of atherosclerosis [4)]. Therefore, the measurement of elasticity has potential for tissue characterization of plaque. In this paper, the reference data of elasticity distributions for respective tissues were constructed to classify arterial tissues from the elasticity images measured with transcutaneous ultrasound. From *in vitro* experiments, the relation between tissue components of arterial wall and the elasticity was investigated by comparing elasticity images measured by ultrasound with the corresponding pathological images.

2. Methods

2.1 System for *in vitro* experiments

In the experimental setup for *in vitro* experiments using extracted human femoral arteries, the change in internal pressure was generated using an artificial heart, and the internal pressure was measured by the pressure detector placed in lumen of the artery. The artery fixed in the water tank was measured in the long-axis plane with a conventional linear-type probe (center frequency: 7.5 MHz).

2.2 Construction of Elasticity Distribution for Each Tissue

In this paper, the elasticity distributions were obtained further with respect to blood clot and calcified tissue. After ultrasonic elasticity measurements, the arteries were fixed in formalin. The plane scanned by ultrasound was identified by imaging a needle, which was fixed in the external surface of the posterior wall, in the B-mode image during the ultrasonic measurement [5)]. The pathological images of the measured sections were made with Elastica-Masson staining for blood clot and with Hematoxylin-Eosin staining for calcified tissue. By referring the pathological images, the regions which correspond to blood clot and calcified tissue were assigned in the cross-sectional elasticity images. From the assigned regions for respective tissues, the elasticity distributions were determined.

2.3 Collagen Content Estimation

Collagen is considered to mainly contribute to the stiffness of the fibrous cap of plaque. Thus, the correlation between the collagen content and the elasticity was investigated. In the elasticity image, there are M ultrasonic beams and N_m regions along m-th beam (m=1, ..., M). The pathological image was divided into M sections in the axial direction of the artery and dividing each m-th section of M sections into N_m regions in the radial direction. The sizes of all regions in the elasticity image are same. However, sizes of regions assigned in the pathological image become different because of the distortion of the arterial wall due to dehydration during formalin fixation. In this paper, the change in size due to distortion is assumed to be homogeneous. Then, the collagen content of each region assigned in the pathological image was estimated using the mahalanobis distance. In this paper, the composition of each region were classified into 4 classes (i=1: collagen, 2: smooth muscle, 3: elastin, 4: background). The mean, $\boldsymbol{\mu}_i = (\mu_r, \mu_g, \mu_b)^T$, and covariance matrix, $\sum_i$, of RGB values were determined for each class, i, by assigning a typical area for each class in the pathological image. From the determined mean, the mahalanobis distance, d_i^2, between each pixel, $\boldsymbol{X}=(x_r, x_g, x_b)^T$, and the center of i-th class can be obtained as follows:

$$d_i^2 = (\boldsymbol{X} - \boldsymbol{\mu}_i)^T \sum_i{}^{-1} (\boldsymbol{X} - \boldsymbol{\mu}_i) . \qquad (1)$$

The pixel, $\boldsymbol{X}$, is classified into class $i_{\min}$ with the least mahalanobis distance to $\boldsymbol{X}$.

3. Experimental Results

3.1 Construction of Elasticity Distribution for Each Tissue

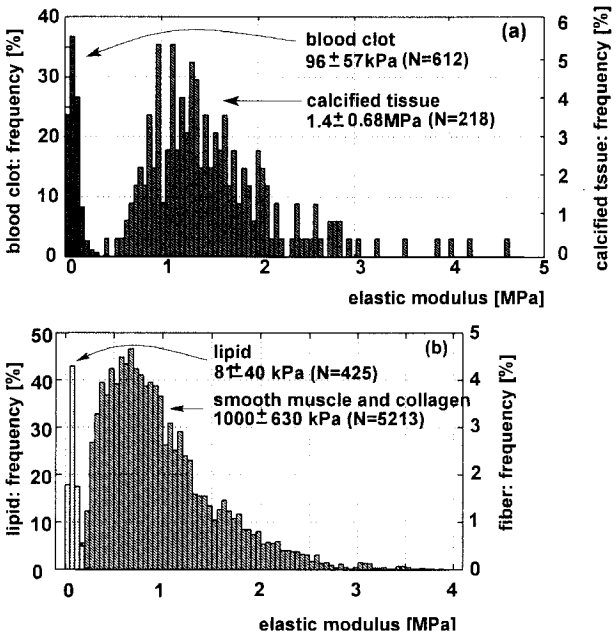

Figure 1: (a) Elasticity distributions of blood clot and calcified tissue. (b) Elasticity distributions of lipid and mixture of smooth muscle and collagen fiber [5].

Figure ?? shows the elasticity distributions of blood clot, calcified tissue, lipid, and fibrous tissue (mixture of smooth muscle and collagen fiber) [5]. By comparing these elasticity distributions, the high similarity was found in the elasticity distributions of lipid and blood clot. It means that the classification of these tissues based on elasticity is difficult. Moreover, the elasticity distributions of fibrous tissue and calcified tissue largely overlapped each other. However, fortunately, it will be possible to classify lipid or blood clot from fibrous tissue or calcified tissue by separating at about 300 kPa.

3.2 Collagen Content Estimation

Figure ?? shows the correlation between the ratio (collagen content) of the area, which was classified into collagen, and the elasticity. In Fig. ??, the mean value of elastic moduli within each region of 600 μm $\times$ 600 μm is plotted as a function of collagen content. The vertical bar shows the standard deviation of elastic moduli. The spatial resolution of the elasticity image was 300 μm by 75 μm in the axial and radial directions [5]. This resolution size was too small comparing with the deformation caused by dehydration during formalin fixation. Therefore, we employed the spatially averaged values. From Fig. ??, the positive correlation between the elasticity and the collagen content was found.

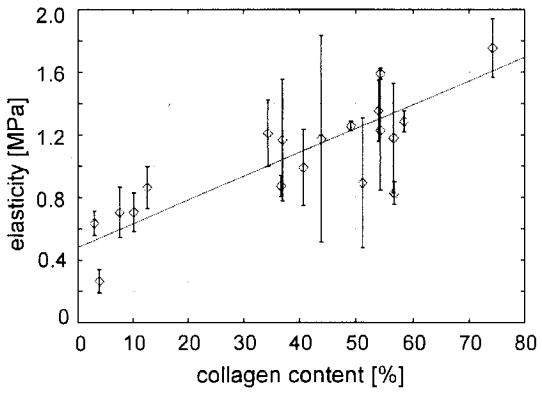

Figure 2: Relation between the collagen content and the elasticity.

4. Conclusion

In this paper, the elasticity distributions for blood clot and calcified tissue were measured with ultrasound. The comparison of the elasticity distributions including that for lipid and fibrous tissue [5], suggest the possibility of classifying the arterial tissues as soft tissues (lipid and blood clot) or hard tissues (fibrous tissue and calcified tissue) from the elasticity image. These two groups are separated at about 300 kPa, this elastic modulus may be important to make a rough estimate of the tissue characterization based on elasticity. Furthermore, the positive correlation between elasticity and collagen content was found in fibrous tissue. It offers the potential for estimation of the collagen content by the elasticity and contributes for the evaluating vulnerability of the atherosclerotic plaque.

References

1. P. R. Moreno, E. Falk, I. F. Palacios, et al: Circulation **90** (1994) 775.
2. H. M. Loree, R. D. Kamm, R. G. Stringfellow, et al: Circ. Res. **71** (1992) 850.
3. E. Falk, K. Prediman, P. K. Shah, at al: Circulation **92** (1995) 657.
4. R. T. Lee, A. J. Grodzinsky, E. H. Frank, et al: Circulation **83** (1991) 1764.
5. H. Kanai, H. Hasegawa, M. Ichiki, et al: Circulation **107** (2003) 3018.

Proc. Symp. Ultrason. Electron., Vol. 25, (2004) pp. 277278-
27-29 October, 2004

Analysis of Thick Phase Distorted Medium based on the Ultrasonic Speckle Intensity

◎ Tjundewo Lawu* and Mitsuhiro Ueda (Tokyo Inst. of Tech.)

1 Introduction

Ultrasonic imaging techniques are widely used in medical diagnosis. Its noninvasive nature, low cost, portability, and real-time image formation make ultrasonic imaging an attractive means for medical diagnosis. One of the limitations of ultrasonic images is poor image quality affected by inhomogeneous tissue layers. Our group proposed a model of thick phase distorted medium that incorporated the cumulative phase distortion effect caused by spatial inhomogeneities along the path of propagation.[1, 2] In the proposed model, a distributed inhomogeneous medium is lumped into a series of parallel screens. The wavefront propagation through multiple phase screens can be computed using the acoustic holography method.[3]

In this research, the relation of directivity deterioration and speckle intensity is analyzed. The focusing of ultrasonic beam, then, can be determined by using the speckle intensity. The fluctuation of the speckle intensity caused by a thick phase distorted medium located between the focused circular transducer and its focal plane is also examined in various parameter of distorted medium.

2 Phase distorted medium

Assuming that the distorted medium can be form as a convolution between the normal random number $\{n_i\}$ and the function $f(x)$. then

$$F(x) = \sum_{i=-\infty}^{\infty} f(x - i\Delta x)n_i, \qquad (1)$$

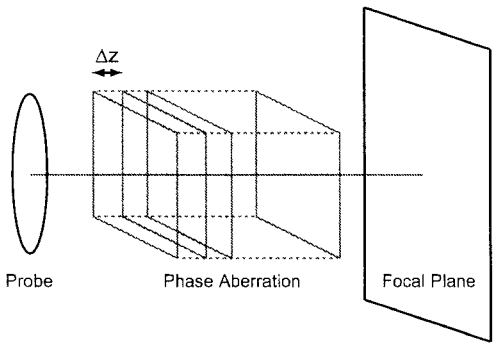

Fig. 2 Simulation Model.

*E-mail: lawu@ide.titech.ac.jp

where $F(x)$ is defined as a real number. This is in order to be able to express numerous properties of a model of distorted medium.

In Eq. (1), a Gaussian function $f(x) = A\exp(-Nx^2)$ is used as a model of a inhomogeneous tissue. A 3-D model of the distorted medium $M(x, y, z)$ is defined as

$$M = \sum_{i=-\infty}^{\infty}\sum_{j=-\infty}^{\infty}\sum_{k=-\infty}^{\infty} A \times e^{-N\left\{(x-i\Delta x)^2+(y-j\Delta y)^2+(z-k\Delta z)^2\right\}} n_{i,j,k}. \qquad (2)$$

If the auto correlation of Eq. (1) is defined by $R(y)$, then

$$R(y) = \frac{1}{\Delta x}\int_{-\infty}^{\infty} f(y - x)f(x)dx. \qquad (3)$$

In other words, a correlation function of a distorted medium is in proportion to a correlation function of a medium characteristic function.

In the case of 3-D, if the medium characteristic function is a Gaussian function $f(x, y, z) = A\exp(-Nx^2 - Ny^2 - Nz^2)$, then the covariance becomes

$$R_M(x, y, z) = \frac{A^2}{\Delta x\Delta y\Delta z}\left(\frac{\pi}{2N}\right)^{\frac{3}{2}} \times \exp\left\{-\frac{N}{2}\left(x^2 + y^2 + z^2\right)\right\}. \qquad (4)$$

In this case, the dispersion σ^2 is the maximum value of R_M and the correlation length ρ is defined as R_M decreases to the value of $\exp(-1)$.

$$\sigma^2 = \frac{A^2}{\Delta x\Delta y\Delta z}\left(\frac{\pi}{2N}\right)^{\frac{3}{2}}, \qquad \rho = \sqrt{\frac{2}{N}}. \qquad (5)$$

The numerical results are shown in Fig. 1, where average value 0 rad/mm, standard deviation $\sigma = 0.05$ rad/mm, correlation length $\rho = 1, 2, 4$ mm were used for generating the tissues.

3 Propagation through the medium

The analysis model is shown in Fig. 2. A 10 mm radius of focused circular transducer (center frequency of 3 MHz, focal length of 90 mm) is set on the origin of xy plane. The interval of sampling points is $\Delta x = \Delta y = 0.2$ mm, the number of sampling

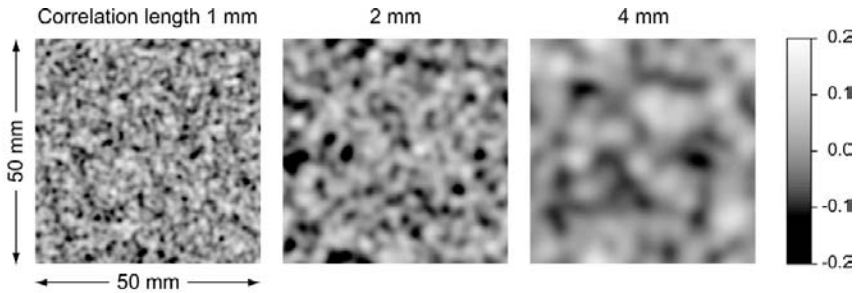

Fig. 1 2-D phase distorted tissue model with average 0 rad/mm, standard deviation $\sigma = 0.05$ rad/mm, and correlation length of 1, 2, and 4 mm.

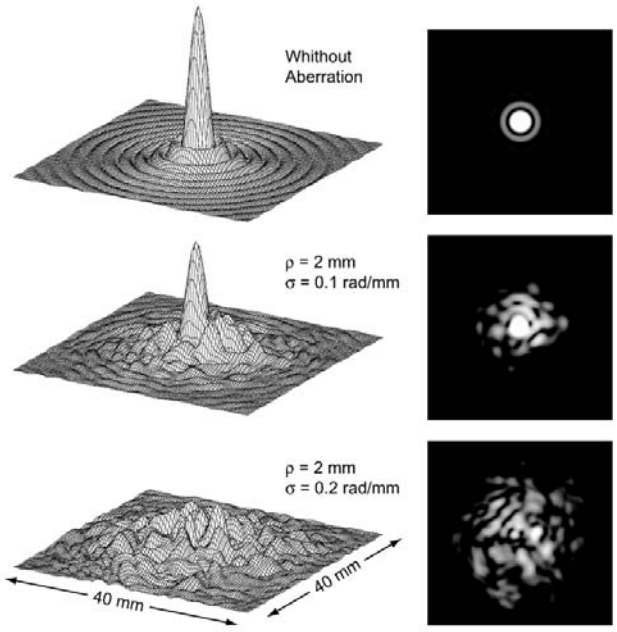

Fig. 3 Directivity on the focal plane without and with phase aberration.

points is $n_x = n_y = 251$, and the distance between each layer is $\Delta z = 1.0$ mm. We can summarize the algorithm to realize the focusing through distorted medium as follows:

(1) Directivity of the transducer is determined by the amplitude and phase generated in each sampling point of a lattice on the transducer face.

(2) A phase distorted medium is arranged at the center of the propagation direction and located at the middle of the focal distance. The other parts are assumed to be homogeneous.

(3) The ultrasonic wave propagates from the transducer face along the medium.

(4) The medium is constructed by 40 layers, each with 1 mm thick.

(5) The obtained directivity after the last screen is propagated to the focal plane.

The correlation length of 1 mm, 2 mm, 4 mm, standard deviation varies from 0 rad/mm to 0.2 rad/mm with interval of 0.01 rad/mm have been used in the simulation. Fig. 3 is an example of a simulation result by phase screen method. If the standard deviation of the medium is increased, the side lobe also becomes larger, and this also influences the main lobe.

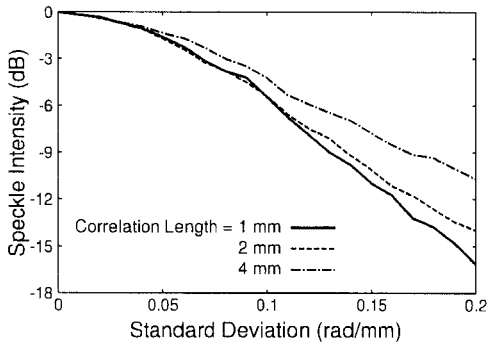

Fig. 4 Average Intensity as a function of standard deviation.

4 Speckle intensity

The average speckle intensity for each medium parameter is shown in Fig. 4. Each calculation result took 10 times of average. From these results, the speckle intensity is inferior if the correlation length is small and the standard deviation is big.

5 Summary

The directivity of the transducer after affected by an inhomogeneous medium was examined in various correlation length and standard deviation. Moreover, the relation between the deterioration of the directivity and the speckle intensity has been also shown. By using this technique, the speckle intensity could be used to examine the focusing factor of the image through a thick distorted medium.

Acknowledgment

The authors would like to thank Natsumi Naka for many useful discussions.

References

1. S. Takahashi, T. Lawu, and M. Ueda: Trans. IEICE (A) **J84-A** (2001) 1533-1540.
2. Y. Uno, T. Lawu, and M. Ueda: Trans. IEICE (A) **J87-A** (2004) 171-179.
3. M. Tabei and M. Ueda: J. Acoust. Soc. Am. **111** (2002) 940-946.

Proc. Symp. Ultrason. Electron., Vol. 25, (2004) pp. 279-280
27-29 October, 2004

Development of Ultrasonic Propagation Analysis Method for Estimation of Inner State of Bone Phantom

Nobuyuki Endoh, Takenobu Tsuchiya and Yoshikazu Saito
Dept. of Electrical, Electronic and Information, Kanagawa University
High-Tech Research Center, Kanagawa University

1. Introduction

Ultrasonic measuring technique is widely using for diagnosis of osteoporosis because of safety. A precise simulation, however, is not reported, because the behavior of ultrasonic pulse propagated in bone is very complicated.[1][2] In this paper, the elastic Finite Difference Time Domain (FDTD) method that is concerning about not only longitudinal wave but also shear wave in bone is proposed for the estimation of illness of the osteoporosis.[3] Since the cancellous bone has two components of the trabecular bone and the bone marrow, a simple phantom composed of two layers is also proposed for the preliminary research.

2. Numerical analysis by elastic FDTD

A phantom contains the cortical bone and the cancellous bone that has two components of the trabecular bone and the bone marrow. The aging process makes the cancellous bone fragile because the trabecular bone has been undermined. Geometry of the simple phantom is shown in Fig.1. The cortical bone is made of acrylic cylinder because an acoustic impedance of acrylic resin is almost the same as that of the cortical bone. The trabecular bone is simulated by steel wire whose diameter is 0.5[mm]. Distance a of wires arranged regularly is changed as an indicator of undermining of trabecular bone. Water is used as bone marrow. The density, sound speed, and attenuation coefficient of water is assumed to be 1000[kg/m^3], 1500[m/s] and 0.025 [neper/m], respectively.

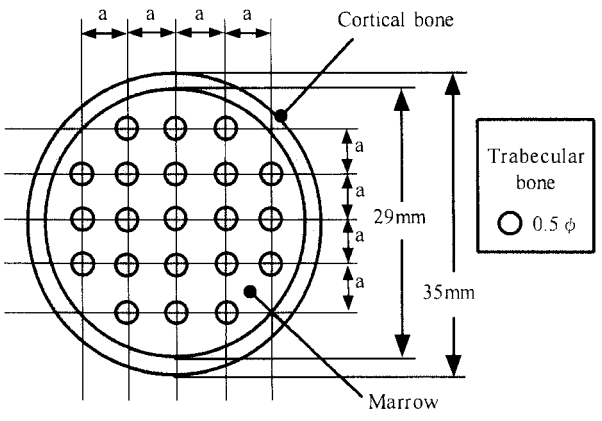

Fig1. Bone phantom composed of acrylic cylinder and steel wires.

The density, sound speed of longitudinal and shear wave, attenuation coefficient of longitudinal and shear wave of the acrylic cylinder is 1180[kg/m^3], 2720 and 1460[m/s], and 16 and 45[neper/m], respectively.

The overall calculation domain is 130[mm] x 60[mm] and is shown as main cell domain in the Fig.2. Increment step is 0.1[mm] in space and is 0.02[μs] in time. In the local cell domain, the sub-grid calculation method is adapted for the reduction of the calculation time, because it takes very long time to calculate the stress/pressure in precisely over all main cell domain.[4] Since the increment of calculation steps in the local domain is one third of that in the main cell domain, more precise results are obtained in the local domain.

3. Pulse transmission method

Figure 2 shows the experimental setup in a water bath for the pulse transmission method. 1MHz PZT disk transducers of 20 and 10[mm] are used for transmission and reception of pulse. Two transducers are linearly scanned every 2[mm] after acquisition of one serial data of the transmitted pulses. In the experiment, one cycle electric pulse drives a transmitter for projection of short pulse in water. In the FDTD analysis, Gaussian modulated pulse of 1MHz is used for calculation.

Rectified amplitude of transmitted pulses is shown in Fig.3. The experimental and calculated pulse waveform is shown in the figure at top and bottom,

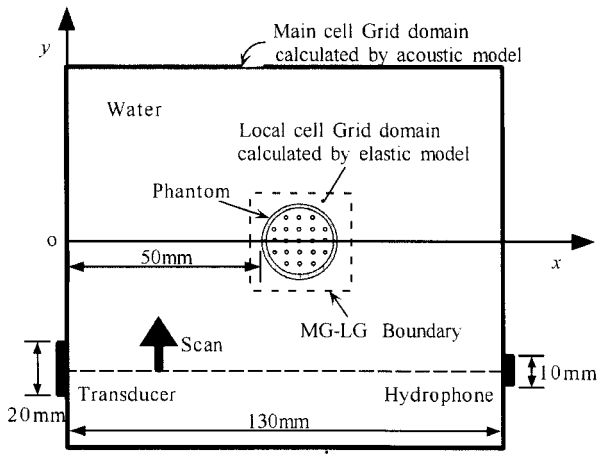

Fig.2 Experimental set up for pulse transmission method

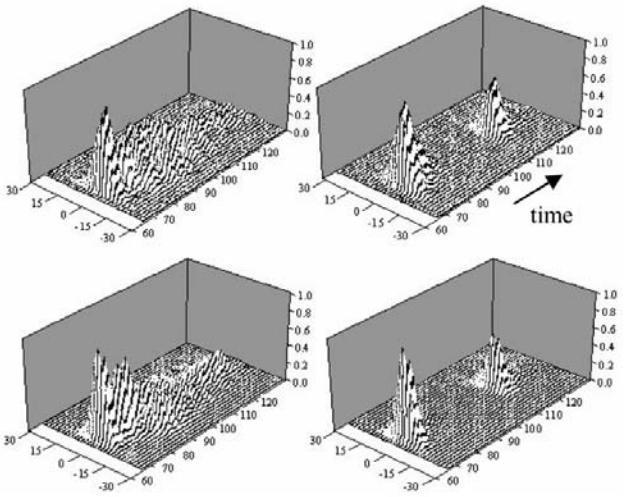

Fig.3 Experiment (top) and calculation (bottom) a =2.5mm (left) and no wire (right)

respectively. The result at a =2.5[mm] is shown on the left, and the result at no wire is on the right. After the first strong echo caused by the acrylic cylinder, many weak scattered pulses from inner wires arrive at the receiver. If there is no wire (no trabecular bone) inside the cylinder (cortical bone), there is no scatted signal from it as shown in the figure. This is a good indicator of undermining of trabecular bone.

4. Reflected directivity of inner wires

Reflected directivity of the same phantom was studied for the probability of diagnosis of illness by this method. Block diagram of the measurement system is shown in Fig. 4. In this measurement, the small PZT receiver was used. The received pulse is truncated to the only reflection pulse from inner wires. Angle dependency of the maximum amplitude of it was measured from 30 to 90 degrees. The estimated reflected directivity is also calculated by the elastic FDTD at a =4.5[mm].

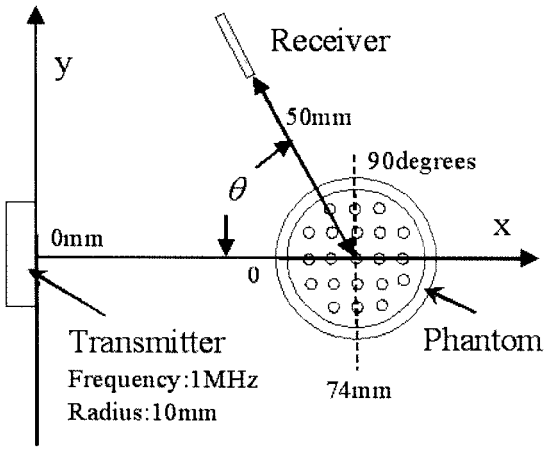

Fig.4 Block diagram of experiment for pulse echo method

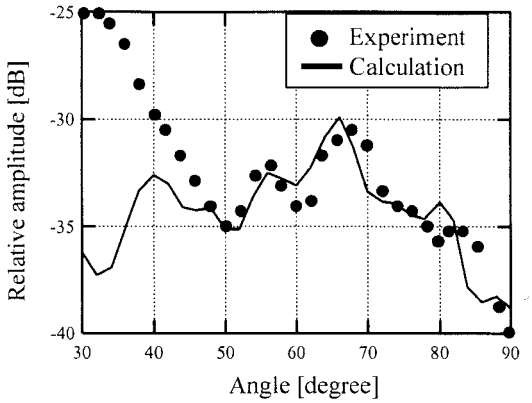

Fig.5 Reflected directivity of inner wires at a=4.5mm

The experimental result and calculation result are sown in Fig.5. It is clearly shown that the experimental result agrees well with calculation. Because of the difficulty of elimination of the first strong echo, two results are in disagreement less than 45 degrees.

5. Conclusions

The elastic FDTD method and simple bone phantom are proposed for the estimation of illness of the osteoporosis. The comparison between experiment and calculation shows that there is a good agreement. It is show the validity of elastic FDTD for estimation of inner state of bone.

Acknowledgment

This study was partly supported by High-Tech Research Center Project from the Ministry of Education, Culture, Sports, Science and Technology, Japan. This study was also partly supported by a 2003 and 2004 Grand-in-Aid for Scientific Research from the Ministry of Education, Culture, Sports, Science and Technology (Grant No. 16500325 and 16500325), Japan.

References

[1] G. Luo et. al; "Computational methods for ultrasonic bone," Ultrasound in Med & Biol Vol.25, No.**5**, 823-830 (1999)

[2] E. R. Hughes et. al; "Ultrasonic propagation in cancellous bone: a new stratified model," Ultrasound in Med & Biol Vol.25, No.**5**, 811-821 (1999)

[3]T.Tsuchiya; J. Med. Ultrasoc. "Numerical Anaysis ofultrasound Pulse Propagation in Phantom by FDTD Method with Local Subgridding," Vol.27 No.**4**, 737-738. (2000) [in Japanese]

[4] R. Uno; "*Analysis of Electromagnetic filed by FDTD*," Corona, (Tokyo, 1998) [in Japanese]

[5] F.Iijima, T.Tsuchiya and N.Endoh; "Analysis of Characteristics of Underwater Sound Propagation in Ocean by a Finite Difference Time Domain Method," Jpn. J. Appl. Phys. Vol.39 No.**5B**. 3200-3203. (2000)

[6] H.Saito, J.Naoi and T.Kikuchi; "Finite Difference Time Domain Anaysis for a Sound Field Including a Plate in Water," Jpn. J. Appl. Phys. Vol.43 No.**5B**. 3176-3179.(2000)

Proc. Symp. Ultrason. Electron., Vol. 25, (2004) pp. 281-282
27-29 October, 2004

Numerical analysis of temperature rise in tissue by ultrasound

◎Yoshikazu Saito, Takahiro Ishizeki, Takenobu Tsuchiya and Nobuyuki Endoh
(Department of Electrical, Electronics and Information Engineering, Kanagawa University,
High Tech Research Center, Kanagawa University)

Introduction

Many Doctors use the ultrasonic imaging equipment, because it is well known that the ultrasonic imaging equipment is safe and noninvasive. The ultrasonic powers of equipment, however, increase rapidly these days. It is important to make sure the temperature rise caused by absorption of high power ultrasound. In this paper, we have simulated temperature rise in phantom of soft tissue using Finite Difference Time Domain (FDTD) method and Heat Conduction Equation (HCE) when the thermal diffusivity was changed. Sound pressure distribution is firstly calculated by FDTD method, and then temperature rise caused by sound pressure in tissue is calculated by HCE method.

Analysis method

FDTD method and HCE method are expressed as a following five equations.

$$-\frac{1}{K}\frac{\partial p}{\partial t}=\frac{\partial v_x}{\partial x}+\frac{\partial v_y}{\partial y}, (1)$$

$$-\rho\frac{\partial v_x}{\partial t}=\frac{\partial p}{\partial x}+\eta v_x, (2) \quad -\rho\frac{\partial v_y}{\partial t}=\frac{\partial p}{\partial y}+\eta v_y, (3)$$

$$\frac{\partial T}{\partial t}=\kappa\left(\frac{\partial^2 T}{\partial x^2}+\frac{\partial^2 T}{\partial y^2}\right)+\frac{H}{\rho C}, (4) \quad H=2\alpha I, (5)$$

where p is the sound pressure, v_x and v_y are the particle velocity, ρ is the density, K is volume modulus, η is attenuation coefficient and t is time. In eqs. (4) and (5), T is temperature, κ is thermal diffusivity, H is heating value, C is specific heat, α is absorption coefficient and I is ultrasound intensity calculated by sound pressure. A phantom of soft tissue placed at 22 mm from a transmitter of 5 mm in radius is radiated by a continuous wave sound of 1 MHz as shown in Fig. 1. To satisfy the Courant's stability equation in FDTD method, calculation increments are chosen that $\Delta x=\Delta y=0.073$ mm in space and $\Delta t=0.02$ μs in time. Higdon's second-order absorbing boundary conditions are provided to eliminate the reflection waveform returned from the outer boundary of the calculation space. In HCE method, calculation increments are chosen Δx and Δy is the same as that in FDTD method and $\Delta t=8$ ms. The tissue is assumed to be immersed into water of 37 degrees in Celsius.

e-mail: r200470096@kanagawa-u.ac.jp

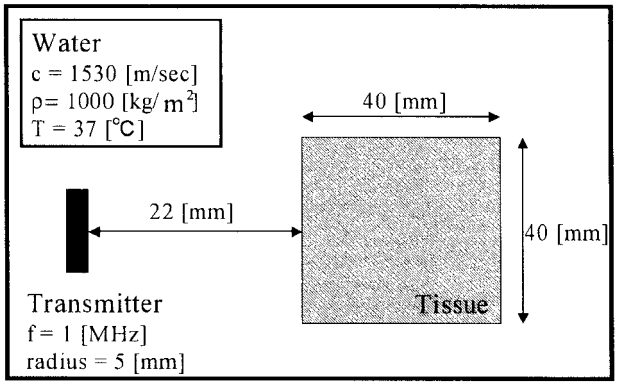

Fig. 1 Analysis model

Numerical Result

In general, eq. (4) shows that the temperature in tissue increases with heating value after the start of radiation. Because the quantity of diffused heat from the center to the outer boundary of tissue was counterbalanced with transmitted quantity of heat into water at the outer boundary, the temperature should reach the equilibrium temperature after a while.
When the C is 3500 J/kg•K, ρ is 1000 kg/m² and α is 0.8 dB/cm , maximum temperature in tissue and the equilibrium temperature caused by ultrasound is shown in Fig. 2 and 3 changing the thermal diffusivity coefficient from $0.9\cdot10^{-7}$•m²/s to $1.5\cdot10^{-7}$•m²/s.

Fig. 2 shows that the maximum temperature on the acoustic axis in tissue and equilibrium time as a function of thermal diffusivity κ.

Fig. 3 shows that the equilibrium temperature decrease with increasing thermal diffusivity because high temperature area was kept inside when thermal diffusivity is small.

Fig. 4 shows the temperature distribution in tissue at the thermal diffusivity of $0.9 \cdot 10^{-7} \cdot m^2/s$ and $1.5 \cdot 10^{-7} \cdot m^2/s$. It is shown that the effect of thermal diffusivity is little because of very short elapsed time in Fig. 4-(a). Fig. 4-(b) shows that the high temperature area spreads more extensively than in Fig. 4-(a). At the center of the tissue, the maximum temperature at thermal diffusivity of $0.9 \cdot 10^{-7} \cdot m^2/s$ is much hotter than that of $1.5 \cdot 10^{-7} \cdot m^2/s$ as shown in shown eq. (4).

Conclusion

The FDTD-HCE method had simulated temperature rise in phantom of soft tissue caused by absorption of ultrasound when the thermal diffusivity was changed. The result showed that equilibrium temperature at the center of tissue was higher when the thermal diffusivity was smaller.

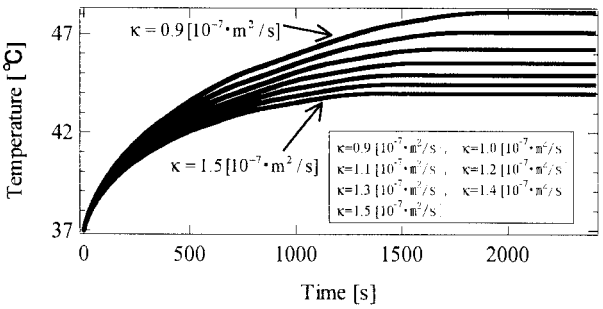

Fig. 2 Time vs. Maximum temperature in tissue

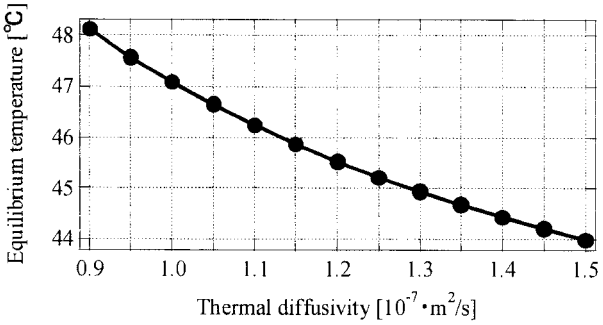

Fig. 3 Thermal diffusivity vs. Equilibrium temperature

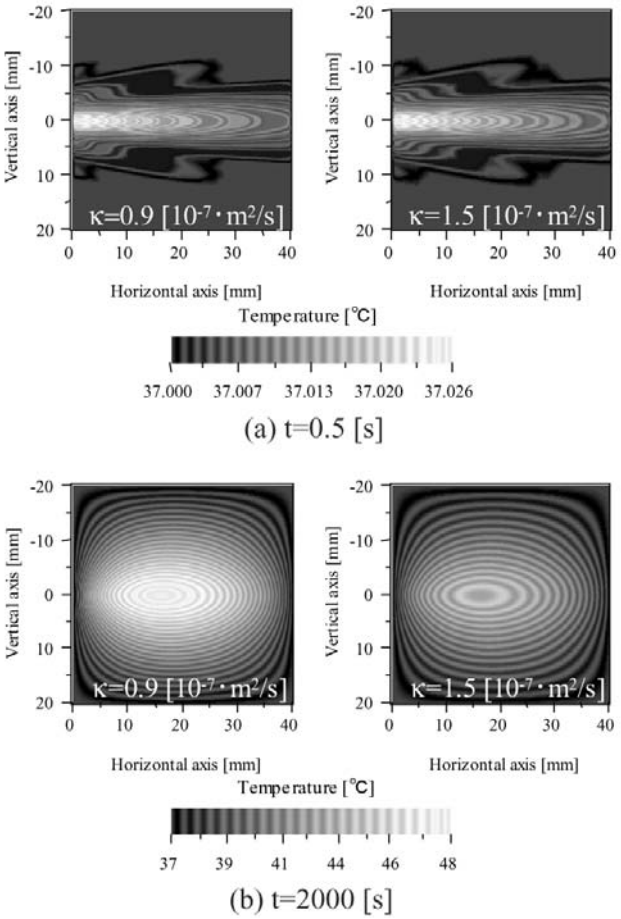

Fig. 4 Temperature distribution in tissue

Acknowledgment

This study was partly supported by High-Tech Research Center Project from the Ministry of Education, Culture, Sports, Science and Technology, Japan. Also this study was partly supported by a 2003 and 2004 Grand-in-Aid for Scientific Research from the Ministry of Education, Culture, Sports, Science and Technology (Grant No. 16500325 and 16500325), Japan.

References

1) F. Iijima, T. Tsuchiya and N. Endoh: Jpn. J. Appl. Phys. **39** (2000) 3200.

2) Y. Tanaka, T. Tsuchiya and N. Endoh: Jpn. J. Appl. Phys. **41** (2002) 3297.

3) K. Kubota, E. Ohdaira, N. Masuzawa and M. Ide: Jpn. J. Appl. Phys. **37** (1998) 3068.

4) H. Inoue, H. Yoshida: Proc. Spring Meet. The Acoust. Soc. Jpn. (2002) 1057 [in Japanese].

5) S. yoshida: *The basis of heat transfer science* (RIKOUGAKU PUBLISHING, TOKYO, 1999) Chap 2.

6) T.Uno: *Finite Difference Time Domain Method for Electromagnetic Field and Antennas* (CORONA PUBLISHING, TOKYO, 1998) Chap. 2, p. 68.

Proc. Symp. Ultrason. Electron., Vol. 25, (2004) pp. 283-284
27-29 October, 2004

Ultrasonic Rotary Motors Using Complex Transverse and Torsional Vibration Rods and Multiple BLT Transducers

Atsuyuki Suzuki, Masaki Kihara, Yasuhiro Katsumata, Naoki Kikuchi and Jiromaru Tsujino (Faculty of Engineering, Kanagawa University)

1. Introduction

Vibration and load characteristics of ultrasonic motors (A) using a torsional vibration cylinder with three bolt-clamped Langevin type longitudinal vibration PZT transducers (BLT transducers) installed in tangential direction and (B) using a longitudinal vibration disk with three BLT transducers installed around a circular disk are studied.

2. Configurations of ultrasonic motors

(1) Torsional vibration cylinder type ultrasonic motor (A)

The ultrasonic motor (A) using a torsional vibration cylinder with three BLT longitudinal transducers is shown in Fig.1. Three BLT longitudinal transducers (15 mm in diameter) are installed in tangential direction around the torsional vibration cylinder. And another BLT longitudinal transducer (30 mm in diameter) is installed in axial direction in the lower part of the torsional cylinder. A cylindrical rotor is installed at the free edge of the torsional cylinder under static pressure using center supporting rod and a pressure source using disk springs. The rotor is made of steel (SK-4) and pressed statically to a driving surface of the cylinder using the pressure source. Three 15-mm-diameter BLT transducers are driven under parallel connection using one SIT power amplifier in the same vibration phase. The 30-mm-diameter BLT transducer installed in the lower part of the cylinder is driven simultaneously in adequate phase difference to induce pressure dynamically to driving surface.

(2) Longitudinal vibration disk type ultrasonic motor (B)

The ultrasonic motor (B) using a longitudinal circular disk with three BLT transducers is shown in Fig.2. The ultrasonic motor (B) consists of a longitudinal vibration circular disk (149 mm in diameter and 32 mm in thickness), three BLT transducers (30 mm in diameter) and two complex transverse vibration rods (30 mm in diameter) installed normally in the center of the disk. The transverse vibration rods are installed in the both sides of the disk Three BLT transducers are installed along the outer circumference of the circular disk in symmetrical positions. Three BLT transducers are driven using an arbitrary waveform generator with variable vibration phase out put and three SIT power amplifiers in the phase difference of 120°.

3. Vibration of a center supporting rod for inducing static pressure

The center rod (bolt) for supporting the pressure source vibrates longitudinally and has some effect on the load characteristics of ultrasonic motor due to the fluctuation of static pressure by vibration. It is desired that the vibration is negligible and / or in a direction to induced pressure at driving surface during the period for driving the rotor. Figure 2 shows longitudinal vibration distribution along a 10-mm-diameter center supporting rod and bolt (stainless steel: SUS304). Longitudinal vibration of the center bolt was measured without rotor, spring and clamping nut. Vibration directions at the stator side and the free edge side are opposite each other.

And furthermore, longitudinal vibration of the free edge of the clumping nut was measured with a rotor, springs and a nut by changing the number of spacer (0 to 12). Thickness of the spacer is 1.6 mm. Longitudinal vibration was larger as the position of nut is nearer to the edge of the center bolt.

4. Load characteristics of the ultrasonic motors

Load characteristics of ultrasonic motors are measured al-

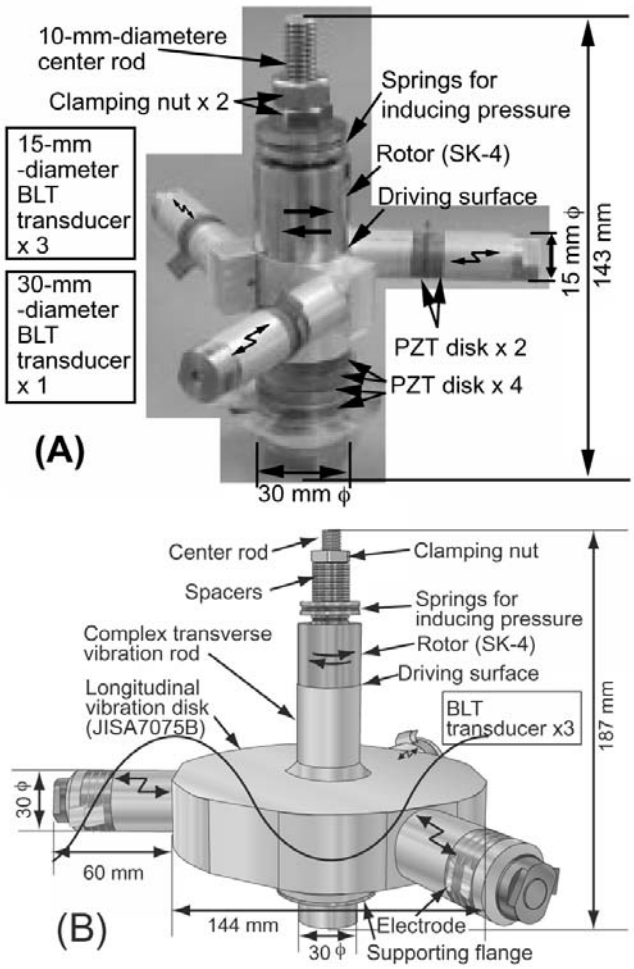

Fig. 1 . Configurations of ultrasonic motors (A) using three BLT transducers installed in rotating direction around a vibration cylinder and (B) using three BLT transducers installed around a circular disk.

E-mail address: suzuka27@kanagawa-u.ac.jp

tering load torque by a powder brake. Torque and revolution are measured by a torque meter and a rotation meter. Input power is measured by a power meter using a electric current probe and a current-voltage multiplier. Mechanical output power is calculated from torque and revolution values measured at various load torques.

(1) Load characteristics of the ultrasonic motor (A)

Figure 4 shows relationships between torque, revolution, electric input power, mechanical output power and efficiency of the ultrasonic motor (A) without spacer. Maximum torque, revolution and efficiency of the ultrasonic motor are 0.42 Nm, 30 rpm and 0.62 % with driving frequency of 29.2 kHz.

Figure 5 shows load characteristics of the ultrasonic motor (A) with 12 spacers. Maximum torque, revolution and efficiency of the ultrasonic motor is increased using the spacers and are 0.75 Nm, 93 rpm and 1.41 % with driving frequency of 30.1 kHz.

(2) Load characteristics of the ultrasonic motor (B)

Figure 6 shows load characteristics of the ultrasonic motor (B). Maximum torque, revolution and efficiency of the ultrasonic motor are 0.32 Nm, 84 rpm and 1.68 % at driving frequency of 40.4 kHz.

5. Conclusions

Vibration characteristics of a system for inducing pressure and load characteristics of two types of ultrasonic motors using a torsional vibration disk and a longitudinal vibration disk with three BLT transducers were studied.

Maximum torque, revolution and efficiency of the ultrasonic motor using torsional vibration cylinder (A) are 0.75 Nm, 93 rpm and 1.41 %.

Maximum torque, revolution and efficiency of the ultrasonic motor using circular disk (B), are 0.32 Nm, 84 rpm and 1.68 %.

The load characteristics may be better by increasing static pressure level and improving dynamic characteristic of the pressure sources.

References

1) J. Tsujino and A. Suzuki: Load Characteristics of Ultrasonic Motor with a Longitudinal-torsional Converter and Various Nonlinear Spring for Inducing Static Pressure, Proceedings of 2001 IEEE International Ultrasonics Symposium (2002.05) pp.545-550.

2) A. Suzuki and J. Tsujino: Load Characteristics of Ultrasonic Motors with a Longitudinal-Torsional Converter and Various Nonlinear Springs for Inducing Static Pressure Jpn. J. Appl. Phys, 41 (2002.05) pp.3267-3271.

3) A. Suzuki, M. Kihara, Y. Katsumata and J. Tsujino: Configurations of an Ultrasonic Motor Using a Circular Vibration Disk with Three Longitudinal Transducers, Proceedings of 5th WCU, World Congress on Ultrasonics (2003.11) pp.1585-1588.

4) A. Suzuki, M. Kihara, Y. Katsumata , Naoki KIKUCHI and J. Tsujino: Configuration of a Transverse Vibration Rod Type Ultrasonic Motor Using Three Longitudinal Transducers Driven in Three Different Vibration Phases, Jpn. J. Appl. Phys. Vol.43 (2004.05) pp.2901-2904.

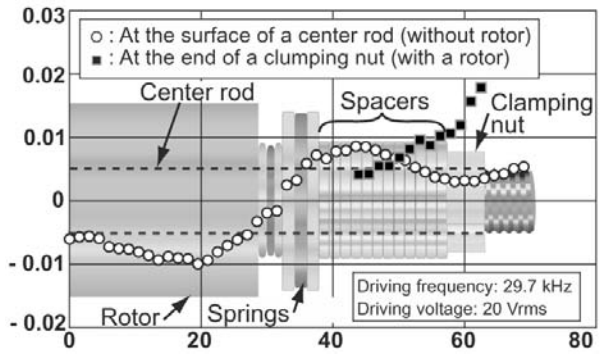

Fig. 2 . Longitudinal vibration distributions along a center bolt for inducing static pressure.

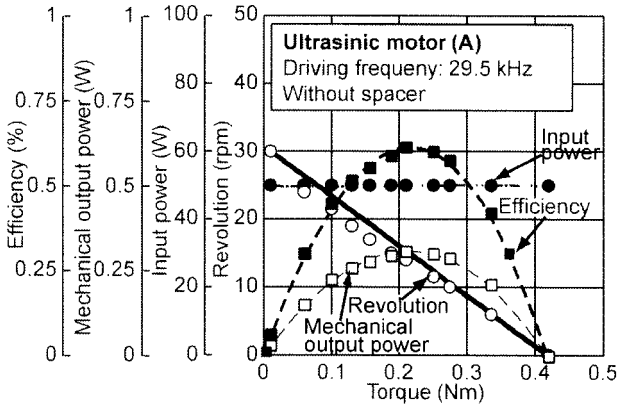

Fig. 3 . Load characteristics of the ultrasonic motor (A) using three BLT transducers installed in rotating direction around a vibration cylinder in the case where no spacer was installed.

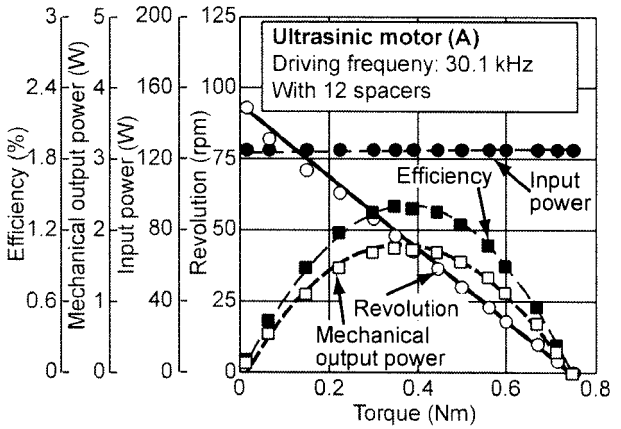

Fig. 4 . Load characteristics of the ultrasonic motor (A) using three BLT transducers installed in rotating direction around a vibration cylinder in the case where 12 spacers were installed.

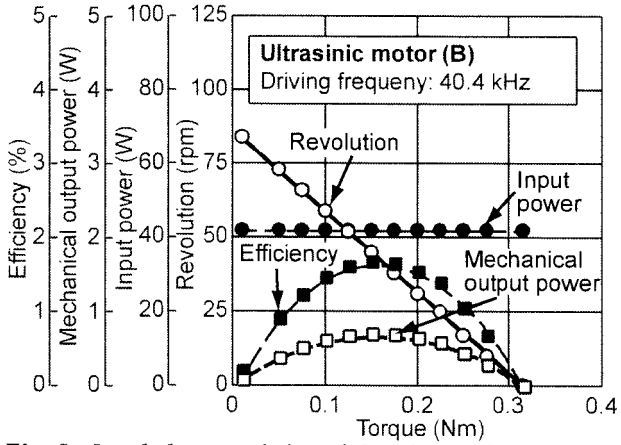

Fig. 5 . Load characteristics of the ultrasonic motor (B) using three BLT transducers installed around the circular disk.

Proc. Symp. Ultrason. Electron., Vol. 25, (2004) pp. 285-286
27-29 October, 2004

Visualization of Acoustically Induced Cavitation Bubbles and Microjets with the Aid of High Speed Camera

◎Takashi Kubo, Mamoru Kuwabara and Jian Yang (Dept. of Material Processing Eng. Nagoya University.)

Abstract

Water model experiments at a frequency of about 42 kHz have been performed to visualize dynamic behaviors of acoustic cavitation bubbles by using high speed digital camera. It is observed that clustered multi-bubbles linearly transfer toward random directions. The behavior of clustered bubbles is discussed in relation to the behavior of microjets as well as phase transition of water between a normal liquid state and a super critical-fluid state. Another experiment has also been carried out to visualize microjets that appeared near around a water/tetralin interface and a water/air interface. It found that a behavior of clustered multi-bubbles should stem that of micro-jets and the jets can give a strong impinge effect on the surfaces. Experimental findings in this paper, behaviors of cavitation bubbles and micro-jets, acoustic cavitation phenomena are quite important to understand and control for intensified macro and micro mixing of liquids.

1. Introduction

Acoustically induced cavitation phenomena in a liquid are expected to create a new engineering field named "Sonoprocessing of Materials". This processing may utilize the effects of macro and micro-mixing of liquids by microjets, cavitation bubble based internal vibration and primary sound waves, sonochemical reaction by instantaneous hot spots in the cavitation bubbles, and so on [1,2]. It is so important to understanding dynamic behavior of cavitation phenomena for utilization, but these phenomena are in their nature random. Lauterborn et al. [3,4] investigated the dynamics of a single bubble and filamentary structures of cavitation bubbles in liquids with high speed photography. However, the process of collapse of the bubbles is still unclear. In this paper, dynamic behaviors of multi-cavitation bubbles and microjets have been visualized by a high speed digital video camera and the results are investigated phenomenologically.

2. Experimental setup

The setup of the experiment for the visalization of cavitation bubbles and microjets are shown in Fig.1. A sinusoidal signal was generated and amplified using function generator and power amplifier. The electric output was fed to a bolted Langevine-type transducer to irradiate ultrasound into an acrylic resin vessel. The cylindrical acrylic resin vessel was filled with water or water at the upper phase and tetralin at the lower phase. Dynamic behaviors of cavitation bubbles and microjets were observed by a high speed digital video camera.

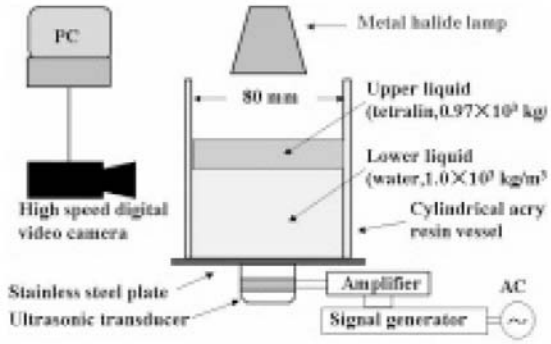

3. Result and discussion

3.1 Motions of clustered multi-cavitation bubbles

Figure 2 shows behavior and motion of clustered cavitation bubbles that were recorded by the high speed digital video camera. The imposed frequency is 42.6 kHz, the ultrasonic power (U.S.P) 60 W, and the water depth 70 mm. A frame size is of 30.9 mm by 26.0 mm, and shutter speed was 1/1000 s. Left side is a photograph of clustered cavitation bubbles and right side is a picture that shows trajectories of clustered cavitation bubbles. Clustered cavitation bubbles generate from loop of sound pressure and linearly moved in random directions with growing larger. At last they disappeared. The average velocities of the clustered cavitation bubbles were estimated to range from 0.2 to 0.8 m/s. The velocities correspond with that of microjets that were observed in other times.

Figure 3 shows a behavior of clustered cavitation bubbles near surface of liquid phase observed by the high speed digital video camera. The imposed frequency is 41.6 kHz, the ultrasonic power (U.S.P) 50 W, and the water depth 60 mm. A frame size is of 16.0 mm by 14.0 mm, and shutter speed was 1/1000 s. Clustered cavitation bubbles came close to the interface from below, and after impinging the interface, a water column was observed on the interface.

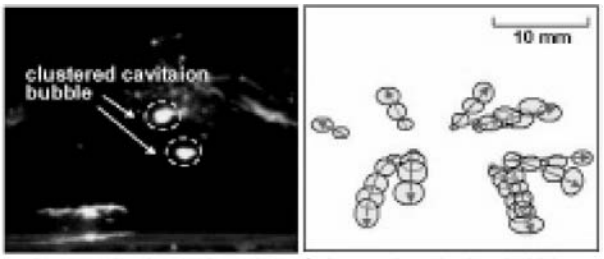

Fig. 2. Behavior and motion of clustered cavitation bubbles.

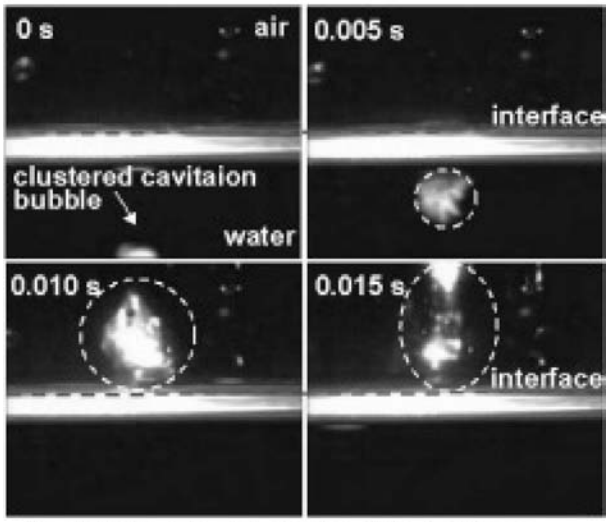

Fig. 3. Photographs of clustered cavitation bubbles near surface of liquid phase.

3.2 Motion of microjets around an interface of two liquid phases

Microjets visualized around an interface of two liquid phases are shown in Fig.4. The driving frequency is 42.3 kHz and U.S.P 15W. The frame size is of 13 mm by 7.8 mm and the shutter speed is 1/500 s. The test tube is filled with water at the upper phase and tetralin at the lower phase. The interface of two liquid phases in the test tube is placed around a node of a standing wave where limited numbers of microjets can be ejected. It can be observed that microjets are linearly ejected from several sites in random directions. They are accompanied by vortex motions of emulsified two liquids. It was found that helix angle is about 20 degrees and the average velocities are estimated to be about 0.4 m/s.

The above experimental results reveal that the velocities of clustered multi bubbles and microjets have the same order and they both move linearly. Thus, both behaviors should stem from the same phenomena. And, a result of Fig.3 shows that a hit of clustered bubbles make a water column, which confirms the existence of microjet. From these results, it is confirmed that clustered bubbles are accompanied by microjets. As a reason of generation of clustered bubbles, it is considered that a transformation of water in the cavitation bubble from super critical state to vapor during collapse of the bubbles. Because, critical point of water is 677.5 K and 226.8 atm, and temperature and pressure in the cavitation bubbles exceed critical point of water.

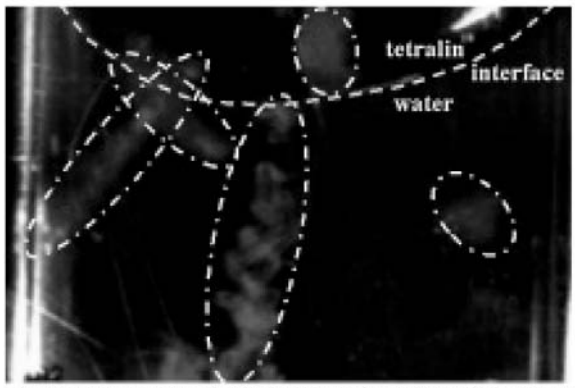

Fig. 4. Photographs of microjets near interface of two liquids.

4. Conclusion

In this paper, dynamical behaviors of cavitation bubbles and microjets were visualized by high speed digital video camera and investigated phenomenologically. It is considered that clustered bubbles move accompanied with microjets and is also considered that the clustered bubbles generate at the process of transformation from super critical state to vapor at cavitation bubble collapse. It is expected that the violent motions of cavitation bubbles and microjets can result an intensified micro and macro mixing of liquid those are included in "Sonoprocessing of Materials".

References

[1] Kuwabara, M., Hatanaka, S., Yamahira, S., Asai, S. and Sano M., "New possibility of ultrasonic processing of materials", *Proc. WCU*, 408-409, 1997.

[2] Kuwabara, M., Komarov, S., Sano M., "Sonoprocessing of materials in metallurgical systems", *Proc.8th Japan-China Sympo, Science and Technology of Iron and Steel,Chiba*, Japan, 175-181, 1998.

[3] Lauterborn W. and Ohl C.D., "Cavitation bubble dynamics", *Ultrasonic Sonochemistry, Vol. 4*, 65-75, 1997.

[4] Luther, S., Mettin, R., Koch, P., Lauterborn, W., "Observation of acoustic cavitation bubbles at 2250 frames per second", *Ultrasonic Sonochemistry Vol.8*, 159-162, 2001.

Proc. Symp. Ultrason. Electron., Vol. 25, (2004) pp. 287-288
27-29 October, 2004

Development and Evaluation of Electromagnetically Driven Wideband Ultrasonic Oscillator

◎Masashi Ohara, Takashi Kubo, Jian Yang, and Mamoru Kuwabara
(Department of Material Processing Engineering, Nagoya University)

Abstract

An ultrasonic oscillator, which electromagnetically generates ultrasound by vibration of an iron plate in the alternating magnetic field, is newly proposed for high temperature use. Low Curie point for a normal transducer made of piezoelectric material is overcome by use of a ferromagnetic iron plate that has a high magnetic Curie point (1043 K). The strain or the amplitude of the plate that is oscillating in a standing wave mode for a given working frequency is measured with the aid of a fiber vibrometer. The effects of various process parameters on the sound pressure and the vibration mode are investigated. Decreased distance between the vibrating plate and an induction coil as well as a selection of resonant frequencies are significantly effective to get an increased strain or a strong sound for a given set of electromagnetic operating parameters.

1. Introduction

In recent years, the present authors [1] have developed ultrasonic technologies for material processing, which is named to be "Sonoprocessing of materials". It is considered that various applied technologies in material processing [2], such as convection control of molten metal and inclusion removal in refining processes, dispersion of reinforced particles and orientation control of reinforced fibers in composite material engineering, can be developed by using the external force of an ultrasonic wave effectively. The transducers made of piezoelectric materials are usually used for generating an ultrasonic wave. But they cannot be directly used in a high temperature field because its Curie temperature is relatively low (about 600 K). An alternative way is possible by use of a ferromagnetic iron plate which has a high magnetic Curie temperature (C.P= 1043 K) and introducing liquid coolant in order to cool the steel plate below the Curie temperature. In this study, an ultrasonic oscillator, which electromagnetically generates ultrasound by vibrating a steel plate in an alternating magnetic field from an induction coil, is newly proposed. The strain or the amplitude of the oscillating plate is measured since the amplitude is in proportion to the pressure of sound to be generated. The effects of various process parameters on the sound pressure and the vibration mode are investigated.

2. Experimental setup

The experimental setup is shown in Fig.1. The alternating current, which was generated by a function generator and amplified with an amplifier, was fed to the induction coil that was wound around a steel pole to generate the alternating magnetic field. The ring type magnet for confining a magnetic field in the circumference of a coil (1000 numbers of turns, a height of 50 mm, diameter of 30 mm) was installed, and the iron oscillating plate with different thicknesses was horizontally attached on the ring magnet. According to the periodic change in the attractive force and the repulsive force of the generated alternating magnetic field and the magnetostatic field, the oscillating plate vibrates and a sound wave is generated. In order to investigate the vibration mode of the oscillating plate, the strain perpendicular to the plate was measured by a fiber vibrometer at the distance from the center of the oscillating plate, which was changed at intervals of 5mm. Measurement was also performed by changing the distance between the coil and the oscillating plate, the oscillating plate thickness, the fixed position of the oscillating

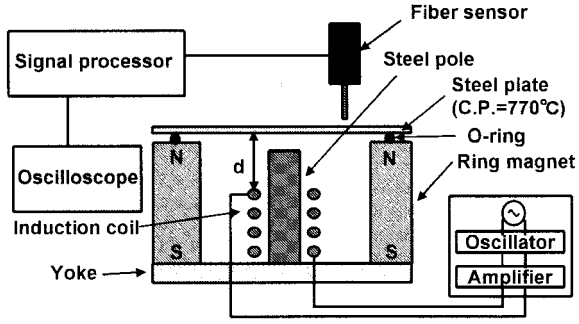

Fig.1 Experimental setup.

plate, frequency and the current value of alternating current power supply.

3. Results and discussion

The radial distribution of the strain perpendicular to the steel plate is shown in Fig.2. The imposed frequency was 3 kHz, and detected alternating coil current was 0.273 A. The distance between the plate and the coil was d=20 mm, and the thickness of the oscillating plate was 0.1 mm. From this figure, the wavelike radial pattern of the strain of the plate is observed. Some of the theoretically expected modes of vibration for a circular membrane are shown in Fig.3. The nomenclature for labelling the modes is ***(m,n)*** where ***m*** is the number of nodal diameters and ***n*** is the number of nodal circles and the colored areas are anti-phase to each other. The ***(0,1)*** mode has one circular node (the outside edge), but no diameter nodes exist and its displacement is centro-symmetrical. The ***(1,2)*** mode has one diameter node and two circular nodes and its displacement is axi-symmetrical. The ***(0,3)*** mode has three circular nodes, but no diameter nodes exist and its displacement is centro-symmetrical. Experimentally found pattern and the ***(0,3)*** mode agree with respect to the number of nodes. It is thus considered that this oscillating plate is likely to take this vibration mode.

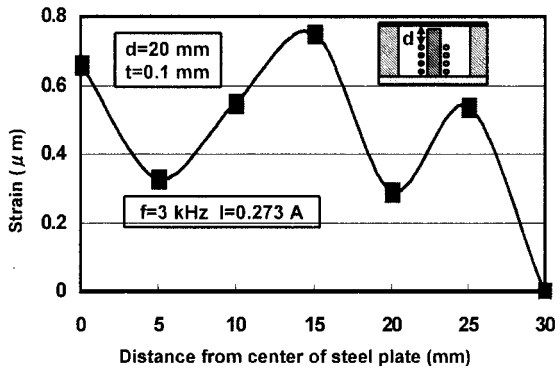

Fig. 2. Distribution of the strain at a working frequency of 3.0 kHz.

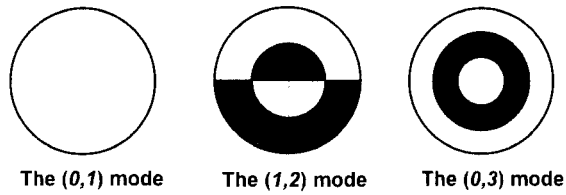

Fig. 3. Schematic views of vibration modes of circular membrane at free vibration.

The result when imposing the alternating voltage of 0.5 kHz to the induction coil is shown in Fig.4. The pattern of the strain is similar to the ***(0,1)*** mode. Comparing with the result of imposed frequency of 3 kHz, the strain has increased by dozens times. From this result, it is considered that the eigenfrequency of the oscillating plate is close to 0.5 kHz and resonance is caused. Moreover, the generating current value is also about 5 times as large as the result of imposing the frequency of 3 kHz. This result is caused by the decrease in the impedance of the circuit with decreasing the imposed frequency. Although the current value becomes low by decreasing the distance between the oscillating plate and the coil, the strain of the oscillating plate is increasing. It is considered that the increase in the electromagnetic power by the decrease of the distance between the coil and the oscillating plate is larger than the reduction of the electromagnetic power accompanied by reduction of a current value.

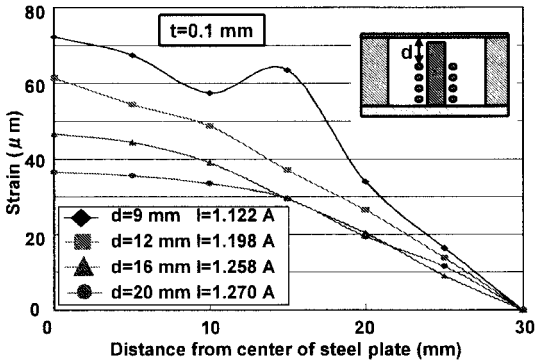

Fig. 4. Distribution of the strain at a working frequency of 0.5 kHz.

4. Conclusion

An ultrasonic oscillator, which electromagnetically generates ultrasound by vibration of a ferromagnetic plate in the alternating magnetic field, is newly designed. Due to a high magnetic Curie point (1043 K) of ferromagnetic iron plate, this ultrasonic vibrator can be utilized for high temperature use. Moreover, wideband frequency can be chosen compared with a case using piezoelectric transducer. The effects of various process parameters on the sound pressure and the vibration mode are investigated.

References

[1] M. Kuwabara et al.:International session, "Recent Innovation in Material Processes", CAMP-ISIJ, 16(2004)

[2] M.Kuwabara, et al.: Proc.8thJapan- China Sympo, Science and Technology of Iron and Steel,Chiba, Japan,1998, p.175.

Proc. Symp. Ultrason. Electron., Vol. 25, (2004) pp. 289-290
27-29 October, 2004

Temperature Distributions of Welding Specimens Using Various Frequency Ultrasonic Plastic Welding Systems

Misugi Hongoh, Masafumi Yoshikuni, Hiroyuki Miura, Yuji Koike, Tetsugi Ueoka and Jiromaru Tsujino (Faculty of Engineering, Univ. Kanagawa, Yokohama)

1. Introduction

Using 27 kHz to 94 kHz ultrasonic plastic welding systems, temperature rises at welding surfaces of 1.0-mm-thick polypropylene sheets are measured using thermo-couples inserted between sheet specimens and also temperature rise distributions at cross sections of the lapped sheet specimens are measured using a thermo-tracer. Maximum temperature measured was over 240 °C.

2. Welding equipments

The vibration systems used for plastic welding of 27, 40, 67 and 94 kHz consist of a longitudinal vibration source with a bolt-clamped Langevin type PZT transducer part and a stepped catenoidal horn with a welding tip of 8 mm diameter. The diameter of the 27 kHz longitudinal driving part is 40 mm and that of 40 kHz, 67 kHz and 94 kHz is 30 mm.

3. Measurements of temperature rise

The arrangements of temperature measuring systems using thermo-couples and a thermo-tracer are shown in Fig. 1 (1) and (2)Temperature rises at welding surfaces of 1.0-mm-thick polypropylene sheets are measured using 0.2-mm-diameter thermo-couples (T type, Copper-constantan) inserted between sheet specimens and also temperature rise distributions at cross sections of the lapped sheet specimens are measured using a thermo-tracer (TH5104) with an enlarging lens installed at near position of the weldment.

4. Welding characteristics and temperature rise at welding parts

(1) Weld strength

Relationships between frequency, vibration velocity and weld strength of two lapped 1.0-mm-thick polypropylene sheet specimens are shown in Fig. 2. Weld strength increases as vibration velocity increases, and larger weld strength is obtained as frequency increases at the same vibration velocity.

(2) Temperature rise at welding surfaces

Relationships between frequency, vibration velocity and temperature rises measured using thermo-couples of three lapped specimens are shown in Fig. 3. Measured temperatures of welding surfaces increases as frequency increases and measured temperatures near to the welding tip (upper part) are larger than that at lower part. Relationships between frequency, input power and temperature rise are shown

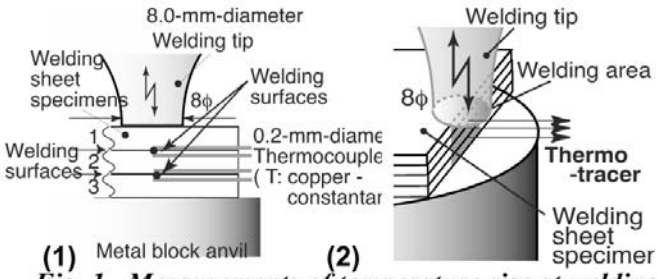

Fig. 1. Measurements of temperature rise at welding parts using (1)thermocouples inserted between welding surfaces and (2)a thermo-tracer.

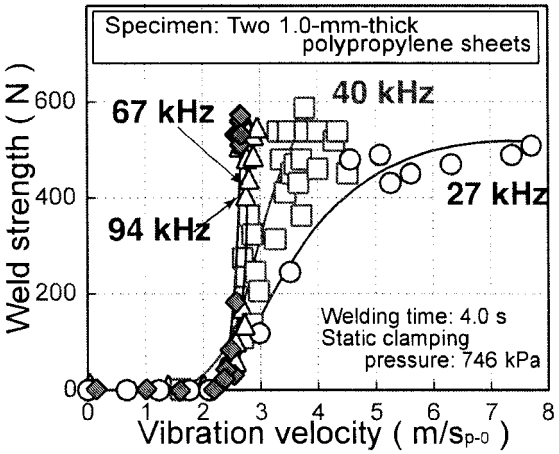

Fig. 2. Relationships between 27 kHz, 40 kHz, 67 kHz and 94 kHz welding tip vibration velocities and weld strength of lapped two 1.0-mm-thick polypropylene sheet specimens.

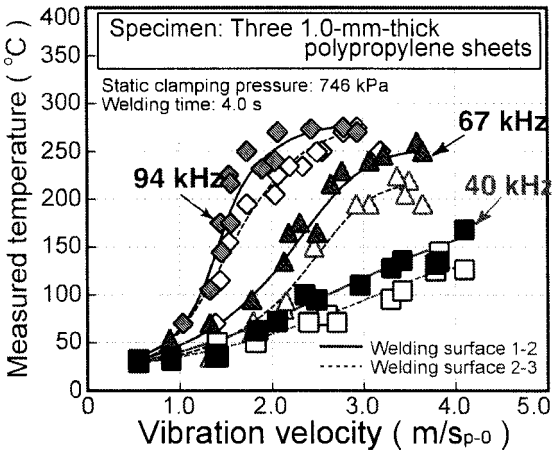

Fig. 3. Relationships between 40 kHz, 67 kHz and 94 kHz welding tip vibration velocities and temperature at welding surfaces of lapped three rise measured using thermo-couples 1.0-mm-thick polypropylene sheet specimens.

hongom02@kanagawa-u.ac.jp

in Fig. 4. Temperature rise increases as input power increases, and measured temperatures of the welding surface welded using 40 kHz and 64 kHz welding tips saturate and decreases adjacent to the end of the welding process.

(3) Temperature rise distributions at the cross sections of the weldments

Figure 5 shows the temperature rise distributions at the cross sections of two, three and four lapped polypropylene specimens welded using 44 kHz, 67 kHz and 94 kHz welding systems. Using the same vibration velocity, temperature rises and high temperature area are larger as frequency increases. Maximum temperature of these welding specimens measured using thermo-couples are over 280 °C and maximum temperature rises measured using a thermo-tracer are over 240 °C.

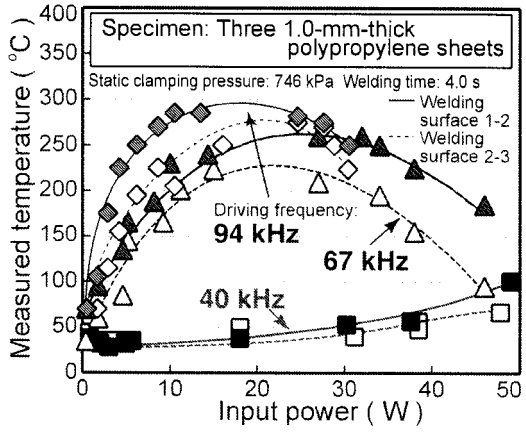

Fig. 4. Relationships between 40 kHz, 67 kHz and 94 kHz input power and measured temperature using thermo-couples at welding surface of 1.0-mm-thick polypropylene sheet specimens.

5. Conclusions

Using 27 kHz to 94 kHz ultrasonic plastic welding systems, temperature rises at welding surfaces and at cross sections of 1.0-mm-thick polypropylene sheet specimens were measured using thermo-couples and a thermo-tracer. Maximum temperature measured was over 240 °C.

References

[1] M. Hongoh, M. Yoshikuni, H. Hashii, T. Ueoka and J. Tsujino: Jpn. J. App. Phys. **42**, No. 5B (2003) 2981.

[2] M. Hongoh, M. Yoshikuni, H. Hashii, T. Ueoka and J. Tsujino: Proceedings of 5th WCU. (2003)439.

[3] J. Tsujino, M. Hongoh, M. Yoshikuni, H. Hashii and T. Ueoka: 2003 IEEE Ultrasonics Symposium (2003)680.

[4] J. Tsujino, M. Hongoh, M. Yoshikuni, H. Hashii and T. Ueoka: Ultrasonics. **42** (2004)131

[5] M. Hongoh, M. Yoshikuni, H. Miura, R. Miyamoto, T. Ueoka and J. Tsujino: Jpn. J. App. Phy. **43** No.5B (2004) 2896

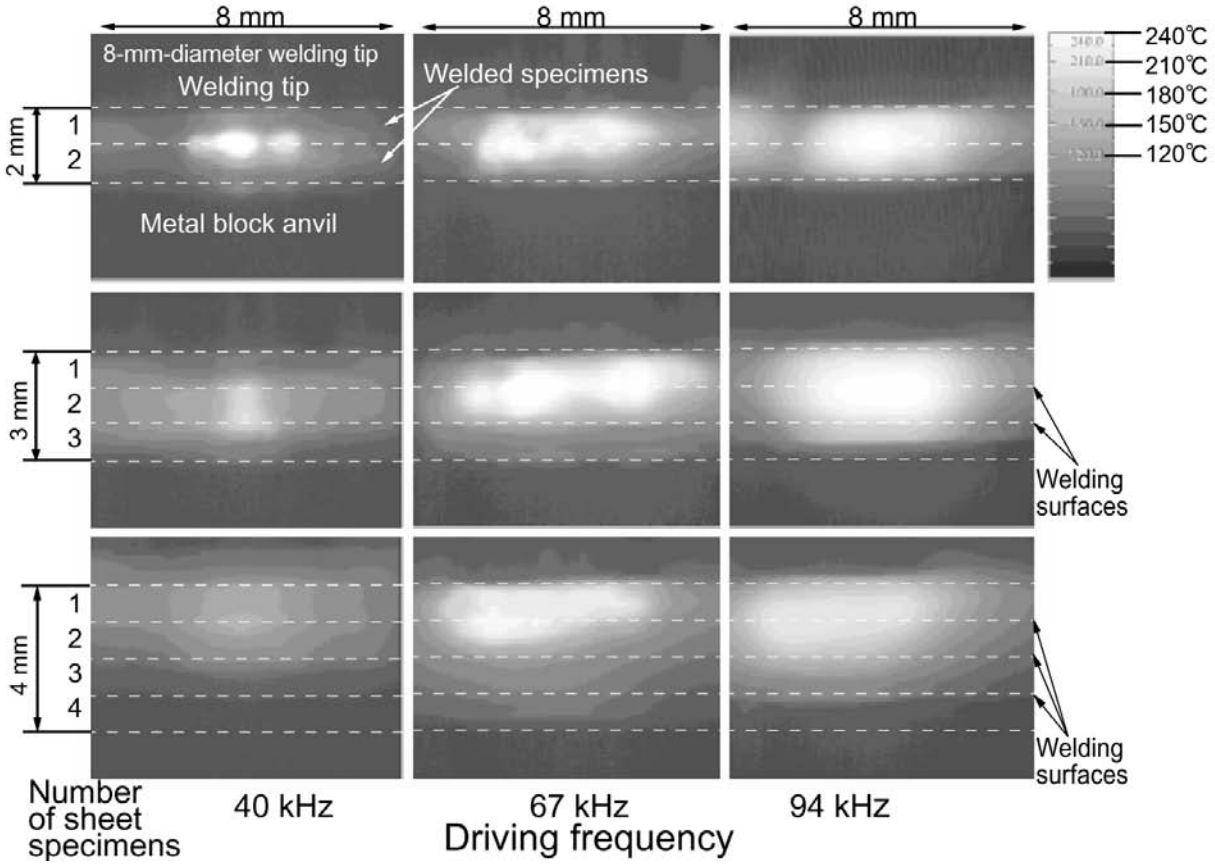

Fig. 5. Temperature rises measured using a thermo-tracer at cross sections of two to four 1.0-mm-thick polypropylene sheet specimens welded using 40 kHz ~ 94 kHz welding equipments. Vibration velocity: 2.7 m/sp-o. Static clamping pressure: 746 kPa. Welding time: 4.0 s.

Proc. Symp. Ultrason. Electron., Vol. 25, (2004) pp. 291-292
27-29 October, 2004

VHDL Description and Simulation of a High Resolution Control System for Linear Ultrasonic Motors

Cesar Rodrigues[1], Rafael Pippi, André Aita and João Martins (UFSM, PPGEE)

1. Introduction

Ultrasonic Motors are devices with micro or even nano-positioning capabilities [1,2], but to accomplish fine positioning, a high resolution control system is required. Since the motor characteristics may change with time, friction conditions, temperature and other parameters [5], an identification of best driving conditions is desirable. This paper presents simulated results from a VHDL implemented adatative micro-positioning control system for linear traveling wave ultrasonic motors (TWUSM). The controller uses motor dynamic characteristics [3] for estimating the exact slider end positioning point in a limited range from real time acquired data, ajuststing its internal parameters to follow the motor parameters changes.

2. Implemented control rules

The proposed control system implements several important features for TWUSM positioning applications, such as:

- ? Identification of the allowed slider displacement range;
- ? Identification of instantaneous speed at each position reading;
- ? Prediction of wait time to the next position;
- ? Estimation of the stop position and the input turn-off time that leads the slider at this point;
- ? Identification and updating of alpha parameter (falling linear coefficient);
- ? Three displacement categories: coarse, fine and one step mode, according to required speed and resolution.

The slider displacement range is divided in 256 positions: two safety sub-ranges with 32 steps each, and a central region with 192 steps, so called "working range".

3. A general description of the control system

The controller implemented in this work applies, in a general way, to any type of linear TWUSM. Control rules adaptation to the motor cha[1]racteristics is made by identifying some of its parameters, as linear falling speed response (alpha coefficient) when driving energy is switched-off.

The system identifies an movement requisition and starts to drive the motor to the target position. Motor parameters are computed during the movement, and then a displacement category is selected concerning the distance from current position to target position and alpha coeficient. When the controller identifies the "estimate stop position", it turns off the input voltage and the axis continues to slide till it stops. The speed and acceleration values acquired during the displacements are employed to compute and actualize the alpha coefficient. The first approach of alpha is used by controller to a possible operation in the fine mode.

Since friction coefficient may change along the displacement range [4], some small positioning errors may occur, typically one or two encoder positions. In the final position approach, the system assumes "one step" operation mode. In this mode, the input pulse width for the exact positioning is determined from the parameters calculated in recent driving cycles. This mode is a particular case of the fine mode and it is enabled when the current possition differs to target position from one or two encoder pulses.

4. Results and discussion

The control system logic was tested with ModelSim 5.6a©, in MentorGraphics© environment using a simulated linear TWUSM. The controller response in representative working conditions is described below.

In order to allow the motor to execute displacements requisitions correctly, the input driving voltages must be applied. This condition is represented by the state variable labeled "power", when assumes logic state 1. If logic variable "direction" is equal to 1, it means that the slider will move to the right. Logic variable "movement"

[1] cesar@smail.ufsm.br

defines the motor driving mode (coarse, fine and "one step"). The variable "task_flag", set to 1, inhibits any other positioning commands during a positioning task.

As showed in **Fig. 1**, when the controller identifies the "position" 223, it cuts off the input voltages by reseting the state of "power". As the system did not compute "alpha" yet (first movement), it could not preview the correct instant to switch off the input power that leads the slider to programmed final position. After the inputs are turned-off, motor speed will decrease till it stops at 226 encoder position (instant A), while "alpha" is calculated (.0.274251) from past speed values. As the slider stops at position 226, that differs by three steps from programmed position 223, controller could not enter the "one step" mode. Thus, the controller drives the motor again in the fine mode, but in the opposite direction (power=1, direction=0).

By using "alpha", each time a new "position" value is received, the controller will compute a new value for the variable "estimate", which contains the hypothetical stopping position 222 if the power was turned-off immediately. As position 222 differs only by one step from the programmed value 223, the controller automatically operates in "one step" mode (instant B, Fig.1). In this mode, the power is switched on and off (burst modulation) till the slider hits the right position. This logic sequence is executed each time a new positioning command is entered.

5. Conclusions

Simulated results obtained from a VHDL description of a dedicated control system for ultrasonic motor micro-positioning are presented and discussed. The controller is designed to drive any TWUSM in three different modes: coarse, fine and "one step". Timing diagrams describing controller inputs and outputs indicate a correct operation for every operation mode, summarizing its successful operation. Several critical situations have been simulated for different TWUSM characteristics, and the controller was always capable of positioning the slider at the exact programmed position. Thus, the positioning resolution of this system depends mainly from the encoder resolution.

Acknowledgment

This work was supported by CAPES and by MentorGrahics® High Education Program.

References

1. K. Hirata and S. Ueha. IEEE Trans. on Ultras. Ferr., and Freq. Control, **42** (1995) 225.
2. C. Rodrigues at al. 18th Symp. on Microelectronins Technology and Devices, **09** (2003) 453.
3. K. Nakamura et al. IEEE Trans. on Ultras. Ferr., and Freq. Control, **38** (1991) 481.
4. T. Ishii and al. Jpn. J. Appl. Phys. **34** (1995) 2765.
5. D. Bai et al. IEEE Trans. on Ultras. Ferr., and Freq. Control, **51** (2004) 680.

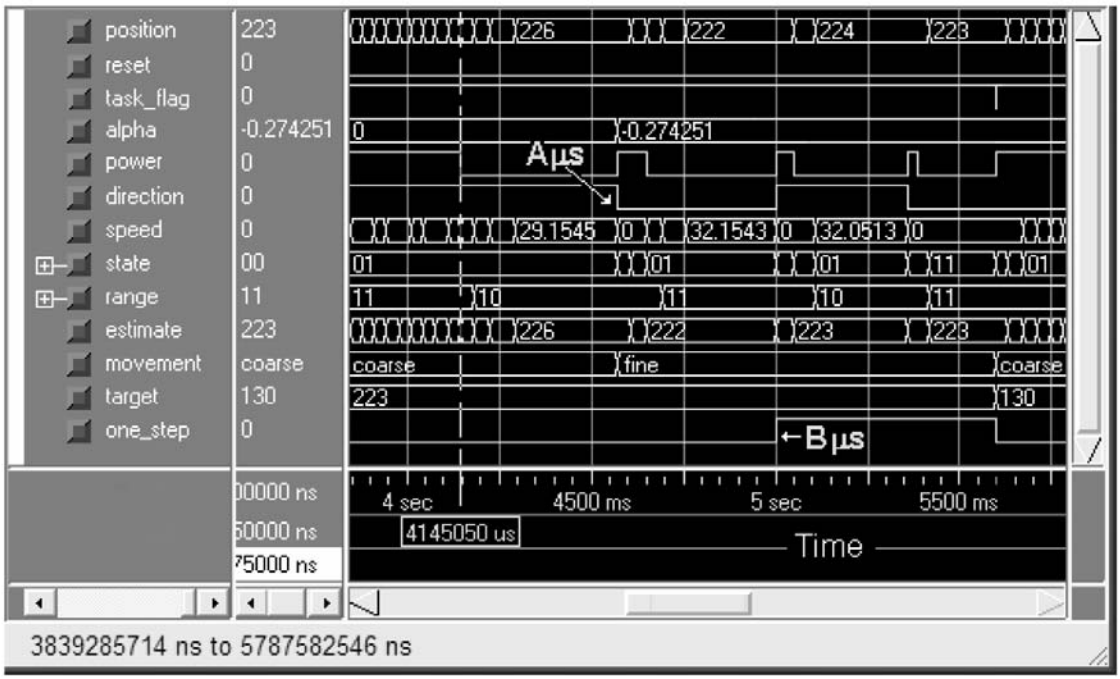

Fig. 1 Typical operation sequence for a positioning command.

Proc. Symp. Ultrason. Electron., Vol. 25, (2004) pp. 293-294
27-29 October, 2004

The underwater sound propagation on and around a seamount -preliminary results-

Yoshihisa Hiyoshi* (AESTO), Jun Naoi, Toshio Tsuchiya, Toshiaki Kikuchi (JAMSTEC)

1. Introduction

Interactions between the sound energy in the water column and the underneath ocean bottom layers play significant roles in changes of its traveling manner. In the coastal area, thick sediment layers could modify the pattern of the sound propagation in the water column[1]. In the open water, scaterring at prominent ocean bottom topography, such as a seamount, effects on the sound propagation in both 2-D and 3-D scales[2)3)4)5)].

Previous research, however, paid less attention to sound fields just around seamounts than to changes of the travel paths in the long-distance sound propagation.

One of the purposes of this research is to investigate and model the 3-D low frequency sound distribution around a seamount. The parabolic equation (PE) method is applied to the 3-D numerical simulation[6)] having flat seabottom and modelled seamount on the bottom.

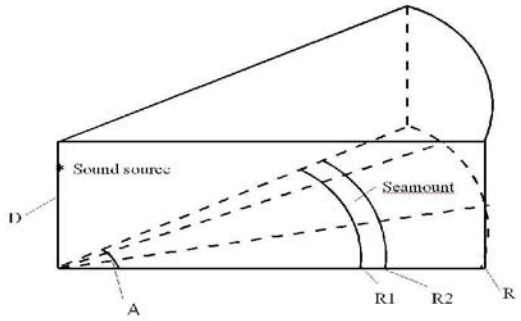

Fig. 1 The region of the 3-D calculation.

2. Experiments and results

We applied the PE method to 3-D numerical simulations to clarify the 3-D sound distribution around a seamount. **Fig. 1** shows the region of the 3-D PE simulation. It is a cylindrical coordinate having the region of the max horizontal range (R) 400 km and the angle (A) 10 degrees. The constant water depth (D) is 5500 m. Below the bottom of the water column, the absorbing layer (the thickness is 1000 m) is attached.

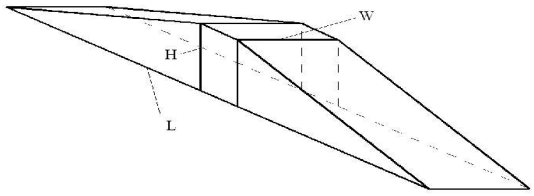

Fig. 2 The shape of the modeled seamount

Fig. 2 illustrates the shape of the modeled seamount, having the height (H) is 3500 m, the length (L) 48 km and the width (W) 10 km. The seamonut is located on the flat bottom between the ranges R1 and R2 in Fig. 1. One vertical sound profile is applied to the whole experimental region in Fig. 1. The horizontal calculation step is 5 m and the vertical step is 5 m.

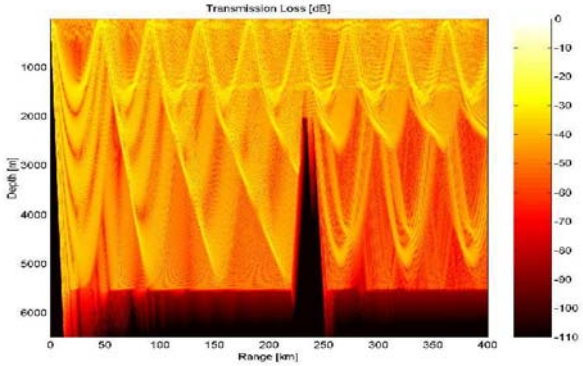

Fig. 3 The depth-range slice of the 3-D sound propagation (Transmission Loss in dB)

Fig. 3 represents a range-depth slice of the result of the 3-D simulation (Transmission Loss(TL) in dB). The sound source at depth of 100 m emits 100 Hz continuous signals.

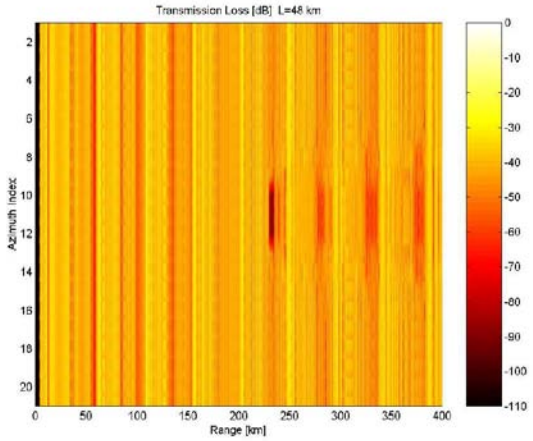

Fig. 4 The horizontal slice (2000 m depth) of the 3-D simulation result

Fig. 4 demonstrates the distribution of the transmission loss at the horizontal depth slice of around 2000 meter, being about the same depth of the top of the seamount. Figures 4 & 5 show that scattering at the seamount causes complex patterns of traveling sound around the seamount. In Fig. 4, the disturbance of the signal by scattering at the seamount is just behind the seamount and reaches even at the range of 400 km.

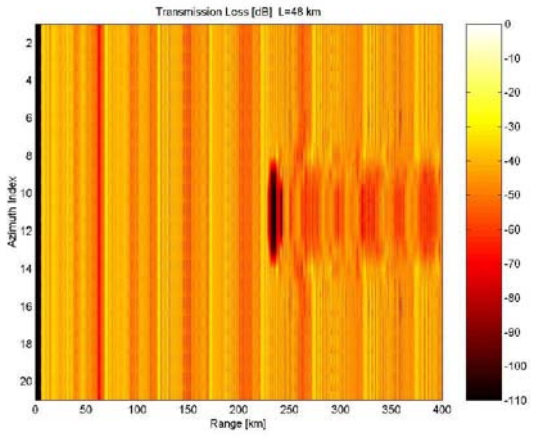

Fig. 5 The same figure as Fig. 4, but the depth of the slice is 3000 m

Fig. 5 maps the horizontal distribution of the transmission loss at the depth of 3000 m. The disturbance of the transmission loss behind the seamount has much stronger values and more complex patterns than the 2000m depth case. In particular, the area between the ranges of 230 km and of 280 km has the complex pattern of the disturbance.

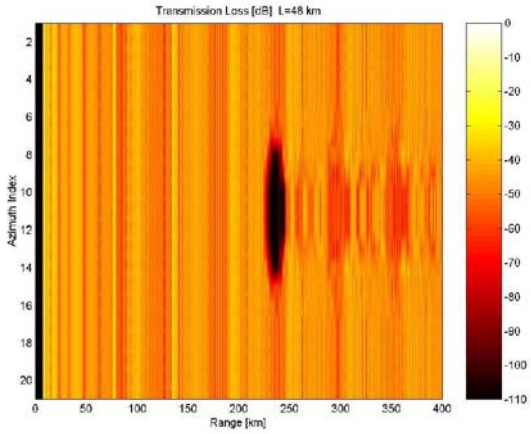

Fig. 6 The same figure as Fig. 4, but the depth is 4000 m

Fig. 6 shows the distribution of the transmission loss at the horizontal depth slice of around 4000 m. The weker and somehow regular pattern of the TL is observed in the range of 230 km to about 400 km than Fig. 5. This is probably because the less amount of sound energy could penetrate to the depth of 4000 m than the 300m case.

3. Conclusions

We performed the 3-D numerical experiment of low-frequency underwater signals (100Hz) interacting with a seamount in its traveling path. Our preliminary results shows that the 3-D pattern of the TL disturbance by scattering at the seamount is complex. To clarify more detailed patterns of the disturbance, it is worth while using pulse-like input signals for the same experiments. In addition, we should focus on back-scattering in the future experiment, because the PE method ignores the term of the back-scattering effect.

4. References

1)M.D. Collins, *J. Acoust. Soc. Am.,* 84, 2114-2125, (1988).

2）N.R. Chapman and G. R. Ebbeson, *J. Acoust. Soc. Am.,* **69(**S1), S59,(1981).

3）G. R. Ebbeson and R. G. Turner, *J. Acoust. Soc. Am.,* **73(**1), 143-152, (1983).

4）N.R. Chapman and G. R. Ebbeson, *J. Acoust. Soc. Am.,* **73**(6), 1979-1984, (1981).

5） D. R. Burns, *J. Acoust. Soc. Am.,* **92**(5), 2784-2791,(1992).

6) D. Lee and M. H. Schultz, *Numerical Ocean Acoustic Propagation in Three Dimensions*, (World Scientific, Singapore, 1995).

Proc. Symp. Ultrason. Electron., Vol. 25, (2004) pp. 295-296
27-29 October, 2004

Neural Network Application for Ship Radiated Noise

○ Kyu-Chil Park and Jong-Rak Yoon (Pukyong National University, KOREA)
Phil-Ho Lee (Agency for Defense Development, KOREA),

1. Introduction

The ship radiated noise appear the various characteristic signals due to the mechanic system in the ship, the propeller and the interaction between ship body and sea water. Generally, it is classified the speed dependent signal from the propeller and the speed independent signal. Therefore, it is required that very complex procedure to classify the signal origin from the ship-radiated noise.
This paper presents techniques using the neural network to detect and classify the tonal signals from ship-radiated noise.

2. Auto detection of tonal signal

Fig. 1 shows an example of line spectrum and LOFAR gram from ship-radiated noise. There are many tonal signals in LOFAR gram. It is required to classify what tonal signal is important and what origin of tonal signal is.
In this paper, we approach the study as following: 1) the analysis of spectrum and LOFAR gram, 2) the reinforcement of continuous tonal signal in LOFAR gram, 3) fix threshold for selection of meaningful tonal signal, 4) classify of tonal signal using pattern recognition technique.
At first, we apply a neural network to reinforce of the tonal signals in LOFAR gram, as shown Fig 2.

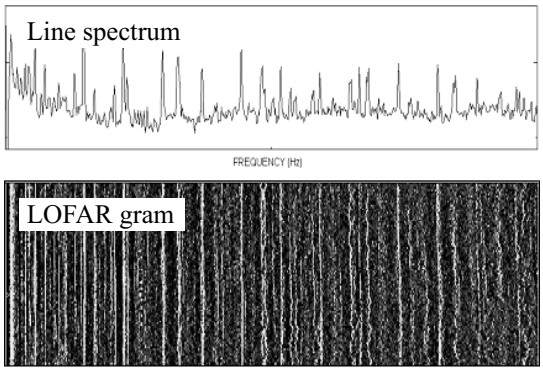

Fig. 1 An example of line spectrum and LOFAR gram from ship-radiated noise.

E-mail : kcpark@pknu.ac.kr

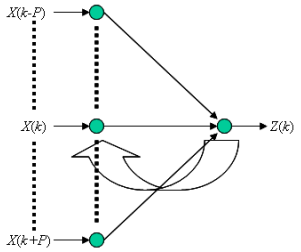

Fig. 2 A neural network system for reinforcement of the tonal signals.

As the tonal signals are sometimes observed in discontinuous lines, it is required to connect the tonal signals in time frame. Therefore, it consists of an input, an output, and a feedback input from the previous network output. The middle output $Y_t(k)$ in time t of the neural network is given as

$$Y_t(k) = \sum_{i=-P}^{P} W(i)\, X_t(i) + \alpha Z_{t-1}(k) \qquad (1)$$

where, W is the weighting between input layer and output layer, α is a feedback transmission coefficient, Z_{t-1} is a network output in a previous frame. The feedback transmission coefficient is chosen 0.7. The weighting is given 1 at a center frequency, others are given –1/2P. The output of a network is given as

$$Z_t(k) = \begin{cases} 1, & Y_t(k) \geq 1 \\ Y_t(k), & 0 < Y_t(k) < 1 \\ 0, & Y_t(k) \leq 0 \end{cases} \qquad (2)$$

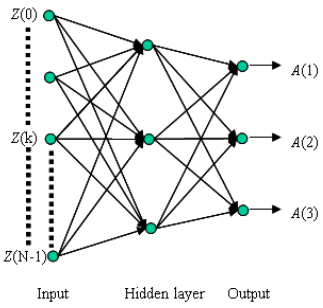

Fig. 3 A neural network system to classify of tonal signals.

Secondly, we apply another neural network system to classify of tonal signals using pattern recognition technique, shown as Fig. 3. It consists of an input layer, a hidden layer, and an output layer. The expected results of the output layer are the speed dependent signal, the speed independent signal, and none signal. Fig. 4 shows some examples of input patterns for the network's training.

Fig. 4 Some examples of input patterns for the network's training : (a) speed dependent signal, (b) speed independent signal, (c) none signal.

3. Numerical experiment and results

Fig. 5 shows the result of the reinforcement of the tonal signals in LOFAR gram using Eq. (2). The result shows more clear and connective than LOFAR gram.

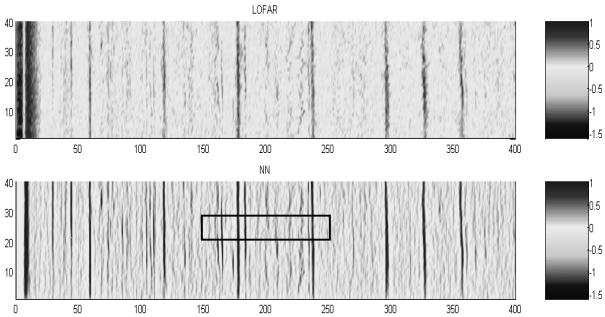

Fig. 5 The result of the reinforcement of the tonal signals in LOFAR gram.

Input patterns	Outputs $A(1)$ $A(2)$ $A(3)$	Judgments
	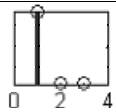	speed dependent signal
	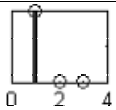	speed dependent signal
	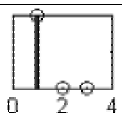	speed dependent signal
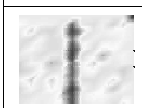	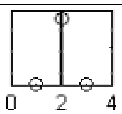	speed independent signal
	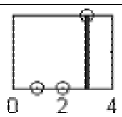	none signal

Fig. 6 Simulation results of the classification of the tonal signals.

Fig. 6 shows simulation results of the classification of tonal signals using pattern recognition technique. Input signals for simulation are added 20% white noise in the input patterns of Fig. 4. From the no error results, the expected results are obtained.
Fig. 7 shows the results of the classification of real application, shown the rectangular area in Fig. 5.

Input patterns	Outputs $A(1)$ $A(2)$ $A(3)$	Judgments
	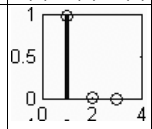	speed dependent signal
	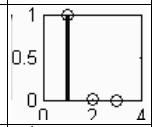	speed dependent signal
	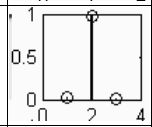	speed independent signal
	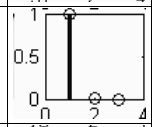	speed dependent signal (incorrect)
	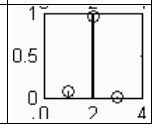	speed independent signal

Fig. 7 Some results of the classification of the tonal signals.

4. Conclusions

This paper presents techniques using the neural network to detect and classify the tonal signals from ship-radiated noise. The results of the reinforcement of the tonal signal of LOFAR gram show more clear and connective than LOFAR gram. And we obtained the reasonable results of the classification of tonal signals using the pattern recognition technique in simulation and real application besides of some incorrect classification.

Acknowledgment

This work was supported by STX RadarSys Co., Ltd. and the Brain Busan 21 Project 2003.

References

1. Thmos L. Hemminger, Yoh-Han Pao: IEEE **5** (1994) 712.
2. Chu-Kuei Tu, Huang-Chia Huang: Underwater Technology (1998) 253.
3. Howard Demuth and Mark Beale: *Neural Network Toolbox* (the Math Works Inc., 2003).

Proc. Symp. Ultrason. Electron., Vol. 25, (2004) pp. 297-298
27-29 October, 2004

Phase transitions in [001]-oriented PMN-PT single crystal with compositions near the morphotropic phase boundary

○Ghulam Shabbir* and Seiji Kojima (Uni. Tsukuba, Inst. Mat. Sci.)

1. Introduction

The complex perovskite lead magnesium niobate, $Pb(Mg_{1/3}Nb_{2/3})O_3$ (PMN), is one of the most important prototype relaxor material, which have low aging, superior coupling, high dielectric constant and a high charge constant. Relaxors are characterized by quenched disorder on B site and show a diffuse phase transition with a broad and frequency dependent dielectric response peaked at the temperature T_m and electrostatic behaviour where strain varies non-linearly. These materials are used for hydrophones, actuators, receivers, projectors, sonar transducers and in micro-positioning devices. Phenomenologically, the so-called polar micro regions (PMRs), first proposed by Burns and Docal [1] are still at the core of physical models.

PMN forms solid solution alloys (PMN-PT) with lead titanate. This system shows significant enhancement in permitivity and piezoelectric properties near morphotrophic phase boundary (MPB) between rhombohedral (*R*3*m*) and tetragonal (*P*4*mm*) structures [2] similar to that of $PbZrO_3$-$PbTiO_3$ (PZT) system. Single crystals of PMN-PT with a composition near the MPB are technologically important due to their excellent electromechanical properties, with a very high piezoelectric constant (d_{33} >2500 pC/N), large electromechanical coupling factor (k_{33} >94%, and high strain levels (1.7%) [3]. A relaxation mode was reported [4] but acoustic anomaly between *R*3*m* and *P*4*mm* could not be observed clearly. In countinuation of our previous work [5, 6], here we report detailed investigations of PMN-PT [001]-oriented MPB single crystal (grown by modified Bridgman method) by the high-resolution Brillouin scattering and dielectric susceptibility meaurements.

2. Experimental

A 3+3 pass tandem Fabry-Perot interferometer was used to measure the Brillouin spectra by employing the right-angle (90A) and the backward scattering geometries. A [001]-oriented PMN-PT single crystal plate of approximate dimensions 10×10×2 mm^3, polished to optical quality, was fixed in a ceramic sample holder and placed inside a tube-furnace for right-angle scattering experiments. In the backward scattering geometry, the crystal was put inside a cryostat cell (THMS 600) placed on the stage of an optical microscope. A single mode Ar^+-ion laser with a wavelength of 514.5 nm at a power of ~100 mW was used for the excitation of phonon modes. Measurements were done from room temperature to ~400 °C. Dielectric permittivity was measured by using a Solartron impedance analyzer (SI1260).

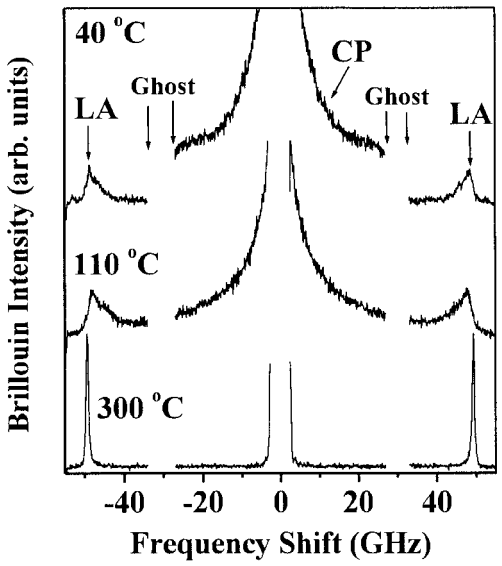

Fig.1. Typical micro-Brillouin spectra of [001]-oriented PMN-PT single crystal at some selected temperatures.

* E-mail: shabbir@ims.tsukuba.ac.jp

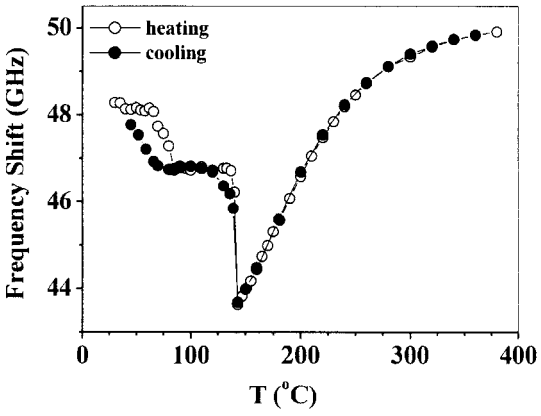

Fig. 2. Temperature dependence of frequency shift of the longitudinal acoustic phonon mode of PMN-PT [001] MPB composition, measured in the micro-Brillouin scattering geometry.

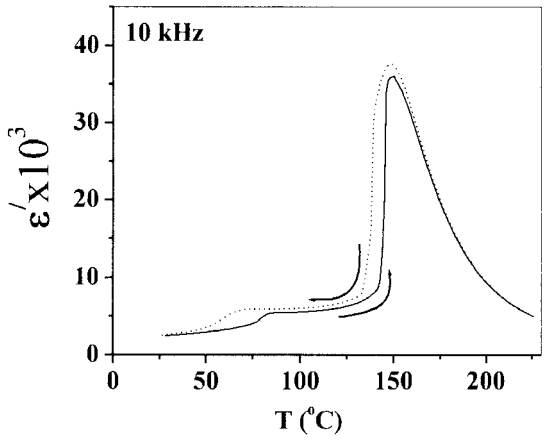

Fig.3. The real part of the complex dielectric constant of a PMN-PT [001] single crystal.

3. Results and discussion

Figure 1 shows typical Brillouin spectra of PMN-PT MPB [001] single crystal at some selected temperatures taken in the backward scattering geometry. A longitudinal acoustic (LA) mode along with a strong quasielastic central peak (CP) was observed in this geometry. The Brillouin frequency shift (ν) calculated from these spectra have been plotted as a function of temperature for heating and cooling runs (**Fig. 2**). The temperature variation of the damping factor (full width at half maximum) also exhibited similar sequence of acoustic transition anomalies. The existence of different structural anomalies can be clearly differentiated from these data.

A first order phase transition occurred at T~142 °C from paraelectric cubic ($Pm\bar{3}m$) to ferroelectric tetragonal ($P4mm$) phase transition and with further cooling, second transition instability appeared at T~75 °C, at tetragonal to rhombohedral transition temperature. As can be visualized from Fig. 1 (and also from separate measurements with larger free spectral range (FSR)) the CP intensity increased first with maximum around 70±10 °C and then started decreasing with further rise in temperature until it disappeared at T~200 °C. In the spectra obtained by using the right angle scattering geometry, one LA and one transverse acoustic (TA) mode were observed. The temperature dependence of the frequency shift and the damping showed both anomalies clearly (**Fig. 2**).

The dielectric susceptibility also exhibited the two transition anomalies showing hysteresis at the tetragonal to rhombohedral transition temperature (**Fig. 3**).

Acknowledgment

This work was supported in part by 21st Century COE program under the Japanese Ministry of Education, Culture, Sports, Science and Technology. One of the authors (G. Shabbir) is thankful to the D. G. PINSTECH, Islamabad Pakistan for grant of study leave, and Japanese Government, for a MONBU-KAGAKUSHO scholarship.

References

1. G. Burns and F. H. Docal: Solid State Commu. **48** (1983) 853.
2. S.-E. Park and T. R. Shrout : J. Appl. Phys. **82** (1997) 1804.
3. J. Kuwata, K. Uchino, and S. Nomura: Jpn. J. Appl. Phys. Part I **21** (1982) 1298.
4. F. M. Jiang and S. Kojima: Phys. Rev. B **62** (2000) 8572.
5. G. Shabbir and S. Kojima: Ceram. Int. **30** (2004) 1707.
6. G. Shabbir and S. Kojima: IUMRS-ICAM, Yokohama, Oct. (2002).

Proc. Symp. Ultrason. Electron., Vol. 25, (2004) pp. 299-300
27-29 October, 2004

Evaluation of ice films by picosecond acoustics

◎Saori Kashiwada, Osamu Matsuda, *Jeremy J. Baumberg, and Oliver B. Wright
(Graduate School of Engineering, Hokkaido University, *School of Physics and Astronomy, University of Southampton, U. K.)

1. Introduction

Thin sub-micron films can be conveniently studied using a non-contact and nondestructive method known as laser picosecond acoustics in which ultrashort light pulses generate and detect ultrasonic pulses in the frequency range ~10-1000 GHz [1,2]. This technique has been applied to transparent films on opaque substrates for purposes of thin film thickness and sound velocity measurements [3]. Here we extend this method to derive not only the thickness and sound velocity, but also to probe the ultrasonic attenuation coefficient of the film that is highly sensitive to the film structure. We apply the method to the in-situ monitoring of the growth process of polycrystalline ice films.

2. Experiment

The experimental arrangement is shown schematically in **Figure 1 (a)**. A 800 nm opaque YBCO ($YBa_2Cu_3O_{7-\delta}$, δ~0.16) film that serves as a transducer layer is sputtered onto a (100) single crystal MgO substrate. The sample is mounted in a cryostat and kept a temperature of 110 K and a vapor pressure of ~10^{-3} Pa. Polycrystalline ice is naturally formed as a thin layer on the YBCO surface from the vapor phase. **Figure 1 (b)** shows a typical plot of the ice film thickness versus exposure time as measured in this study by laser picosecond acoustics.

Optical pulses (the pump pulses) of energy ~0.1 nJ, wavelength 415 nm and duration ~500 fs are normally incident on the YBCO film from the transparent MgO substrate side and excite longitudinal ultrasonic pulses with a typical frequency ~20 GHz. The pump pulse fluence per pulse ~0.15 mJ cm^{-2} produces a transient temperature rise ~70 K in the region of excitation, and a steady state temperature rise ~1.6 K. Optical reflectivity and phase changes are monitored from the opposite side with normally-incident optical probe pulses of wavelength 830 nm as a function of the delay time between the pump and probe pulses.

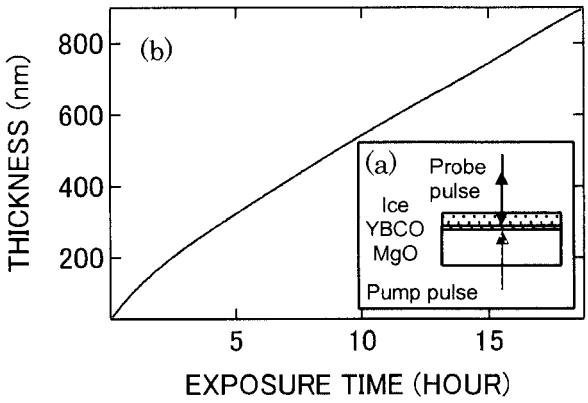

Figure 1. (a) Schematic diagram of the experiment. (b) Ice film thickness versus deposition time as measured by laser picosecond acoustics.

3. Numerical simulation

A time domain simulation was carried out to model the generation, the ultrasonic propagation in the ice film and the optical detection process. In particular, we account for multiple optical reflections, the photoelastic effect, and picosecond transient displacements of the sample surface and interfaces [4]. Ultrasonic attenuation with quadratic frequency dependence is included in the simulation

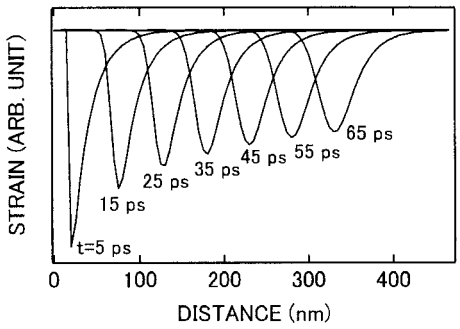

Figure 2. Real-time simulation of the ultrasonic propagation in an ice film.

by means of an effective strain diffusion process. This frequency dependence is common in materials at frequencies in the GHz range.

The ultrasonic attenuation coefficient is given by $\alpha=bf^2$, where b is a constant (2000 m^{-1} GHz^{-2} for our ice films). **Figure 2** shows the calculated ultrasonic strain pulse propagation in the ice film. The initial spatial extent of the pulse is assumed to be governed by the optical absorption depth of the pump light in the YBCO (~45 nm).

4. Results

Figure 3 shows the relative change in the reflectivity $\Delta R/R$ as a function of delay time for ice films of thickness 130 nm and 750 nm at 110 K. The solid curves are experimental results and the dotted curves are theoretical fits from the time-domain simulation. The beat oscillations of period ~100 ps are the result of an interference effect associated with the probe light reflection from the ultrasonic pulse propagating in the ice film. The period τ_B of the beat oscillation for normally-incident probe light is given by $\tau_B=\lambda/2nv$, [5] where λ is the optical wavelength of the probe light and n is the refractive index of the ice film. The low frequency oscillation with ~1000 ps period in the 750 nm curve, for example, coincides with the round trip time of the ultrasonic pulse in the ice film. The surface of the ice moves when the ultrasonic strain pulse arrives there, causing a change in the film thickness and a consequent change in the reflectivity. For a film of thickness d, the period τ_l of the low frequency oscillations is given by $\tau_l=2d/v$.

The refractive index of the ice film n is fixed at the literature value ~1.3, and the sound velocity v is fitted as 3750 m s^{-1}. The theoretical fits in Figure 3 agree reasonably well with the data. The value of the ultrasonic attenuation coefficient at 50 GHz is estimated to be $\alpha \approx 2.5$ μm^{-1}. To our knowledge this is the first determination of the ultrasonic attenuation at such high frequencies in ice.

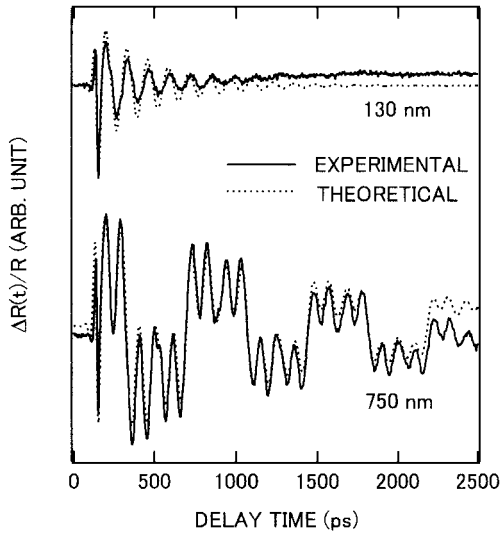

Figure 3. Transient reflectivity change versus delay time for 130 nm and 750 nm ice films on a 800 nm YBCO transducer film. The solid lines are experimental results and the dotted lines are theoretical fits.

References

1. C. Thomsen, H. T. Grahn, H. J. Maris, and J. Tauc: Phys. Rev. B **34** (1986) 4129.
2. O. B. Wright, T. Hyoguchi, and K. Kawashima: Jpn. J. Appl. Phys. **30** (1990) L131.
3. O. B. Wright: J. Appl. Phys. **71** (1992) 1617.
4. O. Matsuda and O. B. Wright: J. Opt. Soc. Am. B **19** (2002) 3028.
5. H. –N. Lin, R. J. Stoner, H. J. Maris and J. Tauc: J. Appl. Phys. **69** (1991) 3816.

Proc. Symp. Ultrason. Electron., Vol. 25, (2004) pp. 301-302
27-29 October, 2004

Ball SAW hydrogen sensor with amplitude and delay time response

○A. Mizukami [1], D. Y. Sim [2], I. Sato [3], T. Miyagishi[3], H. Tanaka[3], T. Fukiura[3], H. Kazato[3], S. Akao [4], T. Ohgi[4], N. Nakaso[4], H. Watanabe [1], T. Mihara [1] and K. Yamanaka [1]
1. Tohoku University, 2. Ball Semiconductor, 3. Yamatake, 4. Toppan Printing

1. Introduction

Hydrogen is expected as the most promising energy source in the future. However, hydrogen is known as explosive gas Therefore, in order to ensure the security of hydrogen society, it is required to fabricate a hydrogen sensor with wide sensing range, fast response time at reasonable price. However, no single element hydrogen sensor satisfying these conditions has been developed. Although combining FET sensor and electric resistance sensor enables wide sensing range [1], such a hybrid system requires complicated electric circuit system which results in relatively large sized, less reliable sensor. However, in SAW (surface acoustic wave) sensors on a planer substrate[2,3]. the sensitivity is not good compared with FET sensor. Therefore, we proposed ball SAW hydrogen sensor [4-6] in order to improve the sensitivity. In this report, we present a practical ϕ 1mm sensor.

2. Principle of ball SAW sensor

We improve the sensitivity using multiple roundtrips of SAW [4,5] (**Fig.1**) Since propagation length much longer than on a planer substrate is realized, not only delay time (or oscillation frequency in usual SAW sensor) but also amplitude response can be employed [6], which has a significant advantage in realizing wide range sensor.

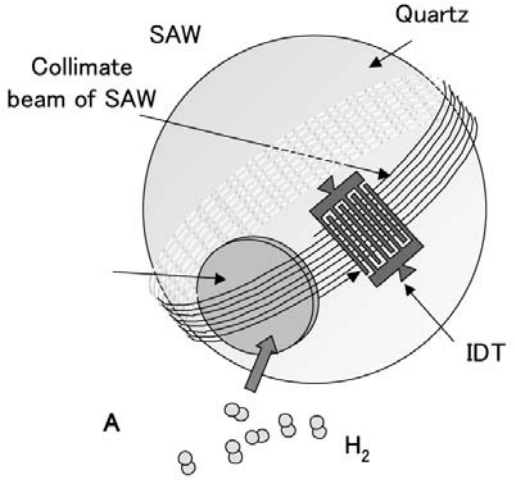

Fig.1. Concept of Ball SAW hydrogen sensor

3. Experiments and results

We deposited a 40nm-thick Pd-Ni alloy thin film on the 1mm ball. The ball was exposed by several hydrogen concentrations from 10ppm to 100% by using mass flow controllers. SAW was excited at 158MHz from IDT and received by the same IDT.

First we measured response from 0.1% to 3% hydrogen concentration. **Fig. 2** shows the delay time response of a sensor. Delay time decreased in each hydrogen atmosphere and its response (magnitude of decrease) increased with hydrogen concentration.

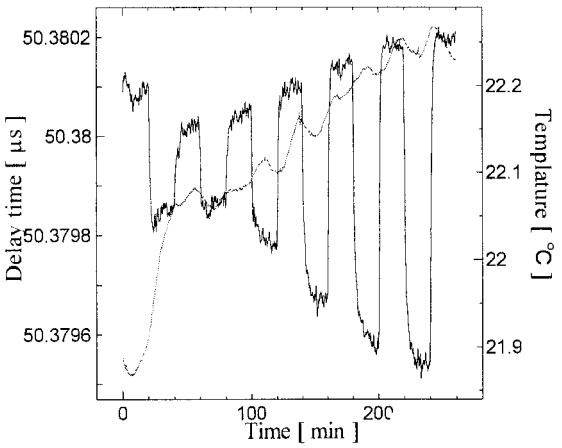

Fig. 2. Delay time change of the sensor in H_2 from 0.1% to 3%

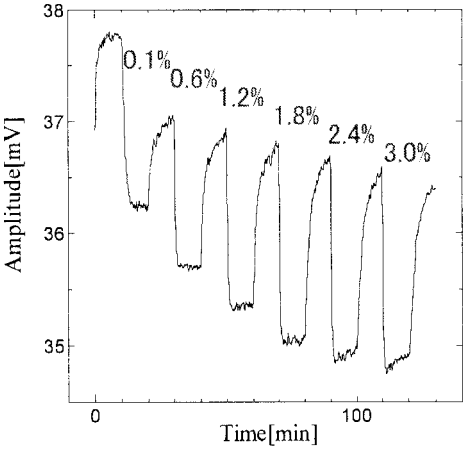

Fig. 3. Amplitude change of the sensor in H_2 from 0.1% to 3%

Since the response was not saturated at 3%, there is possibility to detect higher hydrogen concentration by delay time response. Also, we measured amplitude of SAW. Amplitude also decreased in hydrogen atmosphere and its response increased from 0.1% to 1.2%, but it saturated after 1.8% (**Fig. 3**). Amplitude response has better S/N ration compared with delay time response, there is more possibility to detect lower hydrogen concentration. Therefore, secondly, we measured response in lower hydrogen concentration from 500ppm to 10ppm. Delay time response was not detected at lower than 500ppm, shown as **Fig. 4.**

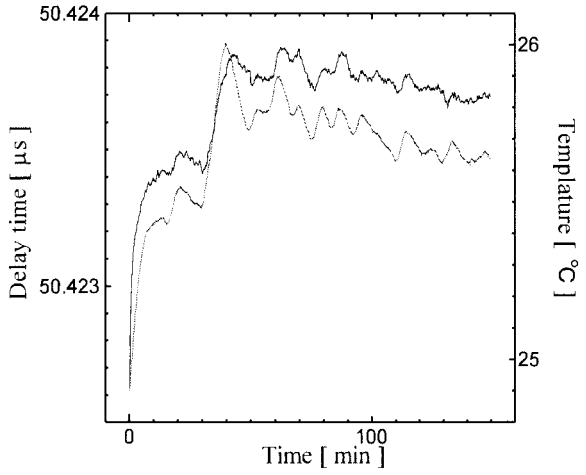

Fig. 4. Delay time change of the sensor in H_2 from 10ppm to 500ppm

Delay time response was too small and seemed to follow the temperature. Therefore, if we eliminate temperature influence, it is possible to detect response at lower hydrogen concentration. On the other hand, we still detected the amplitude response from 500ppm to 10ppm and its response increased with hydrogen concentration (**Fig. 5**).

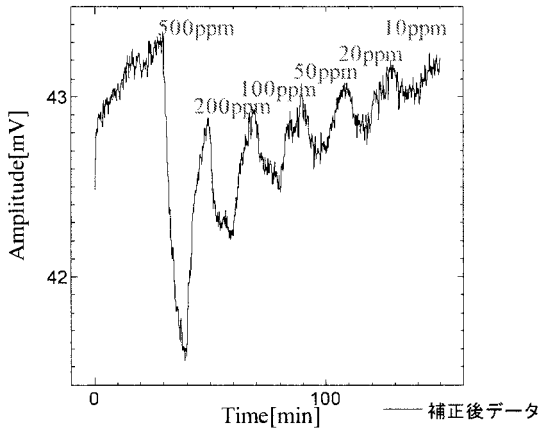

Fig. 5. Amplitude change of the sensor in H_2 from 10ppm to 500ppm

This result indicate that we can realize the same sensitivity as FET sensor by amplitude response.

Table 1 summarizes the feature of ball SAW hydrogen sensor in the concentration range from 0.1% to 3%. Delay time response has sensing range at higher hydrogen concentration (~0.1%) and amplitude response has sensing range at lower hydrogen concentration (10ppm~1%).

H_2 concentration	10ppm-500ppm	0.1%-1.2%	1.2%-3.0%
delay time response	poor?	increase with H_2 conc	
amplitude response	increase with H_2 conc		saturated?

Table 1 Delay time and Amplitude response of the sensor from 10ppm to 3%

4. Conclusion and future perspective

We successfully developed a ball SAW hydrogen sensor by measuring both delay time and amplitude response. Delay time response increased with hydrogen concentration from 0.1% to 3% although the sensitivity was poor under 0.1%. Amplitude response was detected from 10ppm to 1.8% but saturated from 1.8 to 3%. Therefore, it is possible to developed hydrogen sensor with wide sensing range by single device by measuring amplitude response at lower concentration and delay time response at higher concentration.

In the next step, we will measure the response at higher hydrogen concentration (3%~100%) and confirm that a ball SAW sensor has wide sensing range. Also, we measure the response under severer conditions (e.g. higher humidity) and confirm that this sensor can work in practical use.

Reference

[1] R. C. Hughes and W. K. Schubert, J. Appl. Phys. 71, 542 (1992).

[2] A. D'Amico, A. Palma, E. Verona, 1982 IEEE Ultrasonics Symp. 308 (1982).

[3] W. P. Jakubik, M. W. Urbanczyk, S. Kochowski and J. Bodzenta, Sens. Actuators B 82, 265 (2002).

[4] K. Yamanaka, H. Cho, and Y. Tsukahara, Appl. Phys. Lett. 76, 2797 (2000).

[5]K. Yamanaka, H. Cho and Y. Tsukahara, Tech. Rep. Inst. of Electronics, Information and Communication Engineers. US2000-14, 49 (2000).

[6]K. Yamanaka, S. Ishikawa, N. Nakaso, N. Takeda, T. Mihara and Y. Tsukahara, Proc. 2003 IEEE Ultrason. Symp. 299 (2004).

Proc. Symp. Ultrason. Electron., Vol. 25, (2004) pp. 303-304
27-29 October, 2004

Design of High Frequency Ultrasonic Probes with Separation between a Transmitter and a Receiver

○ Dong-Hyeon Kim, Kang-Lyeol Ha, Moo-Joon Kim(Pukyong Nat'l Univ., Korea)
and Jonathan M. Cannata, K. Kirk Shung(Univ. of South. Cal., USA)

1. Introduction

In an ultrasonic diagnosis system, the axial and the lateral spatial resolutions relating to image quality is very important. The axial resolution, particularly important for B-mode image, is determined by the frequency bandwidth of the transducer and the sound velocity in medium. To obtain a wide bandwidth for realizing the high resolution of a microscopic scale, very high frequency(VHF) ultrasound should be used. The VHF ultrasound have been employing for the medical diagnostic application or the UBM(Ultrasonic Backscatter Microscope) in the fields of ophthalmology or dermatology[1, 2]. However, the ultrasonic probes of those systems have the structure of backing/piezoelectric/matching layers, same as the conventional probes so far.

In this study, we have figured out a new structure of transmitting piezoelectric/acoustic buffer/receiving piezoelectric layers as shown in Fig. 1, which can give B-mode images of 5㎜ thick biological tissues with an axial resolution better than 30㎛. Two piezoelectric layers separated by an acoustic buffer are used in order to obtain a higher dynamic range and wider bandwidth.

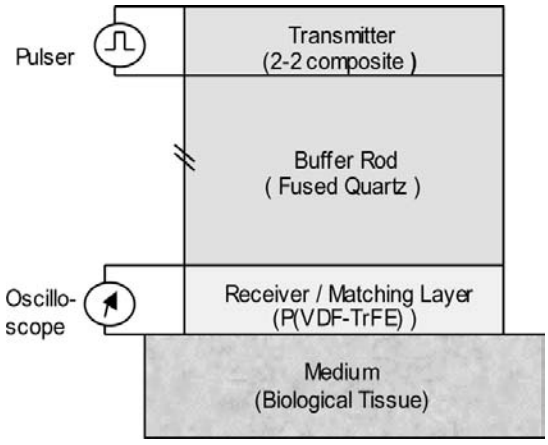

2. Materials and Structural Design

2-1) Selection of Materials

The physical properties of the materials used in the structure are shown in table 1. The materials were chosen as follows: First, we have selected the piezoelectric P(VDF-TrFE) copolymer as the receiver because of its high receiving sensitivity and wide

dhkim@prosonic.co.kr, hakl@pknu.ac.kr

Table. 1. Properties of the materials.

	2-2 Composite	Fused Quartz	Co-polymer	Biological tissue
v [m/s]	3840	5970	2400	1540
ρ[kg/m^3]	3430	2200	1880	1000
Z_a[Mrayl]	13.2	13.1	4.5	1.54
k_t	0.6	-	0.3	-
$\varepsilon/\varepsilon_0$	475	-	6.0	-

bandwidth characteristics. Secondly, a fused quartz was selected for the acoustic buffer because of its appropriate acoustic impedance to makes the copolymer a good matching layer between the buffer and the medium. In this structure, for obtaining the widest bandwidth, the transmitting piezoelectric material should have the same acoustic impedance with the acoustic buffer of the fused quartz. And, for a high dynamic range, it should have high electro-mechanical coefficient K_t. Only the piezoelectric composites that have suitable composition of the filler and resin are possible to satisfy those requirements. Thus, we choose the 2-2 composite as the transmitting transducer, which is more convenient than others in fabrication of VHF transducers. Figure 2 shows the calculation results of the acoustic impedance and the K_t according to the volume fraction of the PZT filler(Motorola 3203HD) in a typical 2-2 composite[3]. From the results, it is shown that 35% volume fraction gives almost same acoustic impedance(13.2Mrayls) as fused quartz and high coupling coefficient of K_t=0.67.

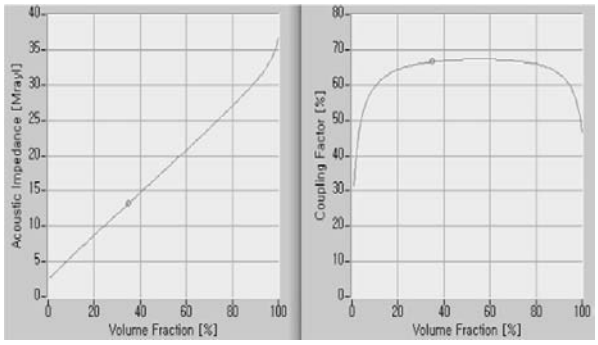

Fig. 2. Variations of acoustic impedance (a) and coupling coefficient (b) according to the volume fraction of ceramic filler.

2-2) Structure and Fabrication

Since we are considering biological tissue as a medium, the sound velocity can be estimated at approximately 1540㎧. The time interval of 6.5㎲ is

necessary for observing 5㎜ thickness. Therefore, the fused quartz rod of 20㎜ length is used, which gives 6.7㎲ of time delay between interior multi-reflections. The axial resolution is generally given by the following equation.

$$\delta_{ax} = 2v \cdot \ln 2 \cdot \frac{1}{\pi \Delta f} \qquad \text{----------} \quad (1)$$

(v : sound velocity, Δf : bandwidth[㎒])

Therefore, a bandwidth 22.6㎒ at least is needed in order to obtain a resolution better than 30㎛. Generally, the fractional bandwidth of an ultrasonic probe is determined by the structure of its backing and matching layer, and higher frequency creates wider bandwidth in the same structure. Here, we have assumed that the transmitting transducer is operating at λ/2 mode for the center frequency 50㎒ in design. Therefore, the thickness of 2-2 composite became to 18㎛. The diameter of the transducers were set at 3㎜ for the good electric impedance matching with 50Ω. The diameter of the fused quartz rod 18㎜ was decided in order to avoid the spurious noises by multi-reflection, scattering, and mode conversion in its inside. When the wave transmits into medium, the co-polymer should work as a matching layer between the fused quartz and the medium. Therefore, the thickness should be controlled with λ/4 for the center frequency. In this structure, the signals from the targets that exist between the direct receiving signal from the transmitter and the first roundtrip reflection in the rod are useful for imaging.

3. Simulation and Measurement

The characteristics of the transducer were simulated using the PSpice model[4]. In the model, parameters for every component were obtained by analogy of acoustical parameters with electrical ones for the electric transmission lines of 3 ㎜ diameter. In the simulation, we assumed a stainless steel plate(42 Mrayls) as the target, located in water at the 3 ㎜ apart from the probe surface. Figure 3(a) and (b), as the simulation results, show the P(VDF-TrFE) received impulse responses when the electric square pulse of -1V amplitude and 10 ㎱ width was applied to the transmitting transducer. In the figure, the second pulse is the signal reflected from the target that we want to obtain. The first pulse is the signal received directly from the transmitter. Others are interior multi-reflection in the rod or between the probe and the target. Figure 3(c) shows the power spectrum of the target signal. The center frequency is 43.0 ㎒ and the -6dB bandwidth is about 31.8 ㎒(% bandwidth 74.0%). Figure 4 shows the measurement results corresponding to Fig. 5. The center frequency is 33.3 ㎒ and the -6dB bandwidth is about 28.2 ㎒(% bandwidth 84.8%). It is supposed that the differences come mainly from the attenuation in the probe line and water, which were ignored in the simulation. By the eq.(1), it is expected that these bandwidths will give the axial resolution of 21 ㎛ approximately.

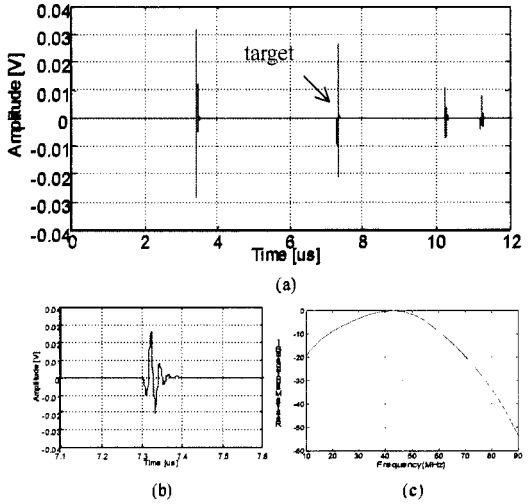

Fig. 3. Simulated impulse response of the probe using PSpice. (a) received pulse train, (b) target signal, (c) power spectrum of (b).

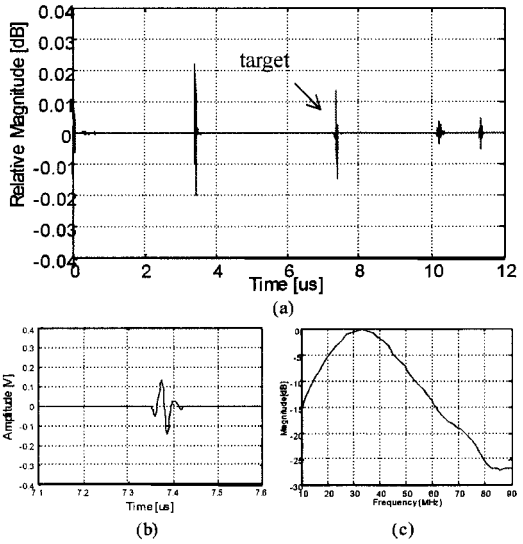

Fig. 4. Measured impulse response of the probe. (a) received pulse train, (b) target signal, (c) power spectrum of (b).

4. Conclusion

In this paper, a new type of high frequency wideband ultrasonic transducer consisting of 2-2 composite transmitter/fused quartz buffer/P(VDF-TrFE) receiver was proposed, and its impulse response was simulated using the PSpice model. The characteristics of a transducer fabricated in this study were also measured. Conclusively, it is revealed that the proposed transducer has a very wide bandwidth which could give an axial spatial resolution better than 30㎛ in the B-mode image for biological tissues.

Reference

1. F. S. Foster, C. J. Pavlin, G. R. Lockwood, L. K. Ryan, K. A. Harasiewicz, L. R. Berube and A. M. Rauth : IEEE UFFC. **40**(1993) 608.
2. C. Passmann and H. Ermert : IEEE UFFC. **43**(1996)545.
3. W. Qi and W. Cao : Ultrasonic Imaging. **18**(1996) 1.
4. E. Maione, P. Tortoli, G. Lypacewicz, A. Nowicki and J. M. Reid : IEEE UFFC. **46**(1999) 399.

Proc. Symp. Ultrason. Electron., Vol. 25, (2004) pp. 305-306
27-29 October, 2004

A Super-Precision Evaluation Method of CTE for Ultra-Low Expansion Glasses Using the LFB Ultrasonic Material Characterization System

Jun-ichi Kushibiki,[a] Mototaka Arakawa, Yuji Ohashi, Kouji Suzuki, and Takahisa Maruyama
(Dept. of Elect. Eng., Tohoku Univ.)

I. INTRODUCTION

For the future key technology to mass produce Super-LSI circuits with a line width of less than 45 nm, a system development of extreme ultraviolet lithography (EUVL) has been conducted in the semiconductor nanoelectronics. The most essential and important issue to realize the EUVL system is to develop ultra-low expansion (ULE) glasses as the basic substrate material suitable for reflective optics and photomask blanks, having the specification for the coefficient of thermal expansion (CTE) within ±5 ppb/K at the desired operating temperature (for example, 22±3°C for EUV mask blanks) [1]. The CTE measurement technology with a very high accuracy is essentially needed for feeding back evaluation results to production process in the development of ULE glasses with the satisfactory CTE characteristics. The conventional CTE measurement methods are a direct CTE measurement using a dilatometer with an interferometric system and indirect measurements of the ultrasonic longitudinal velocities, chemical compositions, and refractive indices that are closely related to the thermal properties of CTE [1]. However, sufficient accuracies in both the direct and indirect CTE measurements have not been obtained for the EUVL-grade glasses.

The LFB-UMC system [2] is expected to apply for the CTE evaluation method for the EUVL-grade glasses because two-dimensional leaky-surface-acoustic-wave (LSAW) velocity distributions on the substrate surface can be measured very precisely under the nondestructive and noncontact measurement condition. In this paper, we apply this system to characterize commercial TiO_2-SiO_2 glasses and study the potential of the LFB-UMC system for the extremely precise CTE evaluation technology.

II. EXPERIMENTS AND DISCUSSIONS

A. Specimens

Three TiO_2-SiO_2 glass (C-7971, Corning Inc.) specimens, termed specimens A, B, and C, were prepared from different lots. The dimensions were 50 mm × 50 mm × 4.8 mm^t for specimen A, 50 mm × 30 mm × 3.0 mm^t for specimen B, and 27 mm × 27 mm × 3.2 mm^t for specimen C. All the specimens were optically polished on both sides with a parallelism within 10 seconds.

B. Calibration line

LSAW velocity measurements of C-7971 specimens were carried out with the LFB-UMC system at an ultrasonic frequency of 225 MHz. **Figure 1** shows the typical V(z) curve in the measurements. The reproducibility of the LSAW velocity was estimated to be ±0.17 m/s (±2σ, σ : standard deviation) from 200-time V(z) curve measurements.

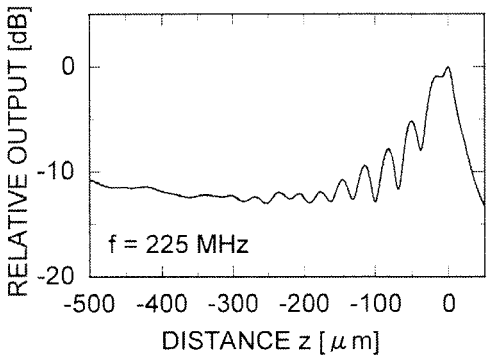

Fig. 1. Typical V(z) curve measured for a C-7971 specimen at 225 MHz.

Table I Sensitivity and resolution in the LSAW velocity measurements to other physical and chemical properties for C-7971.

	Sensitivity	Resolution (±2σ)
LSAW velocity	———	±0.17 (m/s)
CTE	4.33 (ppb/K)/(m/s)	±0.75 ppb/K
TiO_2 concentration	-0.057 wt%/(m/s)	±0.010 wt%
Density	0.0167 (kg/m^3)/(m/s)	±0.0029 (kg/m^3)

The chemical compositions of the specimen B were analyzed by X-ray fluorescence analysis, resulting in a TiO_2 content of 6.9 wt%. The density was also measured to be 2197.98 kg/m^3. Since the CTE is controlled by changing the TiO_2 concentration [1] that has a close relationship with the LSAW velocity, sensitivity and resolution of the LSAW velocity to the CTE, TiO_2 concentration, and density were estimated by comparing those characteristics of the C-7971 specimen and the synthetic silica glass (C-7980, Corning Inc.) with 100-percent SiO_2 [3], using the CTE value of 520 ppb/K for C-7980 [4] and assuming that of 0 ppb/K for C-7971. The results are shown in **Table I**. It was shown that the CTE within ±5 ppb/K needed for EUVL-grade ultra-low expansion glass substrates corresponds to the LSAW velocity within ±1.15 m/s calculated from the sensitivity of 4.33 (ppb/K)/(m/s) obtained above.

[a]Electronic mail: kushi@ecei.tohoku.ac.jp

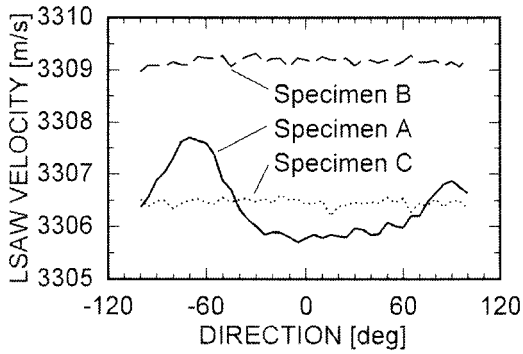

Fig. 2. Angular depdendences of LSAW velocities for C-7971 specimens at 225 MHz.

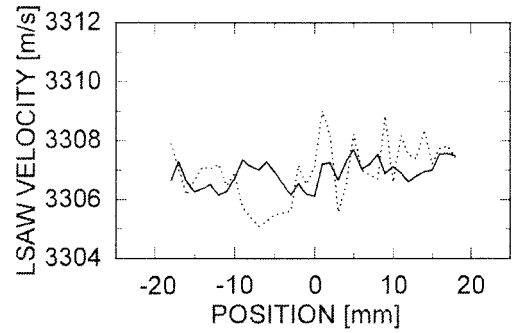

Fig. 3. LSAW velocity distributions for specimen A of C-7971 at 225 MHz. Solid lines: x-direction. Dotted lines: y-direction.

C. Angular dependences

The angular dependences of LSAW velocities at the center of the specimens were measured, as shown in **Fig. 2**. For the specimens B and C, there were almost no angular dependences, while, for the specimen A, there was detected a maximum velocity variation of 2.00 m/s in the angular dependence suggesting structural anisotropy in the specimen.

D. Homogeneity evaluation

Velocities of LSAWs propagating along two perpendicular directions of x and y axes crossing at the center of the surface of each specimen were measured for line scanning in 1-mm steps. The different profiles were observed among the specimens. For specimens B and C, the profiles are simpler, exhibiting gentle variations in the LSAW velocity around 2.5 m/s along the x-axis direction and almost constant along the y-axis direction. In contrast, for specimen A, the profiles exhibit periodical variations along both the x- and y-axis directions with the maximum velocity variations of 3.92 m/s, as shown in **Fig. 3**. The mean values of the velocity distributions were 3306.92 m/s for specimen A, 3309.33 m/s for specimen B, and 3306.92 m/s for specimen C. The maximum difference of the mean values among the three specimens was obtained as 2.41 m/s.

To have a better understanding of the fine periodic variations in the velocity distributions observed for specimen A, LSAW velocities for the x-axis propagation

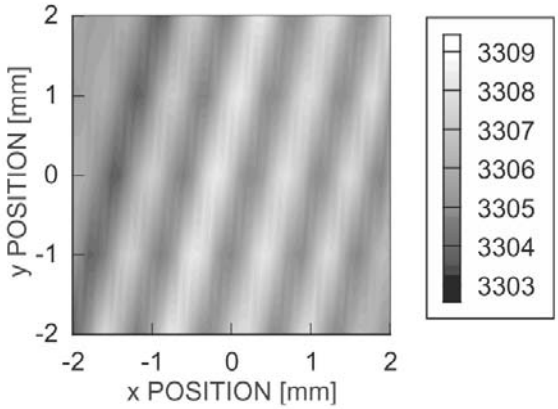

Fig. 4. LSAW velocity distributions near the center of specimen A of C-7971 at 225 MHz.

were measured in detail for an area of 4 mm × 4mm by two-dimensional scanning along the x axis in 0.1-mm steps and the y axis in 1-mm steps, as shown in **Fig. 4**. A periodic interval of about 0.9 mm in the velocity distribution can be seen in Fig. 4 and a maximum velocity change of 4.56 m/s was obtained. The literature [5] reported that there exists the striae with a periodical interval of about 0.16 mm in C-7971 glasses, constructed during the glass production process. Therefore, the significant LSAW velocity variations observed in Figs. 3 and 4 reflect variations in TiO_2 concentration that cause the striae.

The maximum velocity variation of 4.56 m/s in Fig. 4 corresponds to 19.7 ppb/K for CTE, 0.26 wt% for TiO_2 concentration, and 0.076 kg/m^3 for density by calculations from the sensitivity given in Table I. Also, the maximum velocity difference of 2.41 m/s among the three specimens was estimated to be 10.4 ppb/K for CTE, 0.14 wt% for TiO_2 concentration, and 0.040 kg/m^3 for density. The resultant velocity distributions obtained here are larger than the tolerance in the specification for ultra-low expansion glasses in the EUVL system.

III. SUMMARY

We applied the LFB-UMC system to the evaluation of commercial TiO_2-SiO_2 glasses, and demonstrated that this system is extremely useful for characterization of ULE glasses in the EUVL system. We will hereafter improve the measurement accuracy and study the measurement model to establish the striae evaluation method for the TiO_2-SiO_2 glasses.

References

[1] K. E. Hrdina et al., Proc. SPIE Emerging Lithographic Technologies VII, Vol. 5037, pp. 227-235 (2003).
[2] J. Kushibiki et al., IEEE Trans. Ultrason., Ferroelect., Freq. Contr., Vol. 49, pp. 99-113 (2002).
[3] J. Kushibiki et al., IEEE Trans. Ultrason., Ferroelect., Freq. Contr., Vol. 49, pp.827-835 (2002).
[4] Technical Data from Corning Inc.
[5] K. E. Hrdina et al., Proc. SPIE Emerging Lithographic Technologies VI, Vol. 4688, pp. 454-461 (2002).

Proc. Symp. Ultrason. Electron., Vol. 25, (2004) pp. 307-308
27-29 October, 2004

Resonant Ultrasound Microscopy with an Isolated Langasite Oscillator for Quantitative Evaluation of Local Elastic Constant

○Hirotsugu Ogi, Jiayong Tian, Toyokazu Tada, and Masahiko (Osaka Univ.)

1. Introduction

A resonance-ultrasound microscopy has been developed to measure material's local Young's modulus. It detects the effective Young modulus through a resonance frequency of free vibration of a langasite ($La_3Ga_5SiO_{14}$) oscillator touching the specimen. The vibration of the oscillator is excited and detected with a surrounding solenoid coil in a noncontacting way. Thus, oscillator's vibration can be affected only by the contact with the specimen, achieving an absolute quantitative measurement.

2. Measurement Setup

Figure 1 shows the measurement setup [1-3]. An oriented rectangular parallelepiped langasite is located inside the solenoid coil. The langasite crystal contacts a specimen through a tungsten-carbide bearing attached on the center of the bottom surface. Driving the solenoid coil by tone bursts induces an oscillating quasi-static electric field and excites free vibrations of the crystal through the converse piezoelectric effect. After the excitation, the same coil receives the vibration through the piezoelectric effect. A frequency scan provides a resonance spectrum. There are many vibration modes and we select such a mode that shows center antinode spot on the bottom surface and a nodal line on the top surface of the oscillator. A biasing force F_0 is applied for supporting the crystal through three pins touching the vibrational nodes on the top surface. Thus, an acoustic coupling occurs only at the specimen surface, and the vibration of the crystal is isolated from any other contacts, realizing high sensitivity and reproducibility of the measurement.

3. Vibrational Analysis

There are four groups for natural vibrations of an oriented rectangular-parallelepiped crystal with 32 point-group symmetry. They are denoted by Ag, Bg, Au, and Bu, according to the deformation symmetry as tabulated by Ohno [4].

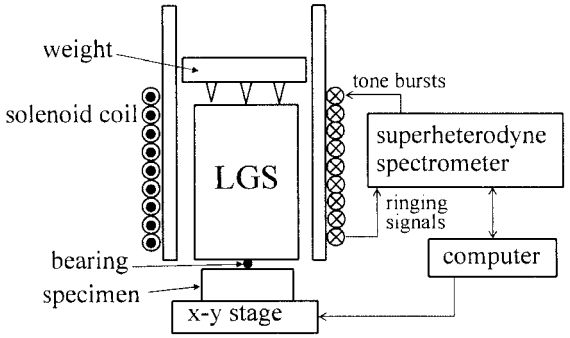

Fig. 1 Measurement setup of resonant-ultrasound microscopy with a rectangular parallelepiped langasite oscillator.

When there is a contact on the surface of the crystal, resonance frequencies change from those at free vibration. According to Herzian-contact model, the contact between the bearing and specimen can be regarded as an elastic spring. The equivalent spring constant for isotropic material is given by $k = \alpha\left(6E^{*2}RF_0\right)^{1/3}$ [3]. α is a parameter to express the dynamic-contact stiffness. R is the bearing radius. E^* denotes the effective Young modulus of the specimen. Thus, Lagrangian of the vibration system consisting of the crystal and the contact spring can be expressed by

$$L = \frac{1}{2}\int_V \left(S_{ij}C_{ijkl}S_{kl} - \frac{\partial\phi}{\partial x_m}\varepsilon_{mn}\frac{\partial\phi}{\partial x_n} + 2\frac{\partial\phi}{\partial x_m}e_{mkl}S_{kl} - \rho\omega^2 u_i u_i \right) dV + \frac{1}{2}k\tilde{u}^2 . \quad (1)$$

Here ϕ denotes the electric potential and u_i the displacement along the x_i axis. ρ and ω are mass density and angular frequency of the system. S_{ij}, C_{ijkl}, e_{ijk}, and ε_{ij} denote strain tensor, elastic constants, piezoelectric coefficients, and dielectric

ogi@me.es.osaka-u.ac.jp

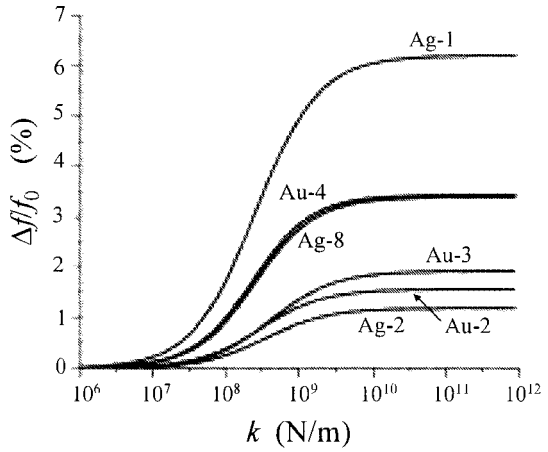

Fig. 2 Sensitivity of resonance frequencies to the contact stiffness when α=1.

constants of langasite. $\tilde{u}$ is the out-of-plane displacement of the langasite at the contacting point. The stationary point of the Lagrangian (δL=0) yields the resonance modes.

We used Ag-1 mode because it shows high sensitivity to the contact stiffness. Figure 2 shows the relationship between the resonance frequency shift and the contact stiffness. Ag-1 mode shows the largest sensitivity to the contact stiffness because it shows an antinode point at the center of the bottom surface and nodal points for the in-plane displacements at the center bottom surface. Thus, this mode is sensitive to the normal Young's modulus.

3. Results and Discussions

We scanned the cross-section of superconductive wire consisting of oxygen-free copper matrix and embedded NbTi filaments with 32-μm diameter [5]. The biasing force was 0.13 N. Figure 3 shows the result. Direction-over-averaged Young's moduli of cupper and NbTi are 128.7 GPa and 84.3 GPa, respectively. Thus, the resonance frequency on copper is larger than that on NbTi. We compare the measurements of the resonance frequency shift with those calculated by the dynamic and static contact models in Fig. 4. Scatterings of measured frequencies are caused by different grain orientations; Copper Young's modulus can vary between 66.7 GPa and 190.8 GPa depending on the grain orientation because of its high anisotropy. Also, Young's modulus of NbTi varies between 63.6 and 107.6 GPa. Our previous study with

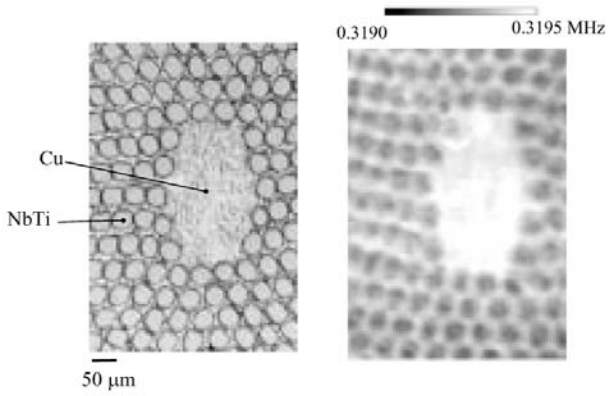

Fig. 3 Microstructure of an NbTi/Cu superconductive wire observed by optical microscopy (left) and resonant-ultrasound microscopy (right).

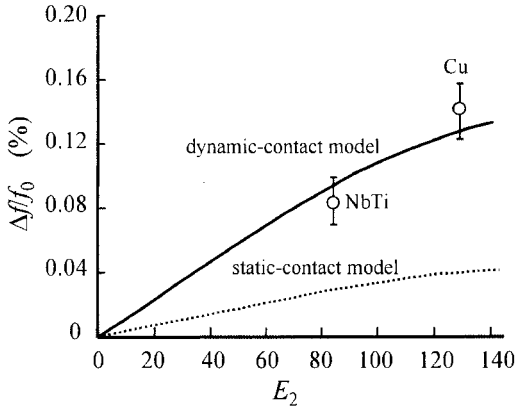

Fig. 4 Resonance frequency shift versus Young's modulus of contacting material. Solid and broken lines are predicted curves for the static (α=1) and dynamic (α=3.3) contact models. Solid circles are measurements.

different crystals and different vibration modes [2, 3] revels that the dynamic contact stiffness is larger than the static contact stiffness by a factor 2.4-3.6. Indeed, the dynamic model in Fig. 4 agrees with the measurement within the error limits when α=3.3. Thus, Figures 3 and 4 demonstrates capability of the present method of a quantitative measurement of elastic constant of local area.

References

1. H. Ogi, J. Tian, T. Tada, and M. Hirao, Appl. Phys. Lett., 83, 464 (2003).
2. J. Tian, H. Ogi, and M. Hirao, J. Appl. Phys., 95, 8366 (2004).
3. J. Tian, H. Ogi, and M. Hirao, J. Appl. Phys., 96, 133 (2004).
4. I. Ohno, Phys. Chem. Minerals, 17, 371 (1990).
5. H. Ledbetter, J. Moulder, and M. Austin, Wire J., 31, 27 (1981).

Proc. Symp. Ultrason. Electron., Vol. 25, (2004) pp. 309-310
27-29 October, 2004

Down Scaling in Piezoelectrics and Polar Materials: Microdevices, Nanofabrication, Small Features and Size Effects

Nava Setter
Ceramics Laboratory, EPFL Swiss Federal Institute of Technology
1015 Lausanne, Switzerland

Piezoelectric materials in the form of thin and thick films are finding new applications in diverse fast growing fields such as wireless communications and environment monitoring. The number of applications that will benefit from availability and implementation of these films is likely to grow.

Size reduction of ferroelectric-based micro-components, both in thickness and in lateral dimensions is required for various applications. This can be achieved by a reductive approach of etching of the sintered continuous layers, or by an additive approach in which a treatment of the substrate results in the creation of patterned structures prior to the annealing step. Recent local characterization techniques, e.g. piezoelectric force microscopy, allow the analysis of properties in such small components and to manipulate them.

Various microdevices are described and issues in fabrication technology (in particular piezoelectric MEMS) are discussed. Data and interpretation of local measurements are reviewed. Size effects in ferroelectrics and their significance in emerging applications are discussed.

～ *Memo* ～

Proc. Symp. Ultrason. Electron., Vol. 25, (2004) pp. 311-314
27-29 October, 2004

Real time imaging of surface acoustic waves on crystals and microstructures

Oliver B. Wright
(Graduate School of Engineering, Hokkaido University)

1. Introduction

The ear as an acoustic instrument is well designed for spectral resolution, but not for spatially visualizing the individual waves of sound. On casting a stone into a pond we can immediately appreciate the spreading of circular water ripples. How could one watch acoustic ripples on solids? Such ripples, best known for their role in earthquakes, were first explained by Lord Rayleigh in 1881 [1]. Just like water ripples, the surface of solids provides a guiding mechanism for acoustic waves. Rather than resorting to the aerial filming of earthquakes, I present in this paper a more practical means for watching ripples on solids, or surface acoustic waves [2].

Surface acoustic waves in solids show a rich array of propagation phenomena owing to the nature of the fourth-order elastic constant tensor. Despite a crystal being homogeneous, a point acoustic source can lead to singularities in acoustic flux in certain directions owing to the angular dependence of the phase and group velocities of the acoustic waves [3]. In two dimensions the acoustic energy is concentrated along lines of intersection of families of rays called caustics, ending in points called cusps. This phonon focusing effect is analogous to the caustic structures one encounters in optics: for example the heart-shaped shadow you sometimes see in your coffee cup. The real-time visualisation of surface acoustic waves offers the possibility for studying the temporal evolution of cuspidal structures. On the practical side, interest in surface acoustic waves has recently intensified because surface acoustic wave filters, made up of microscopic interdigital electrodes on piezoelectric crystal substrates, are widely used in communication systems and cellular phones. Such filters handle gigahertz electronic signals at micron acoustic wavelengths. For a given frequency, the wavelength of sound in crystals is ~10^5 times smaller than that of electromagnetic waves, allowing convenient manipulation of signals through micron-scale engineering. In addition, surface acoustic waves penetrate to a depth of the order of the acoustic wavelength, and are sensitive to the presence of thin films. This sensitivity allows surface acoustic wave devices such as gas sensors to be designed or allows film thickness to be measured from an analysis of the propagation of surface acoustic wave packets.

Imaging methods for surface acoustic waves were developed over the same period as those for bulk phonon focusing [3]. Various methods for imaging surface acoustic waves have been proposed [4-10], but none of these has allowed two-dimensional imaging on anisotropic substrates in real time.

The method I describe here relies on a non-contact technique for imaging surface acoustic waves in real-time using ultrashort optical pulses for excitation and detection [2,11-14]. With this method we impulsively generate surface acoustic waves at frequencies up to 1 GHz at a point source in opaque materials. This allows acoustic wave fronts with an omnidirectional acoustic wave vector distribution to be tracked with picosecond temporal and micron spatial resolution. After outlining the experimental technique I will present results from representative samples with isotropic and anisotropic substrates, including microstructures, and briefly describe how the acoustic dispersion relations can be extracted.

2. Experimental technique

Experiments are carried out with metallic thin films and microstructures on isotropic and anisotropic substrates. The basic setup for transparent substrates is shown in **Fig. 1**. The surface acoustic waves are excited by blue pump pulses of duration ~1 ps, repetition rate 80 MHz (one pulse every 12.5 ns), wavelength 415 nm, and incident energy per pulse 0.1-0.3 nJ, producing a maximum transient temperature rise ~100 K. These optical pulses are derived from the second harmonic output of a mode-locked Ti:sapphire laser. The pump light is focused at normal incidence through a ×50 or ×100 long-working-distance microscope objective lens from the transparent-substrate side of the sample to a spot of diameter typically ~1–3 μm. The generation is governed by the thermoelastic effect, producing surface acoustic waves with wavelengths ~3–30 μm and frequencies in the range 100 MHz–1 GHz. The dominant wavelength of the thermoelastically generated surface acoustic waves, typically ~10 μm, is determined by a combination of the optical spot size, the sample geometry such

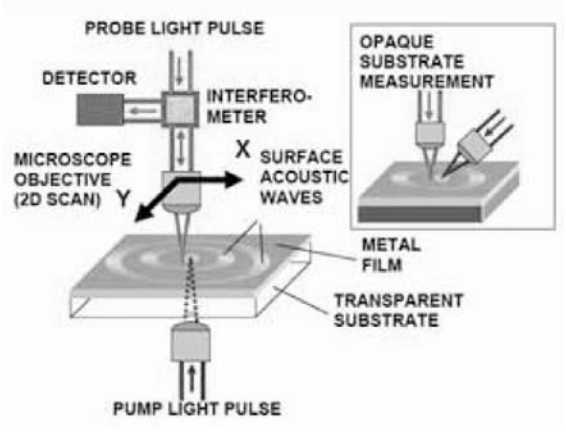

Fig. 1. Basic imaging apparatus for samples with transparent substrates. Inset: imaging apparatus for samples with opaque substrates.

as film thickness, and diffusion processes.

The surface acoustic wave detection is done interferometrically by two ~1 ps optical probe pulses in the infrared of wavelength λ=830 nm (derived from the same laser) that are temporally separated by 300-500 ps from one another, and focused at normal incidence through another objective lens onto the front surface of the film. We use a highly stable Sagnac common-path interferometer, described in detail elsewhere [12,15], that allows a direct measurement of the optical phase change ($\delta\phi$) caused by the sample surface displacement ($\delta z = \lambda\delta\phi/4\pi$). A signal proportional to the phase difference between the two probe pulses is obtained, related to the normal surface displacement of the sample (~10 pm). Because the signal is proportional to the difference in phase between two probe pulses, we are essentially imaging the out-of-plane component of the *velocity* of the surface.

For samples with opaque substrates we use the apparatus shown in the inset of Fig. 1. The *p*-polarized pump light is focused onto the samples at an angle of 60° through a × 20 long-working-distance microscope objective lens. Cylindrical lenses are used to correct the optical spatial profile to produce a pump beam spot with axial symmetry on the sample [11].

By the use of a variable optical delay between the pump and probe and by raster scanning the probe beam laterally over the sample, animations of the surface acoustic wave propagation can be obtained (using typically 10–20 images). A selection of these can be viewed on http://kino-ap.eng.hokudai.ac.jp. Surface acoustic wave fronts can be observed with micron lateral spatial resolution. The typical magnitude of the signal, expressed as a difference in surface displacement, is ~5 pm. The typical noise level corresponding to the above image acquisition rates is ~0.3 pm (peak-to-peak), limited by laser intensity fluctuations and beam pointing stability. The high

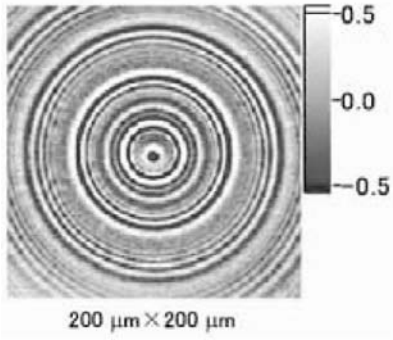

Fig. 2. Image of surface acoustic wave fronts for a crown glass substrate coated with a 70 nm gold film.

resolution for measurement of displacement using optical interferometry is enabled because the interference process converts mechanical motion into an intensity change. Our ability to measure small intensity changes implies that the interferometer resolution is much smaller than the optical wavelength λ, in our case ~λ/3000000.

3. Results for homogeneous samples

The simplest surface acoustic wave fronts are obtained for isotropic samples. **Figure 2** shows an image for a 200 μm × 200 μm region of a sample of crown-glass of thickness 1 mm coated by thermal evaporation with a 70 nm film of polycrystalline gold. The concentric series of rings arises because of the 12.5 ns period for the arrival of pump optical pulses at the centre of the pattern. The circular shape is expected because both film and substrate are isotropic (or at least show axial symmetry). These images are superficially similar to that of the surface of a liquid disturbed by a falling drop. Like ripples on a liquid surface, surface acoustic waves in thin films are subject to dispersion, and this tends to increase the width of the pulse as it propagates outwards. The smaller (wavelength) ripples, more influenced by the denser gold film, go slower than the larger ripples, leading to a dispersion opposite to that of ripples on water.

A simple example of an anisotropic sample is a crystal with cubic symmetry. **Figure 3** (a) shows an approximately 200 μm × 200 μm experimental surface acoustic wave image for the (100) surface of a transparent slab of LiF of thickness 1 mm coated with a 50 nm polycrystalline gold film. This image is represented in a false-colour 3D format. The *x* and *y* axes correspond to the [010] and [001] directions. LiF is cubic crystal which, from a consideration of ratios of its elastic constants, is expected to have a folded group velocity surface with 4-fold symmetry and to show surface phonon focusing. The experimental wave fronts are rounded square shapes.

Because of the impulsive optical excitation the surface acoustic waves travel outwards from the centre of the pattern as coherent wave packets. It is

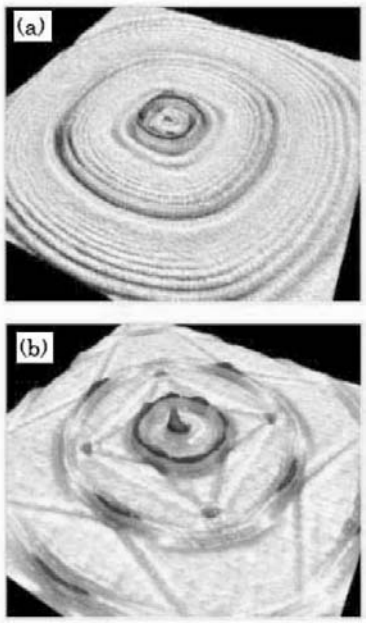

Fig. 3. 3D images of experimental data for surface acoustic wave propagation on single crystals. (a) LiF (100) surface coated with a 50 nm gold film. (b) TeO_2 (001) surface coated with a 70 nm gold film.

natural then that it should be the *group velocity* that determines the speed of the acoustic wave packet. An analytical calculation of the direction-dependent group velocities for surface acoustic waves (SAW) and pseudo-surface acoustic waves (PSAW) gives good agreement with the observed pattern, provided account is taken of the of the effect of phonon focusing and the selective detection of the out-of-plane component of the surface motion [2]. As with the case for the glass substrate, LiF coated with gold also shows wave packet broadening caused by acoustic dispersion associated with the finite film thickness.

We have also imaged a transparent slab of TeO_2 [2], a tetragonal crystal with a much stronger anisotropy. Figure 3 (b) shows an approximately 130 μm × 130 μm surface acoustic wave image for the (001) surface of single-crystal TeO_2 of thickness 1 mm coated with a 40 nm polycrystalline gold film. The x and y axes correspond to the [100] and [010] directions. The pattern shows the expected 4-fold symmetry for this cut. The complicated wave fronts in experiment arise from the strong anisotropy and resulting caustic behavior evident in the group velocity predictions. The square wave fronts (joining the four vertices of the star shape) correspond to those predicted for quasi-longitudinal bulk waves.

Dispersion analysis for such data is best carried out from a full animation of 10-20 images covering the 12.5 ns time period between consecutive laser pulses. We take a dual spatial and temporal Fourier transform of the data to directly obtain the acoustic dispersion relation in ω-**k** space [13]. Instead of directly working with the dual Fourier transform of the full set of data $f(\mathbf{r}, t)$, we add to $f(\mathbf{r}, t)$ an inverted time-reversed component $-f(\mathbf{r}, -t)$ representing incoming wave fronts, matching the two sets of data to produce a combination of converging and diverging acoustic waves, with no acoustic sources. The sign inversion of f stems from an approximation to experimental observations [2,13]. We therefore determine a function $g(\mathbf{r}, t)=f(\mathbf{r}, t)-f(\mathbf{r}, -t)$ and its dual Fourier transform $|G(\mathbf{k}, \omega)|$ for image analysis. This processing has the advantage of improving the sharpness of the Fourier transform, although it is not essential.

Figure 4 (a) shows an example for TeO_2 (001) of a section of the experimentally determined function $|G(\mathbf{k},\omega)|$ for $\omega/2\pi$=570 MHz. This corresponds to a constant frequency surface in wave vector space. Figure 5 (b) shows the corresponding result of theoretical calculations for SAW, PSAW, and quasi-longitudinal bulk waves on the same scale, that is the *slowness surfaces* for these modes with the conventional axes k_x/ω and k_y/ω multiplied by the constant value of ω to give k_x and k_y. (We have ignored small film loading and piezoelectric effects in the calculation.) The slowness surface can be considered as the reciprocal of the *phase velocity* surface, and is considered to be of most interest in characterizing the elastic properties of an anisotropic material. The lines traced out by the experimental $|G(\mathbf{k}, \omega)|$ are reproduced well by the theory. Analogously to the results for group velocity, the combined effects of phonon focusing and the selective detection of the out-of-plane motion prevent some SAW branches being detected [of the type marked with the star in Fig. 4 (b)]. One obvious advantage of using the slowness surface is

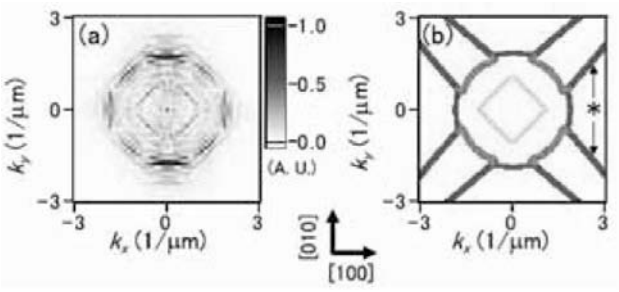

Fig. 4. (a) Experimentally determined dispersion of (001) TeO_2: constant frequency surface of the experimentally-determined function $|G(\mathbf{k}, \omega)|$ for $\omega/2\pi$=570 MHz. (b) The result of theoretical calculations of the slowness surfaces for SAW (blue), PSAW (red) and quasi-longitudinal bulk waves (green). The star shows branches not observed in experiment.

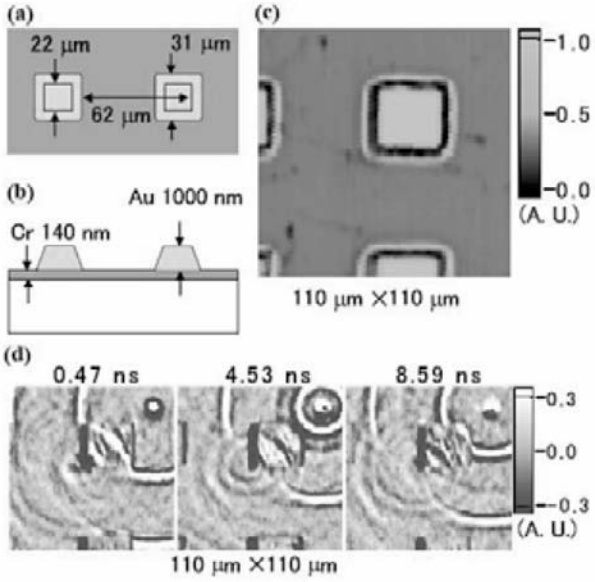

Fig. 5. (a), (b) Geometry of a microstructure consisting of a crown glass substrate coated with a 140 nm chromium film and gold pyramids of thickness 1 μm. (a): surface. (b): cross section. (c) Optical reflectivity image of the sample surface. (d) Experimental surface acoustic wave images, at the different delay times shown, obtained for the same region as (c). The pump pulses are incident at the top right.

that this surface is never folded like the group velocity surface, allowing simpler interpretation.

5. Results for microstructures

The imaging of surface acoustic waves on complex microstructures is of particular interest because of the difficulty of carrying out simulations for samples with complex three-dimensional features. We fabricated a sample consisting of an array of pyramids as shown in **Fig. 5** (a) and (b). The pyramids are sufficiently spaced so that the surface acoustic wave propagation through a single pyramid could be studied. Figure 5 (c) shows an optical reflectivity image (at the probe wavelength) and Fig. 5 (d) shows surface acoustic wave images for a 110 μm × 110 μm region of the sample. The pump optical pulses are incident at the top right. To make the sample a 30 nm polycrystalline chromium film was prepared by electron beam deposition on a 1 mm crown-glass substrate. Polycrystalline gold of thickness 1 μm was then thermally evaporated through a mask. The difference in surface acoustic wave propagation velocities in gold (1.13 km s^{-1}) and in crown glass (3.1 km s^{-1}) is mainly responsible for the refraction at the pyramid boundaries, producing an inversion of the wave front curvature inside the pyramid. The surface acoustic waves are thus concentrated and are strongly scattered on exiting the pyramid.

6. Conclusions

We have demonstrated a method for real time imaging of surface acoustic waves at frequencies in the 100 MHz-1 GHz range with picosecond temporal and micron spatial resolutions using an ultrafast optical pump and probe technique. We have also demonstrated a technique for obtaining the dispersion from a set of images making up a complete animation. This allows the individual modes excited in the sample to be distinguished. Wave fronts in complex nanostructures can also be mapped. This method shows great promise for the study of the physics of surface acoustic waves in very complicated geometries, and in principle there are exciting prospects for extension with near-field optical techniques to frequencies up to 10 GHz or above.

Acknowledgments

I thank Y. Sugawara, O. Matsuda, S. Tamura, Y. Tanaka, V. E. Gusev and D. H. Hurley for experimental support and valuable discussions on the theory of acoustic propagation and dispersion.

References

1. Lord Rayleigh : Proc. London Math. Soc. **17**, 4 (1885).
2. Y. Sugawara, O. B. Wright, O. Matsuda, M. Takigahira, Y. Tanaka, S. Tamura and V. E. Gusev : Phys. Rev. Lett. **88**, 185504 (2002)
3. J. P. Wolfe : *Imaging Phonons* (Cambridge University Press, Cambridge, U.K., 1998).
4. A. A. Kolomenskii, A. A. Maznev : JETP Lett. **53**, 423 (1991); Phys. Rev. B 48, 14502 (1993).
5. R. E. Vines, Shin-ichiro Tamura, J. P. Wolfe : Phys. Rev. Lett., 74 2729 (1995).
6. D. Shilo and E. Zolotoyabko : Phys. Rev. Lett. **91** 115506 (2003).
7. G. Eberharter and H. P. Feuerbaum : Appl. Phys. Lett. 37, 698 (1980).
8. T. Hesjedal and G. Behme : Appl. Phys. Lett. **78** 1948 (2002).
9. K. Nakano, K. Hane, S. Okuma and T. Eguchi : Opt. Rev. 4, 265 (1997).
10. S. Sharples, M. Clark and M. Somekh : Ultrasonics **41**, 295 (2003).
11. Y. Sugawara, O. B. Wright and O. Matsuda : Rev. Sci. Inst. **74**, 519 (2003).
12. Y. Sugawara, O. B. Wright, O. Matsuda and V. E. Gusev : Ultrasonics **40**, 55 (2002).
13. Y. Sugawara, O. B. Wright and O. Matsuda : Appl. Phys. Lett. **83** 1340 (2003).
14. O. B. Wright, Y. Sugawara, O. Matsuda, M. Takigahira, Y. Tanaka, S. Tamura and V. E. Gusev : Physica B **316-317C**, 29 (2002).
15. D. H. Hurley and O. B. Wright : Opt. Lett. **24**, 1305 (1999).

Proc. Symp. Ultrason. Electron., Vol. 25, (2004) pp. 315-316
27-29 October, 2004

Generation and detection of picosecond shear strain pulses with ultrashort light pulses

Osamu Matsuda, Oliver. B. Wright, *David H. Hurley, **Vitalyi E. Gusev, ***Kenichi Shimizu
(Graduate School of Engineering, Hokkaido University, Japan, *Idaho National Engineering and Environmental Laboratory, USA, **Faculté des Sciences, Université du Maine, France, ***University Chemical Laboratory, Keio University, Japan)

Gigahertz to terahertz ultrasonic pulses may be generated and detected with ultrashort optical pulses, allowing the inspection of the interior of nanostructures [1–4]. The generation mechanism in metals, for example, is dominated by thermal expansion. Detection is achieved through the photoelastic effect (the change in refractive index with strain) or through surface displacement monitoring when the ultrasonic pulse returns to the surface after reflection from interfaces or defects in the sample. Usually, with isotropic materials or symmetrically cut crystals, the constraints of symmetry imply that one only excites acoustic waves with longitudinal polarization. For a more complete ultrasonic inspection it would be advantageous to detect shear polarization as well [5]. Shear waves in isotropic solids, for example, give access to the elasticity tensor component c_{44} whereas longitudinal waves give access to c_{11}. In this paper we describe a new method for the direct and efficient optical excitation of picosecond shear ultrasonic pulses in anisotropic media. We also discuss a variety of optical detection configurations.

When the surface of a metal is heated by an ultrashort light pulse, an ultrasonic pulse of picosecond duration is launched in the depth direction through thermal expansion [1]. For arbitrarily cut anisotropic materials the allowed acoustic modes for this propagation direction (the z axis) are not pure longitudinal or shear in general. In particular, if the thermal expansion tensor is itself anisotropic an initial shear stress component can be generated directly. To test this idea we choose an anisotropic metallic substrate coated with a transparent isotropic film. This facilitates the analysis of the photoelastic detection in the isotropic film, which supports only pure shear or longitudinal polarizations. A detailed analysis reveals the following, assuming the x axis (**Fig. 1**) to lie within the plane of incidence [6,7]: 1) p-polarized probe light at *oblique incidence* must be used to detect shear strain in the film; 2) only η_4 shear strain can be detected (where η_I is the strain tensor in compact suffix notation); 3) η_4 scatters s-polarized to p-polarized light and vice versa; 4) a first order change in R ($\delta R \propto \eta_4$) can only be obtained by allowing the s and p polarized probe light to interfere (otherwise $\delta R \propto \eta_4^2$).

We choose for the substrate a uniaxial zinc single crystal (of the hexagonal system). The Zn is cut with a surface $\phi = 24°$ off the (0001) plane, close to the angle 28.8° calculated for maximum thermoelastic shear strain generation. The surface is trimmed with a diamond knife using an ultra-microtome to obtain a highly flat region. An amorphous silica film of thickness 1.1 μm is then rf sputtered on the Zn surface.

A mode-locked Ti:sapphire laser beam (the pump beam) of pulse duration 400 fs, repetition rate 76 MHz and wavelength 814 nm is focused onto the SiO_2-Zn interface with fluence of 0.05 mJ cm^{-2}. For our Zn crystal orientation the resulting z-propagating acoustic modes correspond to quasilongitudinal, quasishear, and pure shear polarizations. Defining the obliquely-oriented c-axis to be contained in the yz plane, only η_4 shear is generated. This strain component gives the dominant contribution to the quasishear mode in Zn for the propagation direction in question. The ultrasonic pulses generated are transmitted to the silica film and bounce backwards and forwards inside it.

For detection we use time-delayed frequency-doubled probe light pulses (of wavelength 407 nm) at 45° incidence with a similar fluence to that of the pump. Four different optical polarization geometries are used (see Fig. 1): p-u (s-u) denotes p (s) polarized incident light and no analyzer, whereas 45-s (45-p) denotes linearly polarized incidence characterized by a polarization axis at 45° to the plane of incidence and an inserted analyzer for s (p) polarized detection. Only 45-s and 45-p enables shear wave detection in the isotropic film.

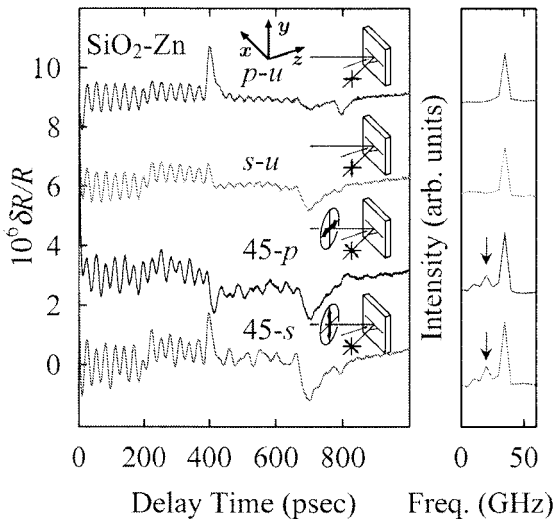

Figure 1: Transient relative reflectivity changes for an a-SiO_2 film on Zn and corresponding Fourier spectra for the first 200 ps. The probe beam polarization configurations are shown in the insets. The arrows indicate the Fourier components for shear acoustic waves.

Figure 1 shows the measured reflectivity variation $\delta R/R$, characterized by oscillations followed by echoes. We have subtracted a slowly varying background caused by temperature decay.

The echoes at 400 ps are due to the arrival of a (pure) longitudinal ultrasonic pulse, of central frequency $\sim$ 50 GHz and duration $\sim$ 20 ps, at the Zn substrate after reflection from the film top surface. The estimated longitudinal velocity $v_l \approx 5.5$ km s^{-1} in SiO_2 is consistent with previous results for sputtered films. Part of this ultrasonic pulse is reflected back into the SiO_2, and its second arrival at the Zn substrate produces inverted second echoes at 800 ps.

The echoes near 700 ps correspond to the arrival of the slower (pure) shear ultrasonic pulses at the Zn substrate. The ratio of the estimated shear velocity $v_t \approx 3.2$ km s^{-1} to v_l is as expected [8]. The relatively low crystal symmetry of Zn substrate allows us to detect the shear strain components regardless of the probe light polarization. The estimated central frequency of the shear pulses from our data is $\sim$ 17 GHz corresponding to a duration $\sim$ 60 ps.

The oscillations in the reflectivity arise from the interference between the light reflected at the surface or interface and the light reflected from the ultrasonic pulses in the transparent film [9,10]. The oscillation frequency f is related to the sound velocity v and probe wavelength λ through $f = 2nv\cos\theta/\lambda$, where n is the refractive index of the film and θ is the angle of probe optical incidence therein. For the p-u and s-u configurations, that prohibit shear ultrasonic pulse detection in the isotropic film, only the single frequency 35.0 GHz is observed, corresponding to the expected value for longitudinal waves (with $n = 1.47$, $\lambda = 407$ nm and $\theta \approx 16°$ from Snell's law). This is confirmed through the Fourier spectra obtained for 0 to 200 ps (Fig. 1). For the 45-s and 45-p configurations, that allow shear ultrasonic pulse detection in the film, we observe an extra frequency component at 20.0 GHz, evident not only in $\delta R/R$ as a 30% modulation in the amplitude envelope but also in the corresponding Fourier spectra in Fig. 1. The frequency is as expected with $v = v_t = 3.2$ km s^{-1}.

In conclusion, we have demonstrated the generation and detection of shear and quasishear ultrasonic pulses with ultrashort optical pulses in the picosecond time domain. In practice one can imagine the use of anisotropic films that are deposited on the material under investigation to play the role of picosecond shear ultrasonic transducers. This work should therefore lead to a useful tool for application in the nondestructive evaluation of nanoscale structures.

References

[1] C. Thomsen, H. T. Grahn, H. J. Maris, and J. Tauc, Phys. Rev. B 34 (1986) 4129.

[2] O. B. Wright and K. Kawashima, Phys. Rev. Lett. 69 (1992) 1668.

[3] B. Bonello, B. Perrin, E. Romatet, and J. C. Jeannet, Ultrasonics 35 (1997) 223.

[4] T. Saito, O. Matsuda, and O. B. Wright, Phys. Rev. B 67 (2003) 205421.

[5] D. H. Hurley, O. B. Wright, O. Matsuda, V. E. Gusev, and O. V. Kolosov, Ultrasonics 38 (2000) 470.

[6] O. Matsuda and O. B. Wright, Anal. Sci. 17 (2001) S216.

[7] O. Matsuda and O. B. Wright, Rev. Sci. Instrum. 74 (2003) 895.

[8] O. L. Anderson, in: Physical Acoustics, ed. W. P. Mason (Academic Press, New York, 1965) Vol. 3B, Chap. 2, p. 43.

[9] H. N. Lin, R. J. Stoner, H. J. Maris, and J. Tauc, J. Appl. Phys. 69 (1991) 3816.

[10] O. Matsuda and O. B. Wright, J. Opt. Soc. Am. B 19 (2002) 3028.

Proc. Symp. Ultrason. Electron., Vol. 25, (2004) pp. 317-318
27-29 October, 2004

Elastic anomaly of glass transitions in Lithium Silicate

◎Hushur Anwar & Seiji Kojima (Inst. Mat. Sci. Univ. Tsukuba.)

Masao Kodama (Dep. Chem., Sojo Univ.)

Ben Whittington, Marty Olesiak, Mario Affatigato & Steven A. Feller (Phys Dep. Coe College.)

1. Introduction

Silicate oxide is a typical strong glass with a strong network structure [1]. Its structure is the simplest of all glass structures [2,3]. The structural unit consists of slightly distorted SiO_4 tetrahedra with all bridging oxygens (BOs). A strongly connected three-dimensional network is established. The disorder in the structure is caused mainly by variations in the bond angles and the torsion angles. The introduction of alkali ions has strong influence on this network structure [4, 5]. It causes the break of Si-O bonds, and the increase of non-bridging oxygens and the reduction of connectivity in glass. In order to better understand the influence of the non-network elements on glass formation, it is useful to investigate their effects on the elastic property and the dynamical behavior related to the structure.

Brillouin scattering is the inelastic light scattering by acoustic phonon. We can easily determine the sound velocity and elastic constants by the measurement of the frequency shift of scattered light from a sample to be studied. Another feature of Brillouin scattering is the observation of broad Rayleigh wings which are related to gigahertz (GHz) dynamics. It has been a powerful tool to investigate acoustic properties and GHz dynamics of condensed matters, because it enables the non-contact and nondestructive measurement, which is very important to study a sample at low or high temperature or under high pressure.

2. Experimental

A series of lithium silicate glasses $JLi_2O{\cdot}SiO_2$ was prepared over an exceptionally wide range of values from J = 0.0~2.2 (0~69 mol.% lithium oxide), where J is the molar ratio of alkali oxide to silica. The process used to obtain excellent glasses with high homogeneity was already reported previously [6, 7].

A 3+3 pass tandem Fabry-Perot interferometer of high contrast combined with an optical microscope (Olympus BH-2) was used. Scattering was excited by an Ar^+ ion laser with a wavelength of 514.5 nm and power of 50 mW. A backscattering geometry of the experiments was employed. A conventional photon-counting system and multichannel analyzer were used to record and to average the signals. The sample was put in a cryo-stat cell (THMS 600) with temperatures varying from -190 °C to 600 °C and with a stability of ± 0.1 °C.

3. Results and Discussion.

The composition dependence of Brillouin scattering spectra was measured on the samples pure and J=0.3, 0,4, 0.5, 0.6 and 1.0 as shown in **Fig. 1**, where J is the molar ratio of alkali oxide to silica. The spectra show the doublet of Brillouin scattering components corresponding to longitudinal acoustic (LA) phonon. These Brillouin spectra were analyzed by the convolution of a Lorentzian spectral function with a Gaussian broadening function. The Brillouin shifts increased with the alkali concentration increases, obtained frequency shift is 33.4 GHz for pure silica, 38.2 GHz for J=0.6 and 40.1 GHZ for J=1.0. We measured the temperature dependence of Brillouin scattering spectra of the sample from J=0.3, 0,4, 0.5, 0.6 and 1.0. **Fig. 2.** shows the temperature dependent Brillouin shift and the full width at half maximum (FWHM) of sample J=0.5. We can clearly see that both Brillouin shift and FWHM show drastic changes. The slope below T_g depends on alkali concentration [8]. The marked decrease of Brillouin shift above T_g is similar as a B_2O_3 glass [9]. It might relate to the rapid increase of the free volume above T_g. Such a behavior is generally observed in glass transitions [10, 11]. Temperature dependence

◎Electronic mail: anwar@ims.tsukuba.ac.jp

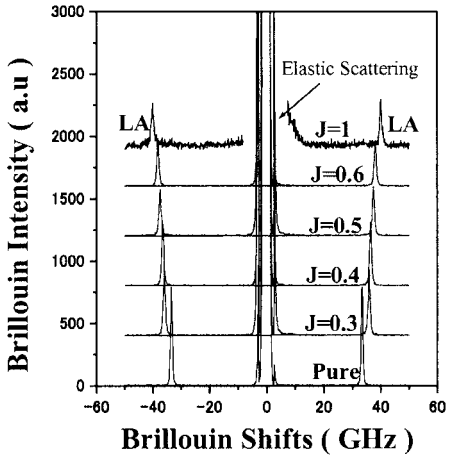

Figure 1 Concentration dependence of Brillouin scattering spectra at room temperature.

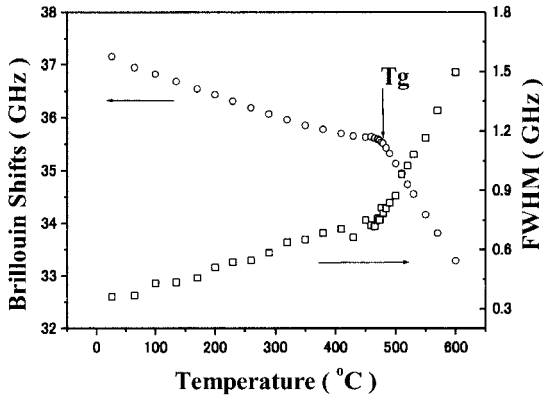

Figure 2 Temperature dependences of Brillouin shifts and FWHM in the sample J=0.5. Circles and squares denote Brillouin shifts and FWHM, respectively. The arrow indicates glass transition temperature.

of FWHM shows the remarkable increase above T_g. The damping of LA mode is strongly related to the structural relaxation, and its relaxation time diverges towards T_g on cooling from high temperatures. Since the frequency range of Brillouin scattering is about 30-40 GHz, the peak of FWHM may occur at about a few hundreds degree above T_g.

Summary

The temperature variation and composition dependence of elastic properties and fast relaxation process have been studied in lithium silicate glasses with different J =0.3, 0.4, 0.5, 0.6 and 1.0 by the micro-Brillouin scattering technique. The room temperature longitudinal elastic modulus increased significantly with increasing Li concentration indicating the additional cross-linking in network structure. the presence of the lithium does not break up the network, the part of the produced non-bridging oxygens brought in by the lithium oxides and result in additional cross-linking between network units. For all components (J=0.3~1.0), the rigidity decrease with increasing temperature. The rate of decrease becomes significantly stronger above the glass transition temperature. This is due to the disruption in network bonds, causing the rigidity of the melt structures to decrease with increasing temperature. The network degradation is more rapid with increasing lithium oxide concentration. The overall increase in full width half maximum of Brillouin peak reflects the thermally activated mechanism at the GHz frequency range, the transport of momentum responsible for viscous dissipation increase with temperature.

Acknowledgements

This work has been supported in part by the Grant-in Aid for Scientific Research (A) (No. 16204032) and 21th Century COE (Center of Excellence) Program from the Ministry of Education, Sports, Science and Culture, Japan.

References

[1] Nakayama T, Rep. Prog. Phys. **65** (2002) 1195-1205.
[2] A. C. Wright, G. A. N. Conell, J. W. Allen, J. Non-Cryst. Solids **42** (1980) 69.
[3] A. C. Wright, A. G. Clare, D. I. Grimley, R. N. Sinclair, J. Non-Cryst. Solids **112** (1989) 33.
[4] Lammert H, Kunow M, Heuer A, Phys. Rev. Lett. **90** (2003) 215901.
[5] MoIntosh C, Toulouse and Tick P, J. Non-Cryst. Solids **222** (1997) 335-341.
[6] Tischendorf B, Ma C, Hammersten E, Venhuizen P, Oeters M, Affatigato M, Feller S, J. Non-Cryst. Solids **239** (1998) 197-202.
[7] Feller S. A, Lower N and Affatigato M, Phys. Chem. Glasses **42** (2001) 1-4.
[8] Vaills Y, Luspin Y and Hauret G, J. Non-Cryst. Solids **286** (2001) 224-234.
[9] Youngman R. E, Kieffer J, Bass J. D and Duffrene L, J. Non-Cryst. Solids **222** (1997) 190-198.
[10] Ko J.-H and Kojima S, J. Non-Crys. Solids **307-310** (2002) 154-160.
[11] Ko J.-H and Kojima S, Phys. Lett. A, **321** (2004) 141-146.

Proc. Symp. Ultrason. Electron., Vol. 25, (2004) pp. 319-320
27-29 October, 2004

Polyacrylamide-Gel Based Phantom for Ultrasonic Elasticity Imaging

◎Ken-ichi Kawabata, Koji Waki*, Tsuyoshi Matsumura*, and Shin-ichiro Umemura
(Central Research Lab., Hitachi, Ltd., *Hitachi Medical Corp.)

Abstract

As a fundamental study for a tissue-mimicking phantom for ultrasound elastography stable and tunable elastic and echographic properties, we have investigated properties of polyacrylamide gel, a typical chemical gel which shows higher stability than physical gels such as gelatin or agar, as the base of phantom and metal oxide fine particles for controlling echogenicity of the gel. It was found that by changing the concentration of acrylamide in the gel in the range of 5 to 20%, gels with appropriate Young's moduli could be obtained and by changing the concentration of TiO2 in the range of 3 to 300 mg/ml, echogenicity was significantly modified in aqueous dispersion. These data suggest the possibility of tissue-mimicking phantom for ultrasonic elastography with polyacrylamide gels.

1. Introduction

Conventional anatomical diagnostic imaging modalities such as X-ray CT, MRI, and ultrasound scanner give information on dimensions of tissues or bone and very useful in real clinical settings and widely used.

Although the above anatomical imaging modalities are useful, there are still great demands for new modalities or methods which can give more information for conclusive diagnosis of diseases especially for those in early stages. Elastic property of tissue is one of such information. It has been recognized as very important information and performed as palpation to locate diseased parts. The problems of palpations are; 1) very subjective and 2) cannot applicable to deep-seated regions.

Ultrasonic elastography[1] is a method to image elastic properties by measuring tissues' deformation rate when external pressures are applied to tissues. Deformation rates are computed by using echographically obtained information. It can quantitatively visualize elastic properties of tissues and applicable to deep-seated regions.

The purpose of this study is to develop a tissue phantom for ultrasonic elastography which is stable and can finely adjust echographic as well as elastic properties.

Hydrogels are very similar in many aspects to tissues and often used for tissue phantom. There are two kinds of gels; one being physical gel which can be obtained by physical procedure such as heating up and cooling (eg: gelatin, agar), the other is chemical gel which can be obtained by chemical reaction such as polymerization (eg:, poly-acrylamide).

The former is preferred for elastic phantom provably because physical procedure is much simpler and safer than chemical ones. However, chemical gels are much more stable than physical ones. Thus we used polyacrylamide gel for the base of phantom which can be made by polymerization of acrylamide.

Gels do not usually scatter ultrasound and requires other components to be visualized echographically. For this purpose, fine particles of metal-oxides were used this time.

In this paper, the results on the investigation of conditions for making polyacrylamide based elastic tissue phantom will be presented.

2. Materials and Methods

· Chemicals: Titanium Dioxide (TiO_2 TN-90) was purchased from Ihsihara Sangyo Kaksha, Ltd., (Osaka, Japan). Chemical reagents for poly-acrylamide gel (acrylamide, bis-acrylamide, Ammonium Persulfate (APS), N,N,N',N'-tetramethylethylenediamine (TEMED)) were purchased from Wako Pure Chemical Industries, Ltd. (Osaka, Japan)

· Gel Preparation: Polyacrylamide gel was prepared as follows;

1) Dilute acrylamide stock solution (40 % (w/v) acrylamide: bis-acrylamide = 39:1) with deionized water and pour TiO2 particle

2) Degas 1) while stirring for 15-30 min

3) Add APS 4mg/ml-acrylamide solution and TEMED 1ml/ml-acrylamide solution

4) Pour 3) into vessels and seal with polyethylene films on an iced water bath

5) Leave 3) for about 10 min

·Elastic and Echographic Imaging: Imaging was performed with Ultrasound Scanner: EUB-6500 modified for elastography (Hitachi Medical Corp.) equipped a linear probe (EUP-L53).

· Young's Modulus Measurement: Young's modulus of gels were estimated by measuring the bending of gels by using an equipment similar to Ewing's apparatus

3. Results and Discussions

·Elastic Properties of Gels: Chemical gels as well as physical gels changes their elastic properties with the concentration of the matrix-consisting polymers. When the concentration of acrylamide was changed in the range from 5 to 20 %, the resulting gels were found to show Young's moduli in the range from 10 to 60 kPa. The value was thought to be adequate for tissue mimicking phantom because Young's moduli of prostate tissues reported are about the same values obtained this time[2].

·Echogenicity of TiO_2: Polyacrylamide gel itself has almost no echogenicity even at the boundary of gels with different concentrations. This time TiO_2 particles were used as ultrasound-scattering material. Fig. 1 shows the echographic images of TiO_2-dispersed water. As the concentration increases, the brightness of the gel increased.

·Gel Preparing Conditions: One significant difference between physical and chemical gels in preparation procedure as a tissue-mimicking phantom for ultrasonics is that the former uses high-viscous polymer solution and the latter low-viscous monomer solutions. This difference affects the dispersion of particles added for modifying echographic property of the gel. This time we dispersed TiO_2 fine particles into low-viscous acrylamide solutions. Due to the low viscosity, it is very easy to make uniform dispersion of TiO_2, but very difficult to prevent sedimentation without agitations. To develop a uniform gel phantom, we first investigated the influence of polymerization time on the resulting gel uniformity.

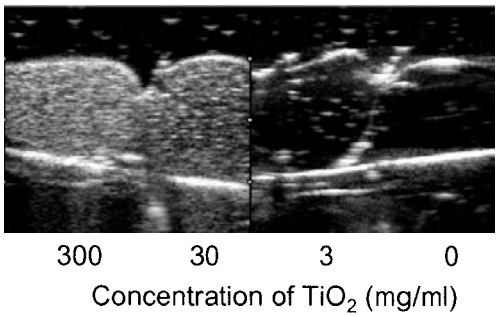

Fig. 1 Echographic image of TiO_2-dispersed water at different concentrations of TiO_2

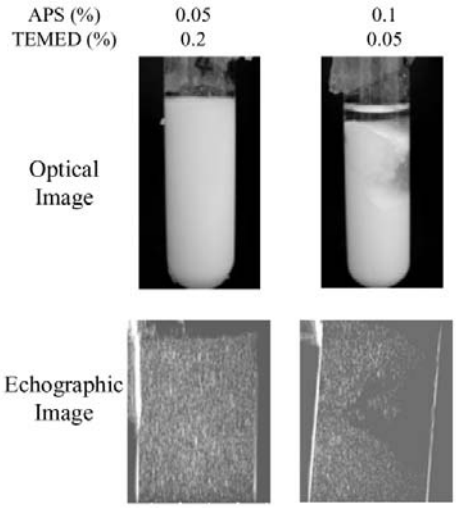

Fig. 2 Uniform(left) and non-uniform(right) gel containing TiO_2 particles

We observed optical and echographical uniformity when the concentration of APS and TEMED were changed. The two reagents are known to affect the polymerization time. Fig.2 shows typical uniform and non-uniform gels. It was found that the concentrations of APS and TEMED should be more than 0.05 and 0.1 percent, respectively.

Above results suggest that a tissue phantom with controlled echogenicity and elastic properties are possible with polyacrylamide gel.

References

1. Parker KJ, et al: IEEE Eng. Med. Biol. **15** (1996) 52.

2. T.A. Krouskop, et al: Ultrasonic Imaging, **20** (1998) 151

Proc. Symp. Ultrason. Electron., Vol. 25, (2004) pp. 321-322
27-29 October, 2004

Effects of Metal Particle Dopant on the Acoustic Attenuation Properties of Si Rubber Lens for Medical Echo Probe

(1 blank line)

○Yohachi YAMASHITA, Yasuharu HOSONO and Kazuhiro ITHUMI (Corporate R&D Center, Toshiba Corp.),

(2 blank lines)

1. Introduction

Medical array probe quality depends on not only active piezoelectric material but also passive materials such as backing, maching layers and acoustic lens materials (see Fig.1). In the case of a probe with center frequency of more than 7 MHz, the acoustic lens material is very important due to its large acoustic attunuation.

Silicone (Si) rubber, which is a material that can be safely used with humans and has a proper sound velocity (1,000m/s) and a reasonably low attenuation, has been applied for acoustic lens material. However, the density of pure Si rubber is about 1.0. So, acoustioc impedance AI (velocity x density) of pure Si rubber is about 1.0 MRalys, which is different from the AI of the human body, 1.5 MRalys. To increase AI of Si rubber, it has been doped with many inorganic dopants, such as fine partiles of SiO2, Al2O3 and TiO2.[1-7] Since these materials have relatively low density ranging from 2.2 to 4.2, it is necessary to dope 50-66wt% (15-30vol%) into Si rubber to obtain a density of more than 1.50. As a rusult, Si rubber shows a large acoustic attenuation of over 0.9 dB/mm@MHz.

In this study effects of heavy-metal particle dopants, such as platinum Pt (D=21.4), gold Au (D=19.3), tungsten W (D=19.3), palladium Pd (D=12), silver Ag (D=10.5) and nickel Ni (D=8.9), on the acoustic attenuation of Si rubber were investigated to obtain a low attenuation Si lens material.

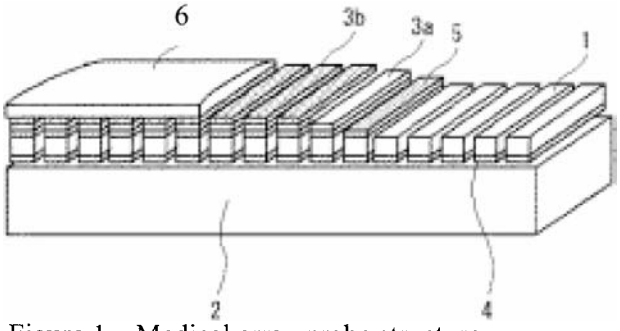

Figure 1 Medical array probe structure
1. Piezoelectric materials, 2. Backing material
3. 3a, 1st maching layers, 3b, 2nd maching layer
4. Bottom electrode, 5.Top electrode, 6. Lens

2. Development Concept

Figure 2 shows a development concept of a low attenuation Si rubber. Heavy metals such as Pt, Au, and W have high densities. Therefore, only 3 vol% doping of Si rubber realizes a density of 1.53. It is well known that the attenuation is proportional to dopant volume quantity. So, heavy metal dopant of Si rubber is one of the strategies for obtaining a low attenuation Si rubber.

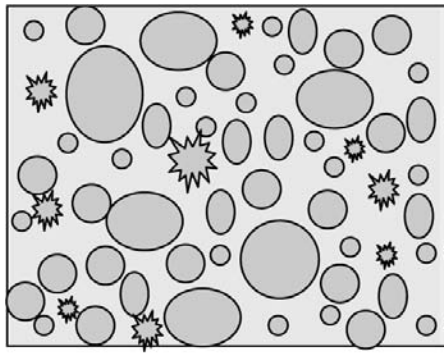

(A) 30vol% SiO_2 particle-doped Si rubber
Density=1.53

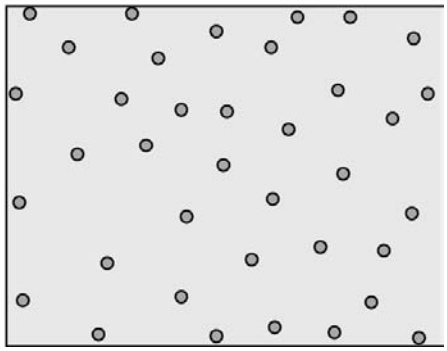

(B) 3vol% Au/W/Pt particle-doped Si rubber
Density=1.53

Fig.2 Concept of low-attenuation silicone rubber lens material. (A) Conventional SiO_2-doped Si rubber, (B) Heavy-metal-doped Si rubber lens material. These two materials have a same density.

3. Sample Preparation and Measurement

Silicone rubber TSE-3032 (GE Toshiba Silicone Co.) was the base material used. Seven dopant powders shown in Table I were added to the base Si rubber. The sample size is 30x30x1mm. The longitudinal wave velocity and attenuation were measured by a reflection method in water using 7.5 MHz probe.

4. Result and Discussion

Tables I and II show physical and acoustical properties of Si rubber with different dopants. Although Pt, Au and W have a similar bulk density, namely a similar volume quantity in the base Si rubber, Pt-doped Si rubber shows the lowest attenuation while those of Au and W doped Si rubber show the highest attenuation. This result indicates the attenuation is not dependent on volume of dopant but on type of metal particles.

It is well known that a smaller particle size dopant in the Si rubber shows a lower attenuation.[10] One of the reasons of the lower attenuation of Pt doped Si rubber is due to the smaller particle size of Pt (10nm) compared to Au (500nm) and W (700nm).

Table I Selected dopant for silicone rubber

Dopant type	Dopant density	Particle size(nm)	wt(%)	vol(%)	Rubber density
None					1.02
SiO2	2.2	16-2000	66	30	1.37
Ni	8.9	300	50.7	6.6	1.52
Ag	10.5	300	56.7	5.4	1.53
Pd	12	300	58.8	4.75	1.54
W	19.3	700	55.6	2.5	1.48
Au	19.3	500	55.6	2.85	1.53
Pt	21.5	10	55	2.55	1.52

Table II Acoustic properties of silicone rubber

Dopant type	Sound velocity(m/s)	Acoustic impedance (MRalys)	Attenuation (dB/mmMHz)	Figure of Merit
None	1025	1.06	0.5	513
SiO2	1015	1.39	0.92	934
Ni	931	1.42	1.2	1117
Ag	920	1.4	2.2	2024
Pd	880	1.39	0.94	827
W	1022	1.52	3.76	3843
Au	854	1.36	3.63	3100
Pt	858	1.37	0.84	721

Another important property of Pt-doped Si rubber is its low sound velocity of 858m/s. It is possible to fabricate thinner acoustic lens if the material has a low sound velocity and results in a high sensitivity compared to ordinary SiO2-doped Si rubber lens[11]. Therefore, Figure of Merit (FOM) for acoustic lens material is set and calculated by multiplying attenuation and velocity. Pt-doped Si rubber shows the best FOM as indicated in Table II.

5. Conclusion

The effects of heavy metal particle dopant on the acoustic attenuation properties of silicone rubber were investigated and the following results were obtained:

(1) Fine particle size, 10nm, Pt powder doping of Si rubber shows the lowest acoustic attenuation.
(2) Using particles of almost the same density, Au and W doping of Si rubber shows higher acoustic attenuation.
(3) Heavy metal dopants such as Au, Pt, Pd decrease sound velocity to lower than 900 m/s of Si rubber.
(4) Pt-doped Si rubber shows the following properties: density=1.52, sound velocity=858m/s, acoustic impedance=1.37Mralys and attenuation=0.84 dB/mm@MHz.
(5) Low attenuation and low sound velocity of Pt-doped Si rubber provides a better figure of merit for acoustic lens material of medical transducer.

References

1) K.Iinuma: Jpn. Pat. KOKAI Publication No. S-53-19869.
2) T.Hayasaka: Jpn. Pat. KOKAI Publication No. H08-615.
3) K.Matsuo: Japanese Patent No.1551320.
4) N.Shimamoto: Japanese Patent No. 1799240.
5) M.Sato and N.Shimamoto: Japanese Patent No. 3105151.
6) G.Vogel: USP5,505,205
7) K.Saito: Jpn. Pat. Appln. KOKAI Publication No. 2002-95081.
8) M.Matukawa and H. Sasaki:Chyouonpa Techno (Sep.10,2002,)p.61. in Japanese.
9) H. Wang, W. Cao and K.K.Shung: IEEE Transaction on UFFC,**48**(2001)78.
10) T.Kikuchi: Nihon Onkyou Gakkaishi, 35(1979).29.
11) R. E. McKeighen, Proc. SPIE (1999).

Proc. Symp. Ultrason. Electron., Vol. 25, (2004) pp. 323-324
27-29 October, 2004

Performance Characteristics of A 0.017 cc Linear Microactuator using Flexural Vibration in A Pair of Asymmetric Fins

Yasuyuki Gouda, James R. Friend, Kentaro Nakamura, and Sadayuki Ueha
(Tokyo Inst. of Tech.)

1. Introduction

The push for smaller and smaller actuators and sensors is the motivation for research on micromotion devices. In particular, piezoelectric actuators have been noted for their low positioning error and remarkable response time, among other features. However, most of these actuators have sizes measured in millimeters, and can use travelling waves generated from phased and paired standing waves, etc., to generate motion. However, at smaller scales, simplicity is key. In this research, we propose a novel small piezoelectric linear actuator, consisting of a 6061T6 aluminum vibrator, machined using electrodischarge machining, fastened to a specially-stepped PZT (lead zirconium titanate) element. Two fins are atop the vibrator body at oblique angles and in contact with a slider. The vibrator is designed so that elliptical motion is excited at the end of each fin. The thrust is generated by the elliptical motion of the fin through friction force. The key to the design is the use of two different masses on the tips of each fin to cause each fin to have slightly different flexural resonance frequencies. The vibrator is driven by a single-phase generator, and the moving direction can be changed by shifting the driving frequency from one fin resonance to the other. The longitudinal resonance of the PZT element is designed to lie between the flexural resonances of the fins. The authors made a very small 0.017 cc prototype, measured the admittance characteristics of the vibrator by using an impedance analyzer and examined the vibration velocity of the fins by using a laser Doppler vibrometer. Finally, using a highly-polished phosphor bronze slider, the motor operating characteristics were determined. At a driving frequency of 509 kHz, the motor moves to the right, while at 500 kHz, it moved to the left. Preliminary data shows the peak sliding velocity to be about 200 mm/s , respectively.

2. Construction

The ultrasonic microactuator's structure is shown in Fig. 1. This motor consists of a PZT element and a vibrator which is fixed at both ends. The PZT vibrates in the fundamental longitudinal mode, and, in this actuator,

E-mail Adress : gouda@sonic.pi.titech.ac.jp

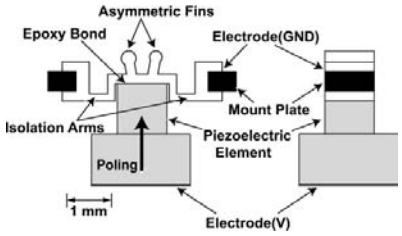

Figure 1: *The linear microactuator's structure.*

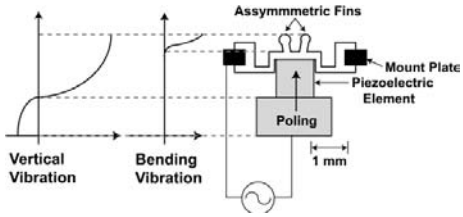

Figure 2: *The principle of the actuator's motion.*

the PZT's vibration is transformed by the slanted fins which are vibrating in their fundamental flexural mode. There is an inherent phase difference between the vertical and bending vibrations depending on the relative resonance frequencies of the bending vibration of each fin and the thickness vibration of the PZT, making it possible to excite vibration that is biased horizontally, and permitting the generation of sliding motion. Elliptical motion can be excited at the fin tips as shown in Fig. 2. The tip of each fin has a cylindrical mass, and the left fin tip has a slightly larger radius than the right fin tip. This causes the resonance frequencies of the left and right fin to be slightly different, allowing a slider pressed against the fin tips to move either right or left depending on the frequency due to a bias of the vertical displacement and therefore the friction forces between each fin tip and the slider.

3. Design and analysis

Using ANSYS, a finite-element analysis software package, the modal and harmonic characteristics of the actuator was estimated and used to choose appropriate values of the actuator's geometric parameters. A resonance frequency of 533 kHz was calculated for the PZT's thickness mode. In the actuator, the fins touch the slider and

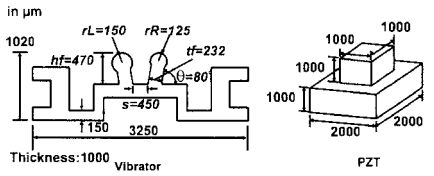

Figure 3: *The parameters of the actuator .*

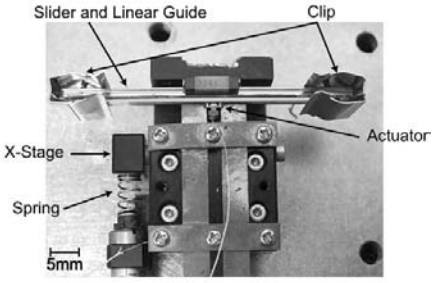

Figure 4: *Experimental setup.*

are central to transforming the motion from the element to move the slider, and so they are the most important parts in the vibrator. From this analysis , we chose each value as shown in Fig. 3.

4. Experiments

4.1. Vibration velocity measurement

A 2-D in plane laser Doppler vibrometer was used to measure the vibration velocity of the fins. The vibration velocity was measured from 450 kHz to 850 kHz and the applied voltage was 100 Vp-p. The fins vibrated most strongly at the 510 kHz, 520 kHz and 522 kHz. At these frequencies, each fin might have sufficient vibration velocity of over 1m/s to act as an ultrasonic actuator but the phase between the fins is also a factor.

4.2. Actuator performances

We measured the slider velocity as a function of the applied voltage for the preload of 0.42 N. As shown in Fig. 5, if the voltage is higher than 30 Vp-p, the velocity increases linearly, and about 200 mm/s was achieved at 100 Vp-p. Figure 6 shows the preload dependence of the velocity at 100 Vp-p. The preload of about 0.4 N gave the highset velocity. Using an experimental setup shown in Fig. 4, the slider operation was obtained between 502 kHz and 517 kHz. The slider moved fastest at 505 kHz. At 509 kHz, we measured the slider displacement for the number of cycles of the applied burst voltage. In this experiment, we used two sliders, phosphor bronze and alumina. As shown in Fig. 7, the minimum step was 33 nm for 10-cycle burst drive.

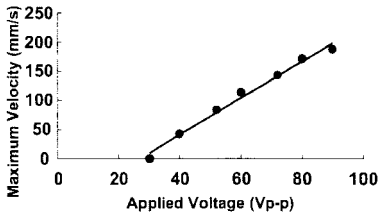

Figure 5: *Maximum velocity vs the voltage.*

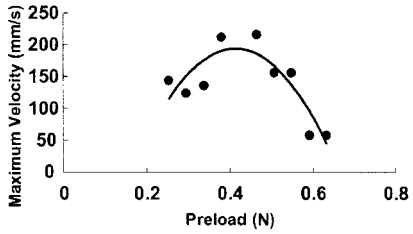

Figure 6: *Maximum velocity of the slider vs the preload.*

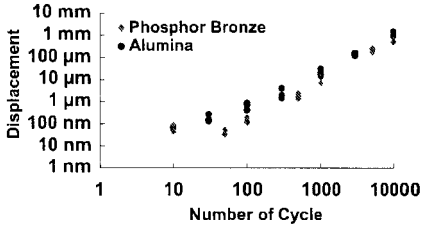

Figure 7: *Characteristic of Positionning Accuracy.*

5. Conclusions

According to initial measurements, the actuator generated 216 mm/s peak sliding velocity in the rightward direction and 108 mm/s peak sliding velocity in the leftward direction. For future work, the authors plan to make improvements on this design, and to reduce its size even further.

6. Acknowledgments

The authors would like to thank Suguru Wada, and Teruya Sugihara for their capable skills in machining the transducer, and the financial support of the Japanese Society for the Promotion of Science.

7. References

[1] Roy R. Craig, Jr "STRUCTURAL DYNAMICS – An Introduction to Computer Methods", John Wiley and Sons :189-192, 207-210 1984.

[2] K, Nakamura et al., IEEE, T-UFFC, 38(5) pp. 481–485 1991.